University of Technology Sydney

Development of Lithium-Ion Battery State Estimation Techniques for Battery Management Systems

Linfeng Zheng

M.E. (Electrical Engineering), B.E. (Electrical Engineering)

School of Electrical and Data Engineering

University of Technology Sydney, Australia

A thesis submitted for the Degree of

Doctor of Philosophy

July 2018

CERTIFICATE OF ORIGINAL AUTHORSHIP

I certify that the work in this thesis has not previously been submitted for a degree nor has it been submitted as part of requirements for a degree except as part of the collaborative doctoral degree and/or fully acknowledged within the text.

I also certify that the thesis has been written by me. Any help that I have received in my research work and the preparation of the thesis itself has been acknowledged. In addition, I certify that all information sources and literature used are indicated in the thesis.

Signature of Student: Production Note: Signature removed prior to publication.

Date: 31/07/2018

ACKNOWLEDGEMENTS

First and foremost, I would like to express sincere gratitude to my supervisors, Professor Jianguo Zhu and Professor Guoxiu Wang, for their forward guidance, invaluable encouragement and unwavering support during my candidature. I am also thankful to Associate Professor Dylan Dah-Chuan Lu for his insightful and constructive inputs and help to improve the quality of my work. It is a great honor for me to have the opportunity to learn from and work with them.

I greatly appreciate the helpful advices and technical support from my colleagues and friends in the Centre for Green Energy and Vehicular Innovations, Centre for Clean Energy Technology, Centre for Electrical Machines and Power Electronics, University of Technology Sydney (UTS), etc. in particular Associate Professor Youguang Guo, Dr. Jane Yao, Dr. Lei Zhang, Dr. Gang Lei, and Mr. Shane Chen.

I would also like to acknowledge the National Active Distribution Network Technology Research Centre, Beijing Jiaotong University, for the prior work on battery tests. The financial supports from the Automotive Australia 2020 Cooperative Research Centre (AutoCRC), the Rail Manufacturing Cooperative Research Centre (RMCRC), and the International Research Scholarship (IRS) from UTS for this research are gratefully acknowledged.

Last but not least, I am highly obliged for the unconditional love and support given by my beloved parents and wife. Without the countless encouragement and trust from them in the past several years, I could not have achieved this.

TABLE OF CONTENTS

LIST OF SYMBOLS

c_e	Lithium-ion concentration in electrolyte
c_s	Lithium-ion concentration in solid electrode
c_{sd}	Discretised lithium-ion concentration in solid electrode
c_{suf}	Surface lithium-ion concentration
$c_{s,max}$	Maximum possible solid-phase lithium-ion concentration
c_{s_mean}	Mean lithium-ion concentration in solid electrode
c_{s_total}	Total number of lithium-ions in solid electrode
DCR	Battery direct current resistance
D_e	Lithium-ion diffusion coefficient in electrolyte
D_s	Lithium-ion diffusion coefficient in solid electrode
E_a	Maximum available energy
F	Faraday's constant
I	Battery loading current
$I_{D,max}$	Maximum discharge current
$I_{C,min}$	Minimum charge current
i_e	Local current in the electrolyte
i_0	Exchange current density
j_n	Molar flux
n_p	The number of cells connected in parallel
n_s	The number of cells connected in series
P_{chg}	Charge power capability
$P_{C,min}$	Minimum charge power
P_{dis}	Discharge power capability
$P_{D,max}$	Maximum discharge power
P_{Gibbs}	Battery Gibbs power
P_{inst}	Battery instantaneous available power
P_{res}	Power dissipation in battery internal resistance
Q_0	Battery initial capacity

Q_a	Battery actual capacity
Q_N	Battery nominal capacity
R^2	Coefficients of determination
R_c	Empirical contract resistance
R_p	Radius of spherical solid particles
r_{eff}	Kinetic rate constant
SOC	Battery state of charge value
SOE	Battery state of energy value
T	Absolute temperature
T_{bas}	Based temperature
U	Cell terminal voltage
V_{max}	Permitted maximum cell terminal voltage
V_{min}	Permitted minimum cell terminal voltage
V_{OCV}	Open circuit voltage
η_s	Over potential
Φ_s	Electric potential in solid electrode
Φ_e	Electric potential in the electrolyte
ΔQ	Cumulative capacity

LIST OF ABBREVIATIONS

ADB	Active discharge balance
AEKF	Adaptive extended Kalman filter
BMS	Battery management system
CB	Charge balance
CC	Constant current
CDB	Charge-discharge balance
CV	Constant voltage
DCR	Direct current resistance
DEKF	Dual extended Kalman filter
DST	Dynamic stress test
DV	Differential voltage
DVA	Differential voltage analysis
ECM	Electrical circuit model
EKF	Extended Kalman filter
EM	Electrochemical model
EOC	End of charge
EOD	End of discharge
EV	Electric vehicle
FL	Fuzzy logic
FP	Feature point
GHG	Greenhouse gas
HPPC	Hybrid pulse power characterization
IC	Incremental capacity
ICA	Incremental capacity analysis
KF	Kalman filter
LS	Least-square
MAE	Maximum absolute error
MAPE	Mean absolute percentage error

MPC	Model predictive control
NN	Neural network
NPF	Nonlinear predictive filter
OCV	Open circuit voltage
PDB	Passive discharge balance
PDE	Partial differential equation
PF	Particle filter
PI	Proportional-integral
RE	Relative error
RMSE	Root mean square error
SEI	Solid-electrolyte interphase
SMO	Sliding-mode observer
SOC	State of charge
SOE	State of energy
SOH	State of health
SOP	State of power
SPM	Single particle model
SVM	Support vector machine
SVR	Support vector regression
UDDS	Urban dynamometer driving schedule

LIST OF FIGURES

LIST OF TABLES

ABSTRACT

Lithium-ion batteries are being widely used as an enabling energy storage for electric vehicles, renewable energy storage systems, and power grids, etc., as they always exhibit high energy density and long life cycle along with environmental friendliness. However, overly pessimistic or optimistic estimates of lithium-ion battery states would result in waste or abuse of battery available capabilities and may even lead to fire and explosion risks. The safety and reliability of battery utilization necessitate the accurate and reliable state estimation techniques in battery management systems (BMSs). This thesis focuses on the development of the estimation methods of lithium-ion battery states of interest, which are capable of determining internal battery status accurately.

The first phase of this thesis centers on battery electrochemical model simplification and discretization for incorporating the co-estimation algorithm of battery state of charge (SOC), capacity, and resistance based on the proportional-integral (PI) observers. A physics-based battery model that has the capability to describe the electrochemical reaction process inside the battery is first developed. Trinal PI observers are then employed to implement the co-estimation task. It takes the influence of battery aging on SOC estimation by furnishing the state equations with up-to-date capacity and resistance estimates into account, thereby improving the SOC estimation accuracy.

To achieve high estimation accuracy with low computation costs, SOC and capacity estimation approaches based on the incremental capacity analysis and differential voltage analysis are subsequently investigated. Feature points extracted from the SOC based incremental capacity/differential voltage (DV) curves are applied for developing the estimation algorithm of battery SOC and capacity. Besides, an extended Kalman filter and a particle filter are served as the state observers in an SOC estimator based on the DV model for further improving the performance of estimation.

With the credible SOC estimates, a state of energy (SOE) estimator based on a quantitative relationship between SOC and SOE is proposed in the next step, and a

moving-window energy-integral technique is then incorporated to estimate the battery maximum available energy. Through the analysis of ambient temperature, battery discharge/charge current rate, and cell aging level dependencies of SOE, the relationship between SOC and SOE can be quantified as a quadratic function for SOE estimation. The simplicity of the proposed SOE estimation method can avoid the heavy computation cost required by the conventional model-based SOE estimation methods.

Finally, two state of power capability predictors are designed for a battery to sufficiently absorb or deliver a certain amount of power within its safe operating region. A battery direct current resistance model for quantitatively describing its temperature dependence is proposed and implemented on the battery capability prediction in the first method, which is beneficial to reduce the memory-consumption and dimension of the power characteristic map embedded in BMSs for applications. Different from the conventional methods using the limits of macroscopically observed variables for power prediction, the second method investigates a physical mechanism-based power prediction method and quantifies the relationship between battery power capability and surface lithium concentration for instantaneous peak power prediction. The proposed methods are experimentally verified with various cell aging levels and ambient temperatures.

The proposed approaches for accurately modelling and estimating lithium-ion battery states in this thesis can contribute to safe, reliable and sufficient utilization of the battery. The developed methods are pretty general, and therefore are promising to provide valuable insight to the investigations of other types of batteries with various chemistries.

CHAPTER 1

INTRODUCTION

1.1 Background and Significance

Global climate change and energy supply shortages are now problems of paramount concern. To cope with the climate change caused by the extensive greenhouse gas (GHG) emissions, the Paris Agreement, announced in December 2015 and enforced in November 2016 by the United Nations, clearly set the objective of mitigating the GHG emissions and limiting the global average temperature increase below 2 °C [1.1], [1.2]. This ambitious objective is highly unlikely to be achievable without a significant contribution from the transport sector, which accounts for about 23% of global GHG emissions [1.2].

With the merits of zero or low emissions and high energy efficiency, electric vehicles (EVs), primarily the pure battery EVs and plug-in hybrid EVs, are acknowledged as a major contributor to the goal of GHG emissions reduction in the transport sector [1.3]-[1.6], and have attracted tremendous attentions around the world. Fig. 1.1 depicts the EV stocks from 2011 to 2016 in different countries and their target stocks in 2020, where the EV stocks present a remarkable increase during this period, especially in China. The global EV stock surpassed 2 million vehicles in 2016, and it aspires to bring 13 million EVs on the road by 2020 [1.2], [1.3]. The development of EVs is also beneficial to a reduction of air pollutant emissions in the up-and-coming urbans with ever-growing populations. Besides, EVs, acting as mobile energy storage systems, are regarded as eminent resources for smart grid, due to their potential bidirectional power flow capabilities and high degrees of flexibility [1.7], [1.8].

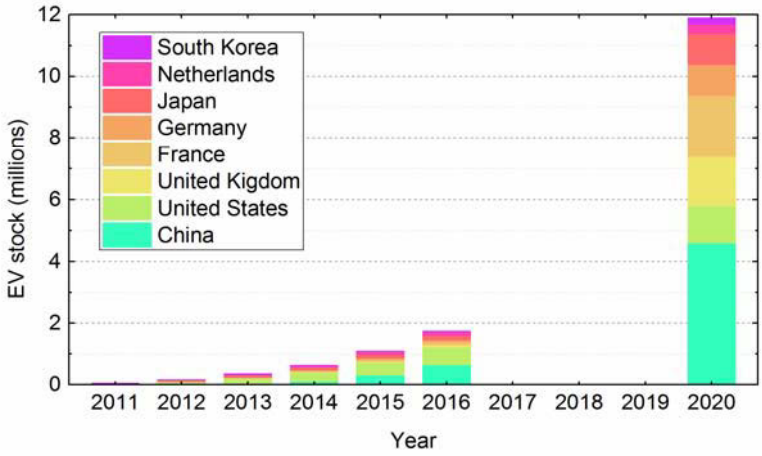

Fig. 1.1 Evolution of the EV stock from 2011 to 2016 in different countries and their target stock in 2020 (data sources from [1.2] and [1.3]).

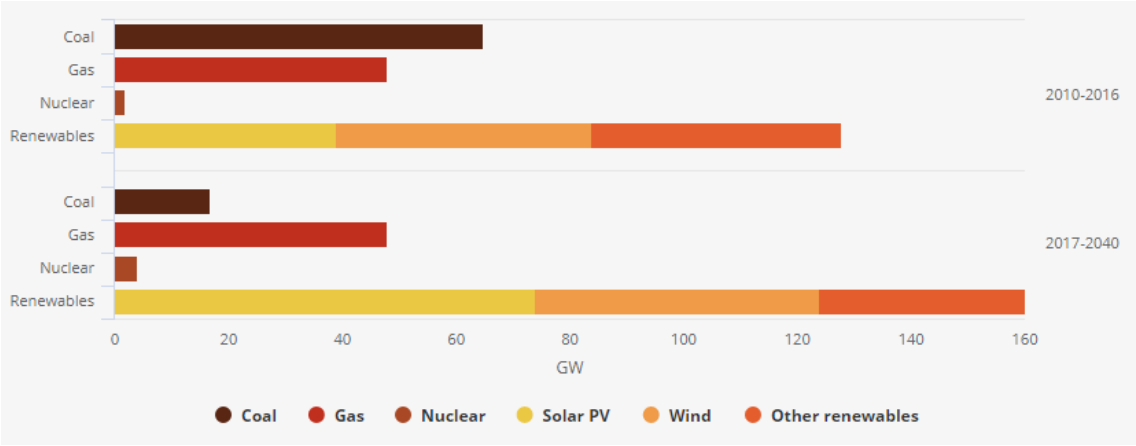

Fig. 1.2 Global average annual net capacity additions by type (from [1.9]).

Another solution for addressing the global issue of climate change as well as the energy supply shortages is provided by exploiting renewable energies [1.10]. Renewable energy is collected from renewable sources that are continually replenished by nature in a human timescale such as sunlight, wind, tides, and geothermal heat. Global electricity generation from renewable energy sources has been growing sharply over the past several years [1.11]. Fig. 1.2 illustrates the global average annual net capacity additions of renewables and conventional energy sources including coal, gas and nuclear. It is anticipated that renewables will be the undisputed energy growth leader in the next 20 years. The rapid

development of renewable energy is resulting in significant benefits in both environment and economy sectors [1.11], [1.12].

All of these trends rely heavily on efficient storage and supply of electric energy [1.10]. One promising candidate for this is the lithium-ion battery, which attributes to its strengths including high energy density, high efficiency, long life cycle, and environmental friendliness [1.13]-[1.15]. The comparisons of energy and specific densities between the lithium-ion battery and other types of batteries are depicted in Fig. 1.3, where the lithium-ion battery exhibits superior gravimetric and volumetric energy densities. In fact, lithium-ion batteries are considered to be the most promising traction batteries for the next-generation EVs, and have been deployed in megawatt-scale renewable energy storage systems for supporting power grids [1.15]-[1.17].

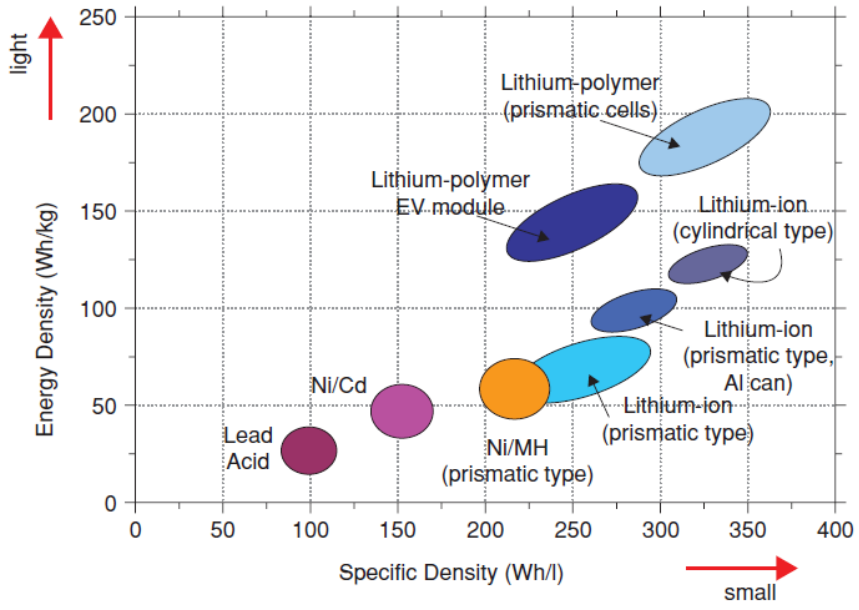

Fig. 1.3 Comparison between different kinds of batteries in terms of energy and specific densities (from [1.18]).

Notwithstanding the desirable performance of lithium-ion battery technology, the reliability, safety, and longevity of lithium-ion battery utilization necessitate an effective and dependable battery management system (BMS) for battery data acquisition, state estimation, and charge/discharge control, etc. [1.19]-[1.23]. Although the functional

requirement of BMS appears to be a more sophisticated and complex trend [1.24], the estimation of battery states is still one of the most crucial challenges in BMSs due to the nonlinear battery characteristics and unpredictable operating conditions [1.25], [1.26]. Overly pessimistic or optimistic estimates of battery states would result in waste or abuse of battery available capabilities [1.27] and could even lead to fire and explosion risks. Accordingly, it is indispensable to develop accurate estimation methods of lithium-ion battery states of interest for BMSs in EVs, renewable energy storage systems, etc., and this is the research focus of this thesis.

1.2 Research Objectives

This thesis aims at developing accurate and reliable estimation methods of lithium-ion battery states of interest, which are capable of determining the internal battery status accurately for safe, reliable, and efficient battery utilization. The main research objectives of this thesis can be described as follows:

- A comprehensive literature survey on the state-of-the-art techniques, challenges and development of BMS and state estimation,
- Development of a high-fidelity battery model as accurate modeling plays a fundamental role in ensuring reliable state estimation,
- Development of battery state of charge (SOC) estimation and actual capacity estimation methods since the state of health (SOH) of a battery is usually represented by its actual capacity,
- Investigation of the incremental capacity analysis and differential voltage analysis techniques since they are capable of analyzing the aging mechanisms of a battery and promising for states estimation, and
- Analysis of the temperature and cell aging dependencies of battery energy and power capabilities, and development of battery state of energy (SOE) and state of power (SOP) estimation methods.

1.3 Outline of Thesis

The background and significance of this thesis as well as its research objectives have been illustrated in this chapter (Chapter 1). The remainder of this thesis is organized as follows.

In Chapter 2, a critical review of the BMS development and estimation techniques of four lithium-ion battery states of interest including SOC, SOH, SOE, and SOP in literature is presented. The focus for each estimation technique is not to detail its solution, but rather to elaborate on its key idea, strengths, and weaknesses as well as its possibilities for improvement.

In Chapter 3, trinal proportional-integral (PI) observers with a reduced physics-based electrochemical model are proposed for an accurate and simultaneous estimate of battery SOC, capacity and resistance. A numerical solution for the employed model is firstly derived, and PI observers are then developed to realize the co-estimation. The moving-window ampere-hour counting technique and the iteration-approaching method are also incorporated for the estimation accuracy improvement.

In Chapter 4, battery SOC and capacity estimation methods based on incremental capacity analysis and differential voltage analysis are proposed and evaluated. Feature points extracted from the SOC based incremental capacity/differential voltage (DV) curves are applied for developing the estimation algorithm of battery SOC and capacity. Besides, an extended Kalman filter and particle filter are employed as the state observers in a DV model based estimator to improve further the performance of SOC estimation.

In Chapter 5, a quantitative relationship between SOE and SOC is proposed for SOE estimation, and a moving-window energy-integral technique is incorporated to estimate the battery maximum available energy. The ambient temperature, battery discharge/charge current rate, and cell aging level dependencies of the battery maximum available energy and SOE are comprehensively analyzed. The robustness and feasibility of the proposed approaches are validated by test results of different operating conditions during battery aging processes.

In Chapter 6, two power capability prediction approaches based on the battery direct current resistance (DCR) model and battery electrochemical model, respectively, are proposed for lithium-ion batteries. Through the analysis of battery DCR values at different SOCs and temperatures, a DCR model for quantitatively describing its temperature dependence is proposed and implemented on a battery power predictor in the first method. Differing from the conventional methods using the limits of macroscopically observed variables for power prediction, the second method investigates a physical mechanism-based power prediction method and quantifies the relationship between the battery power capability and surface lithium concentration for instantaneous peak power prediction. The proposed methods are experimentally verified by experiments at various cell aging levels and ambient temperatures.

The conclusions of this thesis are finally drawn in Chapter 7, and the potential research works that require further investigations are also highlighted.

References

[1.1] United Nations, "Paris Agreement," 2015.

[1.2] International Energy Agency, “Global EV Outlook 2017: Two million and counting,” 2017.

[1.3] International Energy Agency, “Global EV Outlook 2016: Beyond one million electric cars,” 2016.

[1.4] S. Vazquez, S. M. Lukic, E. Galvan, L. G. Franquelo, and J. M. Carrasco, "Energy Storage Systems for Transport and Grid Applications," *IEEE Transactions on Industrial Electronics*, vol. 57, no. 12, pp. 3881-3895, 2010.

[1.5] G. Xu, C. Zheng, Y. Zhang, K. Xu and J. Liang, "Energy efficiency of electric vehicles – energy saving and optimal control technologies," *INTECH*, 2015, http://dx.doi.org/10.5772/59420.

[1.6] K. T. Chau and C. C. Chan, "Emerging energy-efficient technologies for hybrid electric vehicles ", *Proceedings of the IEEE*, vol. 85, no. 4, pp. 821-835, 2007.

[1.7] R. Yu, W. Zhong, S. Xie, C. Yuen, S. Gjessing and Y. Zhang, "Balancing power demand through EV mobility in vehicle-to-grid mobile energy networks," *IEEE Transactions on Industrial Informatics*, vol. 12, no. 1, pp. 79-90, 2016.

[1.8] K. Knezovi´c, S. Martinenas, P. B. Andersen, A. Zecchino and M. Marinelli, "Enhancing the tole of electric vehicles in the power grid: field validation of multiple ancillary services," *IEEE Transactions on transportation electrification*, vol. 3, no. 1, pp. 201-209, 2017.

[1.9] International Energy Agency, "World Energy Outlook 2017," available at http://www.iea.org/weo2017/#section-1-1 (accessed on 06/12/2017).

[1.10] J. Illig, "Physically based impedance modelling of lithium-Ion cells," Ph.D. Thesis, Karlsruhe Institute of Technology, Karlsruhe, Germany, 2014.

[1.11] O. Ellabban, H. Abu-Rub and F. Blaabjerg, "Renewable energy resources: current status, future prospect sand their enabling technology," *Renewable and Sustainable Energy Reviews*, vol. 39, pp. 748-764, 2014.

[1.12] International Energy Agency, “Energy Technology Perspectives 2012: Pathways to a Clean Energy System,” 2012.

[1.13] J. Cho, S. Jeong and Y. Kim, "Commercial and research battery technologies for electrical energy storage applications," *Progress in Energy and Combustion Science*, vol. 48, pp. 84-101, 2015.

[1.14] C. Zhang, Y. Wei, P. Cao and M. Lin, "Energy storage system: Current studies on batteries and power condition system," *Renewable and Sustainable Energy Reviews*, 2017, https://doi.org/10.1016/j.rser.2017.10.030.

[1.15] X. Hu, C. Zou, C. Zhang, and Y. Li, "Technological developments in batteries: a survey of principal roles, types, and management needs", *IEEE Power and Energy Magazine*, vol. 15, no. 5, pp. 21-31, 2017.

[1.16] A. Opitz, P. Badami, L. Shen, K. Vignarooban and A.M. Kannan, "Can Li-Ion batteries be the panacea for automotive applications?," *Renewable and Sustainable Energy Reviews*, vol. 68, pp. 685-692, 2017,

[1.17] J. Arteaga, H. Zareipour and V. Thangadurai, "Overview of lithium-ion grid-scale energy storage systems," *Current Sustainable/Renewable Energy Reports*, vol. 4, no. 4, pp. 197-208, 2017.

[1.18] B. Scrosati, K. M. Abraham, W. van Schalkwijk, and J. Hassoun, "Lithium Batteries: Advanced Technologies and Applications," First Edition, John Wiley & Sons, Inc., 2013.

[1.19] M. T. Lawder, B. Suthar, P. W. C. Northrop, S. De, C. M. Hoff, O. Leitermann, M. L. Crow, S. Santhanagopalan and V. R. Subramanian,"Battery energy storage system (BESS) and battery management system (BMS) for grid-scale applications," *Proceedings of the IEEE*, vol. 102, no. 6, pp. 821-835, 2014.

[1.20] H. Rahimi-Eichi, U. Ojha, F. Baronti and M. Chow, "Battery management system: an overview of its application in the smart grid and electric vehicles" *IEEE Industrial Electronics Magazine*, vol. 7, no. 2, pp. 4-16, 2013.

[1.21] L. Lu, X. Han, J. Li, J. Hua and M. Ouyang, "A review on the key issues for lithium-ion battery management in electric vehicles," *J. Power Sources*, vol. 226, pp. 272-288, 2013.

[1.22] B. Sun, J. Jiang, F. Zheng, W. Zhao, B. Y. Liaw, H. Ruan, Z. Han and W. Zhang, "Practical state of health estimation of power batteries based on Delphi method and grey relational grade analysis," *J. Power Sources*, vol. 282, pp. 146-157, 2015.

[1.23] Z. Wei, C. Zou, F. Leng, B. H. Soong and K. J. Tseng, "Online model identification and state of charge estimate for lithium-ion battery with a recursive total least squares-based observer," *IEEE Transactions on Industrial Electronics*, 2017, DOI 10.1109/TIE.2017.2736480.

[1.24] W. Zhang, W. Shi and Z. Ma, "Adaptive unscented kalman filter based state of energy and power capability estimation approach for lithium-ion battery," *J. Power Sources*, vol. 289, pp. 50-62, 2015.

[1.25] L. Zheng, J. Zhu, G. Wang, T. He and Y. Wei, "Novel methods for estimating lithium-ion battery state of energy and maximum available energy," *Appl. Energy*, vol. 178, pp. 1-8, 2016.

[1.26] L. Zheng, L. Zhang, J. Zhu, G. Wang and J. Jiang, "Co-estimation of state-of-charge, capacity and resistance for lithium-ion batteries based on a high-fidelity electrochemical model," *Appl. Energy*, vol. 180, pp. 424-434, 2016.

[1.27] J. Jiang, S. Liu, Z. Ma, L. Y. Wang, K. Wu, "Butler-Volmer equation-based model and its implementation on state of power prediction of high-power lithium titanate batteries considering temperature effects," Energy, vol. 117, pp. 58-72, 2016.

CHAPTER 2

LITERATURE REVIEW

2.1 Introduction

Lithium-ion batteries are favorable in energy storage applications, such as electric vehicles (EVs), railway transportation systems, renewable energy systems, and smart grids, etc., due to their superior performance in energy density, power density, lifetime, columbic efficiency, and voltage plateau in comparison with the lead-acid, nickel-metal hydride (NiMH), and nick-cadmium (NiCd) batteries [2.1], [2.2]. The reliability, safety, and longevity of lithium-ion battery operations necessitate an efficient battery management system (BMS) with advanced techniques.

The number of research articles of BMS techniques published in journals and conferences have been increasing rapidly in recent years [2.3], especially on battery states estimation. It is worthwhile to summarize systemically the states estimation techniques for BMS practitioners, in the hope of providing some inspiration for their work. Conducted by an up-to-date literature survey in combination with practical applications, this chapter gives a technical review on the development of BMS and key states estimation methods for lithium-ion batteries.

2.2 Battery Management System

In the 1990s, the BMS was developed for monitoring the operation status of lead-acid batteries [2.4], [2.5]. At this stage, the acquisition of battery parameters, including the voltage, current and temperature, and battery charge/discharge control were the main functions of BMSs, and the state of charge (SOC) was mainly indicated by the cell terminal voltage and open circuit voltage [2.4]-[2.6].

From the 2000s, combined with battery models, state observers were developed for lithium-ion battery SOC estimation [2.7], [2.8]. In the following work, different

algorithms were proposed for estimating/predicting more battery states such as state of health (SOH), state of energy (SOE), and state of power (SOP).

In the early 2010s, multiple sampling channels for cell voltage and temperature measurement were commercially integrated as a single chip such as LTC6802 [2.9], BQ76PL536 [2.10], MAX11068 [2.11], etc., which significantly reduces the size and cost of BMSs. Until now, the functional requirement of BMS appears to be a more sophisticated and complex trend [2.12], and the core functions of BMS mainly include cell and pack monitoring and protection, states estimation, cell balancing, thermal management, charge/discharge control, and data communication and record, as shown in Fig. 2.1.

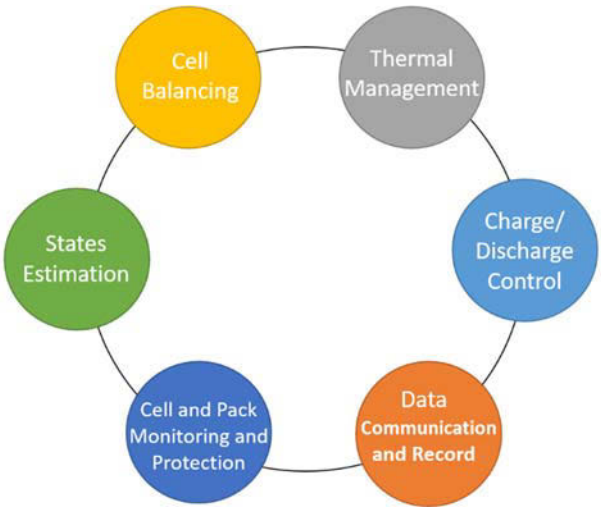

Fig. 2.1 Core functions of BMSs.

Overly pessimistic or optimistic estimates of battery states would result in waste or abuse of battery available capabilities, even lead to fire and explosion risks. This work focuses on the development of battery states estimation methods that are capable of determining internal battery status accurately for the safe, reliable and efficient battery utilization. The battery states of interest include:

- State of charge (SOC) which is a quantity describing the stored charge capability of the battery,

- State of health (SOH) which is a quantity describing the aging level of the battery,
- State of energy (SOE) which is a quantity describing the stored energy capability of the battery, and
- State of power (SOP) which is a quantity describing the delivered or absorbed power capability of the battery.

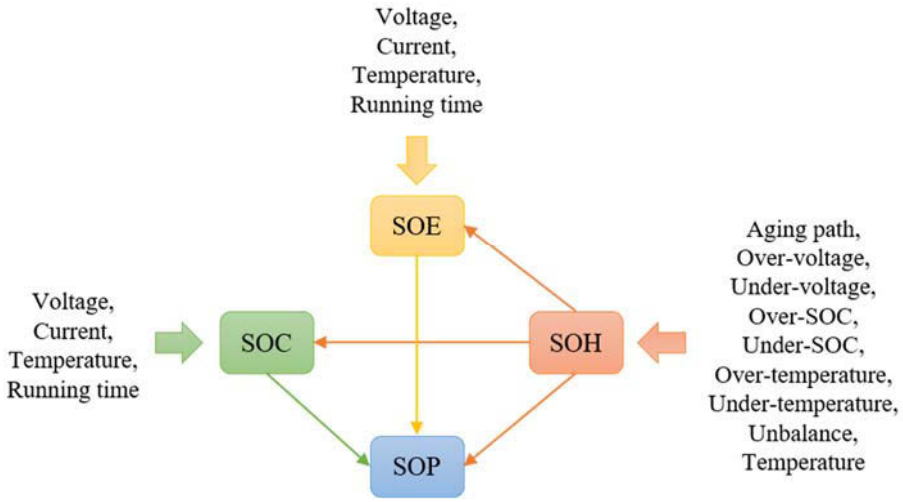

Fig. 2.2 Relationships of battery states.

The relationships and affected factors of the battery states of interest are shown in Fig. 2.2. The SOC is determined by cell terminal voltage, loading current, cell temperature, operating time, and battery aging level, and the SOC usually has fast time-varying dynamics. Likewise, the SOE is also determined by these factors. Traditionally, the SOC is regarded as an indicator of battery available energy. Defined as the ratio of the remaining charge stored in a battery to its full capacity, however, the SOC actually indicates the state of available capacity rather than the state of available energy. The SOE is therefore required for indicating the state of available energy of the battery. The SOH is governed by the aging path of the battery and operating conditions such as fault states and ambient temperature, which is slow time-varying. The SOP is dependent on SOC/SOE and SOH. In particular, the SOP has a short prediction horizon which is

typically limited between 1 s and 20 s [2.13]. The reported techniques for different states estimation/prediction are elaborated in the following parts.

2.3 State of Charge Estimation

Defined as the ratio of the remaining charge to the full charge stored in a battery, the SOC, represents a "fuel gauge" and is an indispensable indicator for the safe operation of batteries. A high number of approaches for estimating battery SOC have been proposed in literature, most of which are classified in Fig. 2.3.

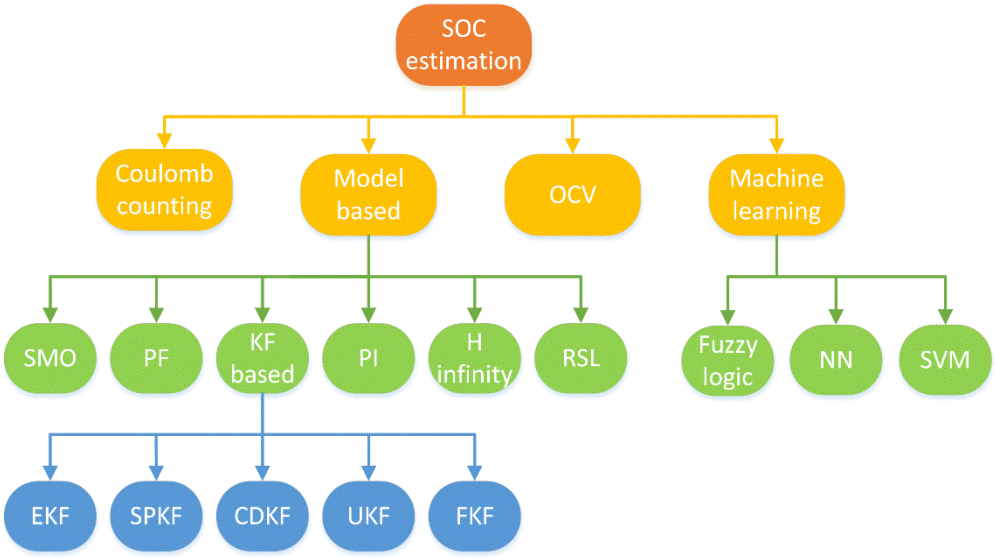

Fig. 2.3 Classification of the approaches for estimating battery SOC.

2.3.1 Coulomb-counting method

Coulomb-counting, also called Ampere-hour integral, is the most basic and simplest method to estimate battery SOC, as given by

$$SOC(t)=SOC(0)+\int_0^t \eta_c i(t)\,dt \Big/ Q \tag{2.1}$$

where $SOC(t)$ and $SOC(0)$ denote the SOC values at time t and the initial time, respectively, $i(t)$ the loading current at time t (positive for charging and negative for discharging), and η_c the coulombic efficiency that can be considered as 1 for lithium-ion batteries.

Due to the primary advantage achieved by its ease of use and implementation with few computation efforts, the Coulomb-counting method has been widely used in real applications, especially during the early stages of the development of BMSs. The effectiveness of this method is essentially dependent on the accuracy of current measurement and initial SOC value. Due to the inevitable cumulative error of current detection, the SOC estimation results suffer from significant divergence problems, especially after performing over a long period. It needs a periodic calibration procedure for correcting the initial accumulated charge value, which limits its direct applications in practices. Hence, the Coulomb-counting method is often used in combination with other techniques, such as the following open circuit voltage (OCV) and model-based methods.

2.3.2 Open circuit voltage method

The OCV method is usually applied to recalibrate the SOC value. An OCV-SOC curve of $LiMn_2O_4$ (LMO) battery is depicted in Fig. 2.4, where the SOC interval is 5%. At each SOC interval, the relationship between the OCV and SOC can be fitted as a segmented function, as given by

$$OCV = k_i SOC + b_i = f\left(SOC\right) \tag{2.2}$$

where k_i and b_i are the parameters of the ith segmented function.

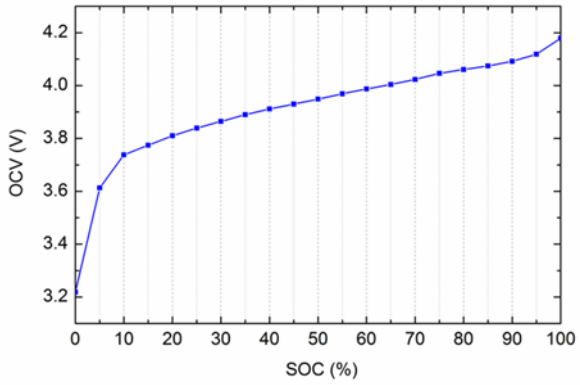

Fig. 2.4 The OCV-SOC curve of a $LiMn_2O_4$ battery cell.

If the OCV is obtained in advance, it is easy to compute the SOC by using (2.2). However, there are several existing points that should be taken into account when applying the OCV method for SOC estimation:

- Accurate SOC estimation requires precise battery OCVs. However, it usually takes a long rest time for batteries to recovery their fundamental OCV, which limits its feasibility in applications. Thus, the strategy for how to obtain the OCV in a short period of time needs to be further developed.

- The OCV method is an open-loop estimator that doesn't have the ability to eliminate voltage detection errors and uncertain disturbances [2.14]. The cell voltage detection sensor with high accuracy and anti-interference capability is therefore needed in this method. Some kinds of batteries have a relatively flat OCV-SOC curve, especially for LiFePO4 cells. This means that a small OCV measurement error may lead to a larger SOC deviation. In this case, it requires cell voltage detection sensors with extremely high accuracy, which increases the cost of BMSs.

- The OCV-SOC curves of batteries may differ from various factors, such as ambient temperature, cell aging level, etc. [2.15]. Xing et al. [2.16] pointed out that the OCV-SOC curve of LiFePO4 cells of the 18650-cylindrical type is related to the ambient temperature, and a single OCV-SOC table used in the estimation algorithm would cause erroneous results. To address this problem, an offline OCV-SOC-temperature table was established to estimate the SOC in the paper, where the verification indicated that it can provide better results than that without considering ambient temperature. In [2.17], it can be observed that OCV-SOC values of a Li-NMC cell differ from different aging levels. For robust and accurate battery SOC estimation at various ambient temperatures and cell aging levels, it is suggested to establish a multi-dimension OCV table including various influenced factors, such as an OCV-SOC-temperature-aging table in advance.

2.3.3 Model-based methods

The schematic of battery model-based methods shown in Fig. 2.5 mainly consists of a battery cell, a state observer or filter, and a battery electrical circuit model (ECM) or electrochemical model (EM). The input for both the real battery and battery model can be the loading current and ambient temperature. The principle of SOC estimation is to compare the cell terminal voltage with the output voltage of the battery model for generating a residual voltage, and then to feed it back to the model through an observer or a filter for revising the model parameters and states. Hence, the residual voltage is gradually eliminated, while the SOC of the battery model is gradually closed to the actual value.

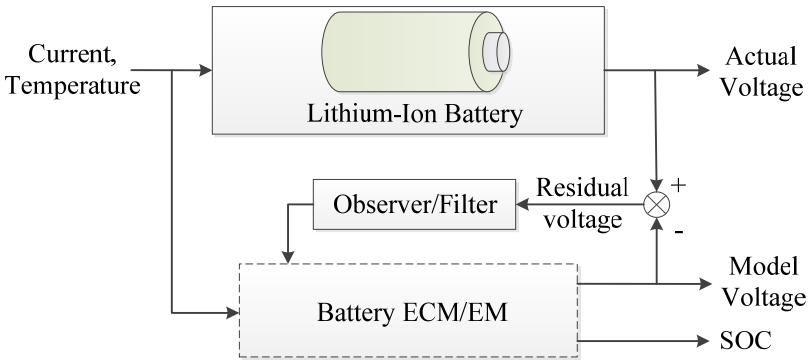

Fig. 2.5 The schematic of battery model-based SOC estimation methods.

Battery model-based SOC estimation methods always exhibit desirable merits, such as closed-loop, insensitive to the initial SOC value and uncertain disturbances, and availability of estimated error bounds, which have attracted enormous attention. Various techniques of observers and filters including sliding-mode observer (SMO), particle filter (PF), proportional-integral (PI) observer, H-infinity (H∞) observer, different extensions of Kalman filter (KF), and so forth, are extensively applied in model-based SOC estimation methods.

A. Kalman filter based methods

The KF is an optimal recursive solution for linear systems, which assume that the noise in both the transition and measurement processes is an independent Gaussian type.

However, KF tends to diverge in nonlinear systems. Different extensions of KF, such as extended KF (EKF), sigma-point KF (SPKF), unscented KF (UKF), central difference KF (CDKF), and fading KF (FKF) have been proposed to address this issue, and therefore were widely employed for estimating the SOC of batteries with non-linear characteristics.

The key idea and steps of the EKF algorithm for battery SOC estimation including prediction update and measurement update were first elaborated in Plett's series of papers [2.7], [2.18]. In the following research, Lee et al. [2.19] employed a modified OCV-SOC relationship and measurement noise models with EKF to achieve more robust estimates for all cells. Since EKF can equilibrate the algorithm complexity and estimation accuracy well, it is regarded as being capable of implementation into a microprocessor for efficient operations in BMSs [2.7], [2.20].

However, an argument against using EKF is that it linearizes battery model nonlinearities, thus leading to linearization errors. To tackle this problem, Plett [2.21] proposed the SPKF method for estimating the SOC of LiPB high-power cells, which highlighted its superiority in terms of estimation accuracy compared with the EKF. It is noted that there is little or no additional cost at the gains of SPKF compared with that of EKF, and the implementation of SPKF requires no analytic derivation or Jacobians as in EKF [2.21], [2.22]. Moreover, the performances of EKF and SPKF for SOC estimation were comparatively studied in [2.23], where both estimated robustness against uncertainties and convergence behaviour with an erroneous initial value were improved in the SPKF method.

Meanwhile, CDKF and UKF are the two most common used variants of SPKF, which are also applied for SOC estimation. A nonlinear enhanced self-correcting battery model was employed with the CDKF estimator to achieve more accurate SOC estimation results in [2.24]. With a UKF algorithm, Santhanagopalan et al. [2.25] obtained accurate estimates while greatly reducing the computational time in inferring SOC from a rigorous battery EM. For relieving the computation requirement of the original UKF, Dai et al. [2.26] proposed a square-root UKF algorithm and implemented it on a Digital Signal Processor

(DSP) based platform. The experimental results demonstrated better accuracy than that of the EKF estimator, and they required almost the same computation complexity, which makes the UKF estimator more competitive. Additionally, due to its capability to compensate battery modelling errors through a fading factor, FKF can effectively avoid the possibility of large estimation errors and therefore it was studied for estimating battery SOC in [2.27], [2.28].

It is noted that accurate knowledge of process and measurement noises covariance is highly required in all variants of KF for precise SOC estimation [2.29]. Erroneous knowledge of noises covariance may result in considerable errors in estimated results. Aiming at adaptively matching the process and measurement noises covariance in real-time, adaptive KF based estimators, such as adaptive EKF (AEKF) and adaptive UKF (AUKF) were applied for battery SOC estimation. In [2.30], an AEKF estimator was investigated with an improved battery Thevenin model achieved by adding an extra RC branch to a conventional Thevenin model for the estimation. Both the maximum SOC estimation error and mean SOC estimation error can be reduced to low levels in comparison to using EKF thereof. Xiong et al. [2.31] further developed AEKF for estimating the SOC of a series-connected lithium-ion battery pack, in which a battery pack model was established as a cell unit model for avoiding cell-to-cell variations in the battery pack. Besides, AUKF for SOC estimation was presented in [2.32], where the comparative study results indicated that AUKF has a better accuracy than AEKF and EKF.

The other problem is that the model and measurement noises of varied extensions of KF are restricted by the Gaussian distribution. However, it does not relate well to practices, which may have an adverse effect on the convergence behaviour and estimated accuracy [2.29].

B. Sliding-mode observer

The SMO is another effective technique for state estimation in nonlinear systems subject to uncertainties and disturbances [2.33]. It is designed to force and confine the system

state to stay in a pre-constructed surface, known as the sliding (hyper) surface, which exhibits desired dynamics [2.34].

The SMO design for SOC estimation was described by Kim in [2.35], [2.36], where the systematic design approach for SMO in combination with state equations of battery ECMs with was present, and the convergence of SMO was proved by Lyapunov functions. The modelling errors caused by simple ECMs were effectively compensated by the SMO, and therefore, under the real driving environments, the proposed method showed robust tracking performance against modelling errors and uncertainties. Due to its simple calculation and robust estimation characteristic, the SMO was suggested to be directly apply in hybrid EVs [2.35].

However, an inevitable issue of the conventional SMO is the chartering phenomenon, which is caused by the discontinuous switching control. To tackle the above problem, Chen et al. [2.37], [2.38] proposed adaptive switching gain SMO approaches for minimizing chattering levels. In the meantime, the accuracy of SOC estimation was improved by adaptively adjusting switching gains for compensating modelling errors. With the same aim, Kim et al. [2.39] employed an adaptive discrete-time SMO for estimating the OCV of a battery cell and then predicting the SOC with an enhanced Coulomb-counting algorithm. In [2.40], the elimination of chattering in both the output voltage and SOC estimates was achieved by the application of a second order discrete-time SMO that can drive not only the sliding variable but also its derivative to zero. Compared with the conventional first-order SMO approach, the proposed method showed a drastic reduction in both the estimation error and chattering phenomenon while maintain the robustness of the SMO approach. Although the effectiveness of adaptive SMO approaches and the second-order SMO method for attenuating chattering levels was validated, this benefits from the additional complexity and computation cost of the algorithms.

C. Particle filter

The PF is a sequential Monte Carlo approach, which aims to obtain a set of particles (also called samples or individuals) as well as importance weights assigned to the particles for representing the posterior probability density of the system [2.41]. The main operations of PF include particle propagation, importance weight computation, and resampling [2.42].

A PF based battery SOC estimation algorithm was proposed in [2.43], where the experimental results showed that PF and EKF have similar performance in estimation accuracy, but the execution time of PF is six times faster than that of EKF. Since LFP batteries have very flat OCVs with hysteresis between charging and discharging which bring challenges for estimating the SOC, Schwunk et al. [2.44] employed a PF framework and modelled the OCV hysteresis by multimodal probability functions to overcome this problem. The algorithm was able to track the SOC well over time with current profiles of photovoltaic and EV applications. However, the tracking behaviour of the algorithm under various ambient temperatures during battery aging needs further analysis. Considering the effects of dynamic current noise and temperature changes, Wang et al. [2.45] established a temperature and capacity retention ratio composed battery EM and then combined it with PF for eliminating the noise effects and estimating battery SOC. For improving the estimation robustness, Zhou et al. [2.46], [2.47] presented a PF based multi-model data fusion technique for battery SOC estimation. In this approach, a battery ECM and EM with PF were employed to infer SOC values, separately, and then the SOC values and their weights were adjusted by using PF and weighted average methodology. Although the validations indicated that this method can achieve better accuracy compared with conventional approaches of the single battery model, it was at the expense of additional computational efforts.

It was reported that the calculation process of conventional PF requires a massive number of particles for accurate SOC estimation [2.48]. To avoid this, an estimation approach based on Unscented PF (UPF) was proposed in [2.48], where UKF was employed to

update each particle at the measurement time while the resampling was performed using measurements. Accordingly, the proposal distribution of PF included the new observation information, and the number of particles can be significantly reduced. Moreover, with the consideration of the cells' inconsistencies in a battery pack, Zhong et al. [2.49] developed a UPF based approach for the estimation of the battery pack SOC. The UPF algorithm was applied for estimating SOCs of the first over-discharged cell and the first over-charged cell in the battery pack, and then the pack SOC was governed by these two SOCs through varied expressions related to different balancing control strategies.

D. H-infinity observer

H-infinity (H∞) observer has been effectively applied to handle state estimation problems involving multivariate systems with cross-coupling since the late 1990s [2.50]-[2.53]. It is a worst-case robust design approach, which means that it is less sensitive to model uncertainties and disturbances [2.53], [2.54]. The satisfactory battery SOC estimates can be obtained by the application of H-infinity in model-based estimation schemes.

Yan et al. [2.55] designed a H-infinity observer for addressing SOC estimation problems of nickel metal hydride (NiMH) batteries in noised and uncertain environments. The verification indicated that the proposed approach has the stronger robustness than current integral and KF methods. In [2.56], when unknown or erroneous statistical properties of errors were provided, the H-infinity observer based method still offered good SOC estimation accuracy for a battery-powered robot that is used for inspecting power transmission lines. Likewise, for accurately estimating battery SOC and terminal voltage without a prior knowledge of process and measurement noises, H-infinity observer with a battery ECM whose parameters were extracted by a genetic algorithm was utilized in [2.53], where the SOC and voltage estimation error bounds are invariant with different measurement noise levels.

Furthermore, to weaken the errors caused by a single battery model, Lin et al. [2.57] focused on a multiple battery ECMs fusion approach using the H-infinity algorithm for

SOC estimation. In the proposed method, three H-infinity observers were applied with three different kinds of ECMs to predict their respective SOCs. Then, the SOCs were synthesized with optimal weights to determine the battery SOC by the Bayes theorem. It was stated that the proposed approach highlighted its superiority in terms of robustness and estimation accuracy for both LMO and LFP batteries operated under dynamic conditions in comparison with the methods using sole battery ECM. However, the proposed distributed architecture with three observers, three models, and a fusion technique inevitably increases the computational burden, and the computational efficiency has not been evaluated in the article.

For increasing the robustness and accuracy of the conventional H-infinity algorithm, the adaptive H-infinity estimator was designed for both SOC and SOE estimation by Zhang et al. [2.58], where a moving estimation window of samples was employed to develop the covariance of the error innovation for adaptively updating the observation and system noise covariance. Compared with the conventional H-infinity and EKF methods, the adaptive H-infinity estimator can reduce both the maximum SOC estimation error and the mean SOC estimation error as well as the convergence time. According to the authors, the estimation results kept extremely high accuracy within 0.1% when an erroneous initial SOC value was provided. However, the robustness of the proposed method against various ambient temperature and cell aging levels is suggested for further evaluation.

E. Proportional-Integral observer

The PI observer inherits the advantages of the proportional controller and integral controller and exhibits strong robustness against system uncertainties, which is the most widely used control approach in engineering applications. The PI observer has the merit over other observer and filter techniques in that it is computationally efficient, and therefore, it is well-suited to be embedded in low-cost target BMSs [2.59].

Since it is hard to establish an accurate battery model for exactly matching a battery's dynamic behaviours, the PI observer was employed to improve the robustness against

modelling uncertainties for SOC estimation in [2.60], where the structure of the proposed method with a battery ECM was presented, and its convergence with model errors was validated. Furthermore, Zhao et al. [2.61] quantitatively analysed the error sensitivity of battery ECM parameters including OCV, ohmic resistance, polarization resistance, and capacity for the PI observer based SOC estimation method. It was stated that the OCV has a more significant influence on the estimation accuracy than other parameters. To suppress the drifting current errors and achieve desirable SOC estimation results, Tang et al. [2.62] proposed a dual-circuit state observer for LFP batteries, which was a combination of a PI observer and current integrator with drifting corrector. In [2.59], the authors developed PI observers with a high-fidelity EM for simultaneously estimating battery SOC, capacity, and resistance. It is noted that the battery SOC was indicated by lithium ion concentration values, and the PI observer was therefore applied for obtaining the gain of residual voltage to modify the lithium ion concentration in solid electrodes. The estimation accuracy and robustness against aging and temperature variations were systematically verified, but the complexity of the EM may hinder its implementation into microprocessors with limited capabilities in embedded BMSs.

Additionally, the PI observer was comparatively studied with other observers and filters, such as EKF, H-infinity, and SMO for SOC estimation in [2.54], [2.63]. The PI observer always achieves similar estimation accuracy yet outperforms others in terms of computational efforts due to its simplicity. The proportional gain and integral gain of the PI observer, however, are usually obtained from practical experiences. It may take a tedious tuning procedure to achieve optimal gains.

F. Least-squares based filters

Least-square (LS) technique provides a solution that minimizes the sum of the squares of the errors between the estimated values and actual values [2.64]. Since the basic LS method requires all the input and output data for a one-off estimation, it is not well-suited to the online applications where measurement data are not available all at once but instead arrive sequentially. To tackle this difficulty, Verbrugge et al. [2.65] applied a first-in and

first-out method that keeps the most recent 91 data points rather than all data for the LS regression to yield an estimate of the SOC. Likewise, the moving-window LS approach that employs a certain number (window) of input and output data of past steps for estimating parameters was reported in [2.64], [2.66]. In the articles, the authors employed the moving-window LS approach to extract battery parameters, which were then fed to an optimal observer gain that was calculated by a linear quadratic approach for estimating battery SOC. It was stated that the proposed approach showed a better performance in terms of estimation accuracy and convergence time than EKF and SMO methods in a typical current profile containing both charging and discharging cycles. But the moving-window LS approach requires a high demand of memory consumption for storing the certain numbers of measurement data.

Instead of computing the estimate by using all the available data, recursive LS (RLS) updates the estimates on the basis of the last estimate and newly collected data. The RLS is popularly used for on-board parameters identification. To avoid the saturation phenomenon of the standard RLS caused by the exponential growth of the covariance matrix [2.67], weighting and forgetting factors are usually incorporated with the RLS algorithms. For example, Verbrugge et al. [2.68], [2.69] developed the weighted RLS (WRLS) approach with exponential forgetting for battery SOC and other parameters estimation. In the proposed method, time weighing factors were applied to accentuate impact to recent measurement data for determining the SOC. The effectiveness of the proposed method was verified with Lead Acid, NiMH, and lithium-ion batteries. He et al. [2.67] employed a RLS algorithm with an optimal forgetting factor for on-board identification of battery parameters, and then used a pre-built lookup table between OCVs and SOCs to infer the battery SOC. The authors set the optimal forgetting factor as a fixed value, 0.98, for equilibrating the parameter tracking capability and maladjustment.

Moreover, considering that a single fixed forgetting factor may not accurately identify battery parameters, Duong et al. [2.70], [2.71] focused on RLS based SOC estimation with multiple adaptive forgetting factors for LFP batteries. The proposed method utilized

multiple adaptive forgetting factors to cope with different dynamics of the parameters variation, and therefore, it provided a better solution to the divergence problem than the RLS with a single forgetting factor.

Another RLS based approach reported for battery SOC estimation is the Frisch scheme bias compensating RLS (FBCRLS) [2.72]. Wei et al. [2.72] designed a FBCRLS based observer to estimate the noise statistics for eliminating the noise effect and enhancing online model identification, thus leading to a more reliable estimate on the SOC. It was stated that the proposed method outperformed the EKF based SOC method with RLS model identification technique in terms of estimation accuracy and convergence speed. However, the battery capacity used in the proposed method was regarded as a known variable. Due to the capacity fading during the battery aging process, it would degrade the estimation accuracy without a reliable capacity update.

It was noticed that no matrix inversion is needed as the RLS requires low computational cost and demonstrates fast convergence. However, the RLS based methods for SOC estimation need a sophisticated battery model that can effectively reproduce the cell's dynamic behaviour. Otherwise, it may suffer from severe divergence problems.

2.3.4 Machine learning methods

Without the physical knowledge of a system, machine learning methods such as neural network (NN), support vector machine (SVM), and fuzzy logic (FL) have the ability to learn and approximate the relationship between the input and the output of the system, which have been widely applied to battery systems to estimate SOC.

A. Neural network

Neural network (NN) is inspired by the way that the human brain processes information [2.73] and is an intelligent mathematical tool for system modelling. A NN typically consists of an input layer, one or more hidden layers, and an output layer to demonstrate a complex nonlinear system. Different learning algorithms can be employed to train the input data and the target data to acquire the parameters of the network. The most often

used learning method, back-propagation, was employed to train the relationship between battery parameters including cell terminal voltage and loading current and targeted SOCs in [2.73] for estimating battery SOC. The experimental results indicated that the NN method could perform well if the trained data is identical to the real experience. Considering the effect of battery capacity degradation, a battery capacity aging model that was built according to the test data at various temperatures was introduced as an input parameter of a Radial Basis Function NN (RBFNN) in response to the varying aging levels and temperatures in [2.74]. The verification of the proposed method showed a good robustness against varying battery degradation, temperature, and loading profiles. However, a large amount of reliable experiment data are required for accurately deducing the battery aging model and training the network.

B. Support vector machine

Support vector machines (SVMs), originally introduced as support vector networks [2.75], are supervised learning models that are used for data classification and regression analysis. SVMs can effectively transform a non-linear model using kernel functions and regression algorithms to a linear model in high dimension by using creditable training data [2.76]. The training process is also likely to be time-consuming. A battery SOC estimator using the SVM technique was proposed in [2.77]. The battery test data including cell terminal voltage, loading current, temperature, and SOC were used for training the parameters of the SVM model. With the input variables of battery cell voltage, current, and temperature, the SVM model was able to estimate battery SOC accurately with an estimated coefficient of determination of 0.97. It is noted that a relatively large estimated error can be observed for some points of discontinuity of the current. This may cause problematic estimates in real applications especially with dramatically changed loading current.

With the goal of achieving robust SOC estimation, an iterative weighted least squares SVM (WLS-SVM) algorithm was proposed by Chen et al. [2.78], where the key idea is similar to that of [2.77], namely establishing a relationship of SOC to cell voltage, current

and temperature. The verified results showed that the proposed estimator can achieve good robustness for SOC estimation. An optimized SVM for regression (SVR) with double search optimization process was employed for SOC estimation in [2.79]. The main purpose of the double step search was to reduce the time of training processes for selecting the optimal parameters. The proposed SOC estimator outperformed the estimations based on artificial NN in terms of efficiency and accuracy. However, since the results were verified in a vehicle simulator ADVISOR, it is recommended to evaluate the performance of the proposed method in real situations.

C. Fuzzy logic

Fuzzy logic (FL) mimics human control logic and is a way of processing data which incorporates a simple and rule-based approach to solving a control problem. The implementation process of FL includes fuzzifying inputs into membership functions, computing the output based on the rules, and de-fuzzifying the fuzzy output. Singh et al. [2.80] used ac impedance and voltage recovery measurements as the input of an FL model for estimating battery SOC. The proposed method was implemented in a microcontroller for the application of portable defibrillators. Dai et al. [2.81] proposed an adaptive neuro-fuzzy inference system (ANFIS) for online SOC correction. The average SOC of the battery pack was estimated by the KF method and then was corrected by the ANFIS with the information of cell differences and current. The proposed method has good accuracy and robustness against varying loading current, battery state, and aging, but it needs relatively high computational efforts.

A brief comparison of the aforementioned SOC estimation methods regarding to their complexity and accuracy is summarized in Table 2.1.

Table 2.1 The comparison of different SOC estimation methods regarding to their complexity and accuracy.

	Methods	Complexity	Accuracy
SOC estimation	Coulomb-counting method	Low	Low (especially after performing over a long period)
	OCV method	Low	Low (especially for batteries with flat voltage plateau)
	Model-based methods	High (especially with a battery electrochemical model)	High
	Machine learning methods	Medium	Dependent on training data

2.4 State of Health Estimation

There is no clear consensus for the definition available in literature for the SOH, although the importance of the SOH is really high [2.82]. The SOH can be quantified based on two measures: battery capacity fade and internal resistance increase [2.82]-[2.85]. Most studies consider the battery actual capacity in order to evaluate the SOH of a battery, and the SOH is determined by

$$SOH = Q_{act} / Q_N \times 100\% \tag{2.3}$$

where Q_{act} denotes the battery actual capacity and Q_N denotes the battery nominal capacity. Generally, a battery cell is regarded as being at the end of life when the actual capacity declines to 80% of its nominal capacity.

There are three main degradation modes including loss of lithium inventory, loss of active anode material, and loss of active cathode material that are considered to be the primary causes of battery capacity fade [2.86]. The formation and growth of surface of electrolyte interphase (SEI) consume cyclable lithium ions, resulting in an irreversible capacity fade, particularly during the initial few charging cycles [2.87], [2.88]. Lithium plating occurs at charging processes of a lithium-ion cell especially with high SOC, high current rate, and low temperature [2.89]. Although plated lithium can partially dissipate and intercalate into the anode active material, parts of deposited lithium would react with battery electrolyte and therefore consume lithium ions [2.90]. Active cathode material often suffers from transition metal dissolution, especially with high cathode potentials and high temperature [2.88], [2.91]. The intercalation and de-intercalation of lithium ions into active materials of electrodes lead to mechanical stress, structural damage and particle cracking [2.86], [2.88], thus resulting in loss of active materials.

The reported estimation approaches of battery actual capacity for evaluating the capacity fade and indicating the SOH are mainly classified into three categories: model-based methods, incremental capacity analysis (ICA) and differential voltage analysis (DVA) methods, and machine learning methods, which are elaborated in the following parts.

2.4.1 Model-based methods

The model-based methods for SOC estimation usually outperform others in terms of robustness and availability. However, the continuous capacity fade is prone to result in considerable errors in SOC estimation. To address this issue and simultaneously estimate SOH, the dual/joint model-based methods are introduced to co-estimate battery SOC, SOH, and other parameters [2.59].

A. Kalman filter based methods

A dual EKF (DEKF) framework for concurrently estimating battery state and parameters was first introduced by Plett [2.7]. In the article, two EKF estimators were designed to run in parallel for adapting battery state and parameters so that the relationship between

the model input and output values could closely match the real data. In the verifications, the estimates of battery capacity were able to converge to referenced values.

Generally, battery parameters and states have different variation rates. For example, the characteristics of battery internal resistance and capacity are usually slow time-varying, and the SOC has fast time-varying dynamics. In this regard, multiple time scales were popularly applied in the scheme of dual EKFs for SOC and SOH/capacity estimation in [2.92]-[2.95]. A micro-scale EKF was used to update battery SOC, and a macro-scale EKF was applied to adapt battery capacity/SOH. The advantage of the multi-time-scale design is that it reduces computational efforts of BMSs while keeping desirable estimates.

Besides, the DEKF algorithm was investigated with NN technique to estimate battery SOH in [2.96]. For eliminating the dependency of SOC and SOH estimation on empirical battery models including ECMs and EMs, Bai et al. [2.96] developed a NN based battery model to approximate the relationship between cell voltage, current, SOC, and capacity. The trained NN model was then employed in the DEKF method for adaptively updating model parameters and estimating battery SOC and SOH. The proposed method could achieve high accuracy for both short-term and long-term capacity estimates. However, the introduction of the NN would increase the computational efforts of the algorithm of the DEKF framework.

B. Other observers and filters

The dual SMO technique for estimating battery SOH was designed by Kim [2.97]. In the article, the dual SMOs consist of a fast time-varying observer for estimating SOC, cell terminal voltage, and polarization effects and a slow time-varying observer for estimating capacity fade and resistance deterioration. The Lyapunov equation was employed to design and ensure the convergence of the observers. The estimates were exchanged between the observers for updating new parameters and states through moving average filters, which were used for reducing the chattering in the estimated values. The test results exhibited good tracking performance for both SOC and SOH estimation.

Chen et al. [2.98] proposed multi-scale dual H-infinity filters for real-timely estimating battery SOC and capacity. The authors employed dual time scales with respect to fast-varying battery state and slow-varying battery parameters. The offline experimental results indicated the proposed method has superior performance in terms of robustness and accuracy compared with single/multi-scale DEKFs. The proposed method was further validated in a battery-in-loop test bench for EV applications, and the SOC and capacity estimates could effectively converge to the referenced values with high accuracies of 2% and 4%, respectively. However, when considering practical EV applications, the operation time of the proposed method in an embedded BMS should be evaluated, and the temperature effects on the battery model should be taken into account.

In [2.59], Zheng et al. employed a reduced physics-based EM and three PI observers for co-estimating battery SOC, capacity, and resistance. The first PI observer was applied to feed back the voltage difference between the measurement voltage and model output voltage to estimate the SOC. A moving window with Coulomb-counting method was then used for computing a comparative SOC. The second PI observer was then applied to feed back the SOC difference between the estimated value and the comparative value for estimating battery capacity. With erroneous initial model parameters, the proposed method could successfully reduce the capacity estimation error to less than 3% after several iterative estimation times for various battery aging levels and ambient temperatures. The primary concern comes from the computation burden of the proposed method in BMSs due to the complicated EM, although some efforts have been made for the model reduction.

Generally, the joint/dual estimators for battery model parameters identification and state prediction may suffer from the cross interference. To address this issue, Wei et al. [2.99] proposed decoupled multi-timescale estimators integrated by a KF-based SOC estimator and a RLS-based capacity estimator. In particular, a vector-type RLS (VRLS) approach which uses multiple forgetting factors was applied to cope with the different variation rates of battery parameters for solving the wind-up problem in the standard RLS. The

proposed approach was verified on different types of batteries including the lithium-ion battery and vanadium redox flow battery with high accuracy and fast convergence. It is noted that the computational cost of the proposed algorithm is lower than other existing methods, which was attributed to the lower filtering order of the state estimator and larger timescale of the parameter estimator. However, it should be pointed out that the temperature dependencies of battery parameters have not been taken into the proposed estimators. It is suggested to consider the affected factors in the battery model and estimation algorithm for enhancing robustness.

Hua et al. [2.100] developed a multi time-scale SOC and SOH estimation framework for the lithium-ion battery pack with passive balance control. As there exists cell-to-cell variation in a battery pack, it is not accurate to describe the pack states using a unit cell model. The authors employed a cell screening process to select the 'weakest in-pack cell' with minimum capacity, and then the SOC and capacity of the battery pack were represented by those of the 'weakest cell'. Dual nonlinear predictive filter (NPF) with different time-scales were employed for cell-level SOC, resistance, and capacity estimation. The NPF outperforms most filters in terms of the process noise in NPF being estimated as a part of the solution and that it can take any distribution form, such as a non-zero mean non-Gaussian process. The Urban Dynamometer Driving Schedule (UDDS) profiles were used to verify the performance of the proposed framework, and promising SOC and capacity estimates with high accuracy could be achieved. However, the results were just validated on a sole aged level of a battery pack, and the tracking performance of pack SOC and SOH estimator for the battery pack from its fresh status to its age status needs to be further investigated.

2.4.2 Incremental capacity analysis and differential capacity analysis based methods

The incremental capacity analysis (ICA) and differential voltage analysis (DVA) methods have been investigated in recent years and reported in [2.101]-[2.110] as effective non-invasive tools to study the behaviour and mechanism of a battery. The ICA approach transforms a battery charge or discharge voltage versus capacity curve to an incremental

capacity (IC) curve using the differential capacity. Likewise, the DVA method utilizes the differential voltage to transform the cell voltage versus capacity curve to a differential voltage (DV) curve. Mathematically, the IC curve is computed as the gradient of charged/discharged capacity (Q) with respect to cell voltage (V) using (2.4), and the DV curve is derived as the gradient of V with respect to Q using (2.5) [2.111].

$$dQ/dV \approx \Delta Q/\Delta V \tag{2.4}$$

$$dV/dQ \approx \Delta V/\Delta Q \tag{2.5}$$

The positions and magnitude of the peaks of IC/DV curves were widely employed for characterizing battery aging mechanisms, such as the loss of active materials, loss of lithium inventory (LLI), and increase of internal resistance. The implementation of ICA techniques on on-board SOH estimation for battery cells and modules were introduced by Weng et al. [2.112], [2.113]. Since it is difficult to calculate the IC curve directly from battery test data with measurement noise, the linear programming based SVR algorithm was employed in [2.112] for smoothing IC curves and improving its computational efficiency. A robust and quantitative correlation between faded battery capacity and IC peaks was extracted from the developed IC curves using the data from one single cell. The proposed algorithms for SOH estimation were then verified with seven other cells, and the predictive errors were confined in a small error bound of 1%. The authors further developed and extended the SOH monitoring algorithm from single cells to battery modules in [2.113]. A $LiFePO_4$ battery module consisting of three cells with different aging conditions connected in parallel was applied for the simulation analysis of IC peaks based SOH characterization of the battery module. The simulation results indicated that the developed SOH estimation framework for single cells could also be used for battery modules. A total of about thirty battery modules with various capacity variations were then employed to validate the proposed estimation method, and promising results with the root mean square error (RMSE) of 1.28% could be achieved, which highlighted the generalizable correlation for battery modules. Note that the ambient temperature has a

significant impact on battery electrochemical processes and therefore influences battery IC peaks. Since the experimental results presented in the articles were only verified under room temperature, the robustness and applicability of the proposed method against various temperatures needs to be further investigated.

Similar techniques based on the quantitative correlation between IC peaks and faded battery capacity for SOH estimation were reported in [2.114]-[2.116]. For obtaining clear IC curves without noise and with only three IC peaks, a Butterworth filter with the advantage of being insensitive to the input data range was applied to calculated the IC curve in [2.114], where the verifications demonstrated that the decrease of the third peak area is consistent with battery capacity fade, thus providing an efficient SOH estimator. However, the current rate and temperature dependencies of IC peaks have not been considered in the proposed method, which may distort battery IC peaks. Different to proposing approaches for directly smoothing IC curves, Feng et al. [2.115] and Han et al. [2.116] proposed voltage point counting based methods for on-board implementations of the ICA in BMSs, which transfer the charge/discharge procedure of a battery to the statistical histogram of cell voltage. The voltage intervals of 1 mV and 10 mV were selected for counting measured voltage points in [2.115], [2.116], respectively, and the charge/discharge ICs in each voltage interval were proportional to the numbers of counted points. Besides, a probability density function (PDF) was employed in [2.115] to smooth the histogram of cell voltage and deduce a PDF map of the voltage, which demonstrated similar results with those of ICA/DVA, and the aging regularity of the peak of PDF results was applied for evaluating battery SOH. The main advantage of voltage point counting based methods is achieved by easily and rapidly deriving the battery IC curve, and therefore they are computationally efficient. However, they require rigorous constant current for the effective voltage statistics, which limits their feasibility in practices, especially in the discharge process of batteries with dynamic changing currents in EVs.

As another effective non-invasive approach for revealing battery degradation mechanisms, the DVA technique, was also developed for real-time SOH estimation for

BMS operation in [2.117], [2.118]. Through the comparison of battery DV curves at various cell aging levels, a measurable special section of DV curves from 60% SOC until an almost full charge was selected by Berecibar et al. [2.117] for estimating the SOH of the battery. The experimental analysis showed that the length of the special section decreases as the SOH decreases. The SOH was then determined by the ratio of the lengths of the special section and a calculated section which was computed by the special section to the fresh capacity. The performance and robustness of the proposed method were verified by cell and battery pack levels at various scenarios, and the average errors of 0.8% and 1.5% could be achieved for cell and pack levels, respectively. However, it requires that the battery is charged or discharged at a low and constant current rate for accurately obtaining DV curves and the special section. In their later work [2.118], features of interest on the DV and IC curves were extracted and applied as inputs of three supervised learning methods including linear regression, NN, and SVM for estimating the SOH of NMC cells. Wrapper methods and filter methods were then employed for feature selection, which aims at reducing feature space while maintaining a desirable predictive capability. The experimental results suggested that the NN method outperformed others in terms of variability of the error, however it was less comprehensive than the linear regression method.

Wang et al. [2.119] proposed an improved centre least squares algorithm for obtaining clear DV curves, and extracted two inflection points from the DV curves for estimating battery SOH estimation. According to the analysis results, the first inflection point stayed at almost the same location, which can be used for eliminating the cumulative error of the charged capacity, while the second inflection point moved with the battery aging, which can be applied for indicating battery capacity fading. The location interval between these two inflection points demonstrated a linear relation to battery capacity, and it was validated by four LiFePO4 cells in various aging states. Furthermore, the authors developed the proposed method for battery pack application. The battery pack SOH was inferred from the difference between the real-time measured DV curve and the original

one. However, no verified results of the battery pack SOH estimation were reported in the article, and its feasibility needs to be investigated.

It can be summarized that the most common way to apply ICA/DVA methods for online implementations is to extract the features of interest of IC/DV curves to indicate battery capacity fading. Compared with the model-based methods for SOH estimation, there is no need to individually identify model parameters for each cell in the ICA/DVA based methods, which is attributed to universal characteristics of IC/DV curves. Accordingly, the ICA/DVA methods are promising to be developed for applications from the cell level to the battery pack level. However, it is noteworthy that the reported ICA/DVA techniques for SOH estimation are primarily based on the analysis of battery charge/discharge with the operating conditions of constant current and/or constant ambient temperature. The temperature and current rate dependencies of IC/DV curves for battery SOH estimation have not been efficiently investigated yet. A more robust ICA/DVA based method against dynamic operating conditions is desirable.

2.4.3 Machine learning methods

Nuhic et al. [2.120] developed an SVM algorithm for establishing a relationship between battery capacity fade and the load that the battery has experienced, which was used for battery SOH estimation. The operating data of six high power lithium-ion cells cyclically stressed at various real driving cycles and load collectives were employed for training the proposed algorithm. A linear SVR kernel function was applied in the SVR parameter determination for reducing computational efforts in further on-board implementations. Promising results for SOH estimation validated on driving profiles and temperatures were achieved, while with load collectives, the proposed method could also be used for the prognosis of the simple remaining useful life of the battery. An improved pattern of the standard SVM, least squares SVM (LS-SVM), was proposed for predicting the actual capacity of battery that can be used to estimate battery SOH in [2.121]. In the article, the Coulomb-counting method with current correction using the Peukert's equation and the dual AEKF algorithm were combined to estimate battery model parameters and SOC. For

improving the estimation accuracy of the proposed method at various temperatures among the lifetime of the battery, the LS-SVM model was implemented to estimate the available capacity of the battery. It is noted that a five-elements vector including temperature, battery series resistance, polarization resistance, voltage change, and voltage was used as each input sample of the proposed LS-SVM model, and therefore, the LS-SVM model took the temperature and degradation into account. The optimal parameters of the LS-SVM model were obtained by a genetic algorithm. According to the verification results, the maximum error of 2% could be obtained for the capacity prediction at the nominal temperature of 25 °C. However, since the temperature has an impact on the battery capacity, it is recommended to evaluate the performance of the capacity prediction method at different ambient temperatures.

Hu et al. [2.122] used the sample entropy of cell voltage sequence under the hybrid pulse power characterization (HPPC) profile as the input of the battery SOH estimator. The battery capacity was expressed as a third-degree polynomial model of sample entropy with different parameters for various temperatures. Although the referenced sample entropy was calculated from a randomly selected cell, the proposed estimator could be well applied for other cells. For improving the accuracy and robustness of SOH monitoring, sparse Bayesian predictive modelling (SBPM) approach was applied to investigate the relationship between the sample entropy and capacity loss in the authors' following work [2.123]. A multivariate Bayesian SOH estimator was proposed to integrate temperature effects. Compared with the SVM scheme, the proposed method exhibited slightly better performance with much fewer parameters.

Another popular choice for classification task, relevance vector machine (RVM), uses Bayesian inference to obtain the solutions for regression and probabilistic classification, which uses dynamically fewer basis functions while offering more reasonable predictions and other additional advantages as compared to SVM [2.124], [2.125]. Widodo et al. [2.126] developed RVM techniques with sample entropy for battery SOH monitoring. The battery discharge voltage and time data were used for extracting the sample entropy,

which gave a degradation trend of tested batteries. Thus, the sample entropy was applied to establish the intelligent ability for SOH prognostics by training SVM and RVM networks. The verification results showed that RVM has better accuracy than SVM in SOH predictions.

Besides, based on thousands of sample experimental data tested in battery charge processes with constant current, representative external features (i.e. the selected voltage samples and velocities of the voltages) of the battery were first extracted by Wu et al. [2.127] using a differential geometry based approach. A group method of data handling (GMDH) polynomial NN consisting of 8 inputs, 4 hidden layers, and maximally 20 nervous in each hidden layer was then constructed for training the relation between battery SOH and the external features. The experimental results showed that the proposed method was able to accurately estimate battery SOH with the maximum error of 5%. However, a large amount of reliable experimental data is required for extracting effective features, which incurs a tedious battery test process, and the presented complicate NN may be computationally expensive.

Additionally, the machine learning methods were also combined with other techniques such as DEKF [2.96] and ICA/DVA [2.118] for incorporating their merits in SOH estimation algorithms, which have been described in previous sections.

A brief comparison of the aforementioned SOH estimation methods regarding to their complexity and accuracy is summarized in Table 2.2.

Table 2.2 The comparison of different SOH estimation methods regarding to their complexity and accuracy.

	Methods	Complexity	Accuracy
SOH estimation	ICA or DVA methods	Low	High
	Model-based methods	High (especially with a battery electrochemical model)	High
	Machine learning methods	Medium	Dependent on training data

2.5 State of Energy Estimation

The SOC was employed for battery energy availability forecasting formerly. However, it is an indicator of battery available capacity rather than battery available energy. Mamadou et al. [2.128], [2.129] proposed a new criterion, SOE, for evaluating battery energetic performances. Represented by the ratio of the remaining energy in the battery to its total energy, the SOE, allows a direct determination of battery available energy, which is critical for energy optimization and management for ESSs and predicting the remaining driving mileage for EVs. The SOE can be governed by

$$SOE(t)=SOE(0)+\int_0^t P(t)\,dt \Big/ E_{ta} \tag{2.6}$$

where $SOE(t)$ and $SOE(0)$ denote the SOE values at time t and the initial time, respectively, $P(t)$ the loading power at time t (positive for charging and negative for discharging), and E_{ta} the battery total available energy.

Note that the definition of SOE is analogous to that of SOC. Most of the approaches for SOC estimation can be effectively applied for SOE estimation, such as the model-based methods and machine learning methods.

2.5.1 Model-based methods

Since the expression of SOE (as given in (2.6)) is similar to the expression of SOC (as given in (2.1)), the model-based methods proposed for SOC estimation can be developed for SOE estimation. Different kinds of filters and observers are also popularly employed in the estimation algorithms.

A. Kalman filter based methods

The AUKF for adaptively adjusting the process noise and measurement noises was applied to estimate the SOE in [2.12], [2.130]. In the proposed algorithms, Lu et al. [2.120] employed a simplified electrochemical combination model that describes the relationship between the battery SOE and terminal voltage, while Zhang et al. [2.12] employed a Thevenin model and a 3-D relationship between the OCV and the SOE considering the aging level and the operating temperature for the estimation. The robustness of the AUKF algorithm against different operation conditions and cell aging levels was verified in [2.12]. Besides, its performance was evaluated in comparison with that of the UKF algorithm, and the results showed that the AUKF algorithm can efficiently improve the estimation accuracy [2.130].

In [2.131], He et al. proposed a Gaussian model with the CDKF algorithm for SOE estimation. The Gaussian model was constructed for simulating the OCV behaviours of batteries, and its parameters were determined by using a genetic algorithm. For equilibrating the model complexity and estimation accuracy, the Akaike information criterion technique was employed to determine the best hysteresis order of the model. The effectiveness of the proposed algorithm was verified by two kinds of batteries including $LiMn_2O_4$ and $LiFePO_4$ batteries.

Additionally, Zhang et al. [2.132] focused on the remaining discharge energy and energy utilization ratio estimation for large format lithium-ion battery packs. Since the cells in the battery pack usually work with different heat dissipation conditions and operating temperatures, the inconsistency of the cells was incorporated in the estimation for the battery pack. According to the authors, the battery pack remaining discharge energy and maximum remaining discharge energy were deduced by the formulas with cells' capacities and SOCs. The RLS technique was employed to identify the model parameters, and the UKF was applied to estimate the cell SOC for the remaining discharge energy prediction. The proposed algorithm was verified under the new European driving cycles and real driven profiles with high accuracy. But the computational task to calculate the capacity and SOC of each cell is extraordinarily time-consuming especially for large-scale series-connected battery packs, and the accuracy of the remaining discharge energy prediction is highly dependent on the accuracy of the SOC and capacity estimation of each cell.

The methods utilizing variants of KF as the state observer for SOE estimation are able to achieve desirable results, but they encounter the same problem for SOC and SOH estimation, which is that the measurement and process noises should be the Gaussian type.

B. Other observers and filters

Wang et al. introduced the PF for battery SOE estimation in [2.133] and embedded the PF algorithm into a real-time operating system μC/OS-II within a BMS for practical EV applications in [2.134], where desirable results can be obtained by both the laboratory test of a LFP battery module and the road test of a $Li(Ni_{1/3}Co_{1/3}Mn_{1/3})O_2$ battery pack. However, the model parameters were identified off-line and may not match the real applications well.

To enhance the on-line performance of a battery model, EKF-PF dual filters were developed as an SOE estimator in [2.135], where the EKF was applied to update the model parameters using real-time cell loading current and terminal voltage, while the PF

was employed to estimate the battery SOE. Although the proposed method can work well against dynamic current and different operating temperatures, the accuracy of the model parameters extracted by the EKF is still highly dependent on the knowledge of the process and measurement noises covariance. With the same aim, Dong et al. [2.136] employed a Wavelet NN (WNN) based battery model for mimicking a battery's dynamic characteristics and a PF for estimating battery SOE. The operating temperatures and discharging rates were taken into account in the modeling so that the battery model can provide good prediction performance. According to the estimates, the proposed method showed good robustness against different operating temperatures and loading currents. However, the complexity of the proposed method may hold back its applicability.

Moreover, Wang et al. [2.137] designed an adaptive SOE estimator that is based on the AEKF and PF. The AEKF functioned to identify parameters on line and provide the prior knowledge for the PF to estimate the SOE. Compared with the EKF algorithm, the proposed estimator provided more accurate and robust results for SOE estimation. However, it is worth mentioning that in the proposed method, the particles resampling step of PF is replaced by the state update of AEKF, and therefore, it requires a certain number of AEKF estimators to update the particles used in the PF algorithm, which significantly increases the computational efforts.

In [2.58], extreme high accuracy within 0.1% was achieved for SOE estimation by using the adaptive H-infinity estimator. This benefits from the proposed estimator having the ability to adaptively update the observation and system noise covariance. Although the proposed method highlighted its superiority in terms of estimation accuracy and convergence speed compared with H-infinity and EKF approaches, the average task execution time of the proposed estimator was almost the same as that of the other two filters. However, since the proposed algorithm was validated in a hardware-in-the-loop approach and executed in a host computer, it is recommended to evaluate its performance in an embedded BMS for real applications.

In consideration of current sensor fails that may occur in practice, Xu et al. [2.138] developed the PI observer for simultaneously detecting the current sensor fault and estimating the battery SOE. In the proposed method, the PI observed was designed to isolate the current sensor fault from the state estimation. With an appropriate compensation of current sensor fault, the SOE estimation error caused by the current fault can be eliminated. It was stated that promising results for SOE estimation with the maximum error of less than 2% could be achieved, even though a large current error existed. A sophisticate battery model with accurate parameters, however, is highly required in this method.

2.5.2 Machine learning methods

Liu et al. [2.139] employed a three-layer Back-Propagation NN (BPNN) for the SOE estimation. Conducted by an investigation on battery discharged energy at different operating conditions, the battery terminal voltage, loading current, and the temperature were selected as the inputs of the BPNN with the consideration of the impact of the current and temperature on the discharged energy. The Levenberg-Marquardt backpropagation algorithm was then applied to train the parameters of the network. According to the obtained results, the proposed approach can effectively suppress the measurement noise and achieve accurate SOE estimates under dynamic temperatures and currents. Since twelve neurons were used in the hidden layer of the proposed BPNN, it would cause a high computational cost. Thus, the complexity of the BPNN approach needs to be further addressed.

2.5.3 Characteristic mapping methods

Through a study on ambient temperature, loading current, and cell aging levels dependencies of battery available energy, Zheng et al. [2.140] revealed that the relationship between the SOE and the SOC of LMO batteries almost keeps unchanged under different battery operating conditions and various cell aging levels. The stable relationship was then quantitatively expressed by a quadratic function. With the accurate SOC value, the battery SOE was readily computed by solving the quadratic function. The

advantage of this method lies in its simplicity, which can avoid heavy computational burden in a low-cost target BMSs with limited computation capabilities. The disadvantage is that the accuracy of SOE estimation is highly dependent on the accuracy of the provided SOC. Besides, the quantitative relationship between the SOE and the SOC needs to be further verified for the applications of other kinds of lithium-ion batteries.

In [2.141], Li et al. analysed the impact of the discharging power rates, charging approaches, and operating temperatures on total available energy of LTO batteries, and then modified the calculation approach of the SOE with the consideration of the influenced factors to realize high reliability and accuracy of SOE estimation. In the proposed method, the real-time battery available energy was determined by a multi-dimensional look-up table that was pre-established on the basis of the test data with various ambient temperatures, initial SOEs, and discharging power rates. The authors stated that the proposed method has an improvement over the classic power integral approach in terms of estimation accuracy and showed a closer description of battery discharging performance. However, the verification was carried out with an accurate initial SOE. An erroneous initial SOE may result in considerable errors in the estimation. Another problem is that a vast multi-dimensional look-up table with the consideration of different influential factors is needed in the proposed method, which requires a tedious battery test procedure.

A brief comparison of the aforementioned SOE estimation methods regarding to their complexity and accuracy is summarized in Table 2.3.

Table 2.3 The comparison of different SOE estimation methods regarding to their complexity and accuracy.

	Methods	Complexity	Accuracy
SOE estimation	Characteristic mapping methods	Low	Low
	Model-based methods	High (especially with a battery electrochemical model)	High
	Machine learning methods	Medium	Dependent on training data

2.6 State of Power Prediction

The SOP describes the peak power capability of a battery that can be delivered to loads or absorbed from regenerative braking or active recharging in a predictive time horizon. It is of great significance to accurately predict battery available power for reliable and optimal utilization of the battery. The reported techniques for SOP prediction can be mainly classified as three kinds of approaches include characteristic map based methods, model-based methods, and machine learning methods.

2.6.1 Characteristic map based methods

To establish a battery SOP characteristic map for various SOCs, the HPPC profile [2.142] has been extensively employed in battery tests. The internal resistance of battery cell for each iteration of the test profile is determined by the pulse current and its resulting voltage response, and is given by

$$R = \Delta V / \Delta I \tag{2.7}$$

where ΔV denotes the cell voltage change, ΔI the pulse current, and R the internal resistance of the battery cell (the discharge and charge resistances are denoted by R_D and R_C, respectively). Within the operating voltage limits, the battery cell power capabilities are governed by

$$\begin{cases} P_{D,\max} = V_{\min}\left(OCV - V_{\min}\right)/R_D = V_{\min}\left(f\left(SOC\right) - V_{\min}\right)/R_D \\ P_{C,\min} = V_{\max}\left(OCV - V_{\max}\right)/R_C = V_{\max}\left(f\left(SOC\right) - V_{\max}\right)/R_C \end{cases} \tag{2.8}$$

where $P_{D,max}$ and $P_{C,min}$ denote the battery cell maximum discharge power and minimum charge power, respectively; and V_{max} and V_{min} denote the upper and lower cut-off voltages, respectively. The peak power capabilities of the battery pack are mainly determined by the "weakest" cell power capability and the cell number connected in the pack, and can be expressed as follows [2.82], [2.143]:

$$\begin{cases} P_{Pack,D,\max} = n_p n_s \min\left(P_{D,\max,k}\right) \\ P_{Pack,C,\min} = n_p n_s \max\left(P_{C,\min,k}\right) \end{cases} \tag{2.9}$$

where $P_{Pack,D,max}$ and $P_{Pack,C,min}$ denote the battery pack maximum discharge power and minimum charge power, respectively; n_p and n_s denote the numbers of cells connected in parallel and series, respectively; and $P_{D,max,k}$ and $P_{C,min,k}$ denote the maximum discharge power and minimum charge power of the kth (k = 1, 2, …, ns) cell, respectively.

Since the ambient temperature has a significant impact on battery available power values [2.144], the cell power capability calculated by the HPPC method (as shown in (2.8)) omits its temperature dependency. An improvement to the HPPC technique took ambient temperature into account based on the varying battery OCV-SOC performances at different temperatures as reported in [2.144]. An exponential function of temperature compensation was introduced to add in (2.8) for reducing the offset caused by ambient temperatures and improving the accuracy of battery power capability prediction.

In addition, the HPPC profile was generally conducted to test battery cells at a wide temperature range for establishing a comparatively comprehensive SOP characteristic

map. The underlying Fig. 2.6 shows a characteristic map of the discharge power capability related to battery SOC and temperature of a large format LMO cell with the rated capacity of 90 Ah for EV applications, which is provided by battery manufactory. The characteristic map is then tabulated in embedded BMSs for online SOP prediction. The main advantage of this approach lies in its simplicity, but it requires a high demand of memory consumption for storing the parameters of the characteristic map.

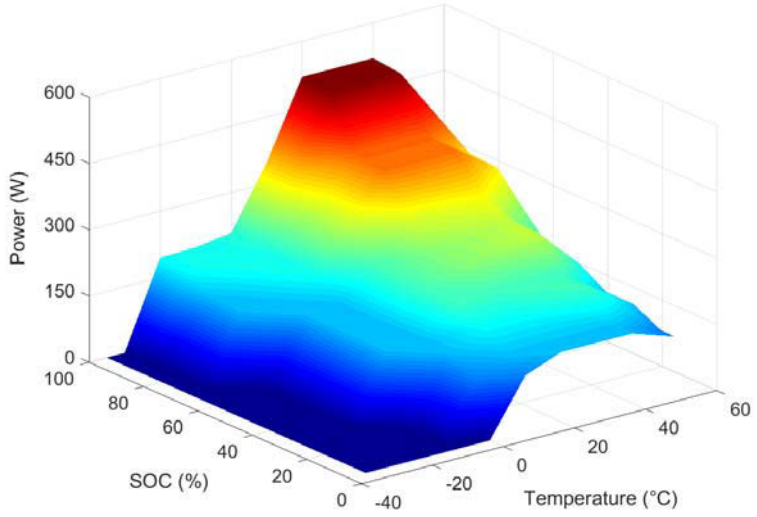

Fig. 2.6 A characteristic map of battery discharge power capability.

One way to reduce the demands of memory storage was introduced by Kim et al. [2.145]. The characteristic maps related to SOC, temperature, and accumulated discharge capacity were incorporated in an equation with three interrelations to determine battery power capabilities. The interrelation between the maximum available power and SOC was governed by a 5th order polynomial function whose coefficients were determined by a 2nd order polynomial function, which represents the interrelation between the maximum available power and temperature. Another 5th order polynomial function was applied to describe the interrelation between the maximum available power and accumulated discharge capacity. The battery maximum available power can be examined under various operating conditions and cell aging levels by the developed equation, but it requires powerful computational capabilities within BMSs to deal with the high order polynomial functions.

Alternatively, Burgos-Mellado et al. [2.146] developed a scheme with two cascaded modules for estimating battery SOC and maximum available power. The PF technique was employed in the first module for approximating the PDF of SOC and SOP. The second module was a look-up table of SOC versus SOP, which was built on the basis of the solution of an optimization problem using the proposed fuzzy battery model with the consideration of the dependencies of the polarization resistance on both SOC and current. Instead of a simple expectation, the output of the second module was an empirical PDF for the SOP. The proposed algorithm was implemented and verified in a DSP system of 16 bit for real-time applications. However, it is recommended to take the impacts of ambient temperature and cell aging level on the polarization resistance and other parameters of the fuzzy battery model into account for improving the adaptiveness of the proposed algorithm.

2.6.2 Model-based methods

The model-based methods are the mainstream solutions reported in literature for battery SOP prediction. In these methods, a battery model is usually employed for forecasting dynamic behaviours of the battery within a certain prediction horizon in order to determine the extreme voltage and current within the safe operating range to compute the battery available power capability. For battery's safe operation, related battery variables that can be used as the control limits in the model based SOP prediction methods are listed as follows:

- Upper and lower cut-off voltages,
- Maximum/minimum SOC/SOE,
- Design current rate,
- Design power.

The more design limits the algorithm uses, the more reliable SOP prediction results it may achieve, but the more computational efforts it requires.

A. Voltage limit

Wang et al. [2.147] proposed an adaptive, multi-parameter battery SOP estimator based on the direct solution of the governing differential equations of a battery Thevenin model. The model parameters were regressed by the WRSL method using the real time measured values of current and voltage, and then the analytical solution of the model response was used for calculating the charge current $I_C(V_{max})$ and discharge current $I_D(V_{min})$ with the upper and lower cut-off voltages, respectively. Sequentially, the charge and discharge power capabilities (positive for discharging and negative for charging) were determined by

$$\begin{cases} P_{D,\max,V} = V_{\min} I_D\left(V_{\min}\right) \\ P_{C,\min,V} = V_{\max} I_C\left(V_{\max}\right) \end{cases} \tag{2.10}$$

where PD,max,V and PC,min,V denote the maximum discharge power and the minimum charge power under the voltage limit, respectively. According to the experimental results, the short-term (0.5 s and 2 s) power predictions agreed well with the measurement values, but the long-term (10 s) power predictions showed a large deviation. The authors attributed the long-term power prediction fails to the limitations of the single RC element in the battery model, which could not effectively mimic the diffusion effect of the battery. For tackling this problem, the authors added a nonlinear diffusion resistance that is proportional to the square root of time to the SOP prediction algorithm in [2.148]. The improved estimator was implemented in a hardware-in-the-loop setup, and the accurate long-term SOP results for the discharge power with the deviation of less than 2% can be attained, while a modest improvement was achieved for the charge power prediction. Since the operating temperature has an impact on the diffusion phenomenon [2.149], it is suggested to take into account the temperature dependency of the diffusion resistance for more accurate and robust SOP predictions. Another problem is that the voltage and current differentials (i.e. dV/dt and dI/dt) were incorporated in the computational process, which requires high measurement accuracy and sampling rate for the voltage and current.

Malysz et al. [2.150] focused on battery power prediction algorithms for longer time horizons (i.e. 15 s and 60 s) than the approaches presented above. According to the authors, variations in the ECM parameters were required to be taken into account in the long prediction horizons for achieving higher prediction accuracy, and thus two different predictive algorithms were proposed. Based on a cell asymmetric ECM, the first method considered the extrapolation of resistor and OCV values, and the second method was a multistep model predictive iterative (MMPI) technique. The proposed algorithms were evaluated with UDDS drive cycles data at two low temperatures of 0 °C and -20 °C by a model-in-the-loop methodology in MATLAB. The verification showed that the first method has a marginal improvement compared with the conventional voltage-limited approach, while a better agreement with the measurement plus terminal voltages can be achieved by the MMPI method. However, this benefit comes at the cost of high computational efforts, and it is recommended to evaluate the performances of the proposed algorithms in practices.

It is well acknowledged that conventional ECMs can demonstrate the electrical behaviours of batteries well, but omit their thermal behaviours. The ECMs based SOP prediction methods, therefore, lead to the omission of the temperature dependency of battery power capability. To address this issue, Jiang et al. [2.151] implemented a Butler-Volmer equation-based model for LTO batteries SOP prediction over a large temperature range even below 0 °C. The Butler-Volmer equation-based battery model proposed in their previous work [2.152] incorporated a Thevenin model and a simplified Butler-Volmer equation, which equilibrated the model simplicity and the representation of a battery's electrochemical behaviours, and the model parameters were identified by the COMPLEX method. Note that two voltage limits based on the OCVs at 0% SOC and 100% SOC rather than only the upper and lower voltage limits were utilized in the proposed method for more appropriately matching the voltage characteristics of LTO batteries, thus contributing to high accuracy in predicting the power capability. However, since the battery model parameters were identified by an offline approach, it may suffer from prediction divergence problem in uncertain operating conditions.

B. Voltage and current limits

When considering that a simple battery model could not capture the battery dynamics while a complex model may be prone to the parameter divergence problem, Feng et al. [2.115] designed a novel battery ECM by adding a moving average noise to a Thevenin model, which enhances the ability to reflect a battery's dynamic effects whilst retaining the simplicity of the model, for a two-level SOP prediction. In the proposed method, the random error of the system was modelled by a moving average white noise, and the parameters of the new model was identified by using a recursive extended LS algorithm in real time. It is noted that the design limits of both voltage and current were considered in the SOP prediction. The power capabilities under the voltage limit was expressed by (2.11), while the predictive values under the current limit was governed by

$$\begin{cases} P_{D,\max,I} = I_{\max} V_D\left(I_{\max}\right) \\ P_{C,\min,I} = I_{\min} V_C\left(I_{\min}\right) \end{cases} \tag{2.11}$$

where $P_{D,max,I}$ and $P_{C,min,I}$ denote the maximum discharge power and the minimum charge power under the current limit, respectively; and $V_D(I_{max})$ and $V_C(I_{min})$ denote cell terminal voltages with the maximum design discharge current and with the minimum design charge current, respectively. The predicted power capabilities for discharging $P_{D,max}$ and charging $P_{C,min}$ were then determined by

$$\begin{cases} P_{D,\max} = \min\left(P_{D,\max,V} \quad P_{D,\max,I}\right) \\ P_{C,\min} = \max\left(P_{C,\min,V} \quad P_{C,\min,I}\right) \end{cases} \tag{2.12}$$

According to the obtained results, the proposed method significantly improved the accuracy of the parameter identification, and the single-step (short-term) SOP was in good agreement with that measured, while the accuracy of the long-term prediction could be increased.

For improving the applicability of SOP prediction, Pei et al. [2.153] designed a training-free estimator and a combined limit of voltage and current approach that the voltage limit

and current limit were simultaneously employed to derive the power capabilities. The training-free estimator was formed by a DEKF, in which the state filter was applied for forecasting battery polarization current, and the weight filter was employed for identifying the parameters of a Thevenin model. Since the designed estimator has the ability to directly estimate the battery model parameters under real-time conditions, the effects of temperature and aging on the parameters were internally included. It was stated that promising results for power capability prediction with the relative error of less than 5% could be achieved under various operating temperature and aging conditions.

It is worth mentioning that a battery model with accurate parameters, which can effectively reproduce battery's dynamics, is highly needed for achieving good performance of the SOP prediction. It appears to lack robustness against model parameter errors. To tackle this problem, Wik et al. [2.154] proposed a power capability prediction approach based on analytical solutions. In the proposed method, the analytical solution for battery equivalent circuits response was derived for calculating the discharge and charge currents, which would lead to the upper and lower voltages at the end of the prediction horizon, respectively. The voltage marginal between the cell terminal voltage and the upper or lower voltage was the driving force to converge the cell terminal voltage towards the design limits of voltage. The proposed algorithm acted like a PI controller, thus possessing good convergence and robustness, which were verified with a characterized vehicle drive cycle. However, since the OCV was assumed to be unchanged at the prediction horizon in the analytical solutions, it may be well-suited for short-term prediction, but lead to large errors for long-term prediction.

The above mentioned SOP prediction approaches with the design limits of voltage and current are aimed primarily at battery cells. It is indispensable to develop the prediction methods from the cell level to the pack level for practical applications. To this end, Waag et al. [2.155] focused the available power prediction on a battery pack with the consideration of the characteristic variances among cells in a battery pack. The power capability of the battery pack is generally limited by the "weakest" cell, which is the first

one to reach the design limits of voltage or current during the battery charging or discharging process. For identifying the "weakest" cell, the straight-forward method needs to estimate the parameters, predict the voltage, and calculate the SOP of each cell. However, it is computationally time-consuming. To overcome this drawback, the authors regarded the cells with the highest resistance or the highest/lowest OCV as the "weakest" ones. The proposed method also took into account the current dependency of battery resistance, which is considerable at low temperatures and high aging cells, thus enhancing the accuracy of SOP prediction. According to the authors, the promising results with the root mean square error within 6.5% could be achieved in the short-term (1 s) predictions, which is more accurate than that in the long-term (5 s and 10 s) predictions. The main advantage of the proposed method is achieved by optimizing the memory consumption and computation efforts, but the disadvantage is that the accuracy of the SOP prediction is dependent on the forecasting horizon.

C. Voltage, current, and SOC/SOE limits

Except for the design limits of voltage and current, the SOC was firstly introduced as a constraint in SOP prediction by Plett [2.156]. To ensure that the battery was operated within the permitted SOC limit, the real-time SOC was applied to compute the maximum discharge current (i.e. $I_{D,max,SOC}$) and the minimum charge current (i.e. $I_{C,min,SOC}$) as

$$\begin{cases} I_{D,\max,SOC} = \left(SOC(k) - SOC_{\min}\right) C_{ta} \big/ \Delta t \\ I_{\mathrm{C},\min,SOC} = \left(SOC(k) - SOC_{\max}\right) C_{ta} \big/ \Delta t \end{cases} \tag{2.13}$$

where SOC_{max} and SOC_{min} denote the permitted maximum and minimum SOC values, respectively, and $SOC(k)$ denotes the SOC value at time k.

Then combined with the limits of voltage and current, the battery maximum discharge current (i.e. $I_{D,max}$) and the minimum charge current (i.e. $I_{C,min}$) were determined by

$$\begin{cases} I_{D,\max} = \min\left(I_{D,\max,V} \quad I_{D,\max,I} \quad I_{D,\max,SOC}\right) \\ I_{C,\min} = \max\left(I_{C,\min,V} \quad I_{C,\min,I} \quad I_{C,\min,SOC}\right) \end{cases} \tag{2.14}$$

where $I_{D,max,V}$ and $I_{C,min,V}$ denote the maximum discharge current and the minimum charge current under the voltage limit, respectively, and $I_{C,min,I}$ and $I_{C,min,I}$ denote the permitted maximum discharge current and minimum charge current, respectively.

In [2.156], two methods with different battery models were proposed to predict battery charge and discharge power. A simple battery model with a constant internal resistance was applied in the first method, which caused significant errors in some SOC ranges. The second proposed method utilized a dynamic model considering battery resistance, capacity, temperature and so forth, for the power predictor. Although more promising estimates can be obtained by the second method, it requires a good cell model and more computational efforts. Similar power predictor was also reported in [2.157], where the authors employed a battery electrochemical-polarization model with the consideration of polarization effects.

Moreover, the battery power design limits which are usually provided by battery manufactures are taken into account in the power prediction, and the predictive power capabilities are then governed by

$$\begin{cases} P_{D,\max} = \min\left(P_{\max} \quad I_{D,\max} V_D\left(I_{D,\max}\right)\right) \\ P_{C,\min} = \max\left(P_{\min} \quad I_{C,\min} V_C\left(I_{C,\min}\right)\right) \end{cases} \tag{2.15}$$

where P_{max} and P_{min} denote the battery discharge and charge power design limits, respectively.

A piece-wise linearized battery ECM and the KF were employed in [2.158] for the joint estimation of LFP battery SOC and peak power capability which was represented by the state of function. The advantage of the proposed algorithm lies in its simple computation without complex operating, such as the Jacobian matrix calculation in EKF, the unscented transform in UKF, and the particle resampling in PF. However, it may result in untrustworthy estimates if the battery characteristics are seriously nonlinear. Likewise, Xiong et al. [2.159] proposed an AEKF based battery SOC and peak power capability

joint estimator. In the presented method, four different charge-discharge currents were employed to redefined the HPPC test for obtaining accurate battery model parameters. According to the authors, promising results with the peak error within 2% can be achieved for available peak power capability prediction. However, the battery model parameters were identified by the offline approach, which could not adapt the real applications well. To address this issue, it is recommended to incorporate the online battery model parameters identification technique for adaptive predictions.

Additionally, with the limits of cell terminal voltage, loading current, and SOC, references [2.160] and [2.161] focused on the power prediction for battery module and pack levels. The battery pack power capabilities are determined by the power capabilities of each cell connected in series and parallel, and can be calculated by

$$\begin{cases} P_{Pack,D,\max} = n_p \sum_{k=1}^{n_s} I_{D,\max} V_{k,D}\left(I_{D,\max}\right) \\ P_{Pack,C,\min} = n_p \sum_{k=1}^{n_s} I_{C,\min} V_{k,C}\left(I_{C,\min}\right) \end{cases} \tag{2.16}$$

where $V_{k,D}(I_{D,max})$ and $V_{k,C}(I_{C,min})$ denote the discharging and charging voltages of the kth cell, respectively. According to the experimental results shown in [2.160], [2.161], more reliable estimates can be obtained by the pack power predictor expressed in (2.16) than the traditional HPPC method. It is noted that the variances of cell power capabilities among the cells connected in series has been incorporated in (2.16), but the variances of cell power capabilities among the cells connected in parallel are omitted. It is recommended to take the variances of cell power capabilities among the cells connected in parallel into account for achieving more reliable battery pack power prediction.

Given that the power capability of a battery is greatly related to its available energy, the SOE was applied as a control limit for the SOP prediction in [2.12]. Analogous to the methods described in the above section that used the SOC for the prediction, a battery Thevenin model was employed for predicting the available peak charge and discharge currents within the design limits of the upper and lower cut-off voltages. The SOE

inferred by the battery model with an AUKF estimator was used for determining the SOE limit based battery available power through the following equation

$$\begin{cases} P_{D,\max,SOE} = \left(SOE(k) - SOE_{\min}\right) E_{ta} \big/ \Delta t \\ P_{C,\min,SOE} = \left(SOE(k) - SOE_{\max}\right) E_{ta} \big/ \Delta t \end{cases} \tag{2.17}$$

where $P_{D,max,SOE}$ and $P_{C,min,SOE}$ denote the maximum discharge power and the minimum charge power under the SOE limit, respectively; SOE_{max} and SOE_{min} the permitted maximum and minimum SOE, respectively; and Δt the prediction horizon. In the article, the design limits of current rate and power were also considered in the calculation of the battery power capability. The minimum value of various limits based maximum discharge power and the maximum value of various limits based minimum charge power were regarded as the predicted battery discharge and charge power capabilities, respectively. Since the AUKF estimator had the ability to adaptively adjust the process and measurement noises covariance, the accurate SOE estimates can be achieved, thus enabling more reliable SOP prediction against different operating temperatures and cell aging levels.

2.6.3 Machine learning methods

The BPNN was investigated for battery SOP prediction in [2.162]. The battery voltage and discharging current were considered as the leading factors that affected the SOP by the authors. Thus, the number of nodes in the input layer was set to two in corresponding to the cell voltage and discharging current, and the number of nodes in the hidden layer was set to twice that of the input layer based on the empirical law. According to the network training results, the TRAINLM function outperformed others in terms of convergence rate and prediction accuracy. Although desirable SOP prediction results with the maximum prediction error of 1.01% can be achieved, the proposed approach was only verified in offline simulations with constant discharging power profiles. It is necessary to examine the performance of the proposed algorithm in practical applications.

With the focus on time forward voltage prognosis, Fleischer et al. [2.163] proposed a framework of adaptive neuro-fuzzy inference system (ANFIS) for online battery SOP prediction. The ANFIS incorporated both the advantages of the fuzzy inference system and artificial NN, and its architecture consisted of five input variables (including pulse current, pulse capacity, time averaged voltage, SOC, and temperature), three rules, three membership functions, and one output. The cell SOC was determined using the robust EKF approach, and the parameters of the proposed network was identified by means of the Levenberg-Marquardt method. The functionality of the proposed algorithm was verified with small prediction errors for voltage prognosis in software-in-the-loop tests. The predictive voltage was then compared with the voltage limits to determine the maximum charging/discharging current with a current bisection method. However, the proposed algorithm must be run iteratively to obtain the maximum possible power/current magnitude for a defined prediction horizon, thus leading to high computational cost. Additionally, the authors optimized the ANFIS architecture by means of reducing the number of rules from three to two for cell voltage prognosis in [2.164], which was expected to reduce the complexity and computation time of the proposed algorithm.

In [2.144], Zheng et al. proposed a SVM based non-parametric model for battery power capability prediction. According to the authors, the radial basis function was selected as the model kernel function since it has a simple form and exhibits good performances in state estimation. The input variables of the SVM based non-parametric model were battery temperature, SOC, and internal resistance, and the output variable was the predicted battery power capability. In the context, three lithium-ion manganese oxide batteries were tested and used for SVR training, and the test data of the other three batteries were applied for the model validation. As depicted in the experimental results, the proposed method captured the referenced power capability better in the high temperature and SOC regimes, but worse in the low temperature and SOC regimes than the HPPC approach with the temperature compensation. Since these two methods can operate well at different temperature and SOC regimes, it is recommended to combine

them to achieve a high accuracy of battery power capability prediction in a wide range of temperature and SOC.

A brief comparison of the aforementioned SOP prediction methods regarding to their complexity and accuracy is summarized in Table 2.4.

Table 2.4 The comparison of different SOP prediction methods regarding to their complexity and accuracy.

	Methods	Complexity	Accuracy
SOP prediction	Characteristic mapping methods	Low	Low
	Model-based methods	High (especially with a battery electrochemical model)	High
	Machine learning methods	Medium	Dependent on training data

2.7 Summary

The functional requirement of the lithium-ion battery management system (BMS) has appeared as a more sophisticated and complex trend, especially in estimating battery states. Overly pessimistic or optimistic estimates of battery states would lead to waste or abuse of battery available capabilities, and the states estimation is therefore one of the major challenges of BMSs. This chapter mainly presents a technical review on key states estimation methods for lithium-ion batteries. It is noted that the machine learning methods can be applied for modelling the relationship of target state to input variables, but the estimated error is highly dependent on the training data. Among the reported techniques, model-based methods are the most popular ones for different states estimation, which is primarily attributed to their inherent traits such as closed-loop and insensitive to the initial

value and uncertain disturbances. However, in order to achieve more reliable and robust states estimation, the exiting issues of different techniques need to be further addressed.

References

[2.1] I. I. Kim, "A technique for estimating the state of health of lithium batteries through a dual-sliding-mode observer," *IEEE Transactions on Power Electronics*, vol. 25, no. 4, pp. 1013-1022, 2010.

[2.2] C. Zou, "Modelling, state estimation & optimal charging control for A lithium-ion battery," 2016.

[2.3] M.U. Cuma and T. Koroglu, "A comprehensive review on estimation strategies used in hybrid and battery electric vehicles," *Renewable and Sustainable Energy Reviews*, vol. 42, pp. 517-531, 2015.

[2.4] C.D. Albright, “Battery management system”, 1993.

[2.5] J. Alzieu, P. Gagnol and H. Smimite, "Development of an on-board charge and discharge management system for electric-vehicle batteries," *J.Power Sources*, vol. 53, no. 2, pp. 327-333, 1995.

[2.6] E.A. Hirzel, “Method and apparatus for measuring the state-of-charge of a battery system”, 1995.

[2.7] G.L. Plett, "Extended kalman filtering for battery management systems of LiPB-based HEV battery packs: Part 3. state and parameter estimation," *J.Power Sources*, vol. 134, no. 2, pp. 277-292, 2004.

[2.8] I. Kim, "The novel state of charge estimation method for lithium battery using sliding mode observer," *J.Power Sources*, vol. 163, no. 1, pp. 584-590, 2006.

[2.9] Linear Technology Corporation, “LTC6802-1 Multicell Battery Stack Monitor”, 2009. Online Available: http://cds.linear.com/docs/en/datasheet/68021fa.pdf

[2.10] Texas Instruments Incorporated, “bq76PL536 3 to 6 Series Cell Lithium-Ion Battery Monitor and Secondary Protection IC for EV and HEV Applications”, 2010. Online Available: http://www.ti.com/lit/ds/slusa08a/slusa08a.pdf

[2.11] Maxim Integrated, “MAX11068 12-Channel, High-Voltage Sensor, Smart Data-Acquisition Interface”, 2010. Online Available: https://media.digikey.com/pdf/Data%20Sheets/Maxim%20PDFs/MAX11068.pdf

[2.12] W. Zhang, W. Shi and Z. Ma, "Adaptive unscented kalman filter based state of energy and power capability estimation approach for lithium-ion battery," *J.Power Sources*, vol. 289, pp. 50-62, 2015.

[2.13] J. Li, “Adaptive model-based state monitoring and prognostics for lithium-ion batteries”, 2016.

[2.14] Y. Zou, X. Hu, H. Ma and S.E. Li, "Combined state of charge and state of health estimation over lithium-ion battery cell cycle lifespan for electric vehicles," *J.Power Sources*, vol. 273, pp. 793-803, 2015.

[2.15] B. Pattipati, B. Balasingam, G. Avvari, K. Pattipati and Y. Bar-Shalom, "Open circuit voltage characterization of lithium-ion batteries," *J.Power Sources*, vol. 269, pp. 317-333, 2014.

[2.16] Y. Xing, W. He, M. Pecht and K.L. Tsui, "State of charge estimation of lithium-ion batteries using the open-circuit voltage at various ambient temperatures," *Appl.Energy*, vol. 113, pp. 106-115, 2014.

[2.17] A. Nikolian, Y. Firouz, R. Gopalakrishnan, J. Timmermans, N. Omar, P. van den Bossche and J. van Mierlo, "Lithium ion Batteries—Development of advanced electrical equivalent circuit models for nickel manganese cobalt lithium-ion," *Energies*, vol. 9, no. 5, pp. 360, 2016.

[2.18] G.L. Plett, "Extended kalman filtering for battery management systems of LiPB-based HEV battery packs: Part 2. modeling and identification," *J.Power Sources*, vol. 134, no. 2, pp. 262-276, 2004.

[2.19] S. Lee, J. Kim, J. Lee and B. Cho, "State-of-charge and capacity estimation of lithium-ion battery using a new open-circuit voltage versus state-of-charge," *J.Power Sources*, vol. 185, no. 2, pp. 1367-1373, 2008.

[2.20] Z. Zhu, J. Sun and D. Liu, "Online state of charge EKF estimation for LiFePO 4 battery management systems," in *Intelligent Signal Processing and Communications Systems (ISPACS), 2012 International Symposium on*, 2012, pp. 609-614.

[2.21] G.L. Plett, "Sigma-point kalman filtering for battery management systems of LiPB-based HEV battery packs: Part 1: Introduction and state estimation," *J.Power Sources*, vol. 161, no. 2, pp. 1356-1368 2006.

[2.22] R. Van Der Merwe, E.A. Wan and S. Julier, "Sigma-point Kalman filters for nonlinear estimation and sensor-fusion: Applications to integrated navigation," in *Proceedings of the AIAA Guidance, Navigation & Control Conference*, 2004, pp. 16-19.

[2.23] J. Li, J.K. Barillas, C. Guenther and M.A. Danzer, "A comparative study of state of charge estimation algorithms for LiFePO 4 batteries used in electric vehicles," *J.Power Sources*, vol. 230, pp. 244-250, 2013.

[2.24] G.L. Plett, "Sigma-point kalman filtering for battery management systems of LiPB-based HEV battery packs: Part 2: Simultaneous state and parameter estimation," *J.Power Sources*, vol. 161, no. 2, pp. 1369-1384, 2006.

[2.25] S. Santhanagopalan and R.E. White, "State of charge estimation using an unscented filter for high power lithium ion cells," *Int.J.Energy Res.*, vol. 34, no. 2, pp. 152-163, 2010.

[2.26] H. Dai, X. Wei and Z. Sun, "Design and implementation of a UKF-based SOC estimator for LiMnO2 batteries used on electric vehicles," *Przeglad Elektrotechniczny*, vol. 88, no. 1, pp. 57-63, 2012.

[2.27] K. Lim, H.A. Bastawrous, V. Duong, K.W. See, P. Zhang and S.X. Dou, "Fading kalman filter-based real-time state of charge estimation in LiFePO 4 battery-powered electric vehicles," *Appl.Energy*, vol. 169, pp. 40-48, 2016.

[2.28] K.C. Lim, H.A. Bastawrous, V.H. Duong, K. See, P. Zhang and S. Dou, "Online SoC estimation of lithium ion battery for EV/BEV using Kalman filter with fading memory," in *2014 IEEE 3rd Global Conference on Consumer Electronics (GCCE)*, 2014, pp. 476-477.

[2.29] W. Waag, C. Fleischer and D.U. Sauer, "Critical review of the methods for monitoring of lithium-ion batteries in electric and hybrid vehicles," *J.Power Sources*, vol. 258, pp. 321-339, 2014.

[2.30] H. He, R. Xiong, X. Zhang, F. Sun and J. Fan, "State-of-charge estimation of the lithium-ion battery using an adaptive extended kalman filter based on an improved thevenin model," *IEEE Transactions on Vehicular Technology*, vol. 60, no. 4, pp. 1461-1469, 2011.

[2.31] R. Xiong, F. Sun, X. Gong and H. He, "Adaptive state of charge estimator for lithium-ion cells series battery pack in electric vehicles," *J.Power Sources*, vol. 242, pp. 699-713, 2013.

[2.32] F. Sun, X. Hu, Y. Zou and S. Li, "Adaptive unscented kalman filtering for state of charge estimation of a lithium-ion battery for electric vehicles," *Energy*, vol. 36, no. 5, pp. 3531-3540, 2011.

[2.33] Y. Xiong and M. Saif, "Sliding mode observer for nonlinear uncertain systems," *IEEE transactions on automatic control*, vol. 46, no. 12, pp. 2012-2017, 2001.

[2.34] J. Zhang, C. Sun, R. Zhang and C. Qian, "Adaptive sliding mode control for re-entry attitude of near space hypersonic vehicle based on backstepping design," *IEEE/CAA Journal of Automatica Sinica*, vol. 2, no. 1, pp. 94-101, 2015.

[2.35] I. Kim, "The novel state of charge estimation method for lithium battery using sliding mode observer," *J.Power Sources*, vol. 163, no. 1, pp. 584-590, 2006.

[2.36] I. Kim, "Nonlinear state of charge estimator for hybrid electric vehicle battery," *IEEE Transactions on Power Electronics*, vol. 23, no. 4, pp. 2027-2034, 2008.

[2.37] X. Chen, W. Shen, Z. Cao and A. Kapoor, "A novel approach for state of charge estimation based on adaptive switching gain sliding mode observer in electric vehicles," *J.Power Sources*, vol. 246, pp. 667-678, 2014.

[2.38] X. Chen, W. Shen, Z. Cao and A. Kapoor, "Adaptive gain sliding mode observer for state of charge estimation based on combined battery equivalent circuit model," *Comput.Chem.Eng.*, vol. 64, pp. 114-123, 2014.

[2.39] T. Kim, W. Qiao and L. Qu, "Online SOC and SOH estimation for multicell lithium-ion batteries based on an adaptive hybrid battery model and sliding-mode observer," in *2013 IEEE Energy Conversion Congress and Exposition*, 2013, pp. 292-298.

[2.40] D. Kim, K. Koo, J.J. Jeong, T. Goh and S.W. Kim, "Second-order discrete-time sliding mode observer for state of charge determination based on a dynamic resistance li-ion battery model," *Energies*, vol. 6, no. 10, pp. 5538-5551, 2013.

[2.41] Y. Wang, C. Zhang and Z. Chen, "A method for state-of-charge estimation of LiFePO 4 batteries at dynamic currents and temperatures using particle filter," *J.Power Sources*, vol. 279, pp. 306-311, 2015.

[2.42] T. Li, M. Bolic and P.M. Djuric, "Resampling methods for particle filtering: Classification, implementation, and strategies," *IEEE Signal Process.Mag.*, vol. 32, no. 3, pp. 70-86, 2015.

[2.43] M. Gao, Y. Liu and Z. He, "Battery state of charge online estimation based on particle filter," in *Image and Signal Processing (CISP), 2011 4th International Congress on*, 2011, pp. 2233-2236.

[2.44] S. Schwunk, N. Armbruster, S. Straub, J. Kehl and M. Vetter, "Particle filter for state of charge and state of health estimation for lithium–iron phosphate batteries," *J.Power Sources*, vol. 239, pp. 705-710, 2013.

[2.45] Y. Wang, C. Zhang and Z. Chen, "A method for state-of-charge estimation of LiFePO 4 batteries at dynamic currents and temperatures using particle filter," *J.Power Sources*, vol. 279, pp. 306-311, 2015.

[2.46] D. Zhou, K. Zhang, A. Ravey, F. Gao and A. Miraoui, "Online estimation of lithium polymer batteries state-of-charge using particle filter-based data fusion with multimodels approach," *IEEE Trans.Ind.Appl.*, vol. 52, no. 3, pp. 2582-2595, 2016.

[2.47] D. Zhou, A. Ravey, F. Gao, A. Miraoui and K. Zhang, "On-line estimation of lithium polymer batteries state-of-charge using particle filter based data fusion with multi-models approach," in *Industry Applications Society Annual Meeting, 2015 IEEE*, 2015, pp. 1-8.

[2.48] Y. He, X. Liu, C. Zhang and Z. Chen, "A new model for state-of-charge (SOC) estimation for high-power li-ion batteries," *Appl.Energy*, vol. 101, pp. 808-814, 2013.

[2.49] L. Zhong, C. Zhang, Y. He and Z. Chen, "A method for the estimation of the battery pack state of charge based on in-pack cells uniformity analysis," *Appl.Energy*, vol. 113, pp. 558-564, 2014.

[2.50] G. Didinsky, Z. Pan and T. Başar, "Parameter identification for uncertain plants using H∞ methods," *Automatica*, vol. 31, no. 9, pp. 1227-1250, 1995.

[2.51] L. Zhang, S. Su, X. Hu and D.G. Dorrell, "Robust state-of-charge estimation of ultracapacitors for electric vehicles," in *2015 IEEE 13th International Conference on Industrial Informatics (INDIN)*, 2015, pp. 1296-1301.

[2.52] V.S. Rao, V. George, S. Kamath and C. Shreesha, "Comparison of LQG controller with reliable H infinity controller designed for TRMS," *International Journal of Control Theory and Applications*, vol. 8, no. 3, pp. 1171-1179, 2015.

[2.53] W. Yang, D. Yu and Y. Kim, "Parameter estimation of lithium-ion batteries and noise reduction using an H∞ filter," *Journal of Mechanical Science and Technology*, vol. 27, no. 1, pp. 247-256, 2013.

[2.54] X. Li, J. Jiang, C. Zhang, L.Y. Wang and L. Zheng, "Robustness of SOC estimation algorithms for EV lithium-ion batteries against modeling errors and measurement noise," *Mathematical Problems in Engineering*, vol. 2015 2015.

[2.55] J. Yan, G. Xu, Y. Xu and B. Xie, "Battery state-of-charge estimation based on h∞ filter for hybrid electric vehicle," in *Control, Automation, Robotics and Vision, 2008. ICARCV 2008. 10th International Conference on*, 2008, pp. 464-469.

[2.56] F. Zhang, G. Liu, L. Fang and H. Wang, "Estimation of battery state of charge with observer: Applied to a robot for inspecting power transmission lines," *IEEE Trans.Ind.Electron.*, vol. 59, no. 2, pp. 1086-1095, 2012.

[2.57] C. Lin, H. Mu, R. Xiong and W. Shen, "A novel multi-model probability battery state of charge estimation approach for electric vehicles using H-infinity algorithm," *Appl.Energy*, vol. 166, pp. 76-83, 2016.

[2.58] Y. Zhang, R. Xiong, H. He and W. Shen, "Lithium-ion battery pack state of charge and state of energy estimation algorithms using a hardware-in-the-loop validation," *IEEE Transactions on Power Electronics*, vol. 32, no. 6, pp. 4421-4431, 2017.

[2.59] L. Zheng, L. Zhang, J. Zhu, G. Wang and J. Jiang, "Co-estimation of state-of-charge, capacity and resistance for lithium-ion batteries based on a high-fidelity electrochemical model," *Appl.Energy*, vol. 180, pp. 424-434, 2016.

[2.60] J. Xu, C.C. Mi, B. Cao, J. Deng, Z. Chen and S. Li, "The state of charge estimation of lithium-ion batteries based on a proportional-integral observer," *IEEE Transactions on Vehicular Technology*, vol. 63, no. 4, pp. 1614-1621, 2014.

[2.61] T. Zhao, J. Jiang, C. Zhang, L. Zheng and F. Wen, "Error analysis of SOC estimation based on PI observer," in *Transportation Electrification Asia-Pacific (ITEC Asia-Pacific), 2014 IEEE Conference and Expo*, 2014, pp. 1-5.

[2.62] X. Tang, Y. Wang and Z. Chen, "A method for state-of-charge estimation of LiFePO 4 batteries based on a dual-circuit state observer," *J.Power Sources*, vol. 296, pp. 23-29, 2015.

[2.63] J. Xu, B. Cao, J. Cao, Z. Zou, C.C. Mi and Z. Chen, "A comparison study of the model based SOC estimation methods for lithium-ion batteries," in *2013 IEEE Vehicle Power and Propulsion Conference (VPPC)*, 2013, pp. 1-5.

[2.64] H. Rahimi-Eichi, F. Baronti and M. Chow, "Online adaptive parameter identification and state-of-charge coestimation for lithium-polymer battery cells," *IEEE Trans.Ind.Electron.*, vol. 61, no. 4, pp. 2053-2061, 2014.

[2.65] M. Verbrugge and E. Tate, "Adaptive state of charge algorithm for nickel metal hydride batteries including hysteresis phenomena," *J.Power Sources*, vol. 126, no. 1, pp. 236-249, 2004.

[2.66] H. Rahimi-Eichi and M. Chow, "Adaptive online battery parameters/soc/capacity co-estimation," in *Transportation Electrification Conference and Expo (ITEC), 2013 IEEE*, 2013, pp. 1-6.

[2.67] H. He, X. Zhang, R. Xiong, Y. Xu and H. Guo, "Online model-based estimation of state-of-charge and open-circuit voltage of lithium-ion batteries in electric vehicles," *Energy*, vol. 39, no. 1, pp. 310-318, 2012.

[2.68] M. Verbrugge and B. Koch, "Generalized recursive algorithm for adaptive multiparameter regression application to lead acid, nickel metal hydride, and lithium-ion batteries," *J.Electrochem.Soc.*, vol. 153, no. 1, pp. A187-A201, 2006.

[2.69] M. Verbrugge, "Adaptive, multi-parameter battery state estimator with optimized time-weighting factors," *J.Appl.Electrochem.*, vol. 37, no. 5, pp. 605-616, 2007.

[2.70] V.H. Duong, H.A. Bastawrous, K.C. Lim, K. See, P. Zhang and S. Dou, "SOC estimation for LiFePO 4 battery in EVs using recursive least-squares with multiple adaptive forgetting factors," in *2014 International Conference on Connected Vehicles and Expo (ICCVE)*, 2014, pp. 520-521.

[2.71] V. Duong, H.A. Bastawrous, K. Lim, K.W. See, P. Zhang and S.X. Dou, "Online state of charge and model parameters estimation of the LiFePO 4 battery in electric vehicles using multiple adaptive forgetting factors recursive least-squares," *J.Power Sources*, vol. 296, pp. 215-224, 2015.

[2.72] Z. Wei, S. Meng, B. Xiong, D. Ji and K.J. Tseng, "Enhanced online model identification and state of charge estimation for lithium-ion battery with a FBCRLS based observer," *Appl.Energy*, vol. 181, pp. 332-341, 2016.

[2.73] A.A. Hussein, "Kalman filters versus neural networks in battery state-of-charge estimation: A comparative study," *International Journal of Modern Nonlinear Theory and Application*, vol. 3, no. 05, pp. 199, 2014.

[2.74] L. Kang, X. Zhao and J. Ma, "A new neural network model for the state-of-charge estimation in the battery degradation process," *Appl.Energy*, vol. 121, pp. 20-27, 2014.

[2.75] C. Cortes and V. Vapnik, "Support-vector networks," *Mach.Learning*, vol. 20, no. 3, pp. 273-297, 1995.

[2.76] M. Hannan, M. Lipu, A. Hussain and A. Mohamed, "A review of lithium-ion battery state of charge estimation and management system in electric vehicle applications: Challenges and recommendations," *Renewable and Sustainable Energy Reviews*, vol. 78, pp. 834-854, 2017.

[2.77] J.Á Antón, P.G. Nieto, F. de Cos Juez, F.S. Lasheras, M.G. Vega and M.R. Gutiérrez, "Battery state-of-charge estimator using the SVM technique," *Appl.Math.Model.*, vol. 37, no. 9, pp. 6244-6253, 2013.

[2.78] Y. Chen, B. Long and X. Lei, "The battery state of charge estimation based weighted least squares support vector machine," in *Power and Energy Engineering Conference (APPEEC), 2011 Asia-Pacific*, 2011, pp. 1-4.

[2.79] J. Hu, J. Hu, H. Lin, X. Li, C. Jiang, X. Qiu and W. Li, "State-of-charge estimation for battery management system using optimized support vector machine for regression," *J.Power Sources*, vol. 269, pp. 682-693, 2014.

[2.80] P. Singh, R. Vinjamuri, X. Wang and D. Reisner, "Design and implementation of a fuzzy logic-based state-of-charge meter for li-ion batteries used in portable defibrillators," *J.Power Sources*, vol. 162, no. 2, pp. 829-836, 2006.

[2.81] H. Dai, P. Guo, X. Wei, Z. Sun and J. Wang, "ANFIS (adaptive neuro-fuzzy inference system) based online SOC (state of charge) correction considering cell divergence for the EV (electric vehicle) traction batteries," *Energy*, vol. 80, pp. 350-360, 2015.

[2.82] A. Farmann and D.U. Sauer, "A comprehensive review of on-board state-of-available-power prediction techniques for lithium-ion batteries in electric vehicles," *J.Power Sources*, vol. 329, pp. 123-137, 2016.

[2.83] A. Farmann, W. Waag, A. Marongiu and D.U. Sauer, "Critical review of on-board capacity estimation techniques for lithium-ion batteries in electric and hybrid electric vehicles," *J.Power Sources*, vol. 281, pp. 114-130, 2015.

[2.84] C. Pastor-Fernández, K. Uddin, G.H. Chouchelamane, W.D. Widanage and J. Marco, "A comparison between electrochemical impedance spectroscopy and incremental capacity-differential voltage as li-ion diagnostic techniques to identify and quantify the effects of degradation modes within battery management systems," *J.Power Sources*, vol. 360, pp. 301-318, 2017.

[2.85] C. Pastor-Fernandez, T. Bruen, W.D. Widanage, M. Gama-Valdez and J. Marco, "A study of cell-to-cell interactions and degradation in parallel strings: Implications for the battery management system," *J.Power Sources*, vol. 329, pp. 574-585, 2016.

[2.86] C.R. Birkl, M.R. Roberts, E. McTurk, P.G. Bruce and D.A. Howey, "Degradation diagnostics for lithium ion cells," *J.Power Sources*, vol. 341, pp. 373-386, 2017.

[2.87] S. Zhang, K. Xu and T. Jow, "Optimization of the forming conditions of the solid-state interface in the li-ion batteries," *J.Power Sources*, vol. 130, no. 1, pp. 281-285, 2004.

[2.88] P. Keil, “Aging of Lithium-Ion Batteries in Electric Vehicles”, 2017.

[2.89] N. Legrand, B. Knosp, P. Desprez, F. Lapicque and S. Raël, "Physical characterization of the charging process of a li-ion battery and prediction of li plating by electrochemical modelling," *J.Power Sources*, vol. 245, pp. 208-216 2014.

[2.90] C. von Lüders, V. Zinth, S.V. Erhard, P.J. Osswald, M. Hofmann, R. Gilles and A. Jossen, "Lithium plating in lithium-ion batteries investigated by voltage relaxation and in situ neutron diffraction," *J.Power Sources*, vol. 342, pp. 17-23 2017.

[2.91] H. Zheng, Q. Sun, G. Liu, X. Song and V.S. Battaglia, "Correlation between dissolution behavior and electrochemical cycling performance for LiNi 1/3 co 1/3 mn 1/3 O 2-based cells," *J.Power Sources*, vol. 207, pp. 134-140 2012.

[2.92] C. Hu, B.D. Youn and J. Chung, "A multiscale framework with extended kalman filter for lithium-ion battery SOC and capacity estimation," *Applied Energy*, vol. 92, pp. 694-704, 2012.

[2.93] R. Xiong, F. Sun, Z. Chen and H. He, "A data-driven multi-scale extended kalman filtering based parameter and state estimation approach of lithium-ion olymer battery in electric vehicles," *Appl.Energy*, vol. 113, pp. 463-476, 2014.

[2.94] Y. Zou, X. Hu, H. Ma and S.E. Li, "Combined state of charge and state of health estimation over lithium-ion battery cell cycle lifespan for electric vehicles," *J.Power Sources*, vol. 273, pp. 793-803, 2015.

[2.95] C. Zou, C. Manzie, D. Nešić and A.G. Kallapur, "Multi-time-scale observer design for state-of-charge and state-of-health of a lithium-ion battery," *J.Power Sources*, vol. 335, pp. 121-130, 2016.

[2.96] G. Bai, P. Wang, C. Hu and M. Pecht, "A generic model-free approach for lithium-ion battery health management," *Appl.Energy*, vol. 135, pp. 247-260, 2014.

[2.97] I. Kim, "A technique for estimating the state of health of lithium batteries through a dual-sliding-mode observer," *IEEE Transactions on Power Electronics*, vol. 25, no. 4, pp. 1013-1022, 2010.

[2.98] C. Chen, R. Xiong and W. Shen, "A lithium-ion battery-in-the-loop approach to test and validate multi-scale dual H infinity filters for state of charge and capacity estimation," *IEEE Transactions on Power Electronics* 2017.

[2.99] Z. Wei, J. Zhao, D. Ji and K.J. Tseng, "A multi-timescale estimator for battery state of charge and capacity dual estimation based on an online identified model," *Appl.Energy* 2017.

[2.100] Y. Hua, A. Cordoba-Arenas, N. Warner and G. Rizzoni, "A multi time-scale state-of-charge and state-of-health estimation framework using nonlinear predictive filter for lithium-ion battery pack with passive balance control," *J.Power Sources*, vol. 280, pp. 293-312, 2015.

[2.101] X. Li, J. Jiang, L.Y. Wang, D. Chen, Y. Zhang and C. Zhang, "A capacity model based on charging process for state of health estimation of lithium ion batteries," *Appl.Energy*, vol. 177, pp. 537-543, 2016.

[2.102] M. Dubarry and B.Y. Liaw, "Identify capacity fading mechanism in a commercial LiFePO 4 cell," *J.Power Sources*, vol. 194, no. 1, pp. 541-549, 2009.

[2.103] M. Dubarry, B.Y. Liaw, M. Chen, S. Chyan, K. Han, W. Sie and S. Wu, "Identifying battery aging mechanisms in large format li ion cells," *J.Power Sources*, vol. 196, no. 7, pp. 3420-3425, 2011.

[2.104] M. Dubarry, M. Berecibar, A. Devie, D. Anseán, N. Omar and I. Villarreal, "State of health battery estimator enabling degradation diagnosis: Model and algorithm description," *J.Power Sources*, vol. 360, pp. 59-69, 2017.

[2.105] I. Bloom, A.N. Jansen, D.P. Abraham, J. Knuth, S.A. Jones, V.S. Battaglia and G.L. Henriksen, "Differential voltage analyses of high-power, lithium-ion cells: 1. technique and application," *J.Power Sources*, vol. 139, no. 1, pp. 295-303, 2005.

[2.106] I. Bloom, J. Christophersen and K. Gering, "Differential voltage analyses of high-power lithium-ion cells: 2. applications," *J.Power Sources*, vol. 139, no. 1, pp. 304-313, 2005.

[2.107] M. Safari and C. Delacourt, "Aging of a commercial graphite/LiFePO4 cell," *J.Electrochem.Soc.*, vol. 158, no. 10, pp. A1123-A1135, 2011.

[2.108] X. Han, M. Ouyang, L. Lu, J. Li, Y. Zheng and Z. Li, "A comparative study of commercial lithium ion battery cycle life in electrical vehicle: Aging mechanism identification," *J.Power Sources*, vol. 251, pp. 38-54, 2014.

[2.109] M. Berecibar, I. Gandiaga, I. Villarreal, N. Omar, J. Van Mierlo and P. Van den Bossche, "Critical review of state of health estimation methods of li-ion batteries for real applications," *Renewable and Sustainable Energy Reviews*, vol. 56, pp. 572-587, 2016.

[2.110] Z. Ma, J. Jiang, W. Shi, W. Zhang and C.C. Mi, "Investigation of path dependence in commercial lithium-ion cells for pure electric bus applications: Aging mechanism identification," *J.Power Sources*, vol. 274, pp. 29-40, 2015.

[2.111] C. Pastor-Fernandez, W.D. Widanage, G. Chouchelamane and J. Marco, "A SoH diagnosis and prognosis method to identify and quantify degradation modes in li-ion batteries using the IC/DV technique," 2016.

[2.112] C. Weng, Y. Cui, J. Sun and H. Peng, "On-board state of health monitoring of lithium-ion batteries using incremental capacity analysis with support vector regression," *J.Power Sources*, vol. 235, pp. 36-44, 2013.

[2.113] C. Weng, X. Feng, J. Sun and H. Peng, "State-of-health monitoring of lithium-ion battery modules and packs via incremental capacity peak tracking," *Appl.Energy*, vol. 180, pp. 360-368, 2016.

[2.114] E. Riviere, P. Venet, A. Sari, F. Meniere and Y. Bultel, "LiFePO4 Battery State of Health Online Estimation Using Electric Vehicle Embedded Incremental Capacity Analysis," in *Vehicle Power and Propulsion Conference (VPPC), 2015 IEEE*, 2015, pp. 1-6.

[2.115] T. Feng, L. Yang, X. Zhao, H. Zhang and J. Qiang, "Online identification of lithium-ion battery parameters based on an improved equivalent-circuit model and its implementation on battery state-of-power prediction," *J.Power Sources*, vol. 281, pp. 192-203, 2015.

[2.116] X. Han, M. Ouyang, L. Lu, J. Li, Y. Zheng and Z. Li, "A comparative study of commercial lithium ion battery cycle life in electrical vehicle: Aging mechanism identification," *J.Power Sources*, vol. 251, pp. 38-54, 2014.

[2.117] M. Berecibar, M. Garmendia, I. Gandiaga, J. Crego and I. Villarreal, "State of health estimation algorithm of LiFePO 4 battery packs based on differential voltage curves for battery management system application," *Energy*, vol. 103, pp. 784-796, 2016.

[2.118] M. Berecibar, F. Devriendt, M. Dubarry, I. Villarreal, N. Omar, W. Verbeke and J. Van Mierlo, "Online state of health estimation on NMC cells based on predictive analytics," *J.Power Sources*, vol. 320, pp. 239-250, 2016.

[2.119] L. Wang, C. Pan, L. Liu, Y. Cheng and X. Zhao, "On-board state of health estimation of LiFePO 4 battery pack through differential voltage analysis," *Appl.Energy*, vol. 168, pp. 465-472, 2016.

[2.120] A. Nuhic, T. Terzimehic, T. Soczka-Guth, M. Buchholz and K. Dietmayer, "Health diagnosis and remaining useful life prognostics of lithium-ion batteries using data-driven methods," *J.Power Sources*, vol. 239, pp. 680-688, 2013.

[2.121] Z. Deng, L. Yang, Y. Cai, H. Deng and L. Sun, "Online available capacity prediction and state of charge estimation based on advanced data-driven algorithms for lithium iron phosphate battery," *Energy*, vol. 112, pp. 469-480, 2016.

[2.122] X. Hu, S.E. Li, Z. Jia and B. Egardt, "Enhanced sample entropy-based health management of li-ion battery for electrified vehicles," *Energy*, vol. 64, pp. 953-960, 2014.

[2.123] X. Hu, J. Jiang, D. Cao and B. Egardt, "Battery health prognosis for electric vehicles using sample entropy and sparse bayesian predictive modeling," *IEEE Trans.Ind.Electron.*, vol. 63, no. 4, pp. 2645-2656, 2016.

[2.124] M. Rafi and M.S. Shaikh, "A comparison of SVM and RVM for document classification," *arXiv preprint arXiv:1301.2785,* 2013.

[2.125] M.E. Tipping, "Sparse bayesian learning and the relevance vector machine," *Journal of machine learning research*, vol. 1, no. Jun, pp. 211-244, 2001.

[2.126] A. Widodo, M. Shim, W. Caesarendra and B. Yang, "Intelligent prognostics for battery health monitoring based on sample entropy," *Expert Syst.Appl.*, vol. 38, no. 9, pp. 11763-11769, 2011.

[2.127] J. Wu, Y. Wang, X. Zhang and Z. Chen, "A novel state of health estimation method of li-ion battery using group method of data handling," *J.Power Sources*, vol. 327, pp. 457-464, 2016.

[2.128] K. Mamadou, A. Delaille, E. Lemaire-Potteau and Y. Bultel, "The state-of-energy: A new criterion for the energetic performances evaluation of electrochemical storage devices," *ECS Transactions*, vol. 25, no. 35, pp. 105-112, 2010.

[2.129] K. Mamadou, E. Lemaire, A. Delaille, D. Riu, S. Hing and Y. Bultel, "Definition of a state-of-energy indicator (SoE) for electrochemical storage devices: Application for energetic availability forecasting," *J.Electrochem.Soc.*, vol. 159, no. 8, pp. A1298-A1307 2012.

[2.130] H.W. Liu, H.F. Wang and C. Guo, "State of energy estimation based on AUKF for lithium battery used on pure electric vehicle," in *Advanced Materials Research*, 2013, pp. 1627-1630.

[2.131] H. He, Y. Zhang, R. Xiong and C. Wang, "A novel gaussian model based battery state estimation approach: State-of-energy," *Appl.Energy*, vol. 151, pp. 41-48, 2015.

[2.132] X. Zhang, Y. Wang, C. Liu and Z. Chen, "A novel approach of remaining discharge energy prediction for large format lithium-ion battery pack," *J.Power Sources*, vol. 343, pp. 216-225, 2017.

[2.133] Y. Wang, C. Zhang and Z. Chen, "A method for joint estimation of state-of-charge and available energy of LiFePO 4 batteries," *Appl.Energy*, vol. 135, pp. 81-87, 2014.

[2.134] Y. Wang, Z. Chen and C. Zhang, "On-line remaining energy prediction: A case study in embedded battery management system," *Appl.Energy* 2016.

[2.135] G. Dong, Z. Chen, J. Wei, C. Zhang and P. Wang, "An online model-based method for state of energy estimation of lithium-ion batteries using dual filters," *J.Power Sources*, vol. 301, pp. 277-286, 2016.

[2.136] G. Dong, X. Zhang, C. Zhang and Z. Chen, "A method for state of energy estimation of lithium-ion batteries based on neural network model," *Energy*, vol. 90, pp. 879-888, 2015.

[2.137] Y. Wang, C. Zhang and Z. Chen, "An adaptive remaining energy prediction approach for lithium-ion batteries in electric vehicles," *J.Power Sources*, vol. 305, pp. 80-88, 2016.

[2.138] J. Xu, J. Wang, S. Li and B. Cao, "A method to simultaneously detect the current sensor fault and estimate the state of energy for batteries in electric vehicles," *Sensors*, vol. 16, no. 8, pp. 1328, 2016.

[2.139] X. Liu, J. Wu, C. Zhang and Z. Chen, "A method for state of energy estimation of lithium-ion batteries at dynamic currents and temperatures," *J.Power Sources*, vol. 270, pp. 151-157, 2014.

[2.140] L. Zheng, J. Zhu, G. Wang, T. He and Y. Wei, "Novel methods for estimating lithium-ion battery state of energy and maximum available energy," *Appl.Energy*, vol. 178, pp. 1-8, 2016.

[2.141] K. Li, K.J. Tseng and L. Moraleja, "Study of the influencing factors on the discharging performance of lithium-ion batteries and its index of state-of-energy," in *Industrial Electronics Society, IECON 2016-42nd Annual Conference of the IEEE*, 2016, pp. 2117-2123.

[2.142] J. R. Belt, “Battery Test Manual for Plug-in Hybrid Electric Vehicles,” Idaho National Laboratory, INL/EXT-07-12536, 2010.

[2.143] C. Zhang, C. Zhang and S. Sharkh, "Estimation of real-time peak power capability of a traction battery pack used in an HEV," in *Power and Energy Engineering Conference (APPEEC), 2010 Asia-Pacific*, 2010, pp. 1-6.

[2.144] F. Zheng, J. Jiang, B. Sun, W. Zhang and M. Pecht, "Temperature dependent power capability estimation of lithium-ion batteries for hybrid electric vehicles," *Energy*, vol. 113, pp. 64-75, 2016.

[2.145] J. Do Yang, Method of estimating maximum output of battery for hybrid electric vehicle, 2009.

[2.146] C. Burgos-Mellado, M.E. Orchard, M. Kazerani, R. Cárdenas and D. Sáez, "Particle-filtering-based estimation of maximum available power state in lithium-ion batteries," *Appl.Energy*, vol. 161, pp. 349-363, 2016.

[2.147] S. Wang, M. Verbrugge, J.S. Wang and P. Liu, "Multi-parameter battery state estimator based on the adaptive and direct solution of the governing differential equations," *J.Power Sources*, vol. 196, no. 20, pp. 8735-8741, 2011.

[2.148] S. Wang, M. Verbrugge, J.S. Wang and P. Liu, "Power prediction from a battery state estimator that incorporates diffusion resistance," *J.Power Sources*, vol. 214, pp. 399-406, 2012.

[2.149] H.J. Ploehn, P. Ramadass and R.E. White, "Solvent diffusion model for aging of lithium-ion battery cells," *J.Electrochem.Soc.*, vol. 151, no. 3, pp. A456-A462, 2004.

[2.150] P. Malysz, J. Ye, R. Gu, H. Yang and A. Emadi, "Battery state-of-power peak current calculation and verification using an asymmetric parameter equivalent circuit model," *IEEE Transactions on Vehicular Technology*, vol. 65, no. 6, pp. 4512-4522, 2016.

[2.151] J. Jiang, S. Liu, Z. Ma, L.Y. Wang and K. Wu, "Butler-volmer equation-based model and its implementation on state of power prediction of high-power lithium titanate batteries considering temperature effects," *Energy*, vol. 117, pp. 58-72, 2016.

[2.152] S. Liu, J. Jiang, W. Shi, Z. Ma, L.Y. Wang and H. Guo, "Butler–Volmer-equation-based electrical model for high-power lithium titanate batteries used in electric vehicles," *IEEE Trans.Ind.Electron.*, vol. 62, no. 12, pp. 7557-7568, 2015.

[2.153] L. Pei, C. Zhu, T. Wang, R. Lu and C. Chan, "Online peak power prediction based on a parameter and state estimator for lithium-ion batteries in electric vehicles," *Energy*, vol. 66, pp. 766-778, 2014.

[2.154] T. Wik, B. Fridholm and H. Kuusisto, "Implementation and robustness of an analytically based battery state of power," *J.Power Sources*, vol. 287, pp. 448-457, 2015.

[2.155] W. Waag, C. Fleischer and D.U. Sauer, "Adaptive on-line prediction of the available power of lithium-ion batteries," *J.Power Sources*, vol. 242, pp. 548-559, 2013.

[2.156] G.L. Plett, "High-performance battery-pack power estimation using a dynamic cell model," *IEEE Transactions on vehicular technology*, vol. 53, no. 5, pp. 1586-1593, 2004.

[2.157] R. Xiong, H. He, F. Sun and K. Zhao, "Online estimation of peak power capability of li-ion batteries in electric vehicles by a hardware-in-loop approach," *Energies*, vol. 5, no. 5, pp. 1455-1469, 2012.

[2.158] G. Dong, J. Wei and Z. Chen, "Kalman filter for onboard state of charge estimation and peak power capability analysis of lithium-ion batteries," *J.Power Sources*, vol. 328, pp. 615-626, 2016.

[2.159] R. Xiong, H. He, F. Sun, X. Liu and Z. Liu, "Model-based state of charge and peak power capability joint estimation of lithium-ion battery in plug-in hybrid electric vehicles," *J.Power Sources*, vol. 229, pp. 159-169, 2013.

[2.160] F. Sun, R. Xiong, H. He, W. Li and J.E.E. Aussems, "Model-based dynamic multi-parameter method for peak power estimation of lithium–ion batteries," *Appl.Energy*, vol. 96, pp. 378-386, 2012.

[2.161] X. Hu, R. Xiong and B. Egardt, "Model-based dynamic power assessment of lithium-ion batteries considering different operating conditions," *IEEE Transactions on Industrial Informatics*, vol. 10, no. 3, pp. 1948-1959 2014.

[2.162] H. Wang, Z. Hao, Y. Hu and G. Li, "Power state prediction of battery based on BP neural network," in *Strategic Technology (IFOST), 2012 7th International Forum on*, 2012, pp. 1-4.

[2.163] C. Fleischer, W. Waag, Z. Bai and D.U. Sauer, "Adaptive on-line state-of-available-power prediction of lithium-ion batteries," *Journal of Power Electronics*, vol. 13, no. 4, pp. 516-527 2013.

[2.164] C. Fleischer, W. Waag, Z. Bai and D.U. Sauer, "On-line self-learning time forward voltage prognosis for lithium-ion batteries using adaptive neuro-fuzzy inference system," *J.Power Sources*, vol. 243, pp. 728-749 2013.

CHAPTER 3

MODEL-BASED BATTERY SOC AND CAPACITY ESTIMATION

3.1 Introduction

Energy storage systems play a vital role in a variety of industrial applications including electrified vehicles (EVs), uninterruptible power supplies and renewable energy systems, etc. [3.1]. Lithium-ion batteries are being widely used as an enabling energy storage since they exhibit high energy and power density along with no memory effect [3.2]. To ensure safe and efficient operation of battery systems under fleeting and even demanding conditions, an effective battery management system (BMS) is highly desirable [3.3]. Primary functions of BMSs include accurate state of charge (SOC) estimation and key parameter identification. These tasks pose significant challenges owing to the unmeasurable and nonlinear internal reaction process, and unpredictable operating conditions of battery systems [3.4].

Myriad methods have been proposed in the literature to address the SOC estimation problem [3.5]-[3.14], such as coulomb-counting method, OCV method, model-based methods, and machine learning methods. Among these methods, the model-based methods have attracted tremendous attention, thanks to their inherent traits such as closed-loop, online access, and availability of estimation error bounds. It is well acknowledged that the SOC estimation accuracy is strongly related to the battery health status. The capacity fade and/or the resistance deterioration may result in considerable errors in SOC estimation. More precise SOC estimated results could be obtained with known capacity information [3.14]. Similarly, the SOC observer with periodical parameter updates outperforms that without real-time parameter renewal [3.15]. Therefore, it is essential to furnish the battery parameters in real-time for credible SOC

A substantial proportion of this chapter has been published as an article [3.38] in *Applied Energy*.

estimation. Considerable effort has been directed to the joint estimation of SOC, capacity, and the underlying model parameters in the literature [3.16]-[3.23].

However, the aforementioned model-based methods are mainly developed on the basis of equivalent circuit models (ECMs). These ECMs are always derived from empirical knowledge and experimental data by employing idealized circuit elements to represent electrical behaviours of batteries. The main advantage of ECMs lies in their simple and flexible model structure, but ECMs are insufficient to adequately depict the internal underlying reactions due to lack of physical-chemical representations, thus leading to limited prediction capability. In contrast to ECMs, electrochemical models (EMs) use partial differential equations (PDEs) to describe the real electrochemical reaction process inside cells, which can capture cell dynamic behaviours with high accuracy. It has been reported that one of the defining features of futuristic advanced BMSs is to use a physics-based EMs rather than an ECMs [3.24]. However, the formidable mathematical structure of EMs heavily curtails their applicability in practice. Accordingly, the task how to tailor EMs towards embedment in advanced BMSs remains a challenge.

The primary goal of this work is to overcome the above-mentioned drawbacks, and improve SOC estimation accuracy through the co-estimation of SOC, capacity and resistance for lithium-ion batteries. To this end, a one dimensional (1-D) EM was adopted for its ease of implementation in a real BMS with limited computation resource. Trinal proportional-integral (PI) observers were then employed to achieve co-estimation. It is worth noted that PI observers always exhibit strong robustness against modeling uncertainties through the addition of integrator [3.25], [3.26]. In particular, they are more computationally efficient and well-suited to be embedded in BMSs relative to other observers. Actually, the utilization of the high-fidelity electrochemical model and the robust PI observers differentiates our study with the presented methods in the literature. This can not only improve the modeling accuracy, but also make the proposed method applicable in realistic BMSs. Additionally, a moving-window ampere-hour counting technique and an iteration-approaching method were incorporated to further improve the

estimation accuracy. The effectiveness of the proposed method was experimentally verified on a well-established test rig. The estimation robustness against erroneous initial parameters and different aging levels.

3.2 Lithium-Ion Battery Modeling

3.2.1 Electrochemical model

On the basis of porous electrode theory and concentrated solution theory, EMs can capture the spatiotemporal dynamics including lithium-ion concentration, electric potential, and intercalation kinetics. The 1D-spatial model is used here strike a balance between mathematical simplicity and accuracy. It describes the dynamic behaviors of lithium-ion batteries by the governing equations from (3.1) to (3.9) (also given in [3.24], [3.27]-[3.29]) based upon the electrochemical principles. It is assumed that the solid spherical particles uniformly disperse along the X-axis, and the intercalation and de-intercalation process of lithium-ions is represented by the insertion of ions in and out of these solid spherical particles [3.24], as shown in Fig. 3.1.

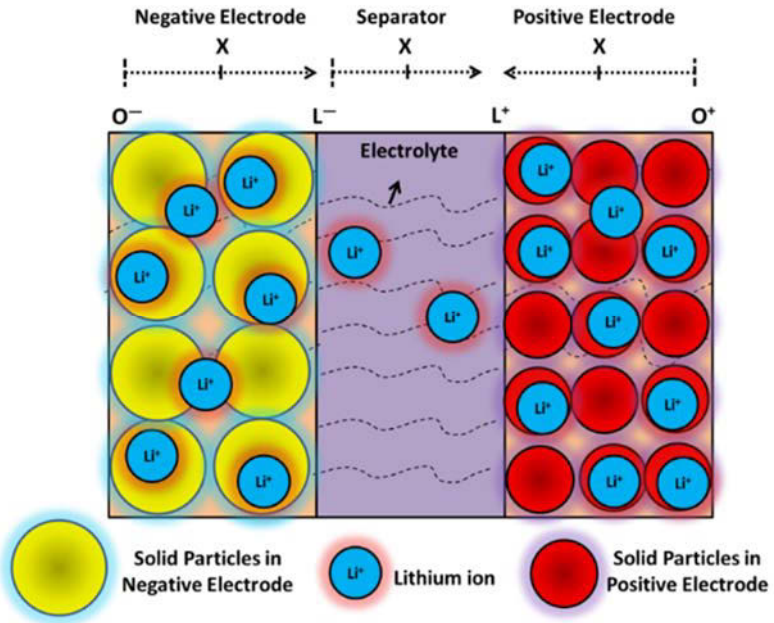

Fig. 3.1 Schematic of a lithium-ion battery electrochemical model.

The cell terminal voltage is governed by

$$U(t)=\Phi_s\left(0^+,t\right)-\Phi_s\left(0^-,t\right)-I(t)R_c \tag{3.1}$$

where $\Phi_s\left(0^+,t\right)$ and $\Phi_s\left(0^-,t\right)$ denote the electric potentials at the ends of two solid electrodes, respectively; R_c represents an empirical contract resistance; $I(t)$ and $U(t)$ are the loading current and the terminal voltage, which serve as the model input and output.

The relationship between the loading current and potentials in the electrode and electrolyte are given by

$$\frac{\partial\Phi_s(x,t)}{\partial x}=\frac{i_e(x,t)-I(t)}{\sigma} \tag{3.2}$$

$$\frac{\partial\Phi_e(x,t)}{\partial x}=-\frac{i_e(x,t)}{k}+\frac{2RT}{F}\left(1-t_c^0\right)\left(1+\frac{d\ln f_{\pm}}{d\ln c_e}(x,\mathrm{t})\right)\frac{\partial\ln c_e(x,t)}{\partial x} \tag{3.3}$$

where σ denotes the effective electronic conductivity in the electrode, i_e the local current in the electrolyte, R the universal gas constant, T the absolute temperature, F Faraday's constant, $f_{\pm}$ the activity coefficient, k the effective ionic conductivity in the electrolyte, and t_c^0 the transference number of the cations.

The relationships between the ionic current and lithium-ion concentrations in the electrode and electrolyte are expressed as

$$\frac{\partial c_e(x,t)}{\partial t}=\frac{\partial}{\partial x}\left(D_e\frac{\partial c_e(x,t)}{\partial x}\right)+\frac{1}{F\varepsilon_e}\frac{\partial\left(t_a^0 i_e(x,t)\right)}{\partial x} \tag{3.4}$$

$$\frac{\partial c_s(x,r,t)}{\partial t}=\frac{1}{r^2}\frac{\partial}{\partial x}\left(D_s r^2\frac{\partial c_s(x,r,t)}{\partial x}\right) \tag{3.5}$$

where D_e denotes the effective ionic diffusion coefficient, ε_e the volume fraction of electrolyte, and t_a^0 the transference number of the anions.

The molar flux $j_n(x,t)$ is related to the divergence of the current in the electrolyte, and can be modeled as

$$\frac{\partial i_e(x,t)}{\partial x} = aFj_n(x,t) \tag{3.6}$$

where a denotes the specific interfacial area.

According to the well-known *Bulter-Volmer* equation, the relationship between the molar flux $j_n(x,t)$ and the overpotential $\eta_s(x,t)$ is given by

$$j_n(x,t) = \frac{i_0(x,t)}{F}\left[\exp\left(\frac{a_a F}{RT}\eta_s(x,t)\right) - \exp\left(\frac{-a_c F}{RT}\eta_s(x,t)\right)\right] \tag{3.7}$$

where a_a and a_c denote the anodic and cathodic coefficients; i_0 the exchange current density.

The overpotential and the exchange current density are given by

$$\eta_s(x,t) = \Phi_s(x,t) - \Phi_e(x,t) - U\left(c_s\left(x,R_p,t\right)\right) - FR_f j_n(x,t) \tag{3.8}$$

$$i_0(x,t) = r_{eff} c_e(x,t)^{a_a}\left(c_{s,\max} - c_s\left(x,R_p,t\right)\right)^{a_a} c_s\left(x,R_p,t\right)^{a_c} \tag{3.9}$$

where $U(c_s(x,R_p,t))$ denotes the open circuit potential of the electrode, R_f the solid-electrolyte interface (SEI) film resistance, r_{eff} a kinetic rate constant, R_p the radius of spherical solid particles, and $c_{s,max}$ the maximum possible solid-phase lithium-ion concentration.

3.2.2 Model reduction

The PDE-based model presented in the previous section is able to represent the battery dynamics with high accuracy. For model derivation, the PDEs are always first converted into ordinary differential equations through diverse methods [3.30]. However, the analytical solution may be infeasible without further model simplification or reduction. To perform model simplification, it is presumed that each electrode can be idealized as a single spherical solid particle that is universally known as the single particle model (SPM). This model significantly enhances state observability while retaining high model

accuracy, which enables it applicable for SOC estimation and SOH monitoring [3.31]. The ionic concentration in the electrolyte $c_e(t)$ is also deemed to be uniform for the further model reduction, which implies $\frac{\partial c_e}{\partial t}=0$ and $\frac{\partial c_e}{\partial x}=0$ [3.24], [3.32]. Then, the two electrode potentials can be derived as

$$\Phi_s\left(0^+,t\right)=\frac{2RT}{F}\ln\left(y^+ +\sqrt{\left(y^+\right)^2+1}\right)+U^+\left(c_s^+\left(R_p^+,t\right)\right)+\frac{R_f^+}{a^+L^+}I(t) \tag{3.10}$$

$$\Phi_s\left(0^-,t\right)=\frac{2RT}{F}\ln\left(y^- +\sqrt{\left(y^-\right)^2+1}\right)+U^-\left(c_s^-\left(R_p^-,t\right)\right)+\frac{R_f^-}{a^-L^-}I(t) \tag{3.11}$$

where $y^+=\dfrac{I(t)}{2a^+L^+r_{eff}^+\sqrt{c_e^0c_s^+\left(R_p^+,t\right)\left(c_{s,\max}^+-c_s^+\left(R_p^+,t\right)\right)}}$

and $y^-=\dfrac{I(t)}{2a^-L^-r_{eff}^-\sqrt{c_e^0c_s^-\left(R_p^-,t\right)\left(c_{s,\max}^--c_s^-\left(R_p^-,t\right)\right)}}$.

The terminal voltage is governed by

$$U(t)=\frac{2RT}{F}\ln\frac{y^+ +\sqrt{\left(y^+\right)^2+1}}{y^- +\sqrt{\left(y^-\right)^2+1}}+U^+\left(c_s^+\left(R_p^+,t\right)\right)-U^-\left(c_s^-\left(R_p^-,t\right)\right)+I(t)R_{sum} \tag{3.12}$$

where R_{sum} is the sum of contract and SEI film resistances.

The boundary and initial conditions in both electrodes are given by

$$\begin{cases}\left.\dfrac{\partial c_s^+}{\partial r}\right|_{r=0}=0\\ \left.\dfrac{\partial c_s^+}{\partial r}\right|_{r=R_p^+}=\dfrac{I(t)}{D_s^+Fa^+L^+}\end{cases} \tag{3.13}$$

$$c_s^+\left(r,0\right)=c_s^{0+}\left(r\right) \tag{3.14}$$

$$\begin{cases} \left.\dfrac{\partial c_s^-}{\partial r}\right|_{r=0} = 0 \\ \left.\dfrac{\partial c_s^-}{\partial r}\right|_{r=R_p^-} = \dfrac{I(t)}{D_s^- F a^- L^-} \end{cases} \tag{3.15}$$

$$c_s^-(r,0) = c_s^{0-}(r) \tag{3.16}$$

Equations (3.12) to (3.16) describe the relationship between the loading current $I(t)$ and the cell terminal voltage $U(t)$ with the lithium-ion concentration $c_s(r, t)$.

3.2.3 Numerical solution for PDEs

The described model has overwhelmingly high complexity due to the employment of a set of PDEs. Therefore, it is pivotal to solve the model in a more efficient manner so that it can be embedded in BMSs for online implementation. To this end, equation (3.5) can be reformulated as

$$\frac{\partial c_s(r,t)}{\partial t} = D_s\left(\frac{2}{r}\frac{\partial c_s(r,t)}{\partial r} + \frac{\partial^2 c_s(r,t)}{\partial r^2}\right) \tag{3.17}$$

For further discretising (3.17), the spatial grids of radius R_p and time t are demarcated as

$$\begin{cases} dr = R_p / node1 \\ dt = t / node2 \end{cases} \tag{3.18}$$

where $node1$ and $node2$ denote the number of grid nodes of the radius and time, respectively.

For $k = 1$ (the lowest grid index is 1) to $k = node2$-1 and $i = 1$ to $i = node1$,

$$\frac{\partial c_s(r,t)}{\partial t} \approx \frac{c_{sd}(i,k+1) - c_{sd}(i,k)}{dt} \tag{3.19}$$

where $c_{sd}(i, k)$ denotes $c_s((i\text{-}1)dr, (k\text{-}1)dt)$.

For $i = 2$ to $i = node1$-1 and $k = 1$ to $k = node2$,

$$\frac{\partial c_s(r,t)}{\partial r} \approx \frac{c_{sd}(i+1,k)-c_{sd}(i-1,k)}{2dr} \tag{3.20}$$

$$\frac{\partial^2 c_s(r,t)}{\partial r^2} \approx \frac{c_{sd}(i+1,k)-2c_{sd}(i,k)+c_{sd}(i-1,k)}{dr^2} \tag{3.21}$$

Then, equation (17) can be approximated as

$$\frac{c_{sd}(i,k+1)-c_{sd}(i,k)}{dt} = D_s\left[\frac{c_{sd}(i+1,k)-c_{sd}(i-1,k)}{(i-1)dr^2}+\frac{c_{sd}(i+1,k)-2c_{sd}(i,k)+c_{sd}(i-1,k)}{dr^2}\right] \tag{3.22}$$

where $i = 2, 3, \ldots, (node1\text{-}1)$, and $k = 1, 2, \ldots, (node2\text{-}1)$.

The boundary conditions can be derived by

$$\begin{cases} \dfrac{c_{sd}^{+}(2,k)-c_{sd}^{+}(1,k)}{dr}=0 \\ \dfrac{c_{sd}^{+}(node1,k)-c_{sd}^{+}(node1-1,k)}{dr}=\dfrac{I((k-1)dt)}{D_s^{+}Fa^{+}L^{+}} \end{cases} \tag{3.23}$$

and

$$\begin{cases} \dfrac{c_{sd}^{-}(2,k)-c_{sd}^{-}(1,k)}{dr}=0 \\ \dfrac{c_{sd}^{-}(node1,k)-c_{sd}^{-}(node1-1,k)}{dr}=\dfrac{I((k-1)dt)}{D_s^{-}Fa^{-}L^{-}} \end{cases} \tag{3.24}$$

where $k = 1, 2, \ldots, node2$.

The initial conditions can be given by

$$\begin{cases} c_{sd}^{+}(i,1)=c_{sd}^{0+} \\ c_{sd}^{-}(i,1)=c_{sd}^{0-} \end{cases} \tag{3.25}$$

where $i = 1, 2, \ldots, node1$.

Based on the above equations, $c_s(r, t)$ can be deduced at various frame of radius and time. Furthermore, in combination with (3.12), the complete model can be obtained.

3.2.4 SOC definition in the SPM

For the SPM modeling, the lithium-ion concentration in electrodes is used to represent the battery SOC. The total number of lithium-ions in the solid electrode can be described as

$$c_{s\_total} = \int_0^{R_p} 4\pi r^2 c_s(r,t)\,dr = \sum_{i=1}^{node1} c_{sd}(i,k)\,4\pi\left[(i-1)\,dr\right]^2 dr \tag{3.26}$$

where c_{s_total} is the total number of lithium-ions in the solid electrode.

The mean lithium-ion concentration in the electrode can be given by

$$c_{s\_mean} = c_{s\_total} \Big/ \left(\frac{4}{3}\pi R_p^3\right) = \sum_{i=1}^{node1} 3c_{sd}(i,k)(i-1)^2\,dr^3 \Big/ R_p^3 \tag{3.27}$$

where c_{s_mean} denotes the mean lithium-ion concentration in the solid electrode.

Thus, the battery SOC can be defined by

$$SOC = \left(c_{s\_mean} - c_{s\_SOC=0\%}\right) \Big/ \left(c_{s\_SOC=100\%} - c_{s\_SOC=0\%}\right) \tag{3.28}$$

where $c_{s\_SOC=0\%}$ and $c_{s\_SOC=100\%}$ denote the mean lithium-ion concentration values at 0% SOC and 100% SOC, respectively. Since the loss of lithium inventory (LLI) is considered as one main cause of capacity degradation [3.33], the total number of lithium-ions in the solid electrode gradually decreases during the battery aging processes. The mean lithium-ion concentration values at 0% SOC and 100% SOC for different aging levels are listed in Table 3.1, which are referenced from [3.28], [3.29] and adjusted for accommodating the charging/discharging characteristics. The relationship between the mean lithium-ion concentration values and battery capacity can be considered as a tabulated function.

Accordingly, $c_{s\_SOC=0\%}$ and $c_{s\_SOC=100\%}$ need to be updated according to the capacity during battery aging processes.

Table 3.1 The mean lithium-ion concentration values in the positive electrode for different aging levels

	92 Ah	87 Ah	82.5 Ah	78.5 Ah	74 Ah	69.5 Ah
$c_{s\_SOC=0\%}$	42430	41000	40000	39000	38080	36750
$c_{s\_SOC=100\%}$	20400	20400	20400	20400	20400	20400

3.3 Proposed Estimation Approaches

The structure of SOC, capacity and resistance co-estimation scheme proposed in this study is shown in Fig. 3.2. It includes three main parts: battery SPM, capacity estimation module and resistance estimation module. The capacity estimation module is used for calculating battery capacity and the comparative SOC. The resistance estimation module is employed to estimate the comparative capacity and resistance that comprises of contract resistance and SEI film resistance. The estimated capacity and resistance are then fed back to the battery SPM to estimate battery terminal voltage and SOC. The detailed co-estimation process is elaborated in the following parts.

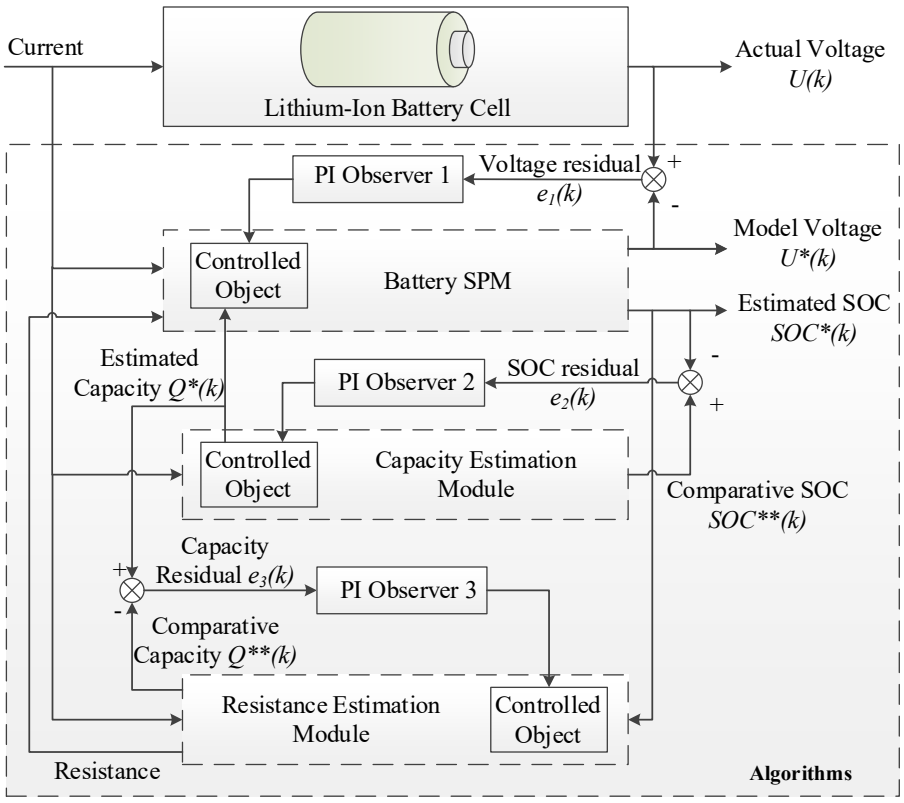

Fig. 3.2 The structure of battery SOC, capacity and resistance co-estimation algorithms.

3.3.1 SOC estimation

In Fig. 3.2, the model output voltage $U^*(k)$ at time index k is given by (3.12). The residual voltage $e_1(k)$ is the difference between the model output voltage $U^*(k)$ and the actual cell terminal voltage $U(k)$. G_1 is the gain of the first PI observer for SOC estimation. As indicated by (3.12), the model output voltage is strongly related to lithium-ion concentration values. Therefore, the first PI observer compensation $G_1e_1(k)$ is fed back to modify the lithium-ion concentration $c_{sd}(i,\ k+1)$ at the next time interval $(k+1)$ for correcting the model output voltage and eliminating the residual voltage. Besides, the SOC value is determined by the mean lithium-ion concentration, c_{s_mean}, which is determined by the lithium-ion concentration $c_{sd}(i,\ k)$ as expressed by (3.26) and (3.27). Accordingly, with the updated lithium-ion concentration $c_{sd}(i,\ k+1)$, the estimated SOC can be amended to have higher accuracy. The modified function is written as

$$\begin{cases} e_1(k) = U(k) - U^*(k) \\ c_{sd}(i,k+1) = c_{sd}(i,k) + G_1 e_1(k) \end{cases} \tag{3.29}$$

3.3.2 Capacity estimation

The battery SOC can also be calculated by Coulomb-counting method by

$$SOC(t_2) = SOC(t_1) + \int_{t_1}^{t_2} \eta i(t) dt / Q \tag{3.30}$$

where η denotes the columbic efficiency that can be considered as 1 for lithium-ion batteries; Q denotes the battery capacity.

A moving window with a range of 200 secs is used for computing the comparative value $SOC^{**}(k)$ according to (3.30). If the estimated capacity equates to the actual battery capacity, the SOC values $SOC^{*}(k)$ determined by (3.28) would be equal to the comparative value $SOC^{**}(k)$. Otherwise, there would be a difference between these two values. The difference can be utilized to modify the estimated capacity. As shown in Fig. 3.2, the residual SOC $e_2(k)$ represents the difference between the model estimated SOC value $SOC^{*}(k)$ and the comparative SOC value $SOC^{**}(k)$. G_2 is the gain of the second PI observer for capacity estimation. The second PI observer compensation $G_2e_2(k)$ is fed back to update the battery capacity $Q(k+1)$. The modified function can be written as

$$\begin{cases} e_2(k) = SOC^{*}(k) - SOC^{**}(k) \\ Q^{*}(k+1) = Q^{*}(k) + G_2 e_2(k) \end{cases} \tag{3.31}$$

The estimated battery capacity $Q^{*}(k)$ needs to be fed back to the battery model, and serves as the initial capacity $Q_0(k+1)$ for the next estimation interval until the estimated capacity is equivalent to the model initial capacity.

3.3.3 Resistance estimation

Despite the model can track the actual terminal voltage with the first PI observer, it may lead to inaccurate SOC estimation due to the erroneous resistance value and lithium-ion concentration. Fig. 3.3 shows the ΔOCV/ΔSOC evolution against SOC values. It can be seen that the ΔOCV/ΔSOC drops significantly from 5% SOC to 10% SOC (the low SOC range), but rises significantly from 90% SOC to 100% SOC (the high SOC range). The SOC estimation error resulting from the erroneous OCV in these two zones would be less than that in other areas (the medium SOC range). In contrast, the SOC estimation error

caused by an erroneous resistance estimate in other OCV range would be greater. Therefore, the low and high SOC zones can be employed to estimate battery resistance. In order to make batteries avoid working in low SOC zones for safety concerns and service life preservation, the resistance estimation is only implemented in the high SOC zone.

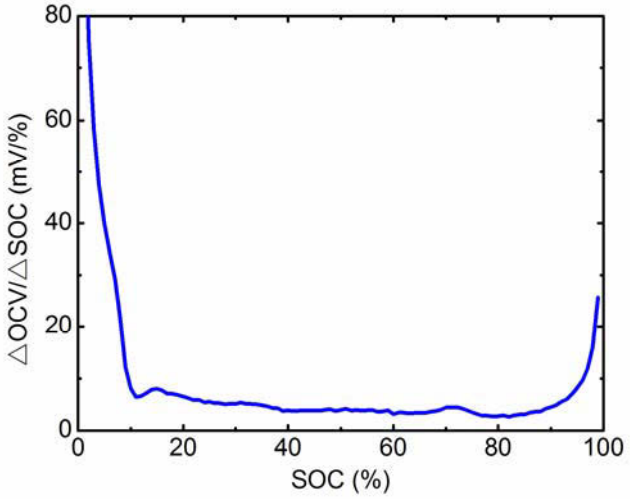

Fig. 3.3 The △OCV/△SOC curve in different SOC.

The method for resistance estimation is similar to that for capacity estimation. The battery capacity can be calculated by

$$Q = \int_{t_1}^{t_2} i(t)dt / \left(SOC(t_2) - SOC(t_1)\right) \tag{3.32}$$

If there is no error in resistance estimation, the comparative capacity $Q^{**}(k)$ calculated by (3.32) would be equal to the estimated capacity $Q^{*}(k)$. As shown in Fig. 3.2, the residual capacity $e_3(k)$ denotes the difference between the model estimated capacity $Q^{*}(k)$ and the comparative capacity $Q^{**}(k)$. G_3 is the gain of the third PI observer for resistance estimation. The third PI observer compensation $G_3e_3(k)$ is fed back to update the resistance value $R_{sum}(k+1)$ with the modified function formulated as (3.33). The estimated resistance needs to be fed back to the battery model for updating the model output voltage at the next time interval.

$$\begin{cases} e_3(k) = Q^*(k) - Q^{**}(k) \\ R^*_{sum}(k+1) = R^*_{sum}(k) + G_3 e_3(k) \end{cases} \tag{3.33}$$

3.4 Experimental Test

3.4.1 Battery test bench

To verify the effectiveness of the proposed method, a test bench is purposely established to obtain battery test datasets as shown in Fig. 3.4. It mainly consists of a battery charger/discharger, a host computer, a thermal chamber and the test lithium-ion battery cells. The battery cycler is used to charge or discharge cells according to preset loading profiles, and measure desirable experimental parameters (e.g. terminal voltage and loading current) with a precision of 0.05% of full the measurement range. The host computer functions to compose the loading profiles, and record the real-time operating parameters of batteries. The thermal chamber can provide various ambient temperatures as required. The lithium-ion battery cells with a nominal capacity of 90 Ah are used to conduct all the tests.

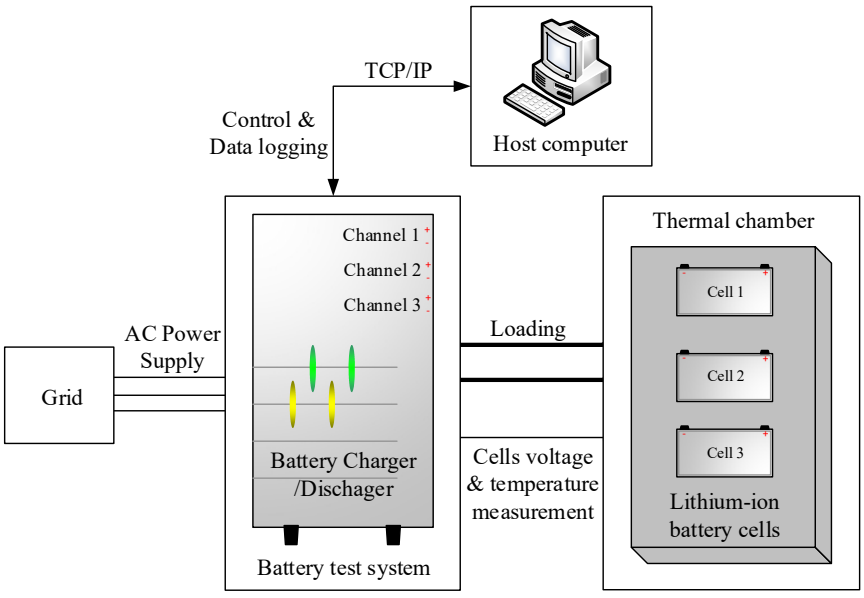

Fig. 3.4 Battery test bench.

3.4.2 Test schedules

A test schedule was specially designed to excite the test batteries under different ambient temperatures, loading currents and aging levels as shown in Fig. 3.5.

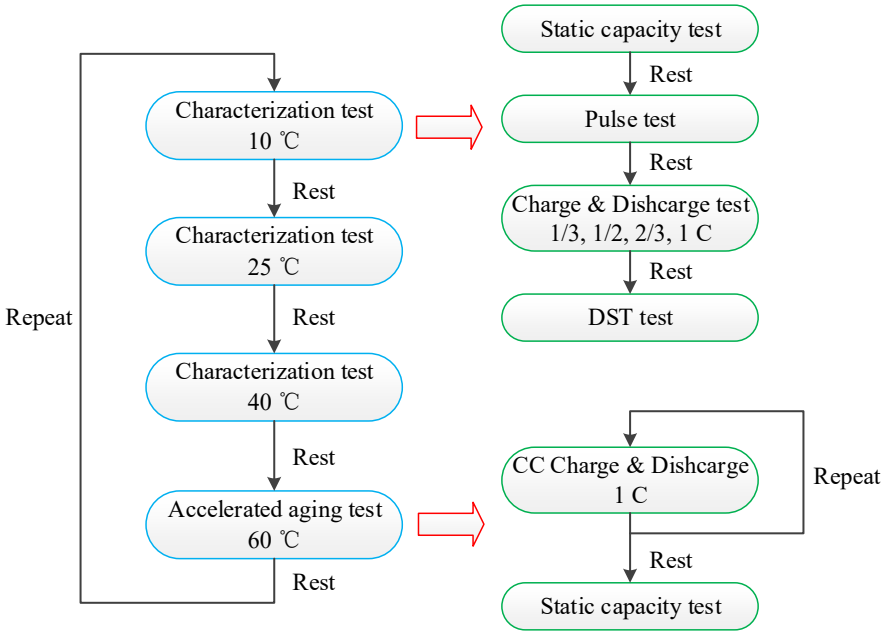

Fig. 3.5 Battery test schedules.

Each experimental procedure begins with a battery characterization test at 10 °C and then a rest for 4 hours. Two identical characterization tests at 25 °C and 40 °C ensue, followed by an accelerated aging test conducted at 60 °C. The battery characterization test includes a static capacity test, a pulse test, a charge/discharge test and a dynamic stress test (DST). The static capacity test is to measure the actual cell capacity. The pulse test is used to obtain the OCV versus SOC curve by charging or discharging at C/3 every 5% SOC increment followed by 1 hr rest until 100% SOC or 0% SOC. The charge or discharge tests are to load the batteries with dissimilar current regimes. In this test, the battery cell was charged by the (constant-current-constant-voltage) CCCV regime and discharged in a (constant-current) CC regime at different loading current rates including C/3, 2C/3, C/2 and 1C. The driving-cycle-based DST cycles were utilized to simulate actual loading conditions in EV applications. The purpose of the accelerated aging test is to attain different aging levels in a limited time. In the accelerated aging test, the battery cell was

charged and discharged in a CC regime at 1C rate and 60 °C. Each accelerated aging test cycle makes the capacity decrease by 5 Ah, approximately.

3.5 Numerical Simulation and Experimental Verification

3.5.1 Cell voltage verification

The model parameters used in this study are obtained from [3.28], [3.29], [3.32] and [3.34], and adjusted by fitting the experimental data based on the Levenberg–Marquardt algorithm [3.35], [3.36]. The battery cell was fully charged using the CCCV regime at 1C rate and 25 °C. The comparison between the simulation and measured data for cell voltage is shown in Fig. 3.6.

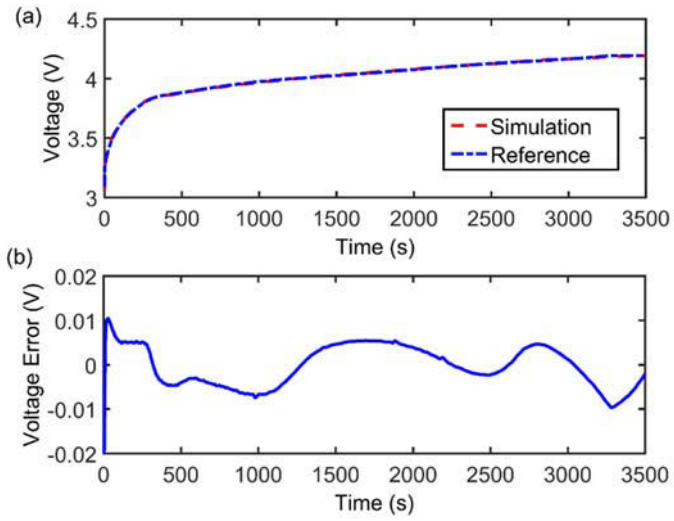

Fig. 3.6 Cell voltage simulation result, where (a) reference voltage and simulation voltage and (b) voltage error.

By observing Fig. 3.6(b), it is apparent that the voltage error between the referenced voltage and simulated voltage can be limited to a band of +/-10 mV. The result shows that the derived model can accurately capture the battery dynamics, which provides a solid foundation for subsequent state estimation.

3.5.2 SOC estimation result

To verify the proposed co-estimation method for lithium-ion batteries under realistic loading conditions, the driving-cycle-based DST cycle is employed to discharge the test battery. Firstly, the battery cell was fully discharged in a CC regime at C/3 rate until full discharged, namely 0% SOC. The referenced SOCs can be calculated using Coulomb-counting method as given by (3.29) with the accurate initial SOC. Since the current sensor used is highly accurate, the referenced SOC can be reasonably regarded as the "real" battery SOC.

With the accurate initial SOC, the SOC estimation results are shown in Fig. 3.7. It can be seen that the estimated SOC can accurately track the referenced SOC during the entire test. The error between the referenced SOC and the estimated SOC can be successfully confined into an error band +/-1.5%. This minor error can be attributed to the modelling deficiency.

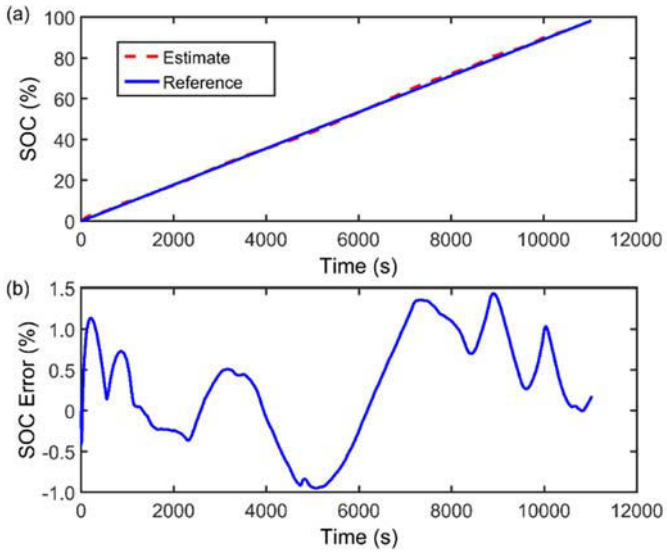

Fig. 3.7 SOC estimation results during CC charge with accurate initial SOC, where (a) SOC estimation and (b) SOC error.

However, it is always difficult to acquire the accurate initial SOC for BMSs in real applications, especially after the batteries have been used for a long time. A deviant SOC initiation often leads to large SOC estimation errors, even a complete failure. Thus, it is

essential to ensure the robustness against inaccurate initiation for an enabling SOC scheme. In this study, in order to verify the robustness of the proposed method against erroneous initial state assumptions, the initial SOC of the model is set to 30% while the actual initial SOC is 0%. The estimation results are shown in Fig. 3.8.

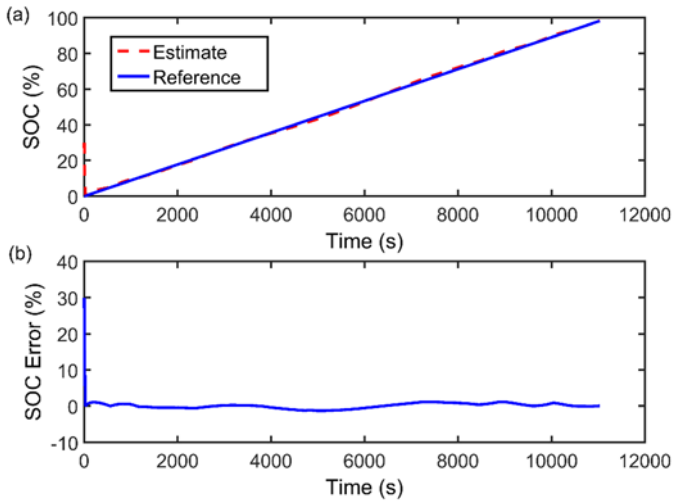

Fig. 3.8 SOC estimation results during CC charge with erroneous initial SOC, where (a) SOC estimation and (b) SOC error.

It is obvious that the estimated SOC can quickly compensate the initial error, and converge to the referenced SOC. Then, the estimated SOC can follow the referenced SOC with an error band of 1.5% SOC.

From the above verification in the CC charging regime, it can be concluded that the proposed method is capable of tracking the referenced SOC accurately with robustness to the initiation nuance.

The DST cycle is a simplified test schedule extracted from the federal urban driving schedule (FUDS) [3.37], which is widely used to simulate actual battery loading conditions in EV applications. The current profile of DST cycle is depicted in Fig. 3.9(a). It is worth mentioning that the battery cell was fully charged in a CCCV regime before the execution of DST, and the initial referenced SOC was 100% while the initial SOC of the model was set to an incorrect value, 50% SOC.

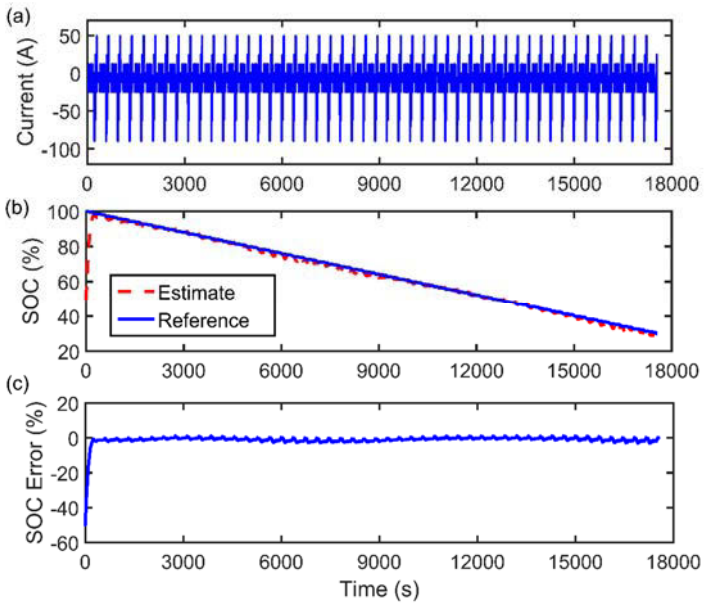

Fig. 3.9 SOC estimation results during DST cycles, where (a) DST cycle current profiles, (b) SOC estimation and (c) SOC error.

From Figs. 3.9(b) and 3.9(c), it can be seen that the maximum SOC error is 50% at the beginning, and the estimated SOC can fast converge to the referenced SOC. Thence, the estimated SOC keeps on following the referenced SOC closely, and the estimation error can be effectively limited to an error band of +/-3%. Discarding the maximum SOC error appearing at the beginning, the root mean square error (RMSE) for SOC estimation is 1.2%. It manifests that the proposed method can estimation the SOC with high accuracy under dynamic loading conditions, even when an erroneous initial SOC value is provided.

3.5.3 SOC and capacity co-estimation results

Usually, the discharging current of a battery pack in EVs changes dramatically due to the varying driving conditions. A short sampling interval and a powerful computation capability are preferred for guaranteeing precision and calculation efficiency. On the contrary, the current varies moderately or even keeps constant during charging period. For example, many manufacturers recommend to charge their batteries in a CC regime. Therefore, this study focuses on battery charging process for capacity estimation.

In the previous section, the proposed method can achieve accurate SOC estimation with known battery capacity. However, in practice, the actual capacity decreases constantly owing to the battery aging. If a BMS fails to take the varying capacity into consideration in SOC estimation, it may result in deviant SOC estimation results.

To demonstrate the influence on SOC estimation caused by erroneous capacity values, two cases are considered here. In the first case, the model capacity is assumed to be greater than the referenced capacity. A battery cell degraded from 92 Ah (the cell initial capacity) to 69.5 Ah was utilized. The referenced capacity is 69.5 Ah, and the referenced initial SOC is set as 0%, while the model capacity and initial SOC are set to 92 Ah and 30%, respectively. The co-estimation results are shown in Fig. 3.10 and Table 3.2. Therein, Q_0 denotes the model initial capacity; Q^* denotes the estimated capacity; e_Q denotes the relative capacity error; e_{SOC_RMSE} denotes the SOC RMSE and e_{SOC_MAX} denotes the maximum absolute SOC error. In each iterative estimation, the estimated capacity at the last time $Q^*(k)$ is used as the model initial capacity $Q_0(k+1)$ for the estimation.

The SOC estimation results with the referenced SOC and estimated SOC at different iteration times are shown in Fig. 3.10. Without any capacity modification, the initial estimated SOC curve is the farthest one from the referenced SOC curve, and most of the estimated SOC values are greater than that of the referenced one. During the process of iterative estimation and capacity modification, the estimated SOC curves get closer and closer to the referenced SOC curve. It validates that the SOC is highly dependent on the actual capacity value, and an erroneous initial capacity value would markedly reduce the accuracy of SOC estimation.

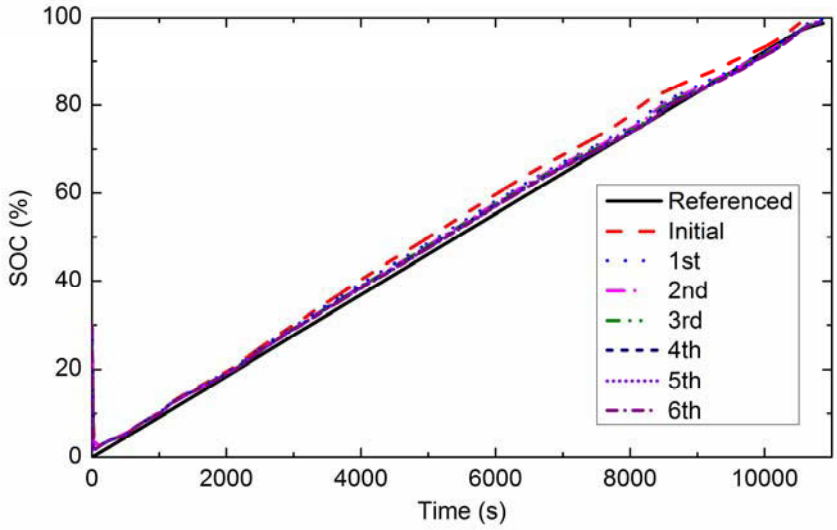

Fig. 3.10. SOC estimation results in the first case.

Table 3.2 Capacity estimation results in the first case.

Iteration times	Q_0 (Ah)	Q^* (Ah)	e_Q (%)	e_{SOC_RMSE} (%)	e_{SOC_MAX} (%)
0	92		32.37	2.45	3.58
1	92	79.59	14.52	2.34	3.38
2	79.59	74.02	6.50	0.83	1.54
3	74.02	71.47	2.83	0.79	1.30
4	71.47	70.36	1.24	0.62	1.00
5	70.36	70.3	1.15	0.58	0.97
6	70.3	70.28	1.12	0.58	0.96
7	70.28	70.28	1.12	0.58	0.96

As shown in Table 3.2, it can be seen that the estimated capacity is equal to the model initial capacity in the seventh iterative estimation, which means that the algorithm finishes the estimation and gets the final estimated capacity, 70.28 Ah. The capacity relative error significantly declines from 32.37% to 1.12%, while the SOC RMSE decreases from 2.45% to 0.58%, and the maximum SOC error drops from 3.58% to 0.96%. In fact, from the fifth to the seventh iterative estimation, there is very little variation for capacity estimation. To reduce the iterative estimation times, it can be considered that the capacity estimation procedure terminates when the estimated capacity difference between two adjacent estimated capacities is less than 0.5% of the rated capacity (i.e. 0.45 Ah in the above case). In Table 3.2, the estimated capacity difference between the fourth and the fifth estimated capacity values reaches 0.06 Ah, which is well less than 0.45 Ah. It proves that it only takes five iterative estimation times to obtain the final estimated capacity with only an infinitesimal error.

Fig. 3.11 shows two zoomed-in figures of estimated SOC and comparative SOC at the initial estimation and the seventh estimation, respectively. As shown in Fig. 3.11(a), without any capacity modification, there is a significant difference between the estimated SOC and the comparative SOC at each moving window during the initial estimation process. However, after seventh capacity modification, the difference shown in Fig. 3.11(b) reduces considerably, and the comparative SOC closely tracks with the estimated SOC. Meanwhile, the battery capacity has also been corrected with a small error. These results validate well the feasibility of the proposed method for the capacity estimation.

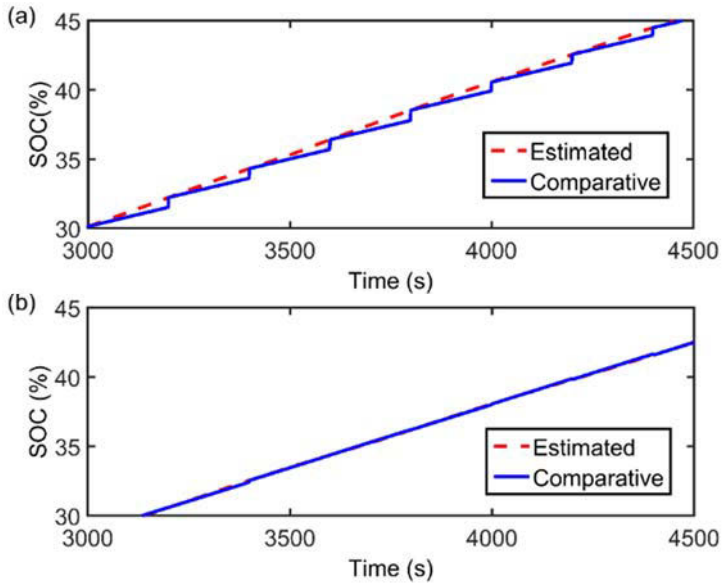

Fig. 3.11 Estimated SOC and comparative SOC, where (a) at the initial estimation and (b) at the seventh estimation.

In the second case, the model capacity is assumed to be less than the referenced capacity. The referenced capacity is 69.5 Ah, and the referenced initial SOC is 0%. While, the model capacity is set to 40 Ah, and the model initial SOC is set to 30%. The results for SOC and capacity co-estimation are shown in Fig. 3.12 and Table 3.3. It presents a similar result to the first case. Due to the deliberately erroneous initial capacity value, the initial estimated SOC curve is far from the referenced SOC curve, and most of the estimated SOCs are less than the referenced values, as shown in Fig. 3.12. However, with several iterative estimation times, the estimated capacity can be rapidly modified so that the estimated SOC curves get closer and closer to the referenced SOC curve.

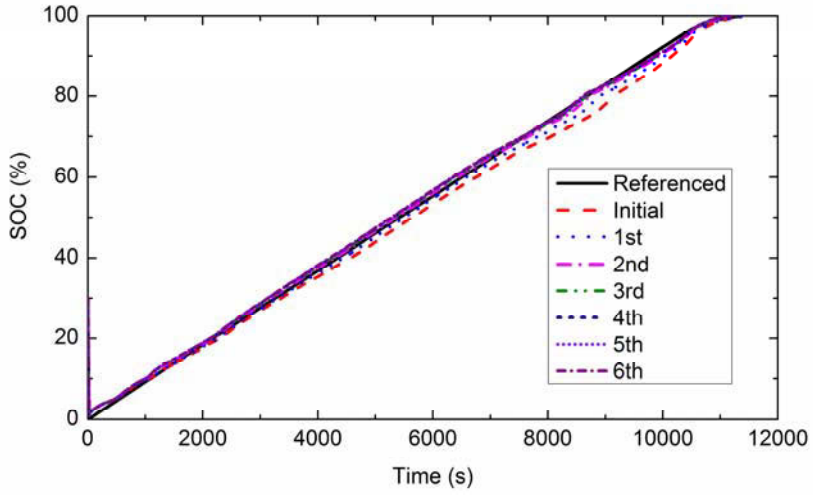

Fig. 3.12 SOC estimation results in the second case.

Table 3.3 Capacity estimation results in the second case.

Iteration times	Q_0 (Ah)	Q^* (Ah)	e_Q (%)	e_{SOC_RMSE} (%)	e_{SOC_MAX} (%)
0	40		-42.45	2.25	4.54
1	40	69.19	-0.45	2.36	5.00
2	69.19	69.96	0.66	0.57	0.95
3	69.96	70.17	0.96	0.57	0.96
4	70.17	70.24	1.06	0.57	0.97
5	70.24	70.27	1.09	0.58	0.97
6	70.27	70.27	1.11	0.58	0.97

In Table 3.3, the estimated capacity is equal to the model initial capacity in the sixth iterative estimation, which means the algorithm finishes the estimation and obtains the final estimated capacity, namely 70.27 Ah. The capacity relative error markedly drops

from 42.45% to 1.11%, while the SOC RMSE decreases from 2.25% to 0.58% and the maximum SOC error goes down from 4.54% to 0.97%. The difference between the second and the third estimated capacity values is 0.21 Ah, which is less than 0.45 Ah, and therefore, it just needs three iterative estimation times to obtain the final estimated capacity with a small error.

It can be concluded that the proposed method for SOC and capacity co-estimation works well, and is quite robust against the erroneous initial capacity and SOC values. During the estimation process, the estimated capacity and SOC gradually converge to the referenced values at the same time.

3.5.4 SOC, capacity and resistance co-estimation results

The previous co-estimation results of SOC and capacity are based on the referenced battery resistances. However, the battery resistance changes with SOCs and aging. An incorrect resistance value may cause an inaccurate model output voltage, and also compromise the SOC and capacity estimation results. Therefore, it is crucial for advanced BMSs to incorporate the real-time resistance estimation with SOC and capacity estimation.

A battery cell with 69.5 Ah, 1.680 mΩ and 0% SOC was used to verify the proposed method, while the model parameters were set to erroneous values: 92 Ah, 1.000 mΩ and 30% SOC. The co-estimation results of SOC, capacity and resistance are shown in Fig. 3.13.

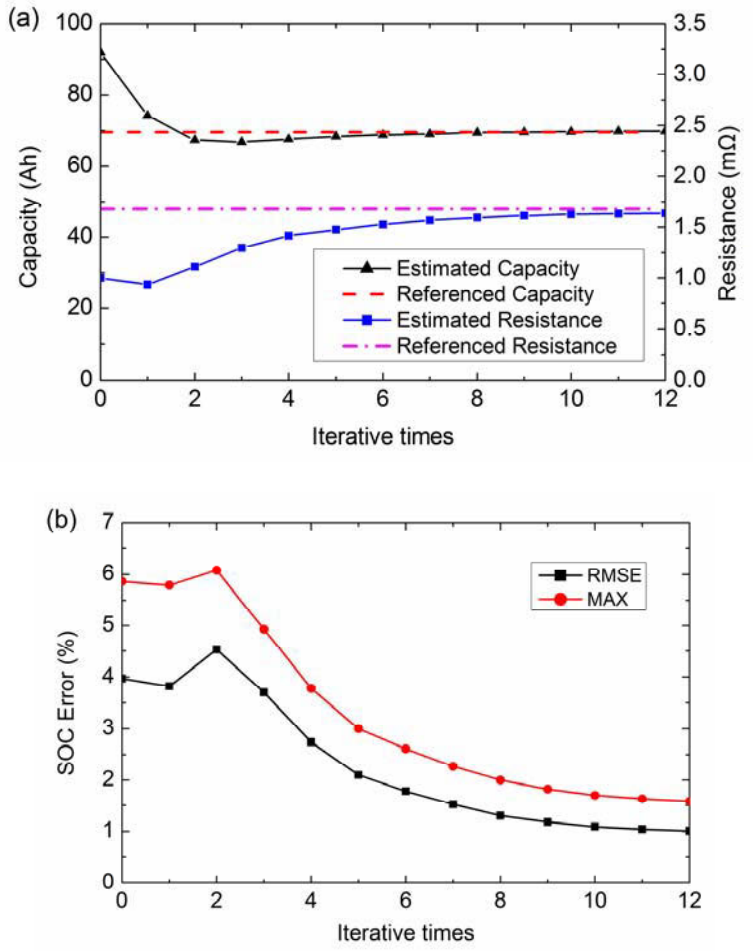

Fig. 3.13 Co-estimation results, where (a) capacity and resistance and (b) SOC error.

As can be identified in Fig. 3.13, after several iterative estimation times, the estimated capacity converges from 92 Ah to 69.83 Ah, and the estimated resistance converges from 1.000 mΩ to 1.636 mΩ. The capacity error is 0.33 Ah (relative error 0.47%) while the resistance error is 0.044 mΩ (relative error -2.62%). Meanwhile, the estimated SOC gets closer the referenced SOC with the increasing iterations. The SOC RMSE drops from 3.97% to 1.01%, while the maximum SOC error declines from 5.86% to 1.58%.

To verify the effectiveness of the proposed method during battery aging process, a battery cell degraded from 92 Ah to 69.5 Ah was used for the investigation. The co-estimation results are shown in Fig. 3.14 at six different aging levels (1-6) with 92 Ah, 87 Ah, 82.5 Ah, 78.5 Ah, 74 Ah and 69.5 Ah, respectively. The initial values of the model were set to 92 Ah, 1.000 mΩ and 30% SOC.

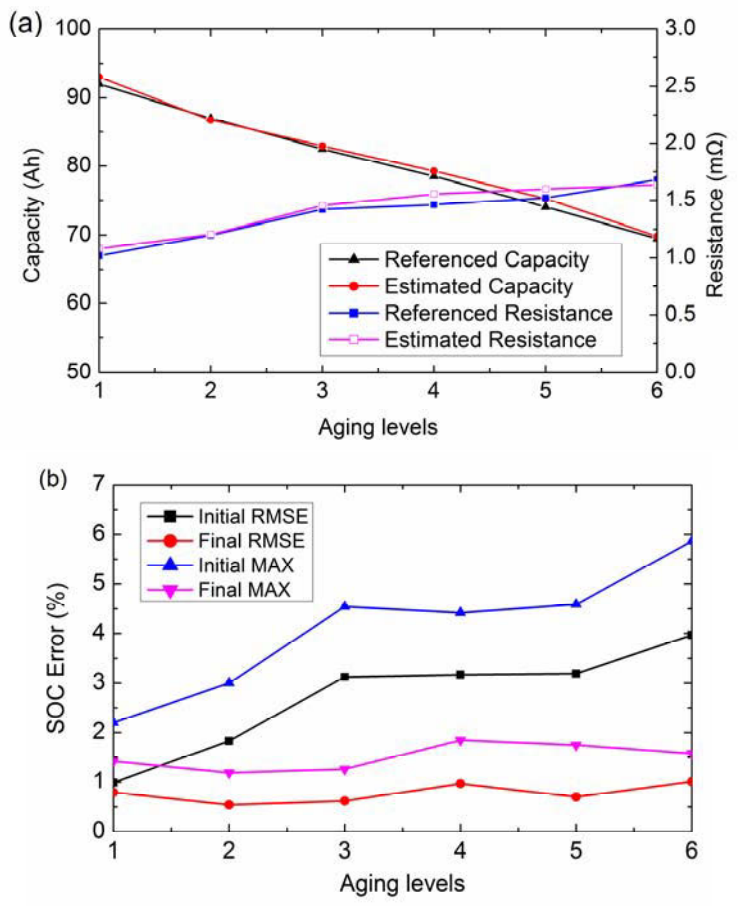

Fig. 3.14 Co-estimation results at different aging levels, where (a) capacity and resistance, and (b) SOC errors.

In Fig. 3.14(a), the co-estimation results show a good performance for both capacity and resistance. At different aging levels, the maximum estimated capacity error is 1.22 Ah (relative error 1.65%) at Level 5 (75 Ah), and the maximum estimated resistance error is 0.094 mΩ (relative error 6.44%) at Level 4 (78.5 Ah). From Fig. 14(b), it can be seen that without capacity and resistance co-estimation, both initial SOC RMSE and maximum SOC error are small at low aging levels such as Level 1 (92 Ah) and Level 2 (87 Ah) while the SOC errors rise with the increased battery aging levels. However, with the proposed co-estimation approach, the final estimated SOC RMSE can be decreased to an error band of 1% SOC, and the maximum SOC can be limited in an error band of 2% for all aging levels, which indicates that the proposed approach handles different battery aging levels quite well.

To verify the effectiveness of the proposed method under different temperatures, the characteristic test data under 10 °C, 25 °C and 40 °C were used. The initial value of the model was set to 92 Ah, 1.000 mΩ and 30% SOC. The co-estimation results under these temperatures are shown in Fig. 3.15.

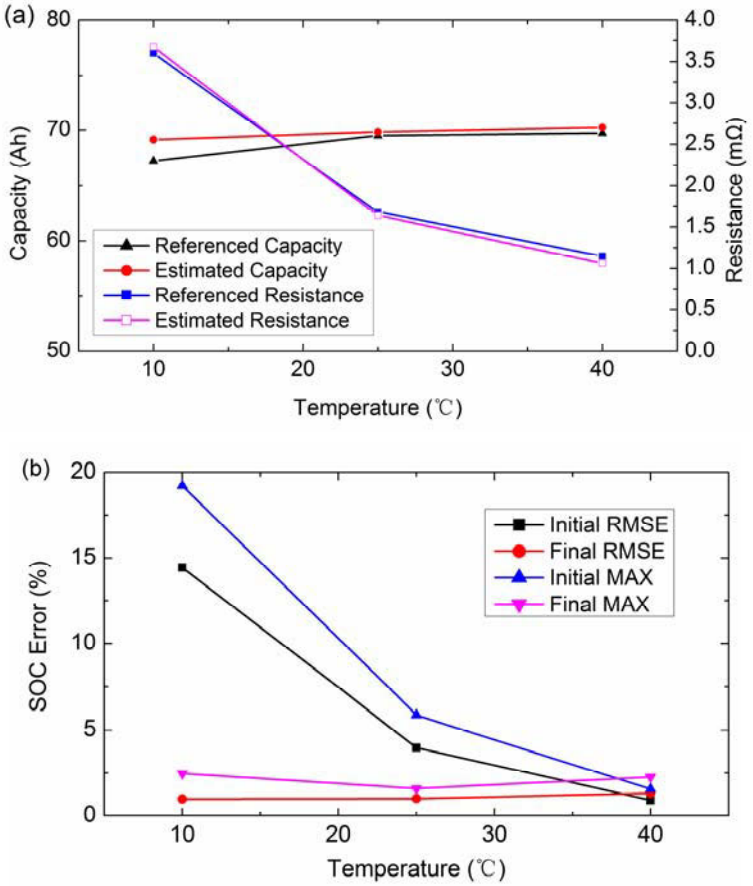

Fig. 3.15. Co-estimation results under different temperatures, where (a) capacity and resistance, and (b) SOC errors.

Under varied ambient temperatures, the co-estimation results presented in Fig. 3.15(a) show that the proposed method perform well for the co-estimation of battery capacity and resistance. The maximum estimated capacity error is 1.89 Ah (relative error 2.81%) at 10 °C, and the maximum estimated resistance error is 0.087 mΩ (relative error -7.5%) at 40 °C. In Fig. 3.15(b), both SOC RMSE and maximum SOC absolute error can be limited in small error bands under different temperatures. It is noted that with incorrect initial capacity and resistance values, the SOC estimation can still work well at 40 °C. This is

the result of both incorrect capacity and resistance values supplied to the model. Although the final estimated SOC errors are a little greater than the initial ones, the capacity and resistance estimates have been refined to be much closer to the actual values.

From above co-estimation results of SOC, capacity, and resistance, it can be concluded that the proposed method for SOC, capacity and resistance co-estimation can tail after the referenced values closely, and presents strong robustness against erroneous initial parameters and different battery aging levels.

3.6 Summary

In this chapter, a novel approach has been proposed to simultaneously estimate SOC, capacity and resistance for lithium-ion batteries. It incorporates the influence of aging on SOC estimation by furnishing the state equations with up-to-date capacity and resistance estimates, thereby improving the SOC estimation accuracy. To this end, a high-fidelity electrochemical model was adopted to capture the battery dynamics with accuracy. The model was further simplified and derived through a numerical method. Trinal PI observers were executed to realize the co-estimation task. Furthermore, the moving-window ampere-hour counting technique and the iteration-approaching method were incorporated for enhancing the estimation precision. To verify the proposed approach, comprehensive characterization tests were carried out under discrepant ambient temperatures and aging levels on a well-established test rig. Experimental results showed that the proposed co-estimation approach could simultaneously estimate SOC, capacity and resistance with high precision. The estimation robustness against erroneous initial parameters, different aging levels and various ambient temperatures was also experimentally verified. However, the proposed EM-based estimation algorithm may be still too complex to implement in a low-cost target BMS although some model reduction efforts have been done. For realizing low computation efforts while maintaining high estimation accuracy, novel data-driven methods based on incremental capacity analysis (ICA) and differential voltage analysis (DVA) are developed in the following chapter.

References

[3.1] L. Zhang, X. Hu, Z. Wang, F. Sun and D.G. Dorrell, "Experimental impedance investigation of an ultracapacitor at different conditions for electric vehicle applications," *J.Power Sources*, vol. 287, pp. 129-138 2015.

[3.2] X. Hu, L. Johannesson, N. Murgovski and B. Egardt, "Longevity-conscious dimensioning and power management of the hybrid energy storage system in a fuel cell hybrid electric bus," *Appl.Energy*, vol. 137, pp. 913-924 2015.

[3.3] L. Zheng, J. Zhu, G. Wang, T. He and Y. Wei, "Novel methods for estimating lithium-ion battery state of energy and maximum available energy," *Appl.Energy*, vol. 178, pp. 1-8 2016.

[3.4] A. Zenati, P. Desprez and H. Razik, "Estimation of the SOC and the SOH of Li-ion Batteries, by combining Impedance Measurements with the Fuzzy Logic Inference," in *IECON 2010-36th Annual Conference on IEEE Industrial Electronics Society*, 2010, pp. 1773-1778.

[3.5] L. Kang, X. Zhao and J. Ma, "A new neural network model for the state-of-charge estimation in the battery degradation process," *Appl.Energy*, vol. 121, pp. 20-27 2014.

[3.6] J.K. Barillas, J. Li, C. Günther and M.A. Danzer, "A comparative study and validation of state estimation algorithms for li-ion batteries in battery management systems," *Appl.Energy*, vol. 155, pp. 455-462 2015.

[3.7] J. Li, J.K. Barillas, C. Guenther and M.A. Danzer, "A comparative study of state of charge estimation algorithms for LiFePO 4 batteries used in electric vehicles," *J.Power Sources*, vol. 230, pp. 244-250 2013.

[3.8] H. He, R. Xiong and J. Peng, "Real-time estimation of battery state-of-charge with unscented kalman filter and RTOS μCOS-II platform," *Appl.Energy*, vol. 162, pp. 1410-1418 2016.

[3.9] L. Lu, X. Han, J. Li, J. Hua and M. Ouyang, "A review on the key issues for lithium-ion battery management in electric vehicles," *J.Power Sources*, vol. 226, pp. 272-288 2013.

[3.10] F. Sun, R. Xiong and H. He, "A systematic state-of-charge estimation framework for multi-cell battery pack in electric vehicles using bias correction technique," *Appl.Energy*, vol. 162, pp. 1399-1409 2016.

[3.11] I. Kim, "The novel state of charge estimation method for lithium battery using sliding mode observer," *J.Power Sources*, vol. 163, no. 1, pp. 584-590 2006.

[3.12] G.L. Plett, "Extended kalman filtering for battery management systems of LiPB-based HEV battery packs: Part 3. state and parameter estimation," *J.Power Sources*, vol. 134, no. 2, pp. 277-292 2004.

[3.13] Y. Xing, W. He, M. Pecht and K.L. Tsui, "State of charge estimation of lithium-ion batteries using the open-circuit voltage at various ambient temperatures," *Appl.Energy*, vol. 113, pp. 106-115 2014.

[3.14] Y. He, X. Liu, C. Zhang and Z. Chen, "A new model for state-of-charge (SOC) estimation for high-power li-ion batteries," *Appl.Energy*, vol. 101, pp. 808-814 2013.

[3.15] H. Rahimi-Eichi, F. Baronti and M. Chow, "Online adaptive parameter identification and state-of-charge coestimation for lithium-polymer battery cells," *Industrial Electronics, IEEE Transactions on*, vol. 61, no. 4, pp. 2053-2061 2014.

[3.16] F. Feng, R. Lu, G. Wei and C. Zhu, "Online estimation of model parameters and state of charge of LiFePO4 batteries using a novel open-circuit voltage at various ambient temperatures," *Energies*, vol. 8, no. 4, pp. 2950-2976 2015.

[3.17] J. Gao, Y. Zhang and H. He, "A real-time joint estimator for model parameters and state of charge of lithium-ion batteries in electric vehicles," *Energies*, vol. 8, no. 8, pp. 8594-8612 2015.

[3.18] G.L. Plett, "Extended kalman filtering for battery management systems of LiPB-based HEV battery packs: Part 3. state and parameter estimation," *J.Power Sources*, vol. 134, no. 2, pp. 277-292 2004.

[3.19] I. Kim, "A technique for estimating the state of health of lithium batteries through a dual-sliding-mode observer," *IEEE Transactions on Power Electronics*, vol. 25, no. 4, pp. 1013-1022 2010.

[3.20] J. Xu, B. Ning, B. Cao, B. Wang and Z. Zou, "Adaptive sliding mode observers for battery state estimation based on parameters identified online," *Appl.Energy* 2016.

[3.21] S. Lee, J. Kim, J. Lee and B. Cho, "State-of-charge and capacity estimation of lithium-ion battery using a new open-circuit voltage versus state-of-charge," *J.Power Sources*, vol. 185, no. 2, pp. 1367-1373 2008.

[3.22] R. Xiong, F. Sun, Z. Chen and H. He, "A data-driven multi-scale extended kalman filtering based parameter and state estimation approach of lithium-ion olymer battery in electric vehicles," *Appl.Energy*, vol. 113, pp. 463-476 2014.

[3.23] Y. Zou, X. Hu, H. Ma and S.E. Li, "Combined state of charge and state of health estimation over lithium-ion battery cell cycle lifespan for electric vehicles," *J.Power Sources*, vol. 273, pp. 793-803 2015.

[3.24] N. Chaturvedi, R. Klein, J. Christensen, J. Ahmed and A. Kojic, "Algorithms for advanced battery-management systems," *Control Systems, IEEE*, vol. 30, no. 3, pp. 49-68 2010.

[3.25] J. Xu, C.C. Mi, B. Cao, J. Deng, Z. Chen and S. Li, "The state of charge estimation of lithium-ion batteries based on a proportional-integral observer," *Vehicular Technology, IEEE Transactions on*, vol. 63, no. 4, pp. 1614-1621 2014.

[3.26] K.K. Busawon and P. Kabore, "Disturbance attenuation using proportional integral observers," *Int J Control*, vol. 74, no. 6, pp. 618-627 2001.

[3.27] S. Santhanagopalan, Q. Guo, P. Ramadass and R.E. White, "Review of models for predicting the cycling performance of lithium ion batteries," *J.Power Sources*, vol. 156, no. 2, pp. 620-628 2006.

[3.28] X. Han, M. Ouyang, L. Lu and J. Li, "Simplification of physics-based electrochemical model for lithium ion battery on electric vehicle. part I: Diffusion simplification and single particle model," *J.Power Sources*, vol. 278, pp. 802-813 2015.

[3.29] X. Han, M. Ouyang, L. Lu and J. Li, "Simplification of physics-based electrochemical model for lithium ion battery on electric vehicle. part II: Pseudo-two-dimensional model simplification and state of charge estimation," *J.Power Sources*, vol. 278, pp. 814-825 2015.

[3.30] W.F. Ames, *Nonlinear partial differential equations*, Academic press New York, 1967.

[3.31] S.J. Moura, N.A. Chaturvedi and M. Krstic, "PDE estimation techniques for advanced battery management systems—Part I: SOC estimation," in *American Control Conference (ACC), 2012*, 2012, pp. 559-565.

[3.32] R. Klein, N.A. Chaturvedi, J. Christensen, J. Ahmed, R. Findeisen and A. Kojic, "State estimation of a reduced electrochemical model of a lithium-ion battery," in *American Control Conference (ACC), 2010*, 2010, pp. 6618-6623.

[3.33] M. Dubarry and B.Y. Liaw, "Identify capacity fading mechanism in a commercial LiFePO 4 cell," *J.Power Sources*, vol. 194, no. 1, pp. 541-549 2009.

[3.34] K.A. Smith, C.D. Rahn and C. Wang, "Control oriented 1D electrochemical model of lithium ion battery," *Energy Conversion and Management*, vol. 48, no. 9, pp. 2565-2578 2007.

[3.35] J.J. Moré, "The Levenberg-Marquardt algorithm: implementation and theory," in *Numerical analysis,* Anonymous : Springer, 1978, pp. 105-116.

[3.36] M.R. Khan, G. Mulder and J. Van Mierlo, "An online framework for state of charge determination of battery systems using combined system identification approach," *J.Power Sources*, vol. 246, pp. 629-641 2014.

[3.37] United States Advanced Battery Consortium, "Electric vehicle battery test procedures manual," *USABC, Jan* 1996.

[3.38] L. Zheng, L. Zhang, J. Zhu, G. Wang and J. Jiang, "Co-estimation of state-of-charge, capacity and resistance for lithium-ion batteries based on a high-fidelity electrochemical model," *Appl.Energy*, vol. 180, pp. 424-434 2016.

CHAPTER 4

ICA AND DVA BASED SOC AND CAPACITY ESTIMATION

4.1 Introduction

The increasing energy crisis and environmental deterioration issues are primary promoting forces for the development of lithium-ion battery systems used in electric vehicles (EVs) and smart-grid systems [4.1]-[4.3]. For reliable and efficient battery systems operation and integration, advanced battery management systems (BMSs) are necessary to detect cells' parameters and estimate key states, such as battery state of charge (SOC) and actual capacity. The SOC that is defined as the ratio of battery remaining capacity to its fully charged capacity acts as an indicator not only for predicting the remaining mileage of EVs but also for determining a safe management strategy to avoid battery over-charge and over-discharge [4.4]. The actual capacity of a battery is another important indicator, which manifests the battery state of health (SOH), and can be used for predicting its remaining useful life [4.5]. However, battery systems usually suffer from unpredictable loading and inevitable degradation during practical applications, which bring challenges for BMSs to accurately track battery SOC and actual capacity.

Incremental capacity analysis (ICA) and differential voltage analysis (DVA) techniques have been recently reported that they can provide a non-invasive means to characterize the electrochemical reaction processes inside the battery, which have attracted tremendous attention for investigating battery degradation mechanisms [4.6]-[4.13]. Unfortunately, there are few publications presenting the on-board implementation of the ICA/DVA method for BMSs. Weng et al. [4.14] used the ICA with support vector regression (SVR) to develop a quantitative correlation between the incremental capacity peak and cell faded capacity for SOH monitoring, which is indicated by cell capacity. An

A substantial proportion of this chapter has been published as articles [4.31] and [4.32] in *Energy*.

SVR based fitting algorithm was required in the approach to obtain a clear ICA curve. The authors also extended the proposed SOH estimation approach from single cells to battery modules in [4.15], where promising SOH estimation results with the root mean square error of 1.28% could be achieved for battery modules. Li et al. [4.16] employed Lorentzian functions to describe the profiles of IC peaks, and the parameters of the functions were determined by the height and width of each IC peak. The battery charged capacity was then governed by the integral of the Lorentzian functions with cell voltages, and the estimated error was less than 4% of the nominal capacity for different batteries and statuses. In [4.17], a Butterworth filter with high cut-off frequency and order was employed to discriminate noise and information for obtaining a smooth ICA curve. The diminution of the third IC peak area was depicted as a function of cell capacity loss, which provided an effective SOH estimator with the accuracy of 2% in the verification. Note that curve fitting algorithms or peak fitting functions in the aforementioned approaches [4.14]-[4.17] are required for obtaining clear ICA curves, which requires high computational efforts in BMSs and also introduces additional errors in the data processing. Considered as a mathematical derivation of ICA/DVA, probability density function was proposed to incorporate the faded height of the peak for evaluating battery SOH [4.18]. It seems a relatively easy ICA/DVA based means to apply in BMSs, but the battery loading current needs to be rigorously limited to allow for efficient probability density statistics.

It is worth mentioning that the above reports rarely discussed the implementation of the ICA/DVA method on battery SOC estimation. Although some efforts on the development of ICA/DVA based capacity estimation have been done, the task how to take advantage of ICA/DVA method for on-board battery SOC and capacity estimation is still an open question.

In this chapter, the development of ICA and DVA methods for battery SOC and capacity estimation is investigated. At first, conventional cell terminal voltage based ICA and DVA methods are transformed to SOC based ICA and DVA methods, which are

insensitive to the changed battery resistance and polarization during battery aging processes. Feature points (FPs) that are potential to be easily identified by BMSs are extracted from SOC based IC/DV curves and applied for developing the estimation algorithms of battery SOC and capacity. Besides, extended Kalman filter (EKF) and particle filter (PF) are employed in the algorithm for further improving the performance of SOC estimation.

4.2 SOC based IC and DV Curves

The $LiFePO_4$ battery cells are applied to investigate the ICA/DVA characteristics during battery aging processes. At each aging cycle, the cells are charged with a constant current (CC) of 0.5 C to the upper limited voltage of 3.65 V, followed by a constant voltage (CV) at 3.65 V charging until it reaches C/20 to cut off the charging. A CC of 0.5 C is applied to discharge the cells to the lower limited voltage at 2.5 V under the room temperature. Since the battery test system employed in the experiment has high measurement accuracies, the battery test data including cell terminal voltage, loading current, and charge/discharge capacity recorded in a host computer can be used for the analysis and as the referenced data.

The remarkable advantage of ICA and DVA methods is the transformation of cell voltage plateaus into clearly identifiable *dQ/dV* and *dV/dQ* peaks on IC and DV curves, respectively, which describe the cell phase transition characteristics during the intercalation and de-intercalation process of lithium-ions of active materials [4.14]. Mathematically, the IC curve is computed as the gradient of charged/discharged capacity (Q) with respect to cell voltage (V) using (4.1), and the DV curve is derived as the gradient of V with respect to Q using (4.2) [4.19].

$$dQ/dV \approx \Delta Q/\Delta V \tag{4.1}$$

$$dV/dQ \approx \Delta V/\Delta Q \tag{4.2}$$

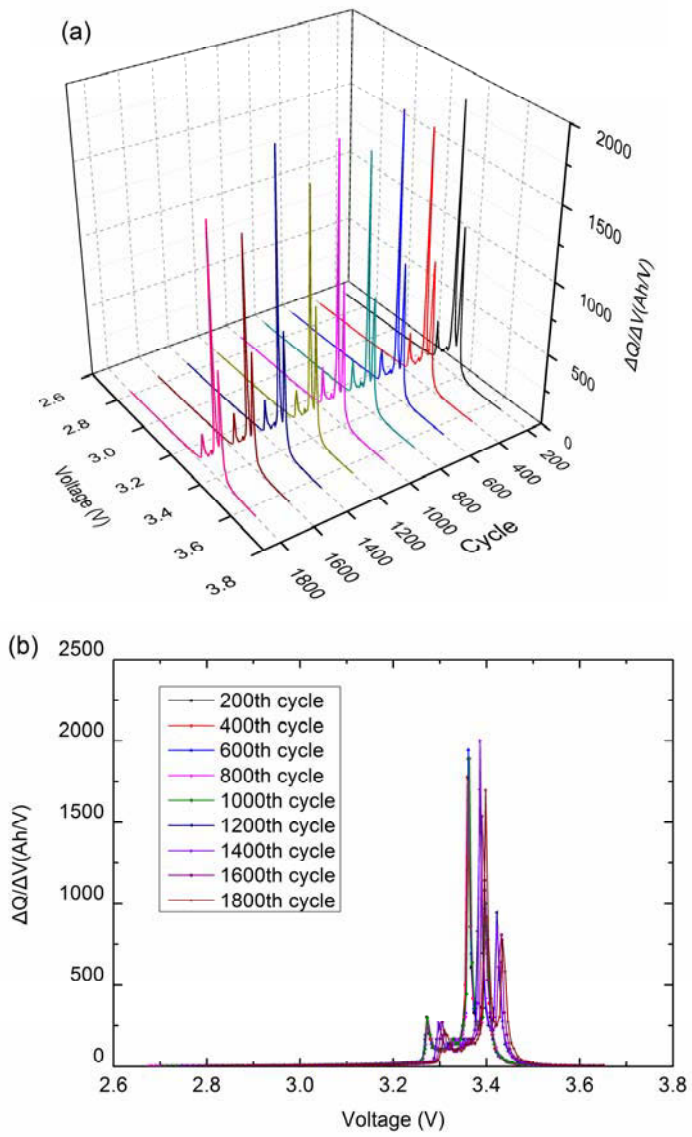

Fig. 4.1 Cell #3 IC curves at different cycles, where (a) from the perspective of 3-D and (b) from the perspective of 2-D.

The IC curves during battery CC charge process at different aging levels are shown in Fig. 4.1(a) where the voltage interval (ΔV) is 5 mV. Fig. 4.1(b) is the 2-D perspective of Fig. 4.1(a). From Fig. 4.1(b), it can be observed that the positions of IC peaks severely drift with aging cycles. This is because the effect of the increase of resistance and polarization has been enacted in the IC curves [4.6], [4.7], and therefore, it is difficult to accurately identify features of interest on IC/DV curves for further applications. Although cell resistance and polarization free methods [4.6], [4.7] were applied to cell terminal voltage to reduce the effect of resistance and polarization, it is hard to real-timely identify

the ohmic resistance and polarization voltage with high accuracy during battery aging process. To address this issue, the SOC based IC curves (i.e. *SOC–dQ/dV*), which are insensitive to cell resistance and polarization and can reflect the relationships between the IC/DV values and battery intrinsic states, are proposed and elaborated in the following parts.

The cell voltage curves at different SOCs and aging cycles are depicted in Fig. 4.2, where each cell voltage can correspond to its SOC value at each aging cycle. Based on the corresponding relationship, the voltage axis shown in Fig. 4.1(a) can be changed as the SOC axis. Thus, the cell voltage based IC curves depicted in Fig. 4.1(a) can be transformed into the SOC based IC curves, as shown in Fig. 4.3(a).

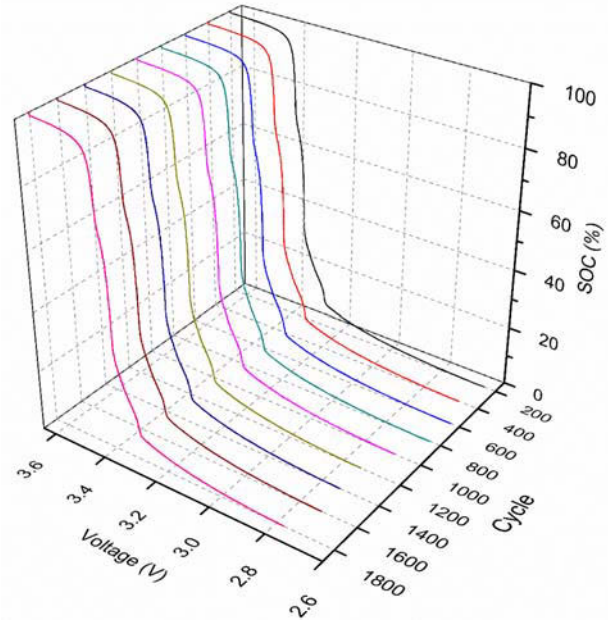

Fig. 4.2 Cell #3 voltage versus SOC curves at different cycles.

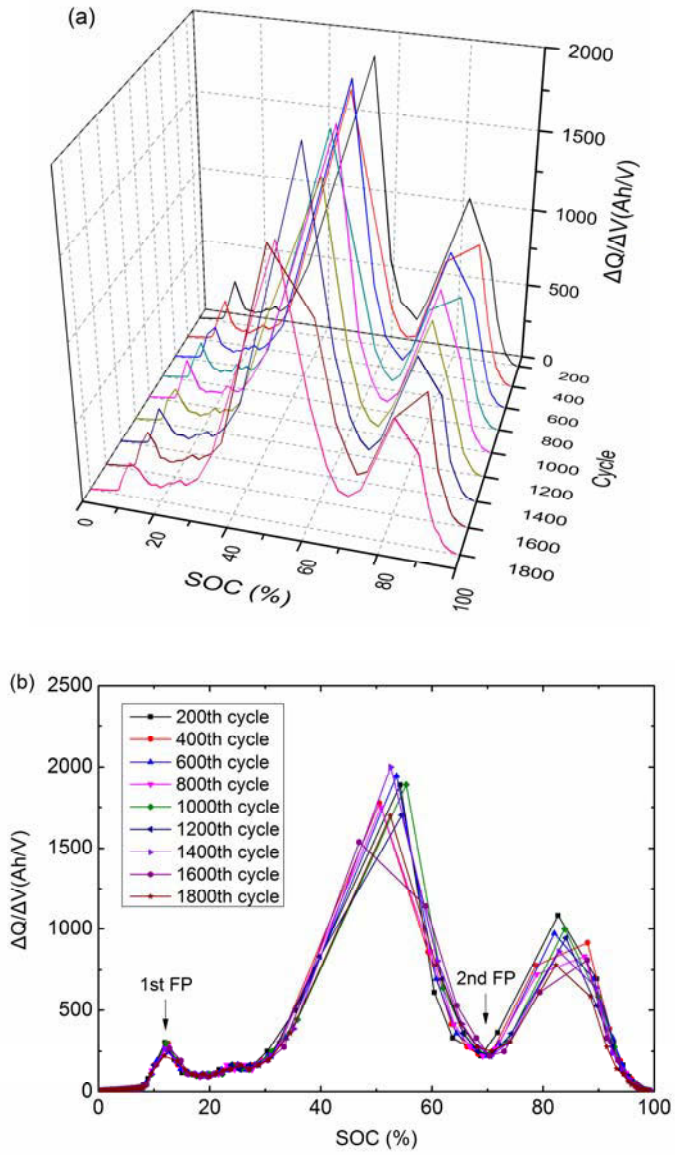

Fig. 4.3 Cell #3 SOC based IC curves at different cycles, where (a) from the perspective of 3-D and (b) from the perspective of 2-D.

Fig. 4.3(b) is the 2-D perspective of Fig. 4.3(a), where the IC curves are insensitive to the changed battery resistance and polarization during battery aging processes and can reflect the relationship between the IC value and SOC.

4.3 SOC and Capacity Estimation Methods with Feature Points

In this section, three points with distinct features that are potential to be easily identified by BMSs, also called feature points (FPs) in this study, are extracted from the SOC based IC and DV curves for SOC and capacity estimation.

4.3.1 FPs in IC and DV curves

In Fig. 4.3(b), the IC values show well overlap at the first peak (about 13% SOC) and the third valley (about 70% SOC) during battery aging process. The SOC based IC curves for two other cells are depicted in Fig. 4.4.

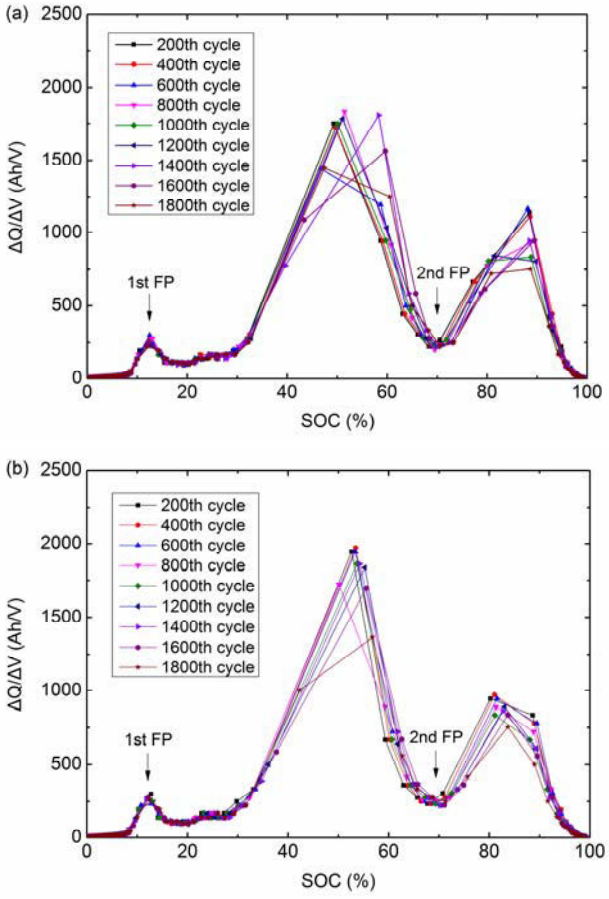

Fig. 4.4 (a) Cell #1 SOC based IC curves and (b) Cell #2 SOC based IC curves at different aging cycles.

In Fig. 4.4, the IC values also present well overlap at almost the same SOC positions (about 13% SOC and 70% SOC) with different aging cycles. Thus, these two SOC positions are considered as the FPs of IC curves. Fig. 4.5(a) shows all SOC positions of the first FP (i.e. the first peak) of the three cells. The average SOC value of the first FPs can be computed, which is equal to 12.49%. The variances between each SOC position value and the average value are shown in Fig. 4.5(b). It can be found that the SOC variances can be limited in a narrow SOC error band of ±0.8%, which suggests that the average value can be considered as the SOC position of the first FP. Thus, when BMSs capture the first FP, the SOC can be accurately corrected to 12.49%.

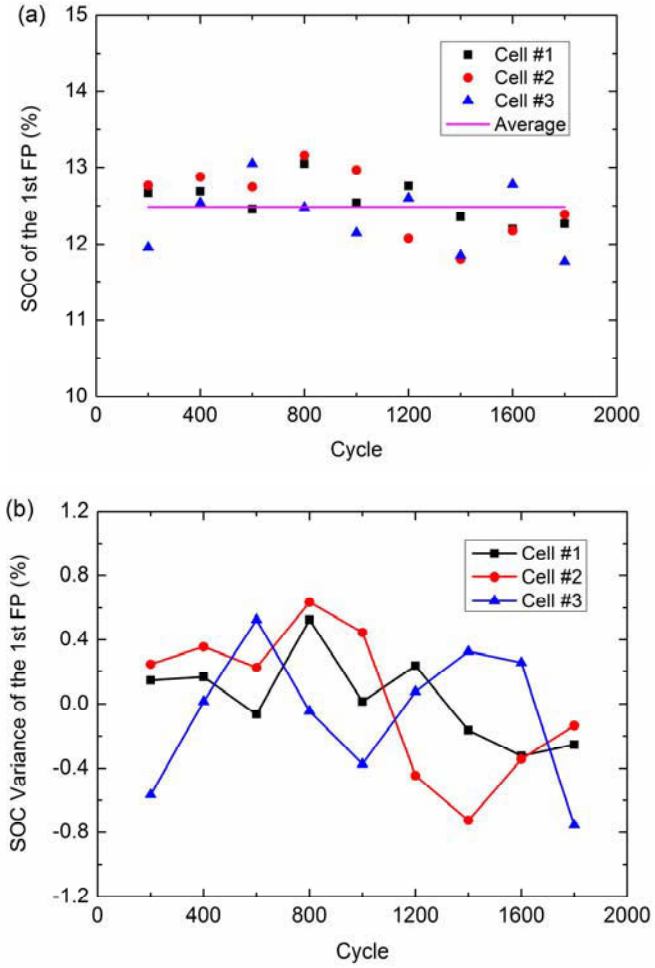

Fig. 4.5 (a) The SOC positions of the first FP for different cells and (b) SOC variances between each SOC position value and the average value.

As shown in Fig. 4.3(b) and Fig. 4.4, the IC values at the third valley (about the SOC position of 70%) exhibit well overlap and therefore are considered as the second FP. Fig. 4.6(a) depicts all SOC positions of the second FP of the three cells.

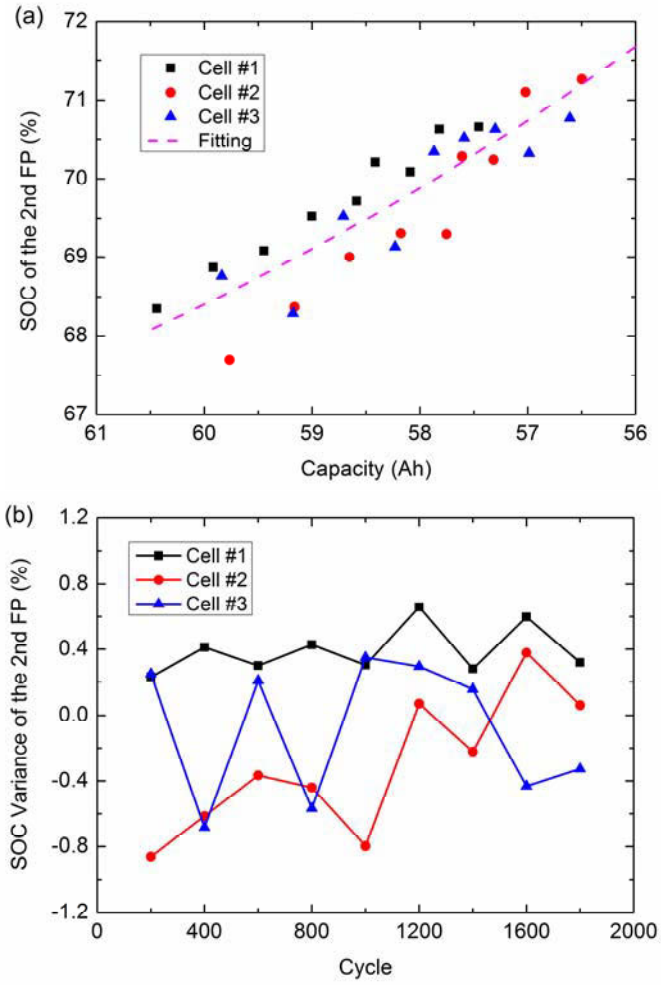

Fig. 4.6 (a) The SOC positions of the second FP for different cells and (b) SOC variances between SOC position values and its fitting values.

From Fig. 4.6(a), it can be observed that the SOC positions of the second FP present an inconspicuous moving and gradually increase with battery aging. The relationship between the aging capacities and the SOC position values can be simply fit as a quadratic function, as given by

$$SOC_{2nd\_FP} = f(Q_a) = aQ_a^2 + bQ_a + c \tag{4.3}$$

where *a*, *b* and *c* are three coefficients of the relationship function. The coefficients were calculated by using Levenberg-Marquardt algorithm [4.20], and their values are listed in Table 4.1.

Table 4.1 Optimal parameters of the relationship function between battery actual capacity and the SOC position value of the second FP.

Parameter	Coefficient
a	0.0388
b	-5.316
c	247.752

With an accurate battery actual capacity, the SOC value of the second FP can be easily computed by (4.3). Once BMSs capture the second FP, the estimated SOC can be corrected as the calculated value. However, with an incorrect battery capacity value, equation (4.3) would result in an erroneous SOC value for the second FP. Accordingly, the second FP could not be directly used for on-board SOC correction, and other stable FPs with strong robustness against erroneous capacities need to be developed.

To extract other FPs, the SOC based DV curves are employed in this work. Fig. 4.7 shows the SOC based DV curves (i.e. *SOC–dV/dQ*) at different aging cycles. The DV values can be easily obtained by calculating the reciprocals of the IC values.

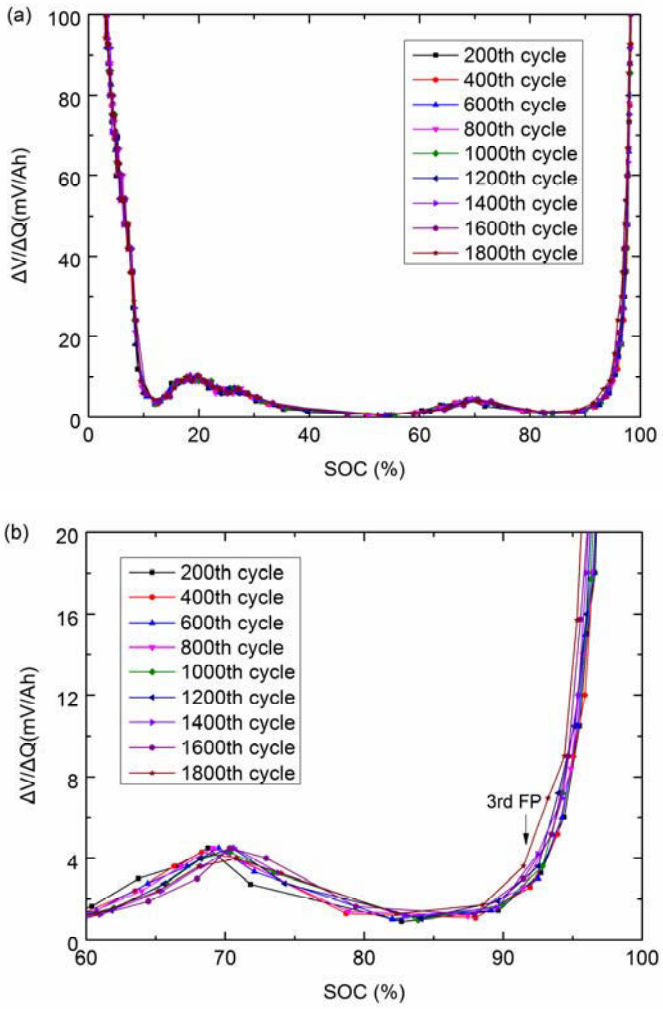

Fig. 4.7 (a) Cell #3 DV curves and (b) zoom figure of DV curves at different aging cycles.

In Fig. 4.7(b), it can be seen that DV values increase significantly from about 92.5% SOC at different aging cycles, which is of great convenience for BMS to identify this point compared to other SOC points. DV curves of the other two cells are depicted in Fig. 4.8, where it demonstrates the same characteristic of remarkable increase at the almost same SOC position. Therefore, this point can be considered as the third FP.

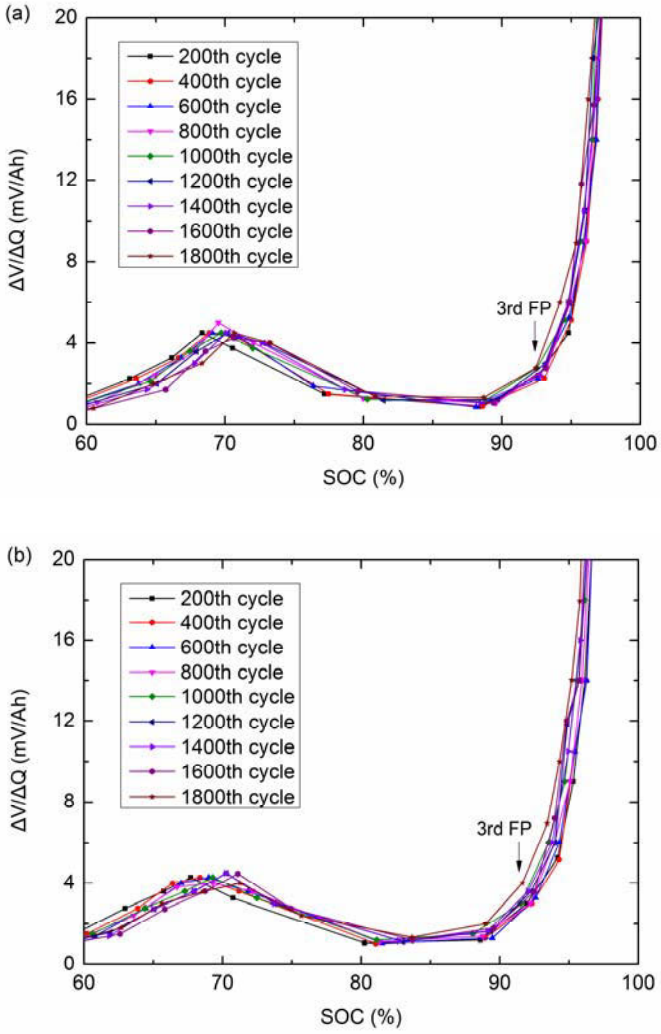

Fig. 4.8 (a) Cell #1 DV curves and (b) Cell #2 DV curves at different aging cycles.

All SOC position values of the third FP are picked up and depicted in Fig. 4.9(a), where the values distribute in the SOC range from about 91.4% to 93.3%, and their average value is calculated as 92.37%. The SOC variances of the third FP between the actual values and the average value shown in Fig. 4.9(b) are limited to a SOC error band of ±1%, which suggests that the obtained average value can be used as the SOC position of the third FP. Since the SOC positions of the third FP keep few changes during battery aging process, the third FP can be applied for on-board applications.

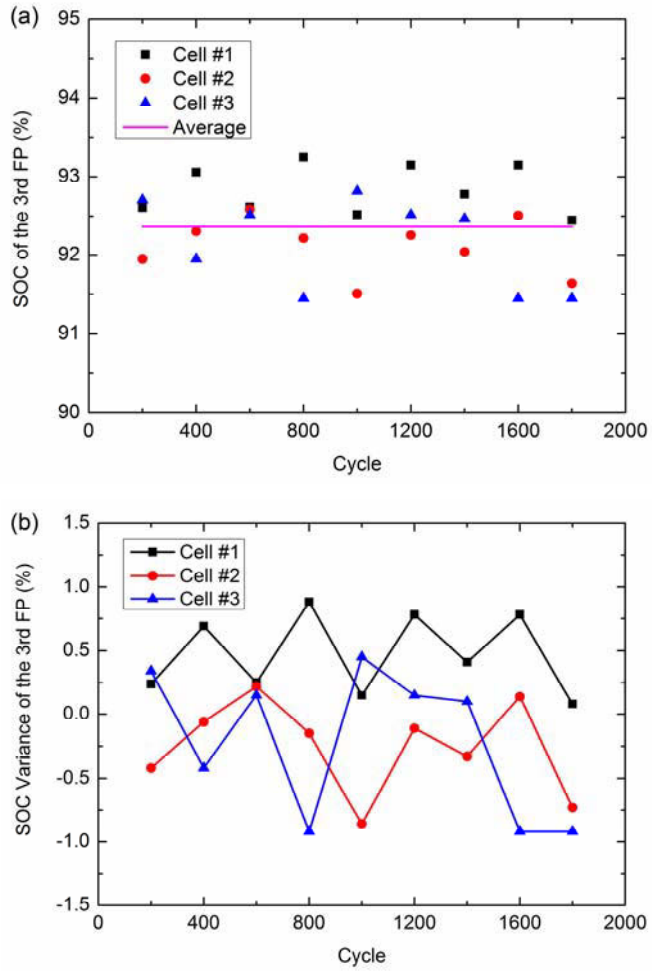

Fig. 4.9 (a) The SOC positions of the third FP for different cells and (b) SOC variances between SOC position values and the average value.

4.3.2 Proposed SOC and capacity algorithms

From the above discussions, it can be seen that the first FP and the third FP have relatively fixed SOC position values, namely 12.49% and 92.37%, respectively. Accordingly, the first FP and the third FP can be utilized for battery SOC correction and actual capacity estimation. If a BMS captures the first FP or the third FP, the estimated SOC can be corrected to the corresponding value.

Furthermore, when a BMS captures both the first FP and the third FP, the battery actual capacity can be determined by

$$Q_a = \Delta Q_{3\_1} / \left(SOC_{3rd\_FP} - SOC_{1st\_FP} \right) = \sum_{t_{1st\_FP}}^{t_{3rd\_FP}} \left(\eta_C I(t) \Delta t \right) / \left(SOC_{3rd\_FP} - SOC_{1st\_FP} \right) \quad (4.4)$$

where ΔQ_{3_1} denotes the cumulative capacity from the first FP to the third FP, Δt the sampling time interval, SOC_{3rd_FP} the SOC value of the third FP (i.e. 92.37%), and SOC_{1st_FP} the SOC value of the first FP (i.e. 12.49%).

It is noted that both the first FP SOC variances and the third FP SOC variances can be limited to SOC error bands of ±1%, and thus, without considering the error of cumulative capacity between the first FP and the third FP, the capacity estimation error would be theoretically less than 2%.

However, measurement and process errors such as over-measured/under-measured loading current and/or sampling time interval possibly existing in computing the cumulative capacity would lead to an erroneous capacity estimation. Since there is a quantitative correlation between the battery actual capacity and the second FP given by (4.3), the second FP is employed to address this issue. The cumulative capacities between the FPs can be expressed as

$$\Delta Q_{2\_1} = \sum_{t_{1st\_FP}}^{t_{2nd\_FP}} \left(\eta_C I(t) \Delta t \right) = \left(SOC_{2nd\_FP} - SOC_{1st\_FP} \right) Q_a \quad (4.5)$$

$$\Delta Q_{3\_2} = \sum_{t_{2nd\_FP}}^{t_{3rd\_FP}} \left(\eta_C I(t) \Delta t \right) = \left(SOC_{3rd\_FP} - SOC_{2nd\_FP} \right) Q_a \quad (4.6)$$

where SOC_{2nd_FP} denotes the SOC value of the second FP, ΔQ_{2_1} the cumulative capacity between the first FP and the second FP, and ΔQ_{3_2} the cumulative capacity between the second FP and the third FP.

The drift (overestimation or underestimation) coefficient of cumulative capacities is assumed to be k during battery charging process. The measurement cumulative capacities are governed by

$$\Delta Q_{2\_1}^{(m)} = \sum_{t_{1st\_FP}}^{t_{2nd\_FP}} \left(k\eta_C I(t)\Delta t \right) = k\Delta Q_{2\_1} \tag{4.7}$$

$$\Delta Q_{3\_2}^{(m)} = \sum_{t_{2nd\_FP}}^{t_{3rd\_FP}} \left(k\eta_C I(t)\Delta t \right) = k\Delta Q_{3\_2} \tag{4.8}$$

where $\Delta Q_{2\_1}^{(m)}$ denotes the measurement cumulative capacity between the first FP and the second FP, and $\Delta Q_{3\_2}^{(m)}$ denotes the measurement cumulative capacity between the second FP and the third FP.

Divide (4.7) by (4.8), and one can obtain

$$\frac{\Delta Q_{2\_1}^{(m)}}{\Delta Q_{3\_2}^{(m)}} = \frac{\Delta Q_{2\_1}}{\Delta Q_{3\_2}} \tag{4.9}$$

From (4.9), it can be observed that although there exist errors in the measurement cumulative capacities, their ratio is still equal to the ratio of the actual cumulative capacities.

In the practical applications, the given capacity of the battery may be greater or less than its actual capacity. Thus, the given capacity is first assumed to be greater than the actual capacity, namely

$$Q_a^* > Q_a \tag{4.10}$$

where Q_a^* denotes the given capacity of the battery.

Since the SOC value of the second FP would increase with the decreased capacity shown in Fig. 4.6(a), an overestimated battery actual capacity would lead to an underestimated SOC value of the second FP, as given by

$$SOC_{2nd\_FP}^{(c)} < SOC_{2nd\_FP} \tag{4.11}$$

where $SOC_{2nd\_FP}^{(c)}$ denotes the calculated SOC position value of the second FP.

Then, the differences among FPs can be compared by

$$\left(SOC_{2nd\_FP}^{(c)} - SOC_{1st\_FP}\right) < \left(SOC_{2nd\_FP} - SOC_{1st\_FP}\right) \tag{4.12}$$

$$\left(SOC_{3rd\_FP} - SOC_{2nd\_FP}^{(c)}\right) > \left(SOC_{3rd\_FP} - SOC_{2nd\_FP}\right) \tag{4.13}$$

Divide (4.12) by (4.13), and one can obtain

$$\frac{\left(SOC_{2nd\_FP}^{(c)} - SOC_{1st\_FP}\right)}{\left(SOC_{3rd\_FP} - SOC_{2nd\_FP}^{(c)}\right)} < \frac{\left(SOC_{2nd\_FP} - SOC_{1st\_FP}\right)}{\left(SOC_{3rd\_FP} - SOC_{2nd\_FP}\right)} \tag{4.14}$$

Furthermore, the given battery capacity and the actual value are added to the both sides of (4.14), respectively, as given by

$$\frac{\left(SOC_{2nd\_FP}^{(c)} - SOC_{1st\_FP}\right)Q_a^*}{\left(SOC_{3rd\_FP} - SOC_{2nd\_FP}^{(c)}\right)Q_a^*} < \frac{\left(SOC_{2nd\_FP} - SOC_{1st\_FP}\right)Q_a}{\left(SOC_{3rd\_FP} - SOC_{2nd\_FP}\right)Q_a} \tag{4.15}$$

According to (4.5) and (4.6), (4.15) can be rewritten as

$$\frac{\Delta Q_{2\_1}^{(c)}}{\Delta Q_{3\_2}^{(c)}} < \frac{\Delta Q_{2\_1}}{\Delta Q_{3\_2}} \tag{4.16}$$

where $\Delta Q_{2\_1}^{(c)}$ denotes the calculated cumulative capacity between the first FP and the second FP (i.e. $\left(SOC_{2nd\_FP}^{(c)} - SOC_{1st\_FP}\right)Q_a^*$), and $\Delta Q_{3\_2}^{(c)}$ denotes the calculated cumulative capacity between the second FP and the third FP (i.e. $\left(SOC_{3rd\_FP} - SOC_{2nd\_FP}^{(c)}\right)Q_a^*$).

Likewise, if the given capacity of the battery is less than the actual capacity, (4.17) can be obtained.

$$\frac{\Delta Q_{2\_1}^{(c)}}{\Delta Q_{3\_2}^{(c)}} > \frac{\Delta Q_{2\_1}}{\Delta Q_{3\_2}} \tag{4.17}$$

Therefore, if and only if a given capacity of the battery is equal to its actual value, the ratio of calculated cumulative capacities is equivalent to that of actual cumulative capacities, as given by

$$\frac{\Delta Q_{2\_1}^{(c)}}{\Delta Q_{3\_2}^{(c)}} = \frac{\Delta Q_{2\_1}}{\Delta Q_{3\_2}} \tag{4.18}$$

Combining (4.9) and (4.18), it can be concluded that the ratio of the measurement cumulative capacities is equivalent to that of the calculated cumulative capacities if and only if the given battery capacity is equal to the actual value, which can be expressed as

$$\frac{\Delta Q_{2\_1}^{(m)}}{\Delta Q_{3\_2}^{(m)}} = \frac{\Delta Q_{2\_1}^{(c)}}{\Delta Q_{3\_2}^{(c)}} \tag{4.19}$$

Moreover, equation (4.19) is reformulated as

$$\frac{\Delta Q_{2\_1}^{(m)}}{\Delta Q_{3\_2}^{(m)}} = \frac{\left(SOC_{2nd\_FP}^{(c)} - SOC_{1st\_FP}\right)Q_a^*}{\left(SOC_{3rd\_FP} - SOC_{2nd\_FP}^{(c)}\right)Q_a^*} = \frac{SOC_{2nd\_FP}^{(c)} - SOC_{1st\_FP}}{SOC_{3rd\_FP} - SOC_{2nd\_FP}^{(c)}} \tag{4.20}$$

By substituting (4.3) into (4.20), one can obtain

$$a\Delta Q_{3\_1}^{(m)}\left(Q_a^*\right)^2 + b\Delta Q_{3\_1}^{(m)}Q_a^* + \left(c - SOC_{1st\_FP}\right)\Delta Q_{3\_2}^{(m)} + \left(c - SOC_{3rd\_FP}\right)\Delta Q_{2\_1}^{(m)} = 0 \tag{4.21}$$

The root of (4.21) that belongs to a possible battery capacity range or an overall capacity range from battery initial capacity to zero can be considered as the optimal actual capacity, namely the estimated actual capacity.

4.3.3 Estimation results

A. Without drift cumulative capacities

Without any drift cumulative capacities, the first and third FPs are directly employed for estimating battery SOC and capacity. Two cases for evaluating the effectiveness of the proposed approaches are discussed in the following parts.

In the first case, a correct battery capacity is applied in the algorithms, but the initial SOC is set to an erroneous value. The referenced initial SOC is 0%, but the erroneous initial SOC is set to 50%. The battery cell is charged from 0% SOC to 100% SOC with the CC and CV charging regime. Once the algorithms effectively capture FPs, the SOC can be corrected as their corresponding values. Otherwise, the SOC value is calculated by Ampere-counting method. The SOC estimation results are shown in Fig. 4.10, in which the blue dot line denotes the referenced SOC, and the black dash line and the red solid line indicate the estimated SOC without any correction and with correction, respectively.

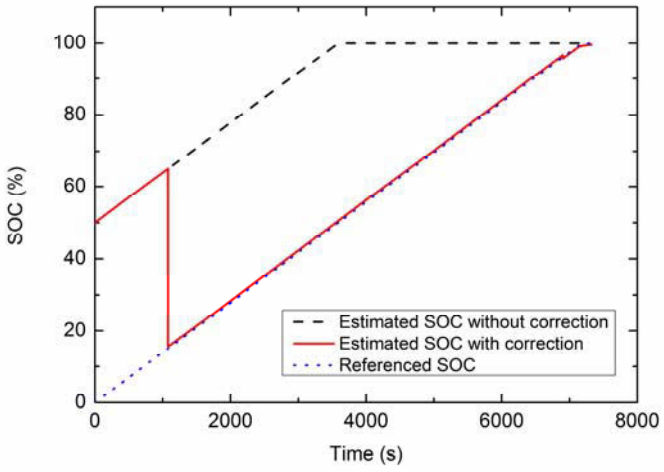

Fig. 4.10 The SOC estimation results of Case 1.

As can be observed in Fig. 4.10, before the BMS algorithm captures the first FP, the estimated SOCs increase with operating time from the initial value 50%. Since the correct battery capacity is employed during the charging process, the growth rate of estimated SOC with time is the same as that of the referenced SOC, and therefore, the estimated SOC error between the estimated value and the referenced value keeps at 50%. It is noted

that without any correction, the estimated SOC keeps going up until 100% SOC, and the estimated SOC error could not be eliminated. With the FPs correction method, the algorithm captures the first FP at about 1100 s, and the estimated SOC is corrected to 12.49%. After that, the estimated SOC can track the referenced SOC well with small errors.

In the second case, the referenced capacity is 59.84 Ah, and the referenced initial SOC is 0%. However, the initial capacity is set to 50 Ah, and the initial SOC is set to 50% in the algorithm. The SOC and capacity estimation results are shown in Fig. 4.11.

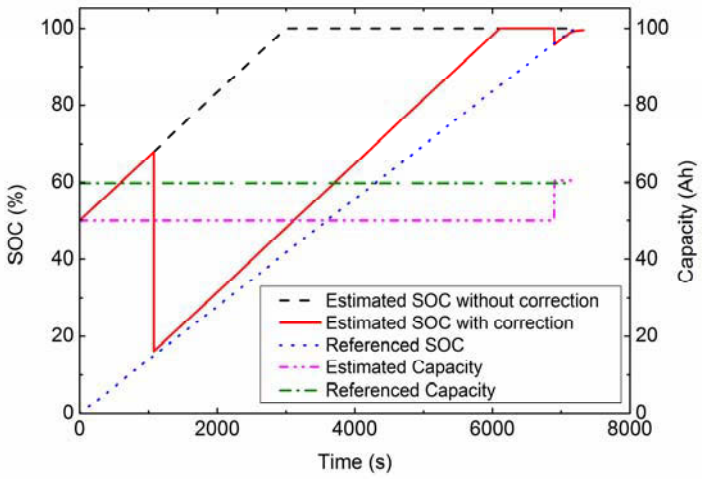

Fig. 4.11 The SOC and capacity estimated results of Case 2.

It is similar to Case 1 that the estimated SOC keeps raising to 100% SOC without any correction. However, with the FPs correction, the estimated SOC can be corrected at the first FP to the value of 12.49%. Subsequently, the growth rate of estimated SOC is faster than that of the referenced SOC. This is because that the capacity is still an incorrect value. The estimated SOC error makes a significant fall compared with the results without any correction, although the estimated SOC with the first FP correction could not tail well after the referenced value. This is because that the given capacity is still less than the referenced value, and the third FP has not been captured for correcting the battery capacity. For achieving accurate SOC estimation, the actual capacity of the battery should be corrected at first. It is noteworthy that when the algorithm captures the third FP at about

7000 s, the estimated SOC and capacity are corrected as 92.37% and 60.5 Ah, respectively, which are very close to referenced values, and the estimated SOC can accurately follow the tracks of the referenced value therefrom.

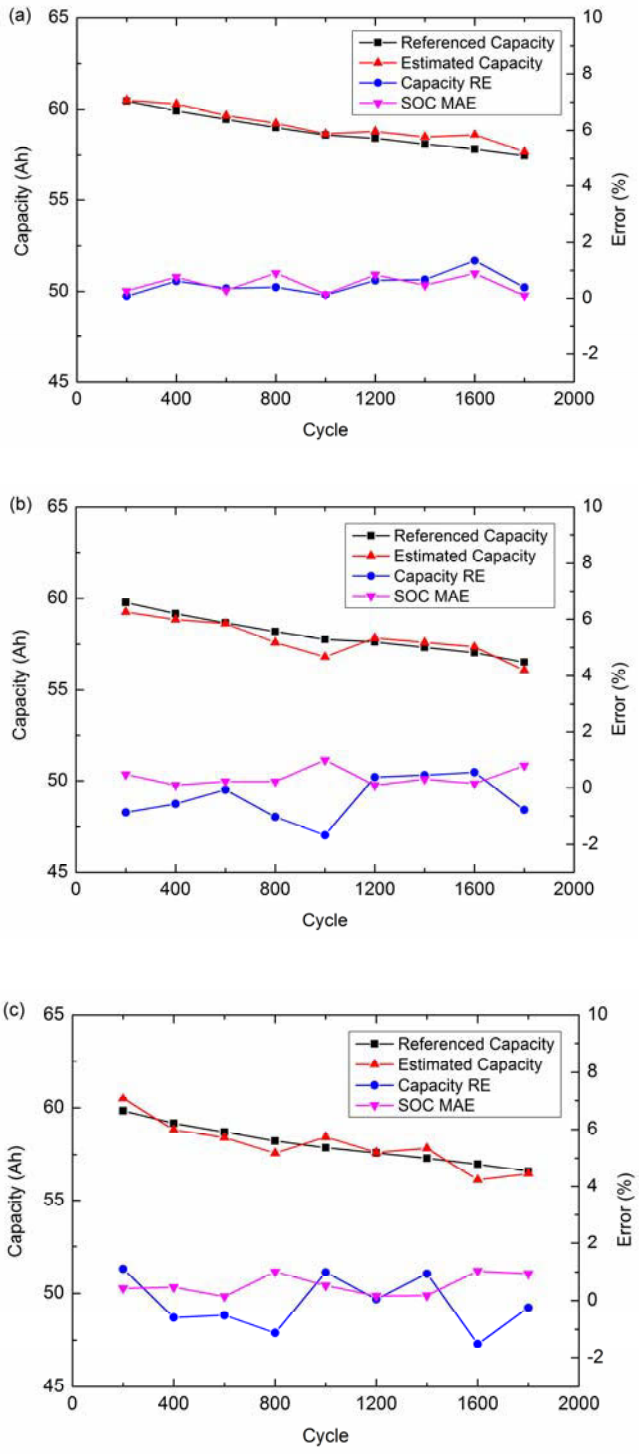

Fig. 4.12 Estimated results at different aging cycles for three cells, where (a) Cell #1, (b) Cell #2, and (c) Cell #3.

The charging data of three cells operated at different aging cycles are applied to investigate the robustness and effectiveness of the proposed algorithm. The relative errors (REs) of battery capacity estimation and the maximum absolute errors (MAEs) of the SOC estimation are depicted in Fig. 4.12. The initial battery capacity and the initial SOC are set to 50 Ah and 50%, respectively, for all the verifications. As can be observed in Fig. 4.12, the estimated capacities can catch up well with the referenced capacities during battery aging processes for these cells. The estimated capacity REs are limited to a narrow error band of ±2%. Meanwhile, most of the estimated SOC MAEs are less than 1%.

B. With drift cumulative capacities

With drift cumulative capacities, it may cause relatively large estimated errors if only employing the first and third FPs to estimate battery capacity. Therefore, the second FP is also employed for more accurate estimation. In the following validation, the drift coefficient of cumulative capacities is set to 1.1, which means that there exist relative errors of 10% in computing cumulative capacities. Conducted by the proposed algorithms, the estimated results are depicted in Fig. 4.13.

The capacity estimated results for the cells with and without the second FP are compared in Figs. 4.13(a) to (c) where the estimated capacities with the second FP can follow the tracks of the referenced values much better than that without the second FP. Their estimated relative errors are drawn in Fig. 4.13(d). It can be observed that without employing the second FP, the relative errors of capacity estimation mainly caused by the drift cumulative capacities distribute in a range from 8% to 12%. It is worth mentioning that the second FP employed in the algorithms can effectively slash the estimated errors, and the relative errors can be limited to an error band of ±2% at different aging cycles, which indicates the proposed method can perform well even with drift cumulative capacities and exhibits strong robustness against battery aging.

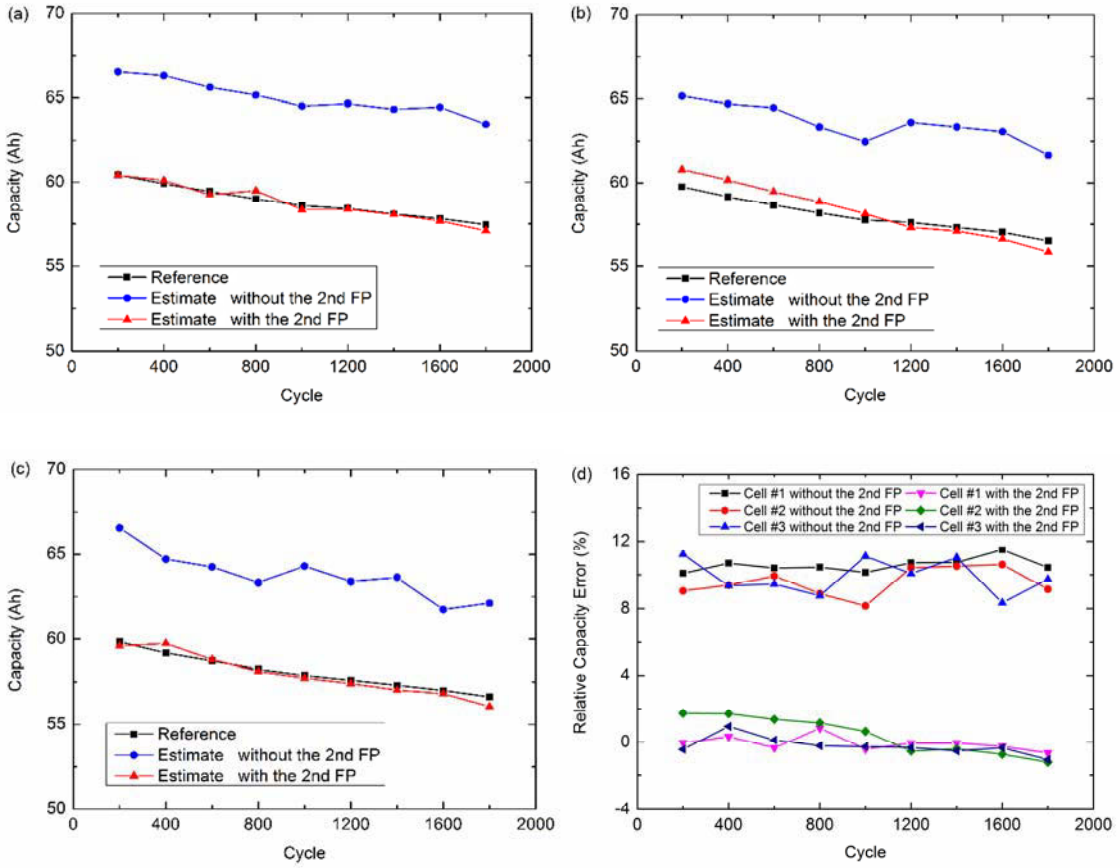

Fig. 4.13 Capacity estimated results with drift cumulative capacities, where (a) Cell #1, (b) Cell #2, (c) Cell #3 and (d) relative errors for these three cells.

As this sections puts more focus on describing the details for obtaining SOC based IC/DV curves from conventional voltage versus charge capacity curves, relatively simple estimation algorithms with FPs are proposed for monitoring battery SOC and capacity. Compared with the existing SOC and capacity estimation approaches, the major limitation of the proposed method is that the SOC and capacity values could not be corrected until a BMS successfully captures FPs. In other words, the BMS may operate with uncertain SOC and capacity values before it captures FPs. Another problem is that it seems to take a long time to capture the first FP and the third FP for the approximate estimate. For addressing these issues, improving SOC estimation approaches using the SOC based IC/DV curves with EKF and PF are developed in the following section.

4.4 Improved SOC Estimation Methods with EKF and PF

In general, the model-based methods have been demonstrated to be an effective approach for the SOC estimation due to their prominent superiorities such as closed-loop control and insensitive to noise. For incorporating the merits of the conventional model-based methods and the SOC based ICA/DVA methods, this section will develop a battery SOC-DV model based SOC estimation approaches.

4.4.1 Battery SOC-DV model

Fig. 4.14 depicts all DV versus SOC values for three tested cells at different aging cycles. As observed in Figs. 4.14(a) and 4.14(b), there is a nonlinear changed tendency that the DV values drop significantly from 0% SOC to about 12% SOC, and then form two peaks at about 20% SOC and 70% SOC with the intensities of about 10 mV/Ah and 5 mV/Ah, respectively, followed by remarkably raising from 90% SOC to 100% SOC. This universal tendency can approximately describe the relationship between DV values and SOC values for all cells with different aging cycles. The process to figure out this tendency which is also regarded as a battery SOC-DV model is described in the following parts.

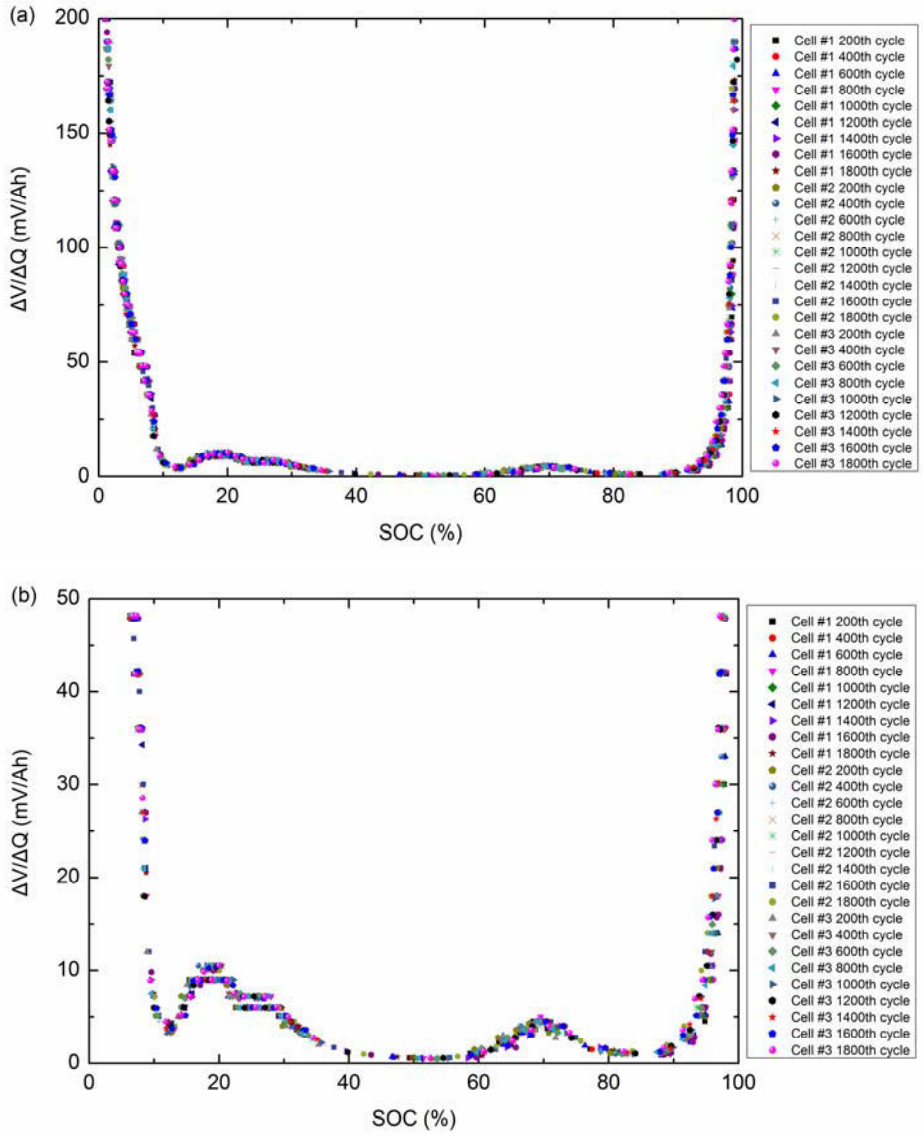

Fig. 4.14 (a) SOC-DV values for three cells at different aging cycles, and (b) zoom figure of (a).

By observing Fig. 4.14, the DV values of each aging cycle do not uniformly distribute along the SOC-axis, and there are very few points in some SOC regions. For obtaining a relatively dense and uniform distribution along the whole SOC range, a natural cubic interpolation algorithm [4.21] is employed in the presented study.

Firstly, the relationship between DV values and SOC values can be considered as a tabulated function, as given by

$$y_i = h(x_i) \tag{4.22}$$

where y_i and x_i ($i = 0, \ldots, N$) denote DV values and SOC values, respectively.

Then, suppose that in addition to the tabulated DV values, another tabulated values for the second derivatives of DV values, y_i'', can also be known. Focus attention on one particular SOC interval (x_i, x_{i+1}), and the cubic interpolation formula in this interval is expressed as (for $i = 0, \ldots, N$-1),

$$y = ay_i + by_{i+1} + cy_i'' + dy_{i+1}'' \tag{4.23}$$

where:

$$a = \frac{x_{i+1} - x}{x_{i+1} - x_i},\ b = \frac{x - x_i}{x_{i+1} - x_i},\ c = \frac{1}{6}\left(a^3 - a\right)\left(x_{i+1} - x_i\right)^2,\ d = \frac{1}{6}\left(b^3 - b\right)\left(x_{i+1} - x_i\right)^2 \tag{4.24}$$

Take derivatives of (4.23) with respect to x, and one can obtain

$$\frac{dy}{dx} = \frac{\partial(ay_i)}{\partial a}\frac{da}{dx} + \frac{\partial(by_{i+1})}{\partial b}\frac{db}{dx} + \frac{\partial\left(cy_i''\right)}{\partial c}\frac{dc}{da}\frac{da}{dx} + \frac{\partial\left(dy_{i+1}''\right)}{\partial d}\frac{dc}{db}\frac{db}{dx} \tag{4.25}$$

By substituting (4.24) into (4.25), the first derivative is given by

$$\frac{dy}{dx} = \frac{y_{i+1} - y_i}{x_{i+1} - x_i} - \frac{3a^2 - 1}{6}\left(x_{i+1} - x_i\right)y_i'' + \frac{3b^2 - 1}{6}\left(x_{i+1} - x_i\right)y_{i+1}'' \tag{4.26}$$

Likewise, take derivatives of (4.26) with respect to x, and the second derivative is governed by

$$\frac{d^2y}{dx^2} = ay_i'' + by_{i+1}'' \tag{4.27}$$

According to (4.24), at $x = x_i$ in the interval (x_i, x_{i+1}), $a = 1$ and $b = 0$, and at $x = x_i$ in the interval (x_{i-1}, x_i), $a = 0$ and $b = 1$. Besides, the key idea of a cubic spline interpolation algorithm is to require the first derivative continuity, which means that the first derivative

value obtained by (4.26) at $x = x_i$ in the interval (x_i, x_{i+1}) must be equal to the value calculated by the same equation at $x = x_i$ but in the interval (x_{i-1}, x_i). With some rearrangement, it can be depicted as (for $i = 1, \ldots, N\text{-}1$)

$$m_{i-1}y''_{i-1} + 2\left(m_{i-1} + m_i\right)y''_i + m_i y''_{i+1} = n_i - n_{i-1} \tag{4.28}$$

where:

$$m_i = \frac{x_{i+1} - x_i}{6}, \quad n_i = \frac{y_{i+1} - y_i}{x_{i+1} - x_i} \tag{4.29}$$

Equation (4.28) demonstrates the relationship among the second derivatives, and therefore, one can obtain a matrix equation for all intervals as given by

$$\begin{bmatrix} m_0 & 2(m_0+m_1) & m_1 & 0 & \text{L} & 0 & 0 & 0 & 0 \\ 0 & m_1 & 2(m_1+m_2) & m_2 & \text{L} & 0 & 0 & 0 & 0 \\ 0 & 0 & m_2 & 2(m_2+m_3) & \text{L} & 0 & 0 & 0 & 0 \\ \text{M} & \text{M} & \text{M} & \text{M} & \text{O} & \text{M} & \text{M} & \text{M} & \text{M} \\ 0 & 0 & 0 & 0 & \text{L} & 2(m_{N-4}+m_{N-3}) & m_{N-3} & 0 & 0 \\ 0 & 0 & 0 & 0 & \text{L} & m_{N-3} & 2(m_{N-3}+m_{N-2}) & m_{N-2} & 0 \\ 0 & 0 & 0 & 0 & \text{L} & 0 & m_{N-2} & 2(m_{N-2}+m_{N-1}) & m_{N-1} \end{bmatrix} \begin{bmatrix} y''_0 \\ y''_1 \\ y''_2 \\ y''_3 \\ \text{M} \\ y''_{N-3} \\ y''_{N-2} \\ y''_{N-1} \\ y''_N \end{bmatrix} = \begin{bmatrix} n_1 - n_0 \\ n_2 - n_1 \\ n_3 - n_2 \\ \text{M} \\ n_{N-3} - n_{N-4} \\ n_{N-2} - n_{N-3} \\ n_{N-1} - n_{N-2} \end{bmatrix} \tag{4.30}$$

In the matrix equation, it can be seen that there are N-1 equations but N+1 variables (i.e. y_i'', $i = 0, \ldots, N$), and thus, equation (4.30) is under determined. To obtain a unique solution for (4.30), two additional variables supposed to be known have to added to the equation. To do this, a stipulation that the second derivatives at the boundary points, x_0 and x_N, are both set to zero is adapted, namely,

$$y''_0 = y''_N = 0 \tag{4.31}$$

Accordingly, the unique solution for y_i'' ($i = 0, \ldots, N$) can be determined by (4.30) and (4.31). By substituting the second derivatives into (4.23), the natural cubic interpolation

formula in each interval can be obtained, and therefore yielding DV interpolation values for all SOC variables.

The natural cubic interpolation algorithm is then applied for varying cells with different aging cycles test data to obtain their respective new SOC-DV curves for the whole SOC range. Subsequently, the mean DV value at each SOC point can be computed according to the obtained SOC-DV curves. The relationship between the mean DV values and SOC points can approximately describe the universal tendency which is considered as a universal SOC-DV model for all cells, as shown in Fig. 4.15.

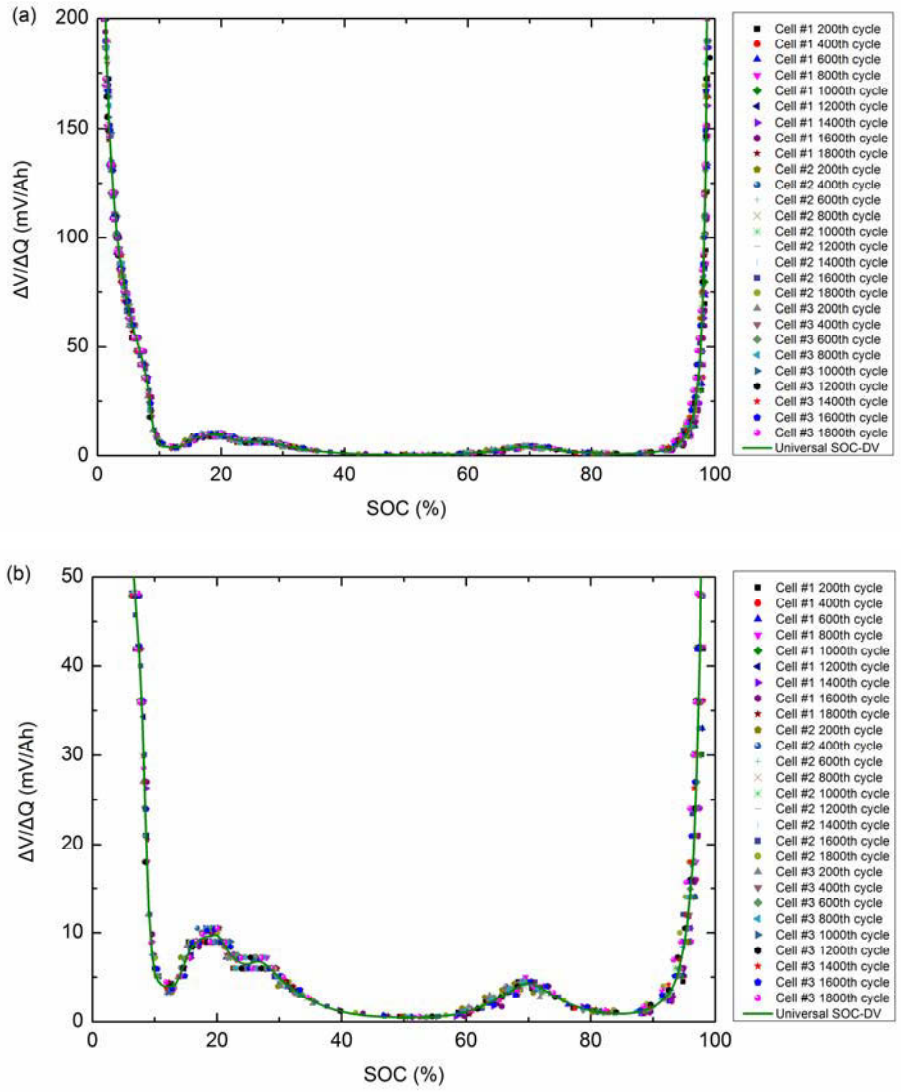

Fig. 4.15 (a) Battery cells SOC-DV values and their universal model, and (b) zoom figure of (a).

From Fig. 4.15, it can be seen that the universal SOC-DV model can accurately fit the changed tendency for all DV-SOC values well. Additionally, Fig. 4.16 demonstrates the differences between the actual values and the universal model values at the fresh level (i.e. the 200th cycle) and the aged level (i.e. the 1800th cycle) of Cell #3. It is observed that at the SOC range from 10% to 90%, most of the DV differences can be effectively limited at an error band of ±1 mV/Ah. In particular, at the SOC range from 40% to 60% and from 80% to 90%, the DV differences are relatively smaller than those at other ranges, which approximately stay at a narrow error band of ±0.5 mV/Ah. The results show that the universal model can well capture the dynamic changes of DV-SOC values, and therefore the model can be confidently applied for subsequent battery SOC estimation.

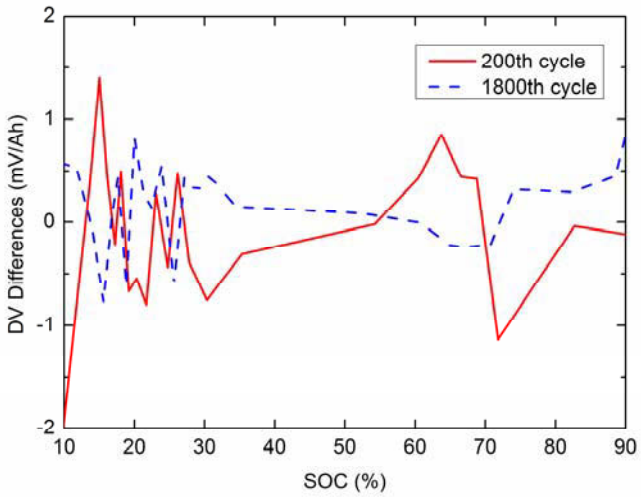

Fig. 4.16 The DV differences between the actual values and the universal model values at the 200th and 1800th cycles of Cell #3.

4.4.2 Proposed SOC algorithms

The conventional structure of the model-based SOC estimation algorithms is shown in Fig. 4.17(a) which mainly includes three parts: a battery cell, a state observer, and a battery model that is an ECM or EM. The principle of SOC estimation is to employ a battery model for generating cell voltage and then to compare it with the actual value. By feeding back the residual voltage between the model output voltage and the actual value through a state observer into the battery model, the residual voltage can be gradually

eliminated, and the estimated SOC can be corrected to follow the tracks of the actual state value.

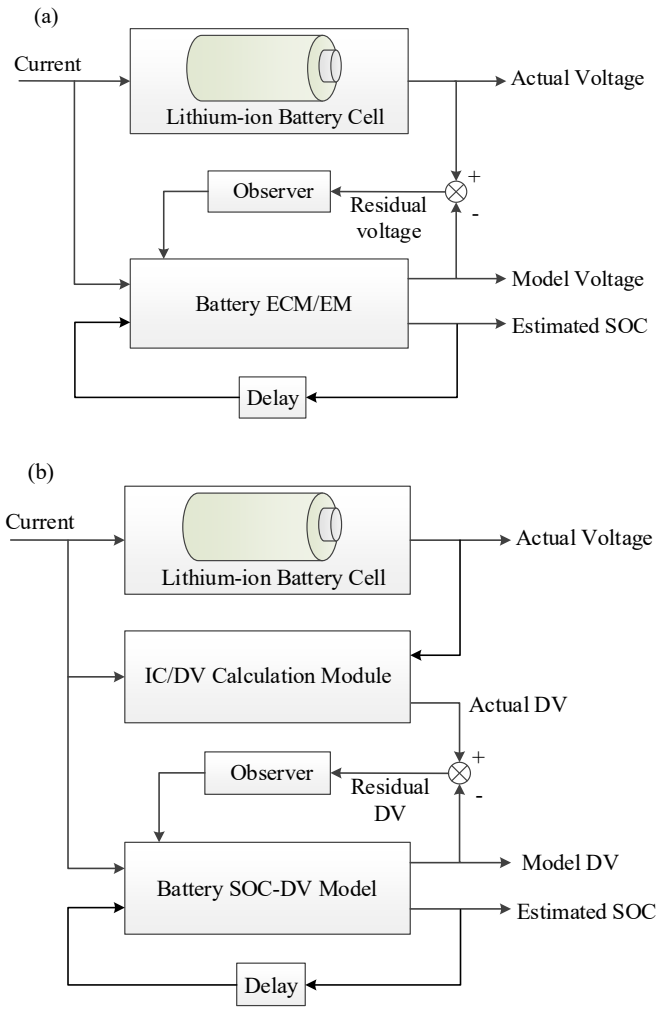

Fig. 4.17 The structures of the model-based SOC estimation methods, where (a) the conventional one and (b) the proposed one.

Drawn but different from the conventional structure, an IC/DV calculation module is added for computing the measurement DV values in the proposed scheme for the SOC-DV model based SOC estimation algorithm, as shown in Fig. 4.17(b). Instead of a battery ECM or EM, the battery SOC-DV model is applied for generating the cell DV, which is compared with the measurement DV value. Hence, the residual DV rather than the residual voltage is fed back into the model for correcting the predicted SOC through a state observer. In this study, EKF and PF are served as the state observer, respectively.

In addition, according to Ampere-hour counting method, the battery SOC is determined by

$$SOC(k)=SOC(k-1)+\eta_C I(k)\Delta t/Q_a \tag{4.32}$$

where *SOC(k)* and *SOC(k-1)* denote the SOC values at time *k* and (*k*-1), respectively; *I(k)* the loading current at time *k* (negative for discharging and positive for charging), Δt the sampling time interval, Q_a the battery actual capacity, and η_c the coulombic efficiency which is approximately equal to 1 for lithium-ion batteries.

Equation (4.32) can be considered as a state function of the SOC-DV model. The output function of the model is given by (4.22). Therefore, a discrete-time nonlinear battery system with noise input is governed by

$$x_k = f(x_{k-1}, i_k) + w_k \tag{4.33}$$

and,

$$y_k = h(x_k) + v_k \tag{4.34}$$

where x_k denotes the battery SOC, i_k the loading current, $f(\cdot,\cdot)$ a nonlinear process model for SOC update given by (4.32), and w_k and v_k the process and measurement noise which are assumed to be zero mean Gaussian noise with covariance *Q* and *R*, respectively. EKF and PF are then incorporated into the proposed SOC estimation algorithms depicted in the following parts, respectively.

A. SOC estimation with EKF

The Kalman filter (KF) is an optimal estimate for linear systems with independent white Gaussian noise in both the transition and measurement processes. However, most of practical systems are nonlinear, where KF may suffer from divergence problems. Varied extensions of KF such as EKF, sigma-point KF, unscented KF and cubature KF have been proposed to address this issue. Among these extensions of KF, EKF has demonstrated

superior performances in terms of the estimation accuracy, algorithm complexity, and computation time-consumption, and therefore it has become one of the most popular approaches for the recursive nonlinear estimation [4.22]. In the present study, EKF algorithm is applied for the SOC estimation with the SOC-DV model.

The basic steps of EKF algorithm include initialization, prediction update and measurement update. Detailed implementation processes of the EKF based SOC estimation algorithm are presented in Appendix A, which are conducted by the filtering schemes described in [4.23]-[4.25].

B. SOC estimation with PF

PF has been proposed for sequential signal processing since two decades ago [4.26]. It is an effective recursive Bayesian estimator, which uses a genetic-type mutation-selection sampling approach and aims at finding a set of particles (also called samples or individuals) as well as importance weights assigned to the particles for representing the posterior probability density [4.27]. PF always exhibits good states observation ability for nonlinear systems and has been popularly developed and adopted in various fields such as robotics, navigation, finance, wireless communications and battery systems [4.27], [4.28]. In comparison with EKF, the noise of the system model in PF applications is not restricted by the Gaussian distribution, and therefore PF may have more flexibility and applicability.

The primary steps of PF algorithm also include initialization, prediction update and measurement update, which are based on three fundamental operations involving particle propagation, importance weight computation, and resampling [4.28]. Detailed implementation processes of the PF algorithm for SOC estimation with the SOC-DV model are presented as follows, which are conducted by the filtering schemes described in [4.25], [4.27]-[4.29].

4.4.3 Estimation results

The performances of the proposed algorithms based on the SOC-DV model with EKF and PF are evaluated by the three metrics including maximum absolute error, root mean square error and computation time, respectively.

The computation time of the proposed algorithms for each estimation cycle (i.e. the prediction update and the measurement update) is evaluated by the Matlab functions *tic* and *toc* in a computer with i5-4570 CPU and 8.00 GB RAM. The *tic* function is placed at the beginning of each estimation cycle, which starts a stopwatch timer for the estimation. Meanwhile, the *toc* function is placed at the end of the estimation, which reads the stopwatch timer and displays the elapsed time of each estimation cycle.

Due to varying driving conditions, the loading current of batteries in electric vehicles normally changes dramatically. In contrast with battery discharging processes, the charging current varies slightly or even keeps constant during battery charging processes [4.30]. It is well acknowledged that ICA/DVA curves can be easily obtained with relatively stable operation current. Therefore, the proposed algorithms are performed for SOC estimation during battery charging processes.

In this section, the battery cells were firstly discharged with a constant current (CC) of 0.5 C to a lower limited voltage of 2.5 V, namely 0% SOC. Then, the verifications were carried out during the cells charging processes, in which a CC of 0.5 C loading current is used to fully charge the cells to an upper limited voltage of 3.65 V, followed by a constant voltage (CV) of 3.65 V charging until C/20 cut-off. The referenced SOC values are drawn from the recorded charging data. A grossly erroneous initial SOC was set to 50% in the algorithms while the referenced initial value was 0%. The parameters of EKF and PF algorithms used in this study are presented in Table 4.2.

Table 4.2 The parameters of EKF and PF algorithms.

$x^*_{0\|0}$ (%)	$P_{0\|0}$	Q	R	N_p	$x^*_{0,j}$ (%)
50	1000	0.1	1	101	[0:1:100]

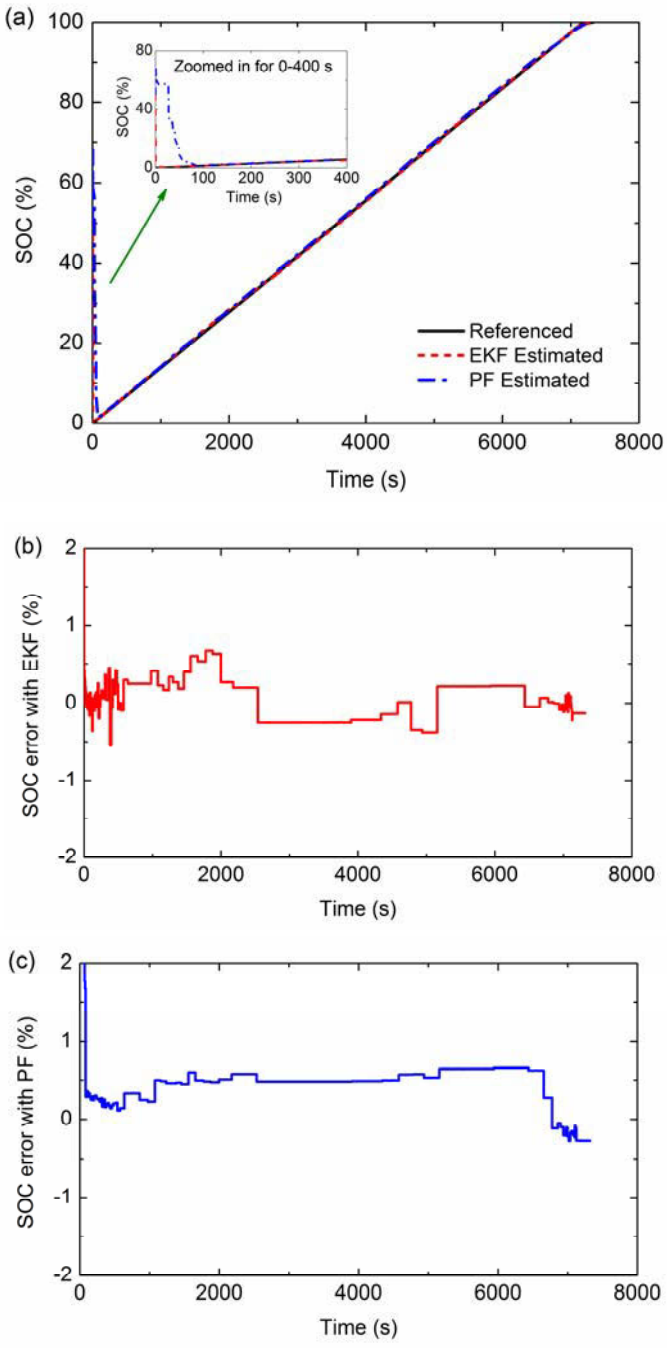

Fig. 4.18 SOC estimation results, where (a) with EKF and PF algorithms, (b) SOC errors with EKF, and (c) SOC errors with PF.

Fig. 4.18 describes SOC estimation results in the case of Cell #3 at the fresh level (i.e. the 200th cycle) with EKF and PF algorithms. It can be observed that both EKF and PF algorithms are capable of following the trails of the referenced SOC values. Notice that in the zoomed-in figure of Fig. 4.18(a), the EKF algorithm can quickly track the referenced SOCs in very few seconds. But for employing the PF algorithm, it takes about 100 s to converge to the referenced values. The SOC estimation absolute errors between the estimated values and the referenced values are depicted in Figs. 4.18(b) and 4.18(c) for the EKF and PF algorithms, respectively. By observing Fig. 4.18(b), except for the initial SOC errors in the first few seconds, the EKF algorithm can achieve accurately estimated results, and the SOC errors can be limited in a narrow error band of ±1%. In this case, the SOC MAE is 0.669% while the SOC RMSE is 0.267%. Due to its relatively slow converging characteristics, the PF algorithm yields large estimated errors in the first 100 s. Afterward, the PF algorithm can also track the referenced SOCs well, and the errors stay in the error band of ±1%, as shown in Fig. 4.18(c). Neglect the estimated errors in the first 100 s, the SOC RMSE and MAE of the PF algorithm are 0.657% and 0.493%, respectively. These results indicate that both the proposed EKF and PF algorithms for SOC estimation can perform well with small errors, even when an incorrect initial SOC is provided.

To investigate the effectiveness and robustness of the proposed approaches against varying cells with different aging levels, the proposed EKF and PF algorithms were validated with the aging cycles test data of three cells. An erroneous initial SOC, 50%, was always applied in the estimation program, and regardless of the initial SOC errors in the first 100 s, the estimated errors including MAEs and RMSEs are demonstrated in Figs. 4.19 and 4.20, respectively.

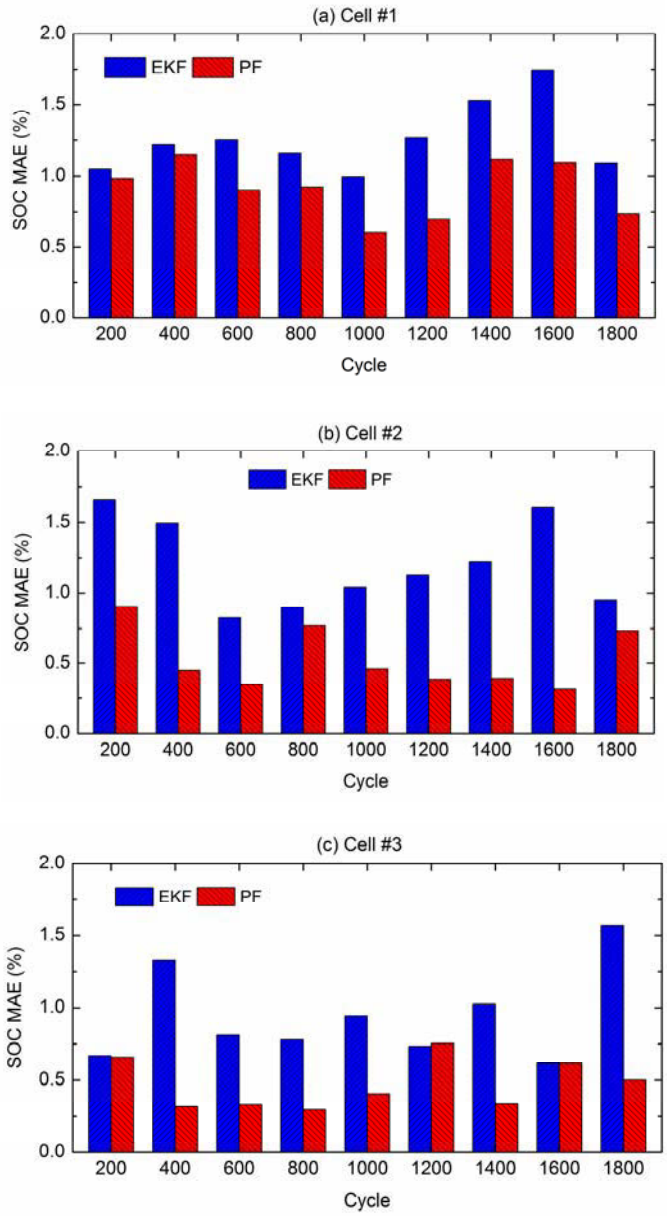

Fig. 4.19 SOC estimation MAEs at different aging levels, where (a) Cell #1, (b) Cell #2, and (c) Cell #3.

As shown in Figs. 4.19(a) to (c), with the EKF algorithm, the SOC estimation MAEs at different aging cycles for all the three cells are less than 1.75%, and the maximum SOC estimation MAE occurs at the 1600th cycle of Cell #1, which is about 1.745%. It is worth mentioning that the PF algorithm demonstrates better results especially for Cell #2 and Cell #3, in which the SOC estimation MAEs at different aging levels can be limited in an

error band of 1%. For Cell #1, the PF algorithm yields the maximum MAE at the 400th cycle, which is approximately equal to 1.146%.

The SOC estimation RMSEs presented in Figs. 4.20(a) to (c) for both EKF and PF algorithms are less than 1.10%. The maximum RMSE value with the EKF algorithm happened at the 1600th cycle of Cell #1 is about 1.017%. In particular, with the PF algorithm, most of the SOC estimation RMSEs stay with a very narrow error band of 0.6%, and the maximum RMSE is about 0.650% at the 200th cycle of Cell #2.

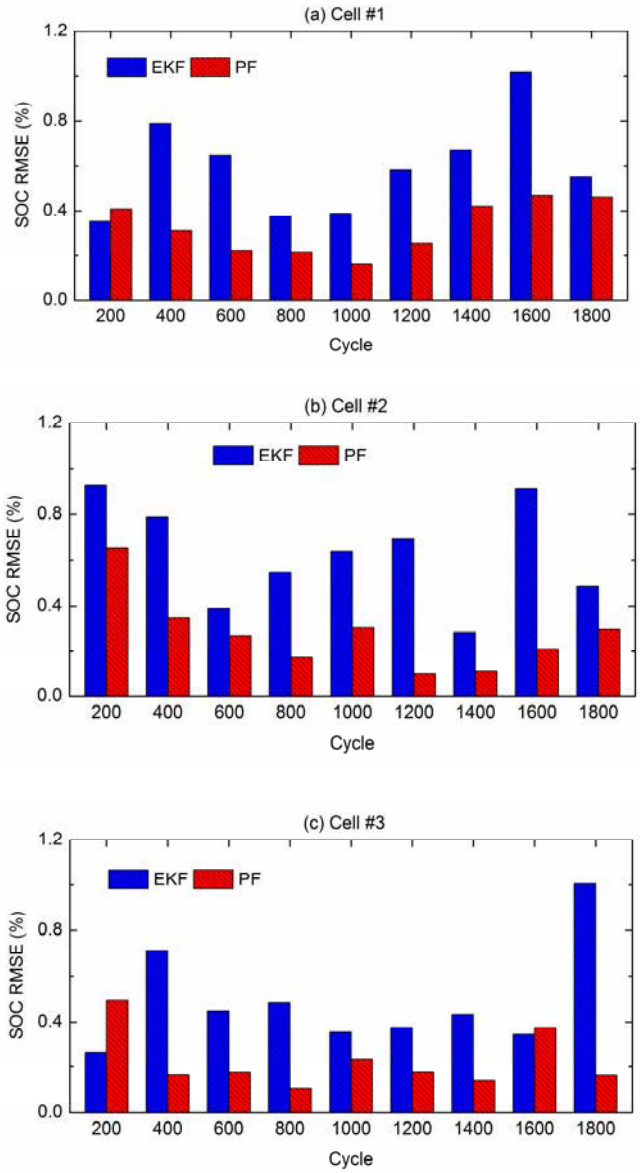

Fig. 4.20 SOC estimation RMSEs at different aging levels, where (a) Cell #1, (b) Cell #2, and (c) Cell #3.

From the above discussions, it can be concluded that both the proposed EKF and PF algorithms can handle the problem of SOC estimation for varying cells at different aging levels quite well. Although a deviant initial SOC value was always applied in the estimation program, the proposed algorithms can still achieve accurate results with small errors. The universal battery SOC-DV model used in the algorithm can work well with different cells, which is totally different from the conventional battery models such as EM and ECM that need to accurately identify their model parameters for each cell to achieve desirable results [4.30]. It is also worth mentioning that there are a handful of cases that the MAE and/or RMSE with the EKF algorithm are less than that with the PF algorithm. But overall, the PF algorithm presents a superior performance in terms of both MAE and RMSE in comparison with the EKF algorithm.

The computation time of the proposed algorithms is evaluated using the approach stated in the previous section. The mean computation time of each estimation cycle for the EKF algorithm is about 7.5 µs, while the PF algorithm (with 101 particles) is much more computationally expensive and needs about 150 µs for each estimation cycle. Actually, the computation time of the PF algorithm is strongly dependent on the number of particles. The more particles the algorithm uses, the more accurate results it may achieve, but the more computational efforts it costs. Thus, to reduce the computational cost, the EKF algorithm is favourable.

4.5 Summary

In this chapter, novel algorithms based on ICA/DVA approaches are proposed for estimating the battery SOC and capacity. Since the conventional cell terminal voltage based ICA/DVA methods are sensitive to the changed battery resistance and polarization during battery aging process, the SOC based ICA/DVA methods are proposed to address this problem. The SOC based IC/DV curves have the ability to reflect the correspondence between IC/DV value and battery SOC. Thus, three FPs extracted from the IC/DV curves are employed for simple implementation of real-time battery SOC and capacity estimation. The robustness of the proposed methods against different aging cycles is

evaluated for varying cells, and the verifications indicate that the proposed approaches are able to achieve desirable estimates with small errors, even operating with drift cumulative capacities. Besides, EKF and PF are employed for further improving the performance of the SOC estimation algorithm. A universal battery SOC-DV model is derived from SOC-DV curves of varying cells with different aging cycles, and a new scheme was proposed for incorporating the SOC-DV model. In the proposed scheme, EKF and PF are served as a state observer for the estimation algorithms, respectively. The robustness and effectiveness of the proposed approaches against different aging levels were validated for varying cells. The verifications showed that the PF algorithm presents superior performance in terms of estimated accuracy at the expense of heavy computational efforts, while the EKF algorithm can achieve desirable results with lower computational cost. In comparison with the popular model-based SOC and capacity estimation methods, it is not required to identify battery parameters for each cell in the proposed methods, and therefore, the proposed algorithms are promising to be extended from cell-level to pack-level.

References

[4.1] L. K. Uddin, T. Jackson, W.D. Widanage, G. Chouchelamane, P.A. Jennings and J. Marco, "On the possibility of extending the lifetime of lithium-ion batteries through optimal V2G facilitated by an integrated vehicle and smart-grid system," *Energy*, vol. doi: 10.1016/j.energy.2017.04.116 2017.

[4.2] Z. Wang, J. Ma and L. Zhang, "Finite element thermal model and simulation for a cylindrical li-ion battery," *IEEE Access*, vol. 5, pp. 15372-15379 2017.

[4.3] L. Zheng, J. Zhu, G. Wang, T. He and Y. Wei, "Novel methods for estimating lithium-ion battery state of energy and maximum available energy," *Appl.Energy*, vol. 178, pp. 1-8 2016.

[4.4] Y. He, X. Liu, C. Zhang and Z. Chen, "A new model for state-of-charge (SOC) estimation for high-power li-ion batteries," *Appl.Energy*, vol. 101, pp. 808-814 2013.

[4.5] C. Hu, B.D. Youn and J. Chung, "A multiscale framework with extended kalman filter for lithium-ion battery SOC and capacity estimation," *Appl.Energy*, vol. 92, pp. 694-704 2012.

[4.6] M. Dubarry and B.Y. Liaw, "Identify capacity fading mechanism in a commercial LiFePO 4 cell," *J.Power Sources*, vol. 194, no. 1, pp. 541-549 2009.

[4.7] M. Dubarry, B.Y. Liaw, M. Chen, S. Chyan, K. Han, W. Sie and S. Wu, "Identifying battery aging mechanisms in large format li ion cells," *J.Power Sources*, vol. 196, no. 7, pp. 3420-3425 2011.

[4.8] I. Bloom, A.N. Jansen, D.P. Abraham, J. Knuth, S.A. Jones, V.S. Battaglia and G.L. Henriksen, "Differential voltage analyses of high-power, lithium-ion cells: 1. technique and application," *J.Power Sources*, vol. 139, no. 1, pp. 295-303 2005.

[4.9] M. Safari and C. Delacourt, "Aging of a commercial graphite/LiFePO4 cell," *J.Electrochem.Soc.*, vol. 158, no. 10, pp. A1123-A1135 2011.

[4.10] X. Han, M. Ouyang, L. Lu, J. Li, Y. Zheng and Z. Li, "A comparative study of commercial lithium ion battery cycle life in electrical vehicle: Aging mechanism identification," *J.Power Sources*, vol. 251, pp. 38-54 2014.

[4.11] M. Berecibar, I. Gandiaga, I. Villarreal, N. Omar, J. Van Mierlo and P. Van den Bossche, "Critical review of state of health estimation methods of li-ion batteries for real applications," *Renewable and Sustainable Energy Reviews*, vol. 56, pp. 572-587 2016.

[4.12] Z. Ma, J. Jiang, W. Shi, W. Zhang and C.C. Mi, "Investigation of path dependence in commercial lithium-ion cells for pure electric bus applications: Aging mechanism identification," *J.Power Sources*, vol. 274, pp. 29-40 2015.

[4.13] C. Pastor-Fernández, K. Uddin, G.H. Chouchelamane, W.D. Widanage and J. Marco, "A comparison between electrochemical impedance spectroscopy and incremental capacity-differential voltage as li-ion diagnostic techniques to identify and quantify the effects of degradation modes within battery management systems," *J.Power Sources*, vol. 360, pp. 301-318 2017.

[4.14] C. Weng, Y. Cui, J. Sun and H. Peng, "On-board state of health monitoring of lithium-ion batteries using incremental capacity analysis with support vector regression," *J.Power Sources*, vol. 235, pp. 36-44 2013.

[4.15] C. Weng, X. Feng, J. Sun and H. Peng, "State-of-health monitoring of lithium-ion battery modules and packs via incremental capacity peak tracking," *Appl.Energy*, vol. 180, pp. 360-368 2016.

[4.16] X. Li, J. Jiang, L.Y. Wang, D. Chen, Y. Zhang and C. Zhang, "A capacity model based on charging process for state of health estimation of lithium ion batteries," *Appl.Energy*, vol. 177, pp. 537-543 2016.

[4.17] E. Riviere, P. Venet, A. Sari, F. Meniere and Y. Bultel, "LiFePO4 Battery State of Health Online Estimation Using Electric Vehicle Embedded Incremental Capacity Analysis," in *Vehicle Power and Propulsion Conference (VPPC), 2015 IEEE*, 2015, pp. 1-6.

[4.18] X. Feng, J. Li, M. Ouyang, L. Lu, J. Li and X. He, "Using probability density function to evaluate the state of health of lithium-ion batteries," *J.Power Sources*, vol. 232, pp. 209-218 2013.

[4.19] C. Pastor-Fernandez, W.D. Widanage, G. Chouchelamane and J. Marco, "A SoH diagnosis and prognosis method to identify and quantify degradation modes in li-ion batteries using the IC/DV technique," 2016.

[4.20] J.J. Moré, "The Levenberg-Marquardt algorithm: implementation and theory," in *Numerical analysis,* Anonymous: Springer, 1978, pp. 105-116.

[4.21] W.H. Press, S.A. Teukolsky, W.T. Vetterling and B.P. Flannery, *Numerical recipes in C*, Cambridge university press Cambridge, 1996.

[4.22] N.J. Gordon, D.J. Salmond and A.F. Smith, "Novel approach to nonlinear/non-Gaussian Bayesian state estimation," in *IEE Proceedings F-Radar and Signal Processing*, 1993, pp. 107-113.

[4.23] G.L. Plett, "Extended kalman filtering for battery management systems of LiPB-based HEV battery packs: Part 3. state and parameter estimation," *J.Power Sources*, vol. 134, no. 2, pp. 277-292 2004.

[4.24] R. Xiong, F. Sun, Z. Chen and H. He, "A data-driven multi-scale extended kalman filtering based parameter and state estimation approach of lithium-ion olymer battery in electric vehicles," *Appl.Energy*, vol. 113, pp. 463-476 2014.

[4.25] G. Dong, Z. Chen, J. Wei, C. Zhang and P. Wang, "An online model-based method for state of energy estimation of lithium-ion batteries using dual filters," *J.Power Sources*, vol. 301, pp. 277-286 2016.

[4.26] A. Doucet, N. De Freitas and N. Gordon, "An introduction to sequential Monte Carlo methods," in *Sequential Monte Carlo methods in practice,* Anonymous : Springer, 2001, pp. 3-14.

[4.27] Y. Wang, C. Zhang and Z. Chen, "A method for state-of-charge estimation of LiFePO 4 batteries at dynamic currents and temperatures using particle filter," *J.Power Sources*, vol. 279, pp. 306-311 2015.

[4.28] T. Li, M. Bolic and P.M. Djuric, "Resampling methods for particle filtering: Classification, implementation, and strategies," *IEEE Signal Process.Mag.*, vol. 32, no. 3, pp. 70-86 2015.

[4.29] C. Burgos-Mellado, M.E. Orchard, M. Kazerani, R. Cárdenas and D. Sáez, "Particle-filtering-based estimation of maximum available power state in lithium-ion batteries," *Appl.Energy*, vol. 161, pp. 349-363 2016.

[4.30] L. Zheng, L. Zhang, J. Zhu, G. Wang and J. Jiang, "Co-estimation of state-of-charge, capacity and resistance for lithium-ion batteries based on a high-fidelity electrochemical model," *Appl.Energy*, vol. 180, pp. 424-434 2016.

[4.31] L. Zheng, J. Zhu, G. Wang, D. D. Lu, and T. He, “Incremental capacity analysis and differential voltage analysis based state of charge and capacity estimation for lithium-ion batteries”, *Energy*, vol. 150, pp. 759-769, 2018.

[4.32] L. Zheng, J. Zhu, G. Wang, D. D. Lu, and T. He, “Differential voltage analysis based state of charge estimation methods for lithium-ion batteries using extended Kalman filter and particle filter”, *Energy*, vo. 158, pp. 1028-1037, 2018.

CHAPTER 5

SOC CORRELATION BASED SOE AND MAXIMUM AVALIABLE ENERGY ESTIMATION

5.1 Introduction

Lithium-ion batteries have many desirable merits such as high energy density, light weight and long cycle life, and are widely developed as energy storage devices in smart grids and electric vehicles [5.1], [5.2], etc. To meet the application power and energy demands, a battery system usually contains hundreds, even thousands of cells connected in series and parallel. To ensure safe and reliable operation, an effective battery management system (BMS) is required to monitor and control these cells. Much of the BMS functionalities, such as the state of charge (SOC) estimation, state of health estimation, cell monitoring and balancing techniques [5.3]-[5.8], have been sophisticatedly developed for applications. Nevertheless, due to the nonlinear battery characteristics and unpredictable operating conditions, accurate and reliable battery state of energy (SOE) and maximum available energy estimations still pose significant challenges.

Traditionally, the SOC is regarded as an indicator of battery available energy. A wide variety of approaches for SOC estimation has been reported in recent literature [5.2], [5.9]-[5.19], and remarkable results have been achieved on novel SOC estimation methods and improving the estimated accuracy. For example, the proportional-integral (PI) observer [5.11], [5.12], Luenberger observer [5.13], Sliding-mode observer [5.14], [5.15] and Kalman-filter-based algorithms [5.2], [5.16]-[5.19] were employed in model-based SOC estimation methods to obtain estimated results of high accuracy. Defined as the ratio of the remaining charge stored in a battery to its full capacity, however, SOC actually indicates the state of available capacity rather than the state of available energy.

A substantial proportion of this chapter has been published as an article [5.32] in *Applied Energy*.

K. Mamadou etc. [5.20], [5.21] introduced a new criterion, the state of energy (SOE), for battery energetic performances evaluation. SOE allows a direct determination of the ratio of battery remaining energy to its maximum available energy, which is critical for energy optimization and management in energy storage systems.

Compared with the SOC estimation approaches, there are few studies report the systematic research for SOE estimation. Neural Network based SOE estimation methods were presented in [5.22], [5.23], where the target batteries were treated as a "black-box" system, and it needs a great number of sample data to train the network parameters. The main disadvantage of these methods is that the estimation errors are strongly dependent on the training data. In [5.24], [5.25], an adaptive unscented Kalman filter algorithm and the relationship between the SOE and open circuit voltage (OCV) were employed in the model-based SOE estimation approaches. In [5.26], the particle filter and a battery model are utilized to develop a method for joint estimation of the SOE and the SOC, and the robustness of the method has been verified under dynamic temperature conditions. H. He etc. [5.27] employed a Gaussian model oriented battery model and proposed a data-driven estimator with a central difference Kalman filter algorithm for SOE estimation, and the approach was evaluated by two kinds of batteries including $LiFePO_4$ and $LiMn_2O_4$ cells. Although these SOE estimation approaches are able to achieve acceptable accuracy, the complex algorithms produce a heavy computational burden on the microprocessor with limited computation capability within BMSs.

Besides, a common drawback of these SOE estimation methods is that they fail to achieve desirable predictions against various operating conditions during battery aging processes. The trajectory of the neural network parameters or battery model parameters cannot be fully described within a limited number of experiments [5.27]. Various battery operating conditions and cell aging levels with pre-set parameters may lead to inaccurate SOE estimated results. It is also noted that the above-mentioned battery available energy studies focus just on the SOE estimation. Unfortunately, there are very few studies involving the estimation of battery maximum available energy (i.e. battery actual energy).

Since the battery maximum available energy is strongly related to the battery operating conditions [5.22], it is necessary to systematically study the effects of ambient temperature, current rate, and aging level in order to estimate the SOE and maximum available energy more accurately, and further improve the robustness of estimation approaches against uncertain operating conditions.

To implement this work, a battery test bench was developed, and the characteristics of $LiMn_2O_4$ battery cells with a nominal capacity of 90 Ah were tested under different aging levels, current rates, and ambient temperatures. The tests cover a broad aging level range from 92 Ah to 69.5 Ah, a wide temperature range from 10 °C to 40 °C and a commonly used current rate range from 1/3 C to 1 C. Based on the test data, the relationships between SOE and SOC under various operating conditions are systematically analyzed and quantified for SOE estimation. A moving-window energy-integral technique is incorporated to estimate the battery maximum available energy. The robustness and feasibility of the proposed approaches are validated in different operating condition tests during battery aging processes.

5.2 Temperature, current and aging level dependencies of battery maximum available energy

The $LiMn_2O_4$ cells with a nominal capacity of 90 Ah were used to investigate the battery energy characteristics at various experimental conditions of different ambient temperatures, current rates, and cell aging levels. Temperature, current and aging level dependencies of battery maximum available energy. To investigate the battery maximum available energy with different currents at various ambient temperatures, the battery cells were loaded with the discharge current rates of C/3, 2C/3, C/2 and 1C at temperatures of 10 °C, 25 °C and 40 °C, respectively. At each temperature, the battery cells were firstly charged with a pre-set constant current to the upper limit voltage 4.2 V followed by a constant voltage charge at 4.2 V until C/20 cut-off. Then, there was a rest time for 1 h followed by the pre-set constant current discharge to the lower limit voltage 3 V. After

that, the battery was given a rest for 1 h and the procedure was carried out repeatedly. During the battery discharge processes, the maximum available energy results with different currents at various temperatures are shown in Fig. 5.1.

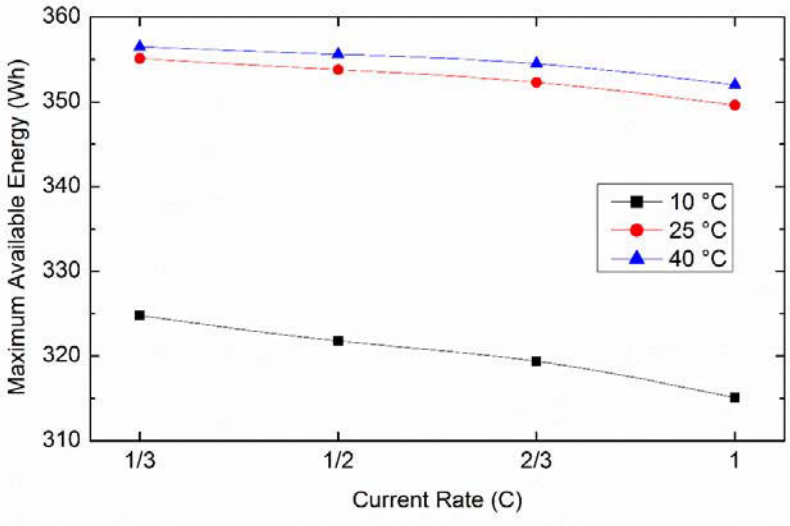

Fig. 5.1 The maximum available energy with different currents at various temperatures.

From Fig. 5.1, it can be found that the battery maximum available energy presents a change with different currents at various temperatures. At the same ambient temperature, the available energy appears a decreasing trend with the increasing discharge current rate. For example, when the discharge current rate was increased from 1/3C to 1C, the available energy dropped from 324.8 Wh to 315.1 Wh at 10 °C. At various temperatures, when the discharge current rate is kept at 1/3C, the maximum available energies are 324.8 Wh, 355.1 Wh, and 356.5 Wh at 10 °C, 25 °C and 40 °C, respectively, presenting an increasing trend with the rising temperature.

To investigate the battery maximum available energy with different currents at various battery cell aging levels, accelerated aging tests with the charge/discharge current of 1C at 60 °C were applied to the battery cell to obtain different cell aging levels including 92 Ah, 87 Ah, 82.5 Ah, 78 Ah, 74.5 Ah and 69.5 Ah, and at each cell aging level, the battery cell was loaded with the discharge currents of C/3, C/2, 2C/3 and 1C at the room temperature (25 °C), respectively. The battery maximum available energy values are plotted in Fig. 5.2.

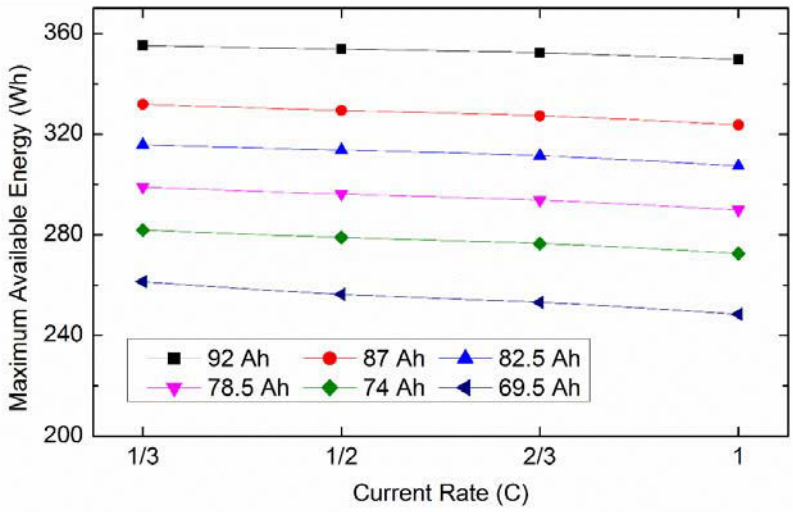

Fig. 5.2 The maximum available energy with different currents at various aging levels.

In Fig. 5.2, when the discharge current rate is 1/3C, the battery maximum available energy values are 355.1 Wh, 331.9 Wh, 315.8 Wh, 299.0 Wh, 281.9 Wh and 261.4 Wh at the battery capacity 92 Ah, 87 Ah, 82.5 Ah, 78.5 Ah, 74 Ah and 69.5 Ah, respectively. The maximum available energy shows similar declining trends with different discharge current rates such as 1/2C, 2/3C, and 1C at different aging levels, indicating that the battery maximum available energy appears a significant decrease during battery aging processes.

It can be summarized that the battery maximum available energy varies with the operating conditions and is greatly related to the ambient temperature and cell aging level. Accordingly, it is necessary to develop reliable approaches for accurate battery maximum available energy and SOE estimations with strong robustness against the varying operating conditions during the battery aging processes.

5.3 Temperature, current and aging level dependencies of the relationship between SOE and SOC

Being similar to the SOC range, the SOE reaches its maximum value 100% when the battery is fully charged which means it has the maximum available energy, and it reaches its minimum value 0% when the battery is fully discharged which means there is not any

remaining energy can be discharged. Since the battery charger/discharger is able to measure cell voltage and loading current with high precision, the referenced data are represented by the measurement data detected by the charger/discharger which are recorded in the host computer. The recorded data include the battery cell terminal voltage, loading current, charge/discharge capacity and energy, and therefore the SOC and SOE can be easily calculated by (5.1) and (5.2), respectively,

$$SOC(k)=SOC(k-1)+\eta_C I(k)\Delta t/C_a \tag{5.1}$$

$$SOE(k)=SOE(k-1)+U(k)I(k)\Delta t/E_a \tag{5.2}$$

where $SOC(k)$ denotes the SOC value at time k, $SOC(k\text{-}1)$ the SOC value at time (k-1), $SOE(k)$ the SOE value at time k, $SOE(k\text{-}1)$ the SOE value at time (k-1), Δt the sampling time interval, $I(k)$ the loading current at time k (positive for charging and negative for discharging), $U(k)$ the battery cell terminal voltage at time k, C_a the battery maximum available capacity (i.e. the battery actual capacity), E_a the battery maximum available energy (i.e. the battery actual energy), and η_C the coulombic efficiency which is considered to be approximately equal to 1 [5.26].

The maximum available energies of different SOCs and SOEs at battery's fresh phase (i.e. 92 Ah) are listed in Table 5.1. From Table 5.1, it can be seen that there is a positive correlation between the SOE and SOC, but their relationship has not yet been clearly explored [5.24]. Thus, the relationship between SOE and SOC should be further studied. To investigate the aging level dependence of the relationship between SOE and SOC, the battery cell was loaded with a discharging current rate of C/3 at battery capacity degraded from 92 Ah to 69.5 Ah, respectively, and the relationships are shown in Fig. 5.3.

Table 5.1 The maximum available energies of different SOCs and SOEs at battery's fresh phase.

SOC (%)	Energy (Wh)	SOE (%)
100	355.1	100.0
90	319.9	90.6
80	284.2	81.0
70	249.4	71.5
60	212.9	61.4
50	176.9	51.4
40	141.4	41.4
30	106.8	31.6
20	71.3	21.5
10	36.0	11.1
0	0	0

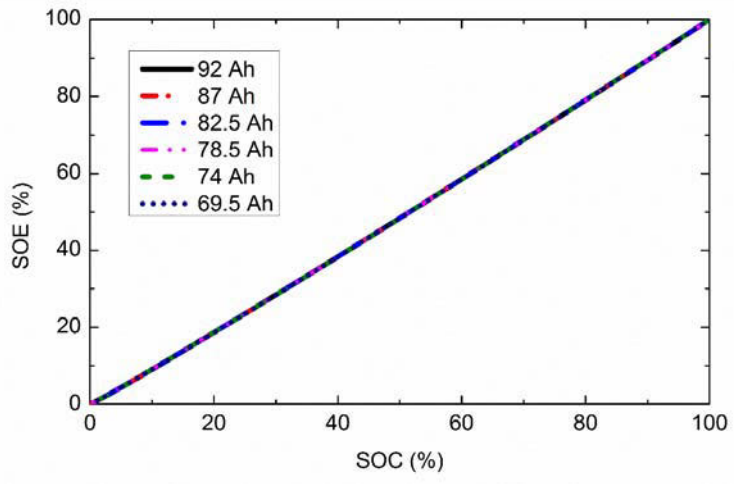

Fig. 5.3 The relationships between SOE and SOC at different aging levels.

In Fig. 5.3, the relationships between SOE and SOC at different aging levels appear a superior overlapping characteristic. It demonstrates that the relationship between SOE and SOC remains steady during battery aging processes and has strong robustness against the battery capacity fade.

To investigate the temperature dependency of the relationship between SOE and SOC, different battery cells of the same batch were loaded with the discharge current C/3 at 10 °C, 25 °C and 40 °C, respectively. The relationships between SOE and SOC at different temperatures are plotted in Fig. 5.4 where the SOC is regarded as the X-axis and the SOE as the Y-axis.

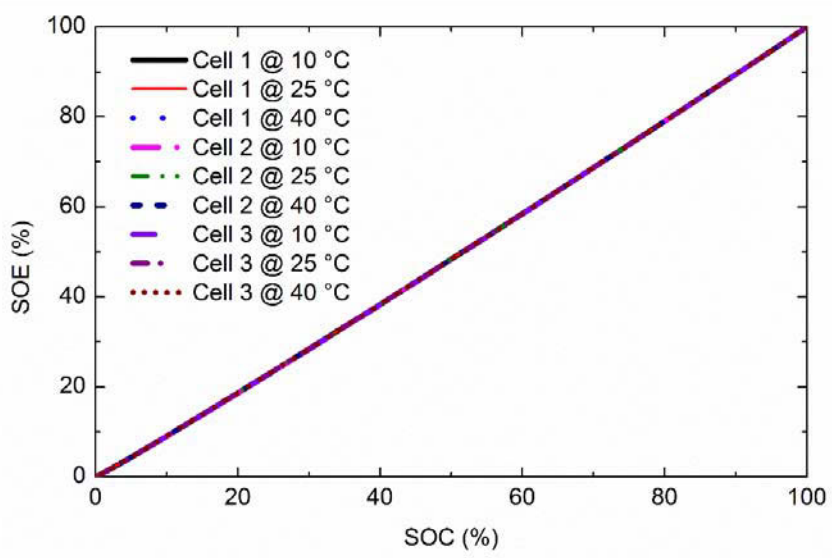

Fig. 5.4 The relationships between SOE and SOC at different temperatures.

Fig. 5.4 shows a perfect coincidence among the relationships between SOE and SOC at different temperatures. It indicates that the relationship between SOE and SOC has strong robustness against the changing ambient temperature. Besides, it is noted that for three different cells of the same batch, the relationships between SOE and SOC also coincide well with each other. Thus, the relationship between SOE and SOC can be readily extended for each cell of whole battery pack operated at different ambient temperatures.

In order to investigate the current dependence of the relationship between SOE and SOC, the battery cells were loaded with the discharge and charge current rates of C/3, C/2, 2C/3 and 1C, respectively. The results are shown in Fig. 5.5.

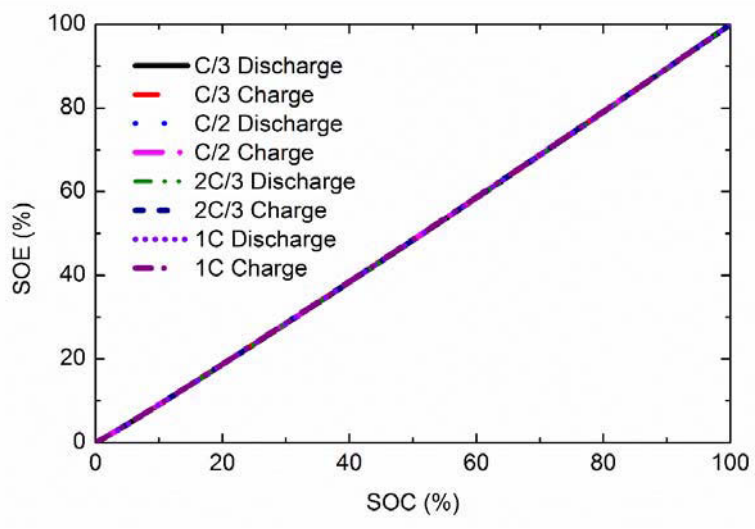

Fig. 5.5 The relationships between SOE and SOC with various current rates.

From Fig. 5.5, it can be seen that the relationships between SOE and SOC with various discharge or charge current rates almost coincide with each other. It manifests that the charging and discharging current rates have little effect on the relationship between SOE and SOC. Thus, the relationship can be applied not only in battery constant current charging/discharging processes but also in dynamic changed current working conditions.

From above experimental results, it can be summarized that under different operating conditions and cell aging levels, the relationship between battery SOE and SOC always keeps unchanged. Although the maximum available energy and maximum available capacity of a battery cell are significantly dependent on its operated ambient temperature, loading current rate and aging level, it is noted that these factors have negligible effects on the relationship between SOE and SOC. This is because the SOE and SOC values were calculated by (5.1) and (5.2) with the maximum available energy and maximum available capacity, respectively, which have already included these influence factors.

5.4 Proposed Estimation Algorithms

It has been reported that the model-based SOC estimation methods are able to achieve high estimated accuracy [5.9-5.19]. Thus, the estimated SOC and the stable relationship between SOE and SOC can be utilized to estimate SOE. According to the results shown in Figs. 5.3-5.5, the relationship between SOE and SOC can be expressed as an explicitly quantitative expression which is assumed to be a quadratic function, as given by

$$SOE(k) = aSOC(k)^2 + bSOC(k) + c \tag{5.3}$$

where a, b and c are three coefficients of the quadratic function.

The coefficients of the quadratic equation are fit by using Levenberg-Marquardt algorithm [5.28, 5.29] for the relationship between SOE and SOC under different temperatures, current rates, and cell aging levels. The optimal parameters are listed in Table 5.2. The coefficient of determination *R-Square* is 0.999989, which means the fitting function can precisely match the real relationship between SOE and SOC.

Table 5.2 Optimal parameters of the relationship function between SOE and SOC.

Parameter	Coefficient
a	0.000600
b	0.944954
c	-0.426930

Based on the quantitative relationship between SOE and SOC with estimation SOC, the overall structure of the proposed algorithms for both battery SOE and maximum available energy estimation is shown in Fig. 5.6.

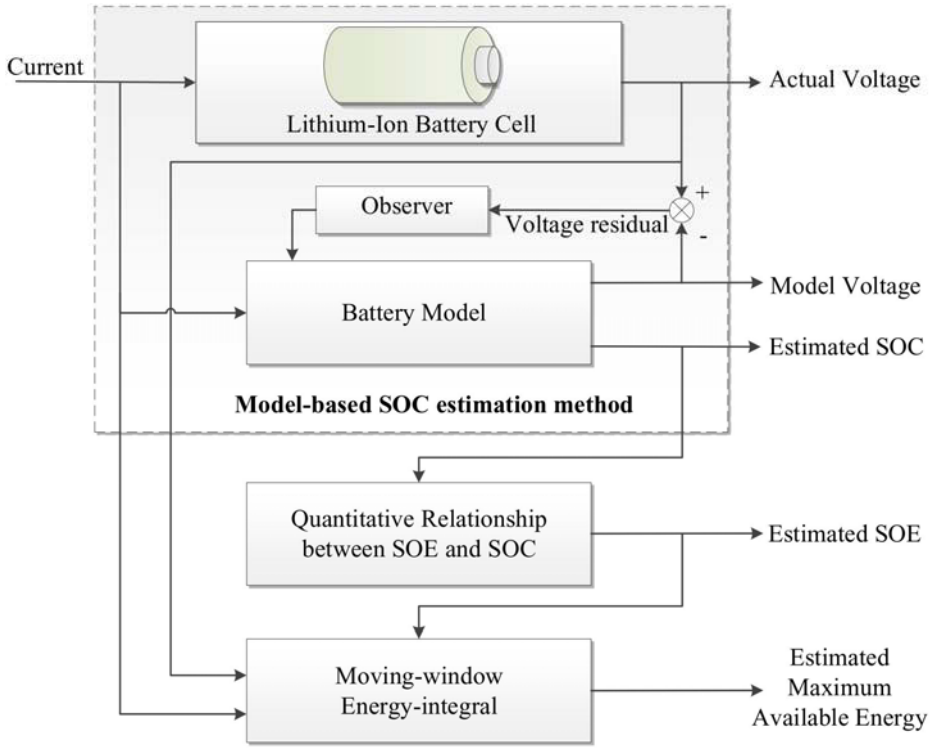

Fig. 5.6 The structure of the proposed algorithms.

The SOC is firstly estimated by a model-based estimation method. Since the model-based SOC estimation method is not the emphasis of this paper, we briefly explain the working principle of the method, and refer readers to [5.11-5.19, 5.30] where give a more comprehensive description on the model-based SOC estimation methods. Briefly, a battery model such as equivalent circuit models and electrochemical models is employed to calculate the model output voltage with the given initial SOC value and loading current. Then the voltage residual between the model output voltage and the cell terminal voltage (i.e. cell actual voltage) is fed to an observer or filter such as PI observer, Luenberger observer, Sliding-mode observer and Kalman-filter-based filters, for producing a compensation value. After that, the compensation value is used to modify state variables of the battery model and therefore the estimated SOC is able to track with the actual SOC.

Subsequently, the estimated SOC and the quantitative relationship are employed to estimate SOE. Furthermore, a moving-window energy-integral technique with the SOE

estimation is incorporated to estimate the battery maximum available energy and its detailed estimation process is described as follows.

Equation (5.2) expresses the relationship between SOE and battery maximum available energy, and therefore the battery maximum available energy can be derived reversely, as given by

$$E_a = \sum_{i=0}^{k} \left(U(i) I(i) \Delta t \right) / \left(SOE(k) - SOE(0) \right) \tag{5.4}$$

where $\sum_{i=0}^{k} \left(U(i) I(i) \Delta t \right)$ is the energy integral from the beginning time to the time *k* and *SOE(0)* is the SOE value at the beginning time.

As mentioned in Section 5.2, the battery maximum available energy is greatly related to the ambient temperature, cell aging level and loading current rate. However, it is noted that these three variables are not included in (5.4). This is because that in (5.4), the battery maximum available energy is calculated with the estimated SOE, which is calculated by (5.3). Equation (5.3) describes the quantitative relationship between SOC and SOE, which was obtained by fitting the experimental SOC and SOE data under various ambient temperatures, cell aging levels and loading current rates. From Figs. 5.3-5.5, it can be observed that these variables have negligible effects on the relationship between SOE and SOC. Thus, the variables are not included in (5.3) and also not included in (5.4). Since the SOC value is considered as the input for calculating the SOE given by (5.3) at different operating conditions, the SOC should be the value under the corresponding operating conditions, which has considered the variables of ambient temperature, cell aging level and loading current rate, and therefore the estimated SOE and maximum available energy values are also related to these variables.

As presented in (5.4), the battery maximum available energy can be calculated by using two certain SOE points such as the beginning charge/discharge point and the final charge/discharge point. However, the SOE estimation errors in these two points may lead

to incorrect battery maximum available energy estimation results. From experience, one way to decrease the uncertainty in experimental data is to make multiple measurements and take the average. Accordingly, a moving-window energy-integral technique with multiple calculations is incorporated for the estimation. The battery maximum available energy is calculated in each 200 seconds' moving-window. Then the average of the maximum available energy values of each moving-window is considered as the final estimated result, as given by

$$E_{a\_avg} = \sum_{i=1}^{n} E_{ai} \Big/ n \tag{5.5}$$

where E_{ai} is the maximum available energy in each moving-window and n the number of moving-windows.

5.5 Verification and Discussion

5.5.1 SOE estimation

As presented in the previous SOC estimation work [5.12], the SOC estimation error can be limited to a +/-2% error band and the estimated SOC can track with the referenced SOC quickly even with an erroneous initial SOC value. Combining the estimated SOC and the relationship between SOE and SOC, the SOE estimation result of a battery cell with 92 Ah and 1/3C discharging current rate is shown in Fig. 5.7 where the referenced SOE values are calculated by (5.2) with the experimental test data.

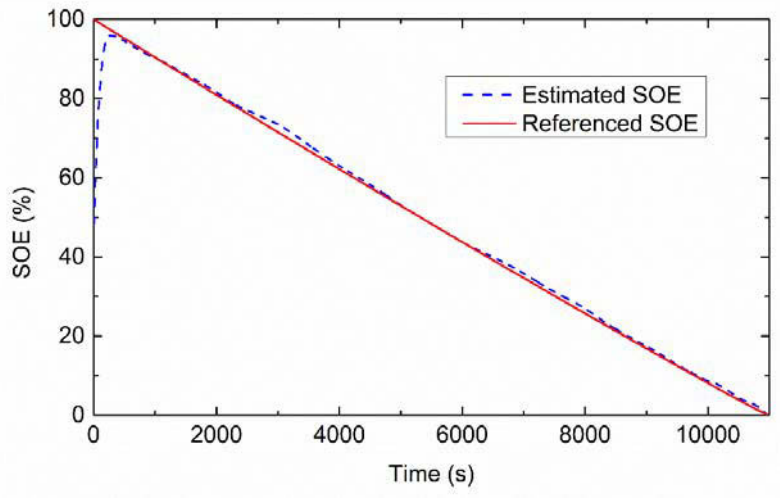

Fig. 5.7 SOE estimation result.

In Fig. 5.7, the referenced initial SOE value is 100% while there is an erroneous initial SOC value of the battery model that caused an incorrect initial SOE value 48%. It can be seen that in the first 400 s, the estimated SOE increases quickly to catch up with the referenced SOE, and therefrom the estimated SOE is able to follow the tracks of the referenced value well. It indicates that the proposed SOE estimation method can work well even when a grossly erroneous initial SOE value is supplied to the program. The detailed SOE estimation errors at different battery aging levels and operation conditions will be depicted as follows.

To investigate the effectiveness of the proposed method during the process of battery aging, the battery cell degraded from 92 Ah to 69.5 Ah was used for the verification. The SOE estimation errors including the maximum absolute error (MAE) and the root mean square error (RMSE) are shown in Fig. 5.8 at six different aging levels with 92 Ah, 87 Ah, 82.5 Ah, 78.5 Ah, 74 Ah and 69.5 Ah, respectively.

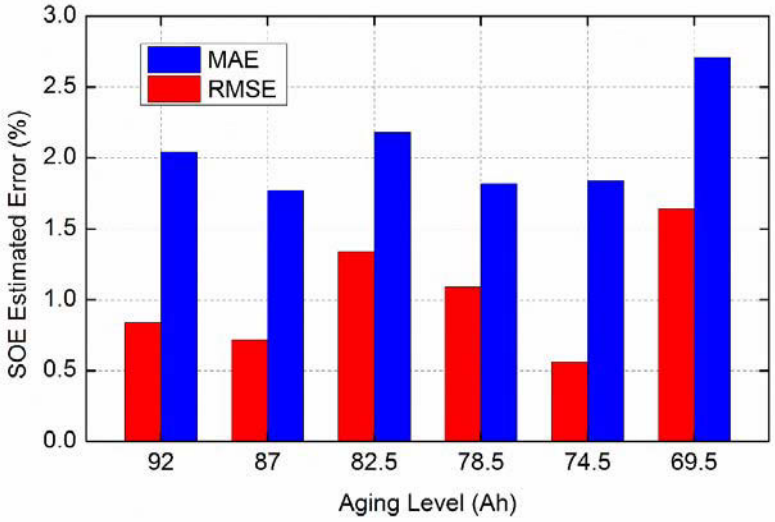

Fig. 5.8 SOE estimation errors at different battery aging levels.

In Fig. 5.8, the SOE estimation MAEs at different battery aging levels are less than 3.0% while the SOE estimation RMSEs are less than 2.0%, indicating that the proposed method can handle different battery aging levels quite well.

The characteristic test data at 10 °C, 25 °C and 40 °C were used to validate the effectiveness of the proposed method under different ambient temperatures. The SOE estimation errors are shown in Fig. 5.9.

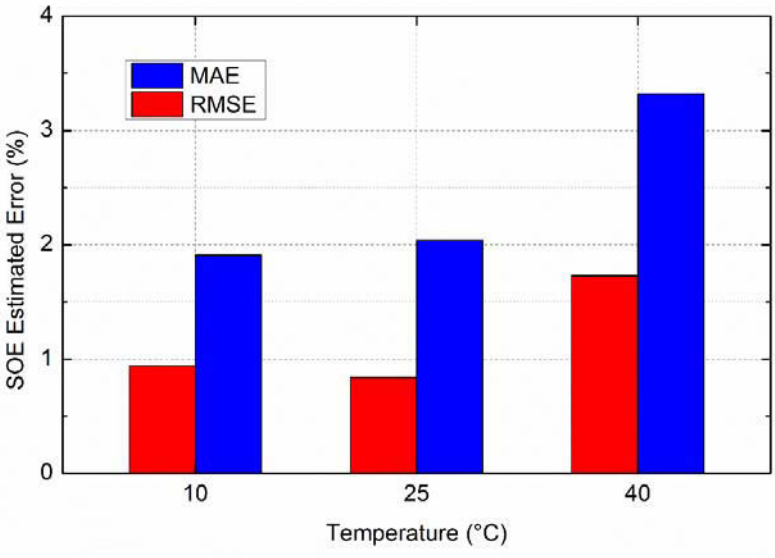

Fig. 5.9 SOE estimation errors under various ambient temperatures.

From Fig. 5.9, it can be seen that the maximum SOE estimation MAE occurred at 40 °C, which is about 3.32%. At different ambient temperatures, the SOE estimation RMSEs are less than 2.0%. It can be concluded that the proposed approach is able to achieve desirable SOE estimation results under various ambient temperatures.

To investigate the effectiveness of the proposed method with different charge current rates, the characteristic test data with four discharging current rates: 1/3C, 1/2C, 2/3C and 1C at the room temperature (25 °C) were used to verify the method. The SOE estimation errors are shown in Fig. 5.10.

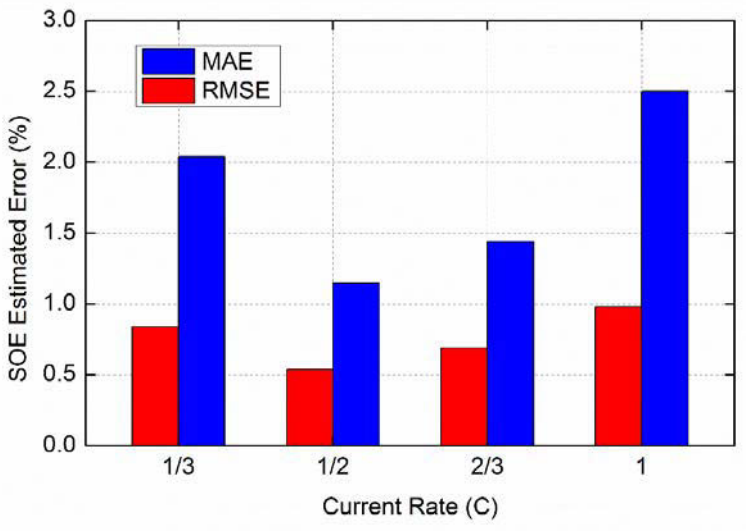

Fig. 5.10 SOE estimation errors with different discharge current rates.

In Fig. 5.10, the SOE estimation MAEs can be limited in a 2.5% error band and the SOE estimation RMSEs are less than 1.0% with different discharging current rates, indicating that the proposed approach can perform well with different discharge current rates.

5.5.2 Maximum available energy estimation

The battery maximum available energy is calculated by the proposed moving-window energy-integral and average methods. During the discharge process of a battery cell with 92 Ah and 1/3C discharging current rate, the maximum available energy estimation results are plotted in Fig. 5.11.

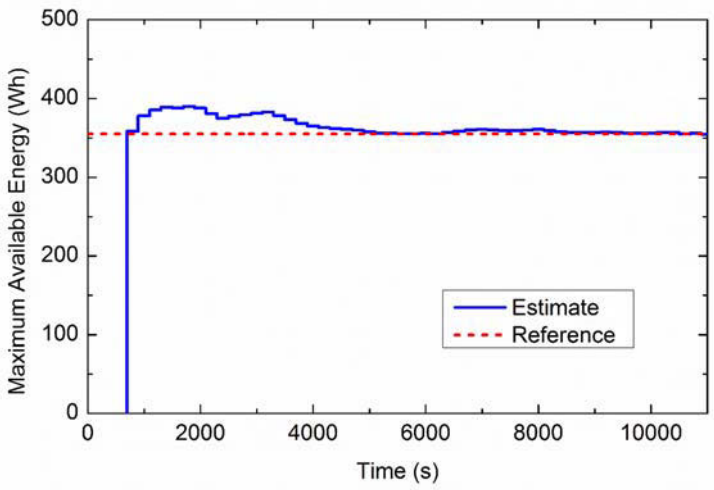

Fig. 5.11 Battery maximum available energy estimation results.

In Fig. 5.11, the proposed algorithm begins to estimate battery maximum available energy at about 700 s. This is because that the first 500 s are used for SOE estimation correction and the followed 200 s are used for the first moving-window calculation. Although some significant estimation errors occurred during the first 4000 s, the estimated maximum available energy can finally converge to the referenced value.

The battery test data at different aging levels are used to verify the effectiveness of the proposed method for battery maximum available energy estimation. The estimated results and relative estimation errors are shown in Fig. 5.12.

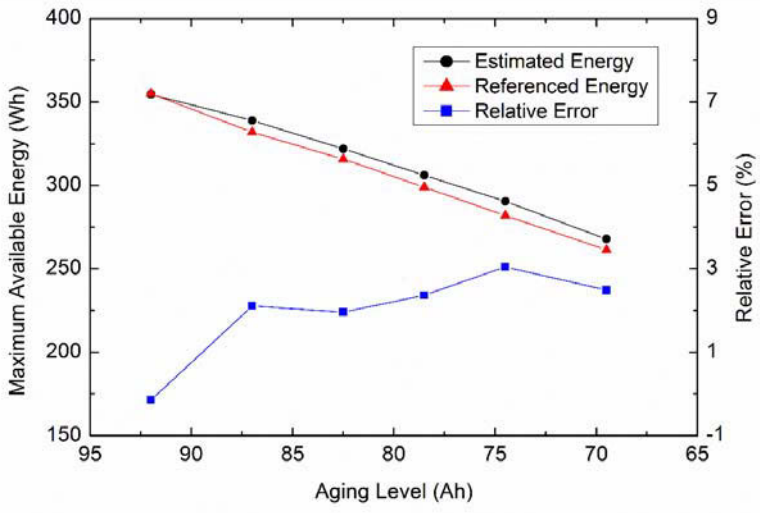

Fig. 5.12 Battery maximum available energy estimation results at different aging levels.

In Fig. 5.12, the estimated maximum available energies can track well with the referenced values at different battery aging levels, and the relative estimation errors can be limited in a +/-3% error band, indicating that the proposed method is feasible for various battery aging levels.

To verify the effectiveness of the proposed approach under different ambient temperatures, the estimated processes were performed at 10 °C, 25 °C and 40 °C, respectively, and the results are shown in Fig. 5.13, where the estimated results indicate that the battery maximum available energy estimation method can work well at the above-mentioned temperatures and the relative estimation errors are able to be limited in a +/-2% error band.

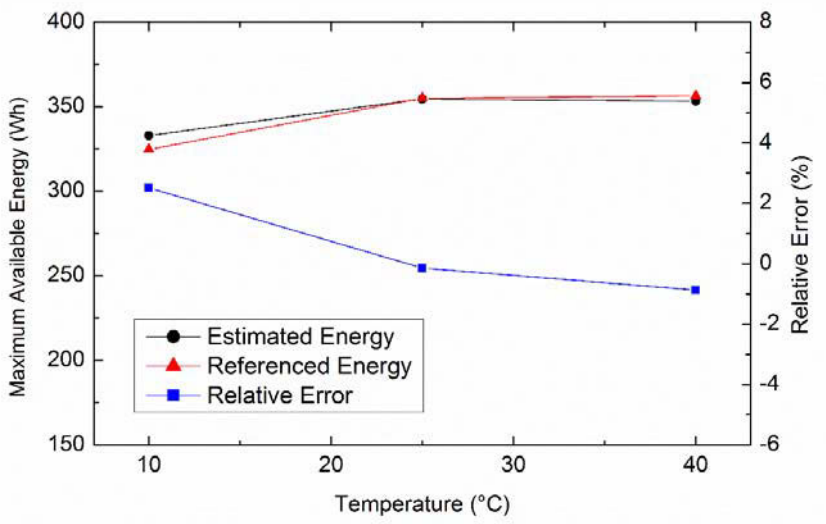

Fig. 5.13 Battery maximum available energy estimation results under different ambient temperatures.

To investigate the effectiveness of the proposed method with different charging current rates, the characteristic test data with four discharging current rates: 1/3C, 1/2C, 2/3C and 1C at the room temperature (25 °C) were used to verify the battery maximum available estimation, and the results are shown in Fig. 5.14.

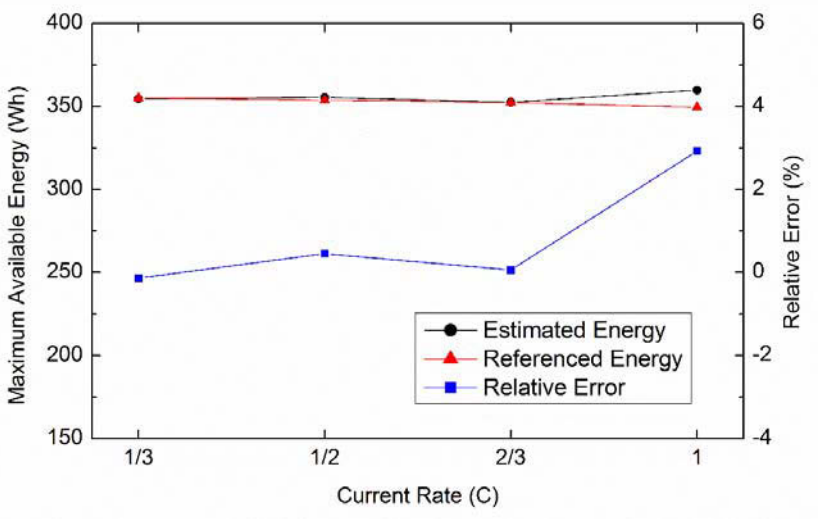

Fig. 5.14 Battery maximum available energy estimation results with different discharge current rates.

From Fig. 5.14, it can be seen that the estimated maximum available energies can follow the tracks of the referenced values well with different battery discharging current rates. The maximum estimated error is 2.92% at 1C current rate, showing that the proposed method can handle different discharging current rates quite well.

5.5.3 Dynamic stress test cycles verification

The dynamic stress test (DST) cycle [5.31] is widely used to simulate the dynamic changed loading conditions of batteries in real applications. The current profiles of DST cycles are depicted in Fig. 5.15(a). Before the DST test, the battery cell was fully charged in a constant current and constant voltage regime and the initial referenced SOE was 100% while the initial SOE of the algorithm was set to an incorrect value, 48%. The referenced SOE and the estimated SOE are compared in Fig. 5.15(b). It can be seen that the estimated SOE is able to track the referenced value quickly. Fig. 5.15(c) shows the estimated SOE errors, in which the SOE estimation MAE and RMSE are 3.2% and 1.2%, respectively. The battery maximum available energy estimation results are plotted in Fig. 5.15(d). The resultant estimated maximum available energy is 324.2 Wh in contrast to the referenced value of 331.9 Wh, and the relative error is 2.32%. The estimated results indicate that the

proposed methods can perform well with small errors even under dynamic loading conditions.

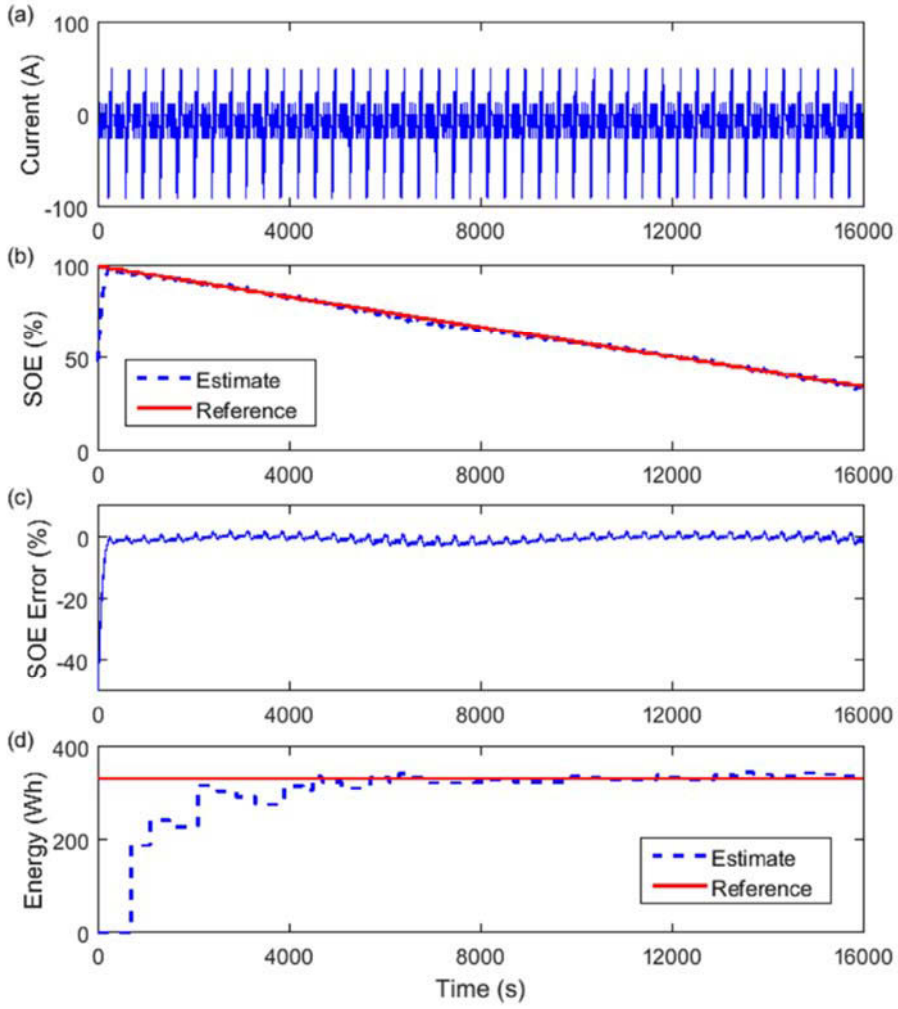

Fig. 5.15 Estimation results with DST cycles, where (a) current profile of DST cycles, (b) SOE estimated results, (c) SOE estimated errors and (d) maximum available energy estimated results.

5.6 Summary

Different from SOC, SOE allows a direct determination of the ratio of battery remaining energy to maximum available energy, which is critical for energy optimization and management in energy storage systems. In order to estimate the battery SOE and maximum available energy accurately, the temperature, current rate and battery aging

level dependencies of battery maximum available energy and SOE were systematically analysed. The relationships between SOC and SOE for different influence factors, such as the ambient temperature, charging and discharging current rates, and battery aging levels, were explicitly quantified for the SOE estimation. Besides, a moving-window energy-integral and average method were incorporated for battery maximum available energy estimation. Experimental results show that the proposed approaches can estimate the battery maximum available energy and SOE with high precision even under the dynamic loading conditions. The robustness of the proposed estimation approaches against various operation conditions and cell aging levels is systematically evaluated. The simplicity of the proposed SOE estimation method can avoid heavy computation cost required by conventional model-based SOE estimation methods, which causes a severe computational burden to the microprocessor with limited computation capability used in BMSs, and therefore the proposed method has the potential to be implemented in practical applications.

References

[5.1] W. Su, H. Eichi, W. Zeng and M. Chow, "A survey on the electrification of transportation in a smart grid environment," *Industrial Informatics, IEEE Transactions on*, vol. 8, no. 1, pp. 1-10 2012.

[5.2] H. He, R. Xiong and J. Peng, "Real-time estimation of battery state-of-charge with unscented kalman filter and RTOS μCOS-II platform," *Appl.Energy*, vol. 162, pp. 1410-1418 2016.

[5.3] H. Rahimi-Eichi, U. Ojha, F. Baronti and M. Chow, "Battery management system: An overview of its application in the smart grid and electric vehicles," *Industrial Electronics Magazine, IEEE*, vol. 7, no. 2, pp. 4-16 2013.

[5.4] L. Lu, X. Han, J. Li, J. Hua and M. Ouyang, "A review on the key issues for lithium-ion battery management in electric vehicles," *J.Power Sources*, vol. 226, pp. 272-288 2013.

[5.5] L. Wang, C. Pan, L. Liu, Y. Cheng and X. Zhao, "On-board state of health estimation of LiFePO 4 battery pack through differential voltage analysis," *Appl.Energy*, vol. 168, pp. 465-472 2016.

[5.6] H. Kim and K.G. Shin, "DESA: Dependable, efficient, scalable architecture for management of large-scale batteries," *Industrial Informatics, IEEE Transactions on*, vol. 8, no. 2, pp. 406-417 2012.

[5.7] S. Wang, L. Shang, Z. Li, H. Deng and J. Li, "Online dynamic equalization adjustment of high-power lithium-ion battery packs based on the state of balance estimation," *Appl.Energy*, vol. 166, pp. 44-58 2016.

[5.8] H. Park, C. Kim, K. Park, G. Moon and J. Lee, "Design of a charge equalizer based on battery modularization," *Vehicular Technology, IEEE Transactions on*, vol. 58, no. 7, pp. 3216-3223 2009.

[5.9] J.K. Barillas, J. Li, C. Günther and M.A. Danzer, "A comparative study and validation of state estimation algorithms for li-ion batteries in battery management systems," *Appl.Energy*, vol. 155, pp. 455-462 2015.

[5.10] L. Zhong, C. Zhang, Y. He and Z. Chen, "A method for the estimation of the battery pack state of charge based on in-pack cells uniformity analysis," *Appl.Energy*, vol. 113, pp. 558-564 2014.

[5.11] J. Xu, C.C. Mi, B. Cao, J. Deng, Z. Chen and S. Li, "The state of charge estimation of lithium-ion batteries based on a proportional-integral observer," *Vehicular Technology, IEEE Transactions on*, vol. 63, no. 4, pp. 1614-1621 2014.

[5.12] L. Zheng, L. Zhang, J. Zhu, G. Wang and J. Jiang, "Co-estimation of state-of-charge, capacity and resistance for lithium-ion batteries based on a high-fidelity electrochemical model," *Appl.Energy*, vol. 180, pp. 424-434 2016.

[5.13] X. Hu, F. Sun and Y. Zou, "Estimation of state of charge of a lithium-ion battery pack for electric vehicles using an adaptive luenberger observer," *Energies*, vol. 3, no. 9, pp. 1586-1603 2010.

[5.14] I. Kim, "The novel state of charge estimation method for lithium battery using sliding mode observer," *J.Power Sources*, vol. 163, no. 1, pp. 584-590 2006.

[5.15] I. Kim, "A technique for estimating the state of health of lithium batteries through a dual-sliding-mode observer," *Power Electronics, IEEE Transactions on*, vol. 25, no. 4, pp. 1013-1022 2010.

[5.16] R. Xiong, F. Sun, Z. Chen and H. He, "A data-driven multi-scale extended kalman filtering based parameter and state estimation approach of lithium-ion olymer battery in electric vehicles," *Appl.Energy*, vol. 113, pp. 463-476 2014.

[5.17] G.L. Plett, "Extended kalman filtering for battery management systems of LiPB-based HEV battery packs: Part 1. background," *J.Power Sources*, vol. 134, no. 2, pp. 252-261 2004.

[5.18] G.L. Plett, "Extended kalman filtering for battery management systems of LiPB-based HEV battery packs: Part 2. modeling and identification," *J.Power Sources*, vol. 134, no. 2, pp. 262-276 2004.

[5.19] G.L. Plett, "Extended kalman filtering for battery management systems of LiPB-based HEV battery packs: Part 3. state and parameter estimation," *J.Power Sources*, vol. 134, no. 2, pp. 277-292 2004.

[5.20] K. Mamadou, A. Delaille, E. Lemaire-Potteau and Y. Bultel, "The state-of-energy: A new criterion for the energetic performances evaluation of electrochemical storage devices," *ECS Transactions*, vol. 25, no. 35, pp. 105-112 2010.

[5.21] K. Mamadou, E. Lemaire, A. Delaille, D. Riu, S. Hing and Y. Bultel, "Definition of a state-of-energy indicator (SoE) for electrochemical storage devices: Application for energetic availability forecasting," *J.Electrochem.Soc.*, vol. 159, no. 8, pp. A1298-A1307 2012.

[5.22] X. Liu, J. Wu, C. Zhang and Z. Chen, "A method for state of energy estimation of lithium-ion batteries at dynamic currents and temperatures," *J.Power Sources*, vol. 270, pp. 151-157 2014.

[5.23] G. Dong, X. Zhang, C. Zhang and Z. Chen, "A method for state of energy estimation of lithium-ion batteries based on neural network model," *Energy*, vol. 90, pp. 879-888 2015.

[5.24] W. Zhang, W. Shi and Z. Ma, "Adaptive unscented kalman filter based state of energy and power capability estimation approach for lithium-ion battery," *J.Power Sources*, vol. 289, pp. 50-62 2015.

[5.25] H.W. Liu, H.F. Wang and C. Guo, "State of energy estimation based on AUKF for lithium battery used on pure electric vehicle," in *Advanced Materials Research*, 2013, pp. 1627-1630.

[5.26] Y. Wang, C. Zhang and Z. Chen, "A method for joint estimation of state-of-charge and available energy of LiFePO 4 batteries," *Appl.Energy*, vol. 135, pp. 81-87 2014.

[5.27] H. He, Y. Zhang, R. Xiong and C. Wang, "A novel gaussian model based battery state estimation approach: State-of-energy," *Appl.Energy*, vol. 151, pp. 41-48 2015.

[5.28] J.J. Moré, "The Levenberg-Marquardt algorithm: implementation and theory," in *Numerical analysis,* Anonymous : Springer, 1978, pp. 105-116.

[5.29] M.R. Khan, G. Mulder and J. Van Mierlo, "An online framework for state of charge determination of battery systems using combined system identification approach," *J.Power Sources*, vol. 246, pp. 629-641 2014.

[5.30] X. Han, M. Ouyang, L. Lu and J. Li, "Simplification of physics-based electrochemical model for lithium ion battery on electric vehicle. part II: Pseudo-two-dimensional model simplification and state of charge estimation," *J.Power Sources*, vol. 278, pp. 814-825 2015.

[5.31] United States Advanced Battery Consortium, "Electric vehicle battery test procedures manual," *USABC,* Jan 1996.

[5.32] L. Zheng, J. Zhu, G. Wang, T. He and Y. Wei, "Novel methods for estimating lithium-ion battery state of energy and maximum available energy," *Appl.Energy*, vol. 178, pp. 1-8 2016.

CHAPTER 6

MODEL BASED BATTERY POWER CAPABILITY PREDICTION METHODS

6.1 Introduction

Lithium-ion batteries with desirable performance in energy density, power density, and cycle life are ubiquitous in electrical energy storage applications, such as smart grids, electric vehicles, railway transportation systems [6.1]-[6.3], etc. Precisely because large amounts of power and energy are required in these applications, lithium-ion battery management systems (BMSs) with essential functions including cell balancing, state of charge (SOC) estimation, state of health estimation, state of available power prediction, etc. are necessary to ensure safe and efficient battery operations [6.4]-[6.10]. State of available power reports the peak power capability of the battery that can be delivered to loads or absorbed from regenerative braking or active recharging in a predictive time horizon. Thus, it is of great significance to accurately predict battery available power for reliable and optimal utilization of the battery.

The reported techniques for predicting battery available power can generally be classified into three groups including characteristic map-based methods, machine learning methods, and model-based methods. The characteristic map-based methods utilize static interdependencies between battery available power and its influenced factors, such as SOC, temperature, and cell aging to build a multidimensional power capability map [6.9], which can be directly stored in the memory of BMSs. The commonest approach for determining the operating point of the characteristic map is to measure the battery voltage response to a reference pulse current and to calculate the battery direct current resistance (DCR) and power capability [6.11], [6.12]. Due to their simplicity and ease of

A substantial proportion of this chapter has been published as an article [6.45] in *IEEE Transactions on Power Electronics* and a conference paper [6.46] in the proceedings of *ICEMS* 2017.

implementation, the characteristic map-based methods are prevailingly adopted by manufacturers of battery and BMS. However, the characteristic map-based methods require a high amount of non-volatile memory to store the multidimensional map [6.13]. The machine learning methods including neural network and support vector machine have been developed for battery available power prediction in [6.14]-[6.16]. Approximate relationships between battery available power and input variables, such as cell terminal voltage, internal resistance, SOC, temperature, etc., can be quantitatively trained with reliable experimental data, but the accuracy of the prediction depends firmly on the training data. Alternatively, a battery model is employed in the model-based methods to predict dynamic behaviours of the battery for computing its peak power capability within the design limits such as the permitted highest and lowest values of cell terminal voltage, current, SOC, etc. [6.17]-[6.20]. The model-based methods have attracted considerable attention due to their high adaptation capabilities and real-time performance. The main differences among the model-based methods are the type of battery model and the estimation technique of battery states and model parameters. Farmann et al. [6.9] summarized and compared different adaptive joint and dual estimation techniques including Kalman filter-based approaches, least-square-based approaches, and other filters and observers for the model-based power prediction methods. It is noteworthy that equivalent circuit models (ECMs) are typically employed in these model-based methods since they have simple and flexible structures as well as few unknown variables [6.21]. However, ECMs idealize battery by applying circuit elements to represent its electrical behaviours but offer little physical explanation of battery performance, thus leading to limited prediction capability [6.22], [6.23].

For overcoming the previously mentioned drawbacks, two novel methods for predicting battery power capability are proposed in this chapter. The first method presented in Section 6.2 aims at enhancing the potential of the characteristic map-based approach to be implemented in BMSs. To this end, the temperature dependence of battery DCR would be analysed and quantitatively modelled for power capability prediction since the battery DCR is typically employed to describe the battery power capability [6.11]. The proposed

DCR model and its implementation on battery power capability prediction will be capable of forecasting battery DCRs and power capabilities under different temperatures, thus significantly reducing battery test work and the dimensions of the characteristic map as well as the memory-consuming. Different from the conventional methods [6.9]-[6.20] using the limits of macroscopically observed variables such as cell terminal voltage and current for power prediction, the second method presented in Section 6.3 used a practical physical limit (i.e. the lithium concentration limit) thus providing a direct insight into electrochemical processes inside batteries. The surface lithium concentration of the solid particle is derived from a simplified battery electrochemical model. Based on the theoretical analysis of battery Gibbs power and dissipation power of battery internal resistance, a relationship between battery instantaneous available power and surface lithium concentration is quantified for the power capability prediction. The proposed methods are experimentally verified with various cell aging levels and ambient temperatures.

6.2 Temperature-Dependent DCR Based Power Prediction Method

It is well recognized that battery resistance characteristic significantly depends on the ambient temperature, and its experimental investigation and analysis can be found in [6.11], [6.24]-[6.26]. The modeling of the temperature dependence of battery charge-transfer resistance that is the difference between battery DCR and ohmic resistance has been reported, which can be described by an Arrhenius expression [6.11], [6.26]. However, the temperature-dependent DCR has not been quantitatively expressed. Accordingly, it is of the essence to investigate systematically the temperature dependence of the DCR and establish an effective DCR model for reliable battery power capability prediction.

6.2.1 Temperature dependence of DCR

To systematically investigate the temperature dependence of battery DCR and power capability, a battery current pulse test schedule was specially designed for identifying the battery DCR at different battery SOCs and ambient temperatures. The current pulse tests were conducted in a commonly-used temperature range from 10 °C to 40 °C at an interval of 5 °C. In each current pulse test, the battery was charged or discharged with C/3 at every 5% SOC increment followed by 1 h relaxation until the battery reaches to 100% SOC or 0% SOC.

For excluding the impacts of the changing open circuit voltage (OCV) and the diffusion process on the measurement of battery DCR, it is recommended to detect the voltage response within a few hundred milliseconds to several seconds after the start of the current pulse. The responded voltage change is mainly caused by battery pure ohmic resistance and charge transfer reaction [6.11]. In this work, the voltage change between 1 s after the start of the current pulse is applied for the DCR and power capability calculation.

The battery charge and discharge DCRs at different SOCs under various temperatures are shown in Figs. 6.1(a) and 6.2(b), respectively. As can be observed, the battery charge and discharge DCRs have an essential dependence on the ambient temperature. For instance, at 5% SOC, the battery charge DCR is about 2.673 mΩ under the temperature of 10 °C, which approximates 2.85 times of that under the temperature of 40 °C (i.e. 0.938 mΩ). It is noted that the DCRs difference between two adjacent temperatures strikingly decreases with the increasing temperature. For example, the charge DCR difference at 50% SOC between 10 °C and 15 °C is about 0.517 mΩ, while it is only the difference of 0.063 mΩ between 35 °C and 40 °C. Additionally, both the charge and discharge DCRs show a relatively large decline in the low SOC range from 5% SOC to 10% SOC, especially under low temperatures, such as 10 °C and 15 °C. From 10% SOC to 95% SOC, the charge or discharge DCRs differ slightly under a certain temperature.

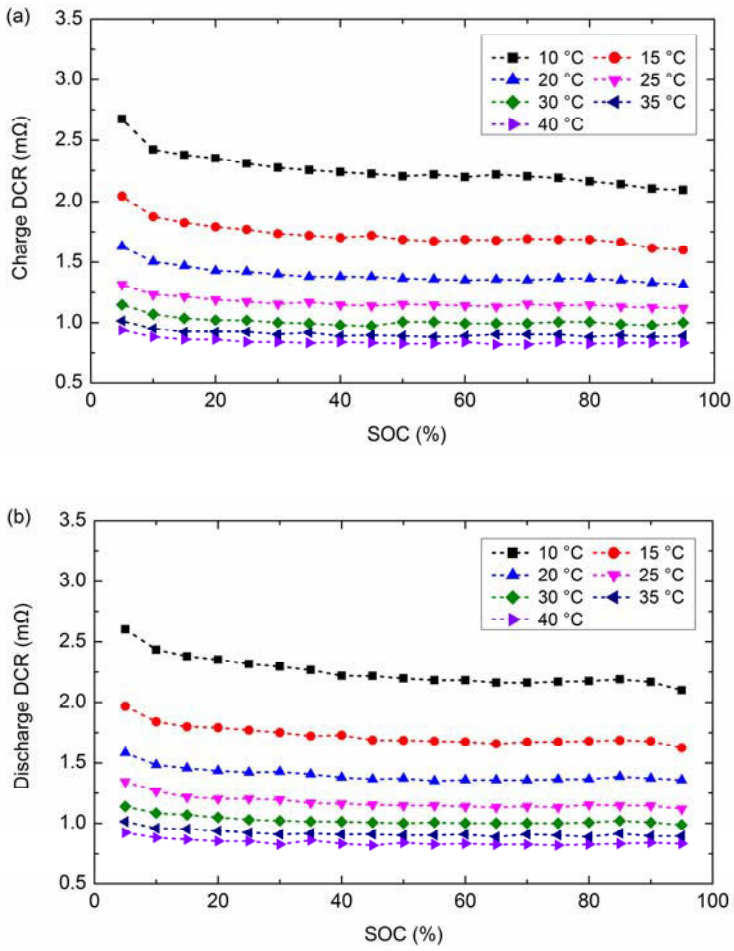

Fig. 6.1 Battery DCRs at different SOCs and temperatures, where (a) charge DCRs, and (b) discharge DCRs.

Fig. 6.2 shows the dependence of battery charge and discharge DCR on the temperature at different battery SOCs. It is worth mentioning that for both battery charge and discharge processes, the DCR has a nearly exponential dependence on the temperature at a certain SOC, which is in line with the results reported in 6.[11]. In Fig. 6.2, it can be found that the rates of exponential increase/decrease of the temperature-dependent DCRs are not identical at different SOCs. For instance, the rate of exponential increase/decrease at 5% SOC is much greater than those at other SOCs. Therefore, it is difficult to apply the exponential dependence directly for the modeling of DCRs and necessary to further develop the relationship between the temperature and DCR.

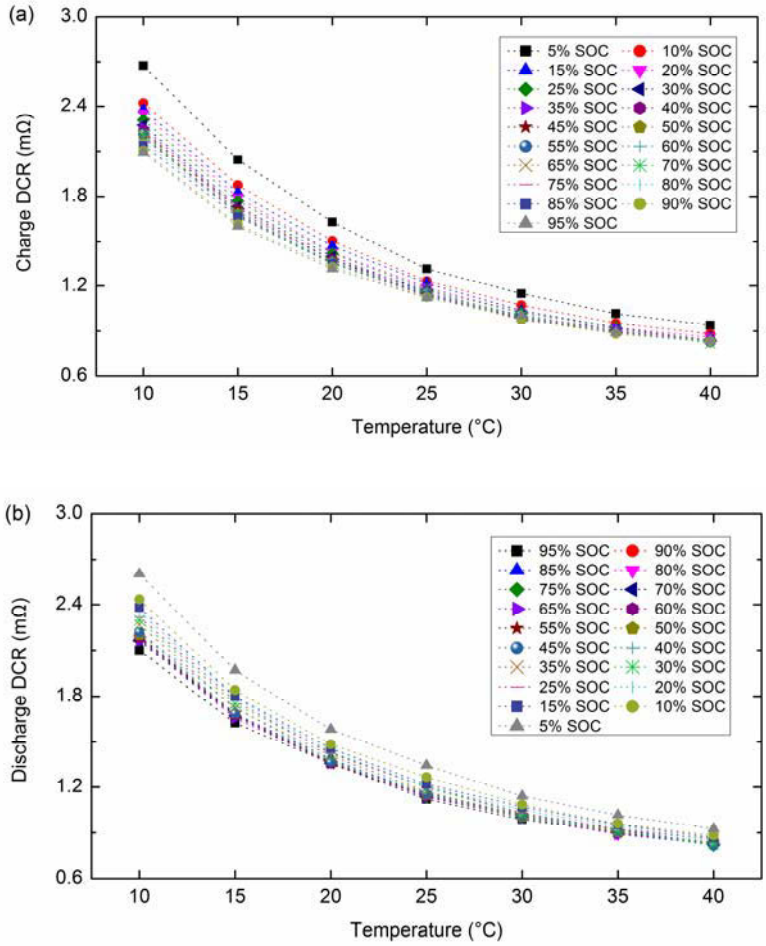

Fig. 6.2 Battery DCR-Temperature curves of different SOCs, where (a) charge DCRs, and (b) discharge DCRs.

6.2.2 Modeling of Battery DCR for Power Prediction

The linear representation of DCRs depicted in Fig. 6.2 is transferred to the logarithmic representation, as shown in Fig. 6.3.

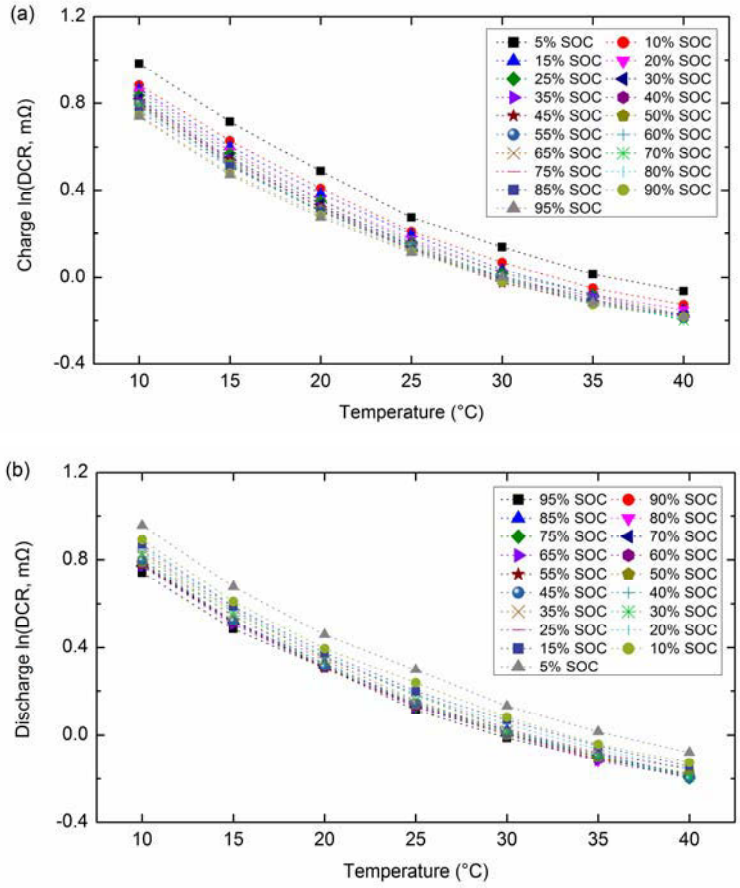

Fig. 6.3 Battery logarithmic DCRs at different SOCs and temperatures, where (a) charge logarithmic DCRs, and (b) discharge logarithmic DCRs.

As can be observed in Fig. 6.3, both charge and discharge logarithmic DCRs appear a similar decreasing tendency with the increasing temperature for all different cell SOCs. It is noteworthy mentioning that the logarithmic DCR versus temperature curves for various battery SOCs are approximately parallel to each other. Accordingly, the relationship between the logarithmic DCR and temperature can be quantitatively expressed as a set of quadratic equations with the same rate of increase/decrease for different SOCs. Thus, at various battery SOCs, the temperature-dependent DCRs are modeled as

$$\ln\left(DCR\left(T,SOC\right)\right)=\alpha T^{2}+\beta T+\gamma\left(SOC\right) \tag{6.1}$$

where $DCR(T, SOC)$ denotes the DCR under the temperature T; α and β are two constant parameters for different SOCs; and $\gamma(SOC)$ denotes the intercept of the equation at the certain SOC.

If one temperature is considered as the based temperature, its corresponding DCR, also called the based DCR in the presented work, is governed by

$$\ln\left(DCR_{bas}\left(SOC\right)\right) = \alpha T_{bas}^2 + \beta T_{bas} + \gamma\left(SOC\right) \tag{6.2}$$

where $DCR_{bas}(SOC)$ and T_{bas} denote the based DCR and temperature, respectively.

By combining (6.1) and (6.2), one has

$$\ln\left(\frac{DCR\left(T,SOC\right)}{DCR_{bas}\left(SOC\right)}\right) = \left(\alpha T^2 + \beta T\right) - \left(\alpha T_{bas}^2 + \beta T_{bas}\right) \tag{6.3}$$

It is worth mentioning that the SOC dependent parameter $\gamma(SOC)$ is counteracted in (6.3), and α and β are constants for different SOCs. Thus, the parameters for DCR calculation are identical for all battery states, which benefits to deduce a universal DCR model.

With some arrangements, (6.3) is rewritten as

$$DCR\left(T,SOC\right) = DCR_{bas}\left(SOC\right)\exp\left[\alpha\left(T^2 - T_{bas}^2\right) + \beta\left(T - T_{bas}\right)\right] \tag{6.4}$$

In the presented study, the room temperature (i.e. 25 °C) and its corresponding DCRs at different SOCs are regarded as the based temperature and DCRs, respectively. Thus, with the based values, (6.4) can be used to compute battery DCRs at different SOCs and temperatures.

The parameters α and β are fit by using the experimental data and Levenberg–Marquardt algorithm for the proposed temperature-dependent DCR model. The Levenberg–Marquardt algorithm is widely applied to solve non-linear least squares problems by finding a model curve so that the sum of the squares of the deviations between the experimental data and model computed values is minimized [6.27]-[6.29]. The optimal

parameters and the resulting coefficients of determination (i.e. R^2) for battery charge and discharge processes are listed in Table 6.1. It is noted that both the charge and discharge coefficients of determination are very close to 1, which means that the proposed model can precisely match the temperature dependence of battery DCR during both battery charge and discharge processes.

Table 6.1 The optimal parameters of the temperature-dependent DCR model.

Parameters	Charge coefficient	Discharge coefficient
α	0.00075446	0.00071906
β	-0.070325	-0.068226
R^2	0.99716	0.99854

A battery cell must be enforced to operate within the safe area of cell terminal voltage, and the battery power capability is therefore constrained by the design limits of the terminal voltage. Two recommended equations (i.e. (6.5)) with the design limits of cell terminal voltage, open circuit voltages (OCV), and DCRs in many studies and standards [6.30]-[6.32] are typically employed for determining the charge and discharge power capabilities, as defined by

$$\begin{cases} P_{chg} = V_{\max}\left(OCV - V_{\max}\right)/DCR_{chg} \\ P_{dis} = V_{\min}\left(OCV - V_{\min}\right)/DCR_{dis} \end{cases} \tag{6.5}$$

The proposed DCR model expressed in (6.4) is then introduced to incorporate in (6.5) for improving the accuracy and robustness of battery power capability prediction against various ambient temperatures. Thus, the battery charge and discharge power capabilities at different SOCs and temperatures are determined by

$$\begin{cases} P_{chg}(T,SOC) = V_{\max}\left(OCV(SOC) - V_{\max}\right) \Big/ \left(DCR_{bas,chg}(SOC)\exp\left[\alpha\left(T^2 - T_{bas}^2\right) + \beta\left(T - T_{bas}\right)\right]\right) \\ P_{dis}(T,SOC) = V_{\min}\left(OCV(SOC) - V_{\min}\right) \Big/ \left(DCR_{bas,dis}(SOC)\exp\left[\alpha\left(T^2 - T_{bas}^2\right) + \beta\left(T - T_{bas}\right)\right]\right) \end{cases} \quad (6.6)$$

where different values of the based DCR may be used for charge and discharge, and are denoted by $DCR_{bas,chg}(SOC)$ and $DCR_{bas,dis}(SOC)$, respectively.

It is noteworthy that the temperature dependence of battery power capability has been involved in (6.6), which can be used to calculate the power capabilities under various ambient temperature, thus effectively lightening battery test work and the dimensions of battery power characteristic map as well as the memory-consuming.

6.2.3 Experimental Verification

To evaluate the performance of the proposed methods for predicting battery DCRs and power capabilities, the metrics including the relative error (RE) and mean absolute percentage error (MAPE) are employed in the presented study. The RE acts as an indicator of how close a measure is relative to the actual value of the thing being measured, which is used to directly evaluate the accuracy of the forecasts of battery DCR and power capability at different SOCs and temperatures. The MAPE gives an indication of how accurate a forecasting method is in statistics, which is applied to evaluate the prediction precision of the proposed methods under different ambient temperatures. The RE and MAPE are governed by the following expressions, respectively.

$$RE = \left(f_i - y_i\right) \Big/ y_i \times 100\% \quad (6.7)$$

$$MAPE = \frac{1}{n}\sum_{i=1}^{n}\left|\left(f_i - y_i\right) \Big/ y_i\right| \times 100\% \quad (6.8)$$

where f_i and y_i denote the predictive and referenced values, respectively, and n denotes the number of data set of predictive and referenced values.

A. Verification of battery DCRs prediction

With the based temperature and based DCRs (i.e. 25 °C and its corresponding DCRs), Equation (6.4) can be applied for predicting battery DCRs under various ambient temperatures. The forecasts of battery charge and discharge DCRs are depicted in Figs. 6.4 and 6.5, respectively.

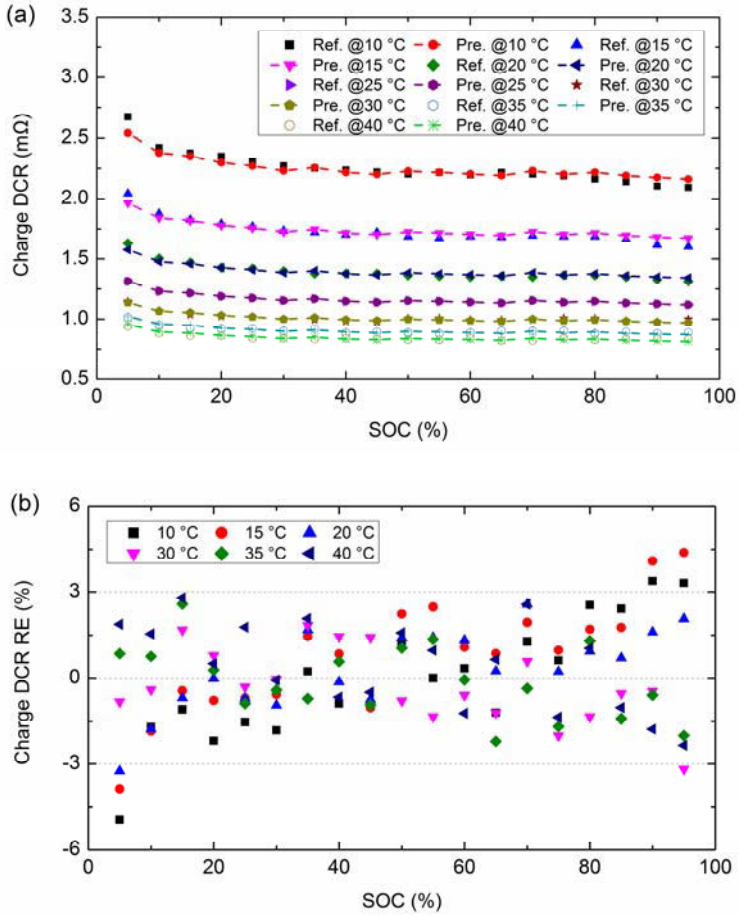

Fig. 6.4 The results of battery charge DCR prediction, where (a) referenced and predictive DCRs, and (b) REs of the predictive DCRs.

Fig. 6.4(a) shows the results of battery charge DCR prediction at different SOCs and temperatures, in which Ref. and Pre. denote the referenced and predictive values, respectively. It can be seen that under various ambient temperatures, the predictive battery charge DCRs can follow the tracks of the referenced values at different SOCs. Since the

DCRs under 25 °C are selected as the based values, the forecasts computed by the DCR model are entirely identical to the referenced values.

The REs of the battery charge DCR predictions are plotted in Fig. 6.4(b). A handful of relatively large absolute values of REs occur at battery low and high SOC, namely 5% SOC and 95% SOC, which may be mainly caused by the deviation of the proposed DCR model, and the maximum absolute value of RE is about 4.95%. It is noteworthy that most of the REs of battery charge DCR are limited in an error band of ±3%. Besides, the MAPEs of battery charge DCR under different ambient temperatures are listed in Table 6.2, where the maximum charge DCR MAPE is 1.74% happened under 15 °C. It suggests that the proposed method can forecast battery charge DCR with small errors at various SOCs and temperatures.

Table 6.2 The MAPEs of battery charge and discharge DCR predictions.

Temperature (°C)	Charge DCR MAPE (%)	Discharge DCR MAPE (%)
10	1.67	0.88
15	1.74	1.19
20	1.18	0.82
30	1.10	1.29
35	1.06	1.54
40	1.39	1.76

Under different ambient temperatures, the forecasts of battery discharge DCR at different SOCs are depicted in Fig. 6.5(a). As can be observed, the predictive discharge DCRs are

capable of tracking the referenced values at various SOCs and temperatures with small deviations. The deviations are quantitatively analyzed through the REs showed in Fig. 6.5(b) and the MAPEs listed in Table 6.2. In Fig. 6.5(b), it presents a similar result to the charge DCR REs, which is that most of discharge DCR REs can be successfully confined into an error band of ±3%. The maximum absolute value of discharge DCR RE is about 5.38% at the battery SOC of 5% and the temperature of 40 °C. Note that the few relatively large REs are all occurred under the temperature of 40 °C, thus leading to the maximum discharge DCR MAPE value, i.e. 1.76%, as listed in Table 6.2. It suggests that the proposed approach can handle the battery discharge DCR quite well at various SOCs and temperatures.

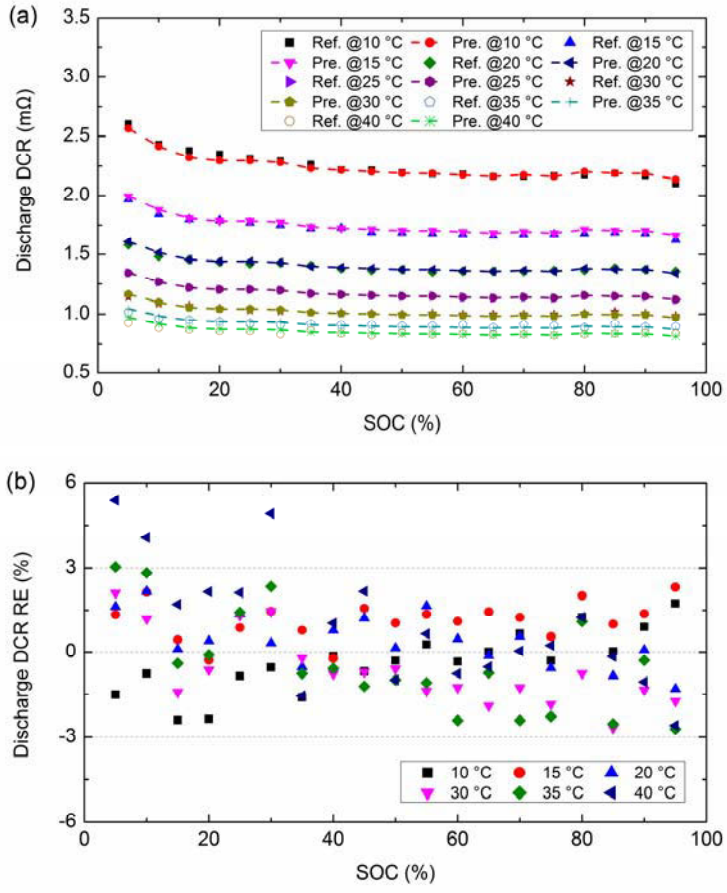

Fig. 6.5 The results of battery discharge DCR prediction, where (a) referenced and predictive DCRs, and (b) REs of the predictive DCRs.

From above discussions, the verified results of battery discharge and charge DCR prediction indicate that the proposed DCR model is able to describe the temperature dependence of both battery charge and discharge DCRs well and estimate the DCR values with high accuracy, which provides a credible foundation for subsequent predictions of battery charge and discharge power capabilities.

B. Verification of battery power capabilities prediction

With the battery DCR forecasts, (6.6) is applied to predict battery charge and discharge power capabilities, and the results are shown in Figs. 6.6 and 6.7, where Ref. denotes the referenced power and Pre. denotes the predictive power.

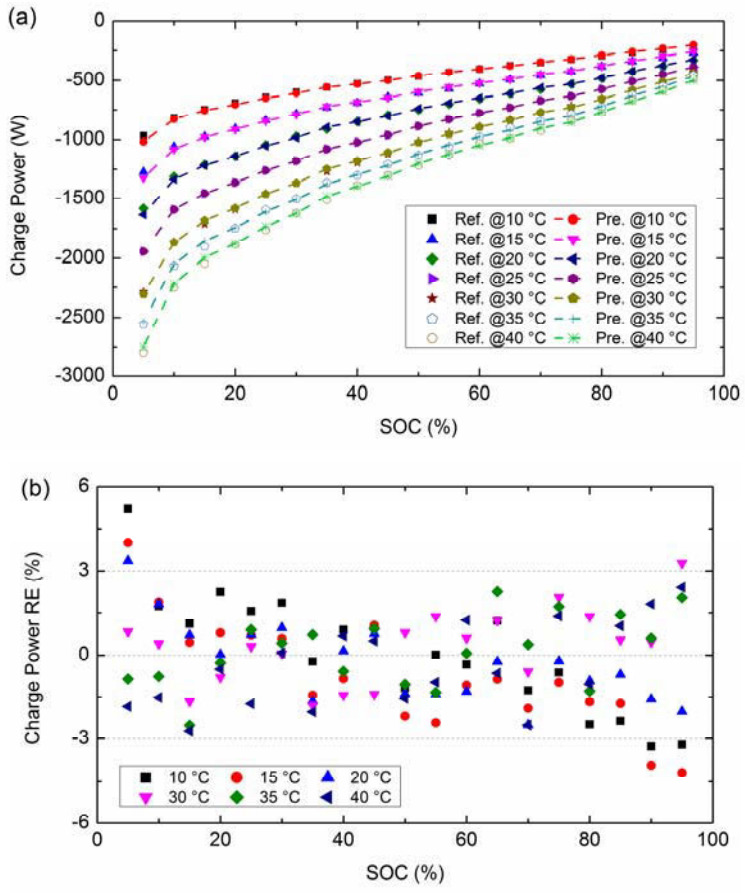

Fig. 6.6 The results of battery charge power capability prediction, where (a) referenced and predictive powers, and (b) REs of the predictive powers.

As can be observed in Fig. 6.6(a), under different ambient temperatures, the battery charge power declines with the decreasing SOC, which is mainly caused by the charge OCV characteristics that decreases with the decreasing SOC. It can also found that battery charge power capability has a significant dependence on the temperature. For example, at the battery SOC of 50%, the absolute values of the referenced charge power capabilities are about 465.93 W, 888.01 W, and 1219.94 W under the temperatures of 10 °C, 25 °C, and 40 °C, respectively. Since the mentioned-above charge DCR forecasts can track well with the actual values, the predictive charge power capabilities can effectively follow the referenced values with small errors at different SOCs and temperatures, as shown in Fig. 6.6(a). Their REs are depicted in Fig. 6.6(b). Strikingly, most of the REs of the battery charge power capability are confined to a small error band, i.e. ±3%, and the maximum RE is about 5.20%. By comparing the charge DCR REs with the charge power REs, it can be found that they are almost opposite in sign. This is because that according to (6.5), an over-estimated charge DCR forecast would result in an underestimated charge power capability, and vice versa.

Table 6.3 The MAPEs of battery charge and discharge power capabilities predictions.

Temperature (°C)	Charge power MAPE (%)	Discharge power MAPE (%)
10	1.67	0.89
15	1.72	1.17
20	1.18	0.81
30	1.10	1.30
35	1.06	1.55
40	1.38	1.72

Moreover, the MAPEs of the predictive charge power capabilities under various temperature are listed in Table 6.3, where all MAPEs are less than 2%. It indicates that the proposed method can effectively forecast battery charge power capability under different battery operating temperatures.

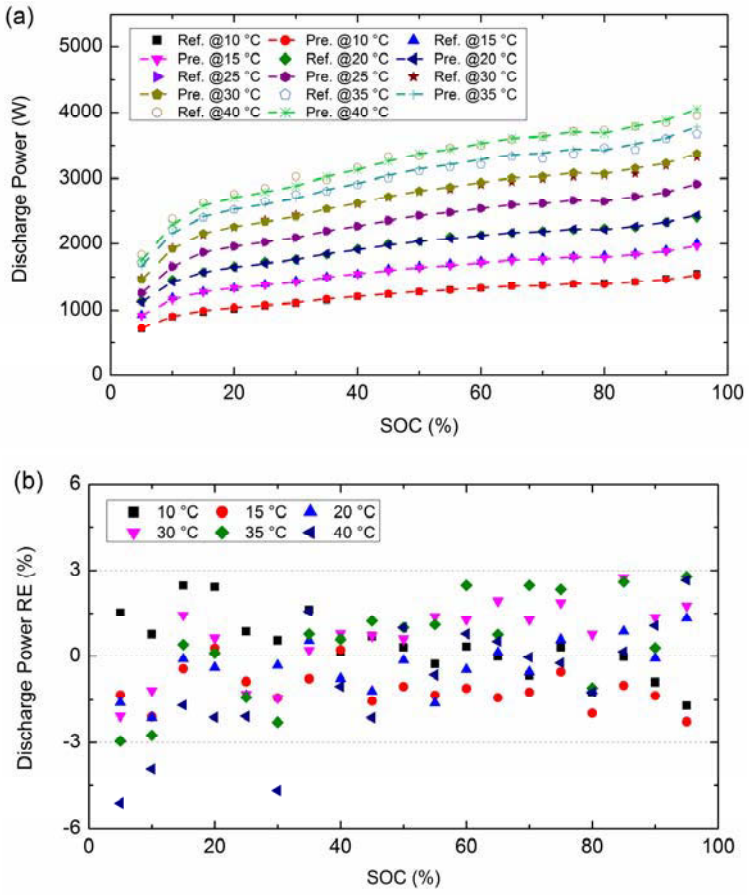

Fig. 6.7 The results of battery discharge power capability prediction, where (a) referenced and predictive powers, and (b) REs of the predictive powers.

Fig. 6.7(a) shows the referenced and predictive values of battery discharge power capabilities. Under different ambient temperatures, the referenced discharge power capability presents an increasing tendency with the increasing battery SOC. At a certain battery SOC, the referenced discharge power capability decreases with the decreasing ambient temperature, which suggests that the ambient temperature has a substantial impact on battery discharge power capability. By observing Fig. 6.7(a), it can be found that the predictive discharge power capabilities can tail closely after the referenced values

at various SOCs and temperatures. Fig. 6.7(b) draws the REs of battery discharge power capability prediction, where most of the REs are effectively limited in an error band of ±3%, and the maximum absolute value of the RE is about 5.10%. The MAPEs of battery discharge power capability forecasts are listed in Table 6.3, where the MAPE under the temperature of 40 °C (i.e. 1.72%) is greater than those under other temperatures, which highlights the effectiveness of the proposed method for battery discharge power capability prediction under various ambient temperatures.

From above prediction results of battery power capabilities, it can be summarized that based on the accurate temperature-dependent DCR model, promising results with small errors can be achieved in both battery charge and discharge power capabilities predictions at different SOCs and ambient temperatures.

6.3 Surface Lithium Concentration Based Power Prediction Method

The available techniques of battery power prediction are primarily derived based on the limits of macroscopically observed variables, such as cell terminal voltage and current, which are insufficient to provide a direct insight into electrochemical processes inside batteries, and consequently, the resulting battery power forecasts may be conservative. To enhance the safety, efficiency, and longevity of the battery system, an advanced BMS with physical insight into batteries should be developed, and a practical physical limit of the battery is highly required for reliable battery power capability prediction. In lithium-ion batteries, high power requires that the lithium diffusion in and out of solid particles of battery electrodes takes place fast enough to supply the loading current [6.33]. Based on the assumption that lithium ions within the inner regions of solid particles fail to fleetly diffuse to the surface of the solid particles for instantaneous applications, the surface lithium concentration can be employed for describing battery instantaneous power capability. It has also been reported that battery instantaneous available power depends

significantly on the surface lithium concentration [6.34]. However, the relationship between the surface lithium concentration and battery instantaneous available power has not been explored sufficiently yet.

6.3.1 Battery electrochemical model and lithium concentration

A lithium-ion battery electrochemical model (EM) consisting of a negative electrode with solid Li_xC_6 particles, an electron-blocking separator, and a positive electrode with solid metal oxide particles is depicted in Fig. 6.8. During battery discharge process, lithium ions de-insert from the solid Li_xC_6 particles in the negative electrode, travel via diffusion and migration through the electrolyte across the separator to the positive electrode where they insert into the solid metal oxide particles. Simultaneously, electrons, blocked by the separator, transfer from the negative electrode to the positive electrode through an external circuit. During battery charge process, the opposite moving processes of lithium ions and electrons occur.

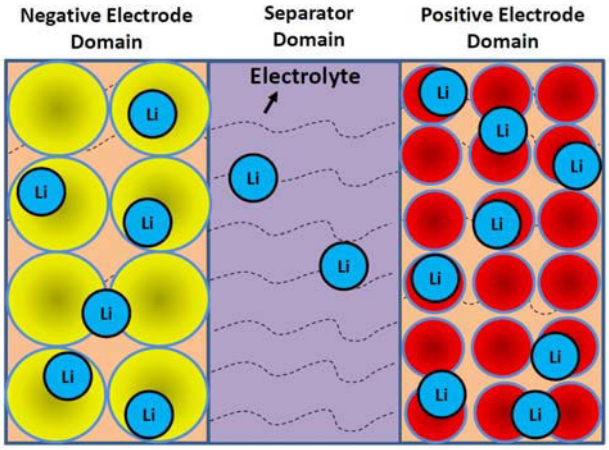

Fig. 6.8 Schematic of a lithium-ion battery EM.

Coupled nonlinear partial differential equations (PDEs) are inevitably used in the lithium-ion battery EM for describing underlying dynamics of the battery, thus leading to the expensive computation and impracticability of the model [6.35]. To reduce the computational complexity, a simplified lithium-ion battery EM, known as single particle model (SPM), has been widely investigated in the literature [6.22], [6.34], [6.36]-[6.38].

In the SPM, each electrode is idealized as a single spherical solid particle, which can well strike a balance between the mathematical simplicity and modeling accuracy while sufficiently enhancing the state observability [6.22], [6.36]. The mean lithium concentration of the solid particle of the SPM has been sophisticatedly applied for battery state of charge (SOC) estimation, and remarkable results with high accuracy can be achieved [6.22], [6.36]-[6.38]. It has been reported that surface lithium concentration of the solid particle is strongly related to the instantaneous power capability of the battery [6.34], but their relationship has not been investigated sufficiently yet. Thus, this work focuses on developing the surface lithium concentration of the solid particle for modeling and predicting battery instantaneous available power.

As reported in our previous work [6.22], the lithium concentration at various radii of the solid particle can be obtained by using the discretized governing equations, and the experimental results confidently validated the robustness and availability of the developed SPM, which provides a solid foundation and convincing calculation results of surface concentration for this work. The governing equations for computing the lithium concentration of the solid particle are briefly listed in Table 6.4, and we refer readers to [6.22] therein gives more details.

Table 6.4 The governing equations for computing the lithium concentration of the solid particle [6.22].

Equation		Description
$dr = R_p / node$	(6.9)	Node meshing of radius
$\frac{\partial c_s(r,t)}{\partial t} = D_s\left(\frac{2}{r}\frac{\partial c_s(r,t)}{\partial r} + \frac{\partial^2 c_s(r,t)}{\partial r^2}\right)$	(6.10)	Solid phase transport of lithium
$\frac{\partial c_s(r,t)}{\partial t} = \frac{c_{sd}(i,k+1) - c_{sd}(i,k)}{dt}$	(6.11)	Lithium changing with time
$\frac{\partial c_s(r,t)}{\partial r} = \frac{c_{sd}(i+1,k) - c_{sd}(i-1,k)}{2dr}$	(6.12)	Lithium changing with space
$\frac{\partial^2 c_s(r,t)}{\partial r^2} = \frac{c_{sd}(i+1,k) - 2c_{sd}(i,k) + c_{sd}(i-1,k)}{dr^2}$	(6.13)	Lithium changing with space
$c_{s\_mean} = \sum_{i=1}^{node} 3c_{sd}(i,k)(i-1)^2 dr^3 / R_p^3$	(6.14)	Mean concentration
$\begin{cases} \frac{c_{sd}(2,k) - c_{sd}(1,k)}{dr} = 0 \\ \frac{c_{sd}(node,k) - c_{sd}(node-1,k)}{dr} = \frac{I((k-1)dt)}{D_s FaL} \end{cases}$	(6.15)	Boundary conditions
$c_{sd}(i,1) = c_{sd}^0$	(6.16)	Initial condition

In the developed SPM [6.22], each solid particle was meshed as 40 nodes for equilibrating the model accuracy and computational efforts. Fig. 6.9 shows the lithium ion concentrations in different nodes of the negative solid particle during battery charge process with the current rate of 1/3 C. As can be observed, the lithium concentration in the outmost node can be acquired during the whole process of battery operation, which is regarded as the surface concentration of the solid particle and is employed to develop the prediction method for battery instantaneous available power capability.

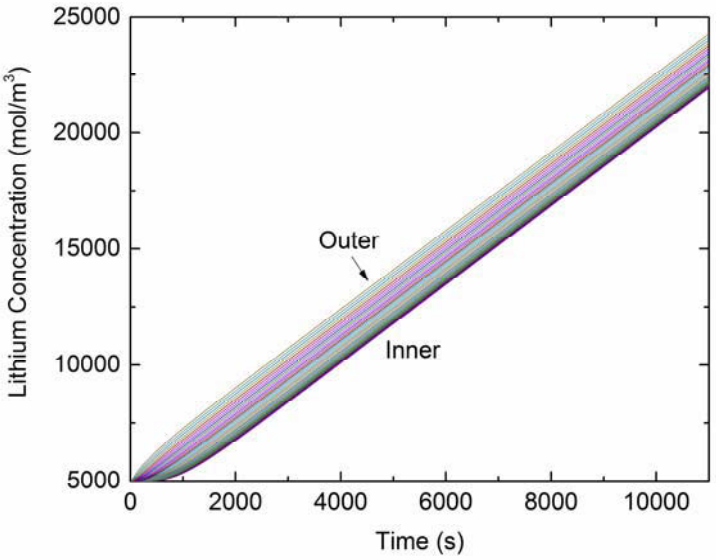

Fig. 6.9 Lithium ion concentrations in different nodes of the negative solid particle during battery charge process with the current rate of 1/3 C.

6.3.2 Proposed instantaneous available power prediction method

The reaction Gibbs free energy of the battery is determined by

$$\Delta G = -nFV_{OCV} + RT\ln Q_r \tag{6.17}$$

where ΔG denotes the Gibbs free energy, n the number of electrons transferred, F the Faraday constant, V_{OCV} the open circuit voltage (OCV), R the gas constant, T the absolute temperature, and Q_r the reaction quotient.

If all the Gibbs free energy is converted to work that would be the maximum electrical work (W_{Gibbs}), one has

$$W_{Gibbs} = -\Delta G = nFV_{OCV} - RT\ln Q_r \tag{6.18}$$

As previously mentioned, the internal resistance of a battery is a primary source of power dissipation, which could not be omitted when applying a large loading current. With this in consideration, the charge and discharge power capabilities of the battery are governed by (6.19) and (6.20), respectively.

$$P_{chg} = P_{Gibbs} + P_{res} = \frac{dW_{Gibbs}}{dt} + P_{res} \tag{6.19}$$

$$P_{dis} = P_{Gibbs} - P_{res} = \frac{dW_{Gibbs}}{dt} - P_{res} \tag{6.20}$$

where P_{chg} and P_{dis} denote the charge and discharge power capabilities of the battery, respectively, P_{Gibbs} the Gibbs power, and P_{res} the power dissipation in battery internal resistance. It is noted that the charge power provides the Gibbs power of the battery reaction and the power dissipation during battery charge process, while the Gibbs power of the battery reaction affords the discharge power and the power dissipation during battery discharge process.

The time horizon is defined as 1 s for the instantaneous power prediction in the presented study. During this instantaneous time horizon, the reaction quotient (Q_r) that is determined by the concentrations of chemical species involved in the battery reaction is deemed to be not significantly changed and remain constant. Thus, the instantaneous Gibbs power can be arranged as

$$P_{Gibbs} = \frac{d\left(nFV_{OCV}\right)}{dt} = FV_{OCV}\frac{dn}{dt} + nF\frac{dV_{OCV}}{dt} \tag{6.21}$$

With the lithium concentration limit, it is regarded that battery instantaneous available power achieves its peak value when the surface concentration of the solid particle increases to its permitted maximum value. The change of the number of electrons transferred in the instantaneous time horizon is represented by the growing number of lithium ions inserted to the surface of the solid particle, namely

$$\frac{dn}{dt} = \sigma\left(c_{surf,\max} - c_{surf,0}\right) = \sigma\Delta c_{surf} \tag{6.22}$$

where $c_{surf,0}$ and $c_{surf,\max}$ denote the initial value and the maximum value of the surface concentration of the solid particle, respectively, Δc_{surf} the maximum change of the surface concentration which is the difference between $c_{surf,\max}$ and $c_{surf,0}$, and σ the transformational coefficient between the surface concentration and the number of electrons.

The number of electrons transferred is represented by the mean lithium concentration of the solid particle and can be described as

$$n = \gamma c_{s\_\mathrm{mean}} \tag{6.23}$$

where γ denotes the transformational coefficient between the number of electrons transferred and the mean lithium concentration of the solid particle, and c_{s_mean} denotes the mean lithium concentration of the solid particle, which can be computed based on the concentration of each node [6.22], as given by

$$c_{s\_\mathrm{mean}} = \sum_{i=1}^{node} 3c_{sd}\left(i,k\right)\left(i-1\right)^2 dr^3 \Big/ R_p^3 \tag{6.24}$$

The battery OCV change with time can be expressed as

$$\frac{dV_{OCV}}{dt} = \frac{dSOC}{dt}\frac{dV_{OCV}}{dSOC} = k\Delta c_{surf}\frac{dV_{OCV}}{dSOC} \tag{6.25}$$

where the SOC change is determined by the maximum change of the surface concentration in the instantaneous time horizon, and k denotes their transformational coefficient.

Likewise, the loading current applied to battery internal resistance is also considered as being determined by the maximum change of the surface concentration in the instantaneous time horizon, and therefore the power dissipation is given by

$$P_{res} = i^2 R_{bat} = \varepsilon \Delta c_{surf}^{\ 2} R_{bat} \tag{6.26}$$

where i denotes the loading current of the battery, ε the transformational coefficient between the loading current and the maximum change of surface concentration, and R_{bat} the battery internal resistance that refers to battery direct current resistance, which is the sum of the ohmic resistance and the polarization resistance [6.39]. Different battery internal resistance values may be used for charge and discharge, and are denoted by R_{chg} and R_{dis}, respectively.

As mentioned in the previous section, the lithium ions de-intercalate from the negative electrode and intercalate into the positive electrode during battery discharge, and the opposite process occurs during battery charge. Thus, the surface concentration of the positive solid particle is applied for predicting battery discharge power capability, and the surface concentration of the negative solid particle is employed for forecasting battery charge power capability. Combining (6.19) to (6.26), the maximum values of instantaneous charge and discharge power capabilities can be expressed as

$$P_{chg,inst} = \sigma^- \Delta c_{surf}^- F V_{OCV} + \lambda^- \Delta c_{surf}^- c_{s\_\mathrm{mean}}^- F \frac{dV_{OCV}}{dSOC} + \varepsilon^- \Delta c_{surf}^{-\ 2} R_{chg} \tag{6.27}$$

$$P_{dis,inst} = \sigma^+ \Delta c_{surf}^+ F V_{OCV} + \lambda^+ \Delta c_{surf}^+ c_{s\_\mathrm{mean}}^+ F \frac{dV_{OCV}}{dSOC} - \varepsilon^+ \Delta c_{surf}^{+\ 2} R_{dis} \tag{6.28}$$

where a parameter with the superscript "+" (or "-") denotes the parameter using in the positive (or negative) solid particle, $P_{chg,inst}$ and $P_{dis,inst}$ the instantaneous charge and discharge power capabilities, respectively, and λ the product of γ and k.

Since the cell aging and ambient temperature have a significant impact on battery power capability, the cell aging and temperature dependencies of the parameters in (6.27) and (6.28) should be taken into account to achieve more promising results in battery power capability prediction. In [6.40], [6.41], the maximum possible concentration in the solid phase was expressed as being proportional to the capacity of the electrode. Thus, the permitted maximum surface concentration of the solid particle would also change with the cell aging level and is formulated by

$$c_{surf,\max} = \alpha + \beta Q \tag{6.29}$$

where Q denotes the battery capacity, and α and β are two fitting coefficients for the maximum surface concentration.

Thus, the maximum change of surface concentration can be rewritten as

$$\Delta c_{surf} = \alpha + \beta Q - c_{surf,0} \tag{6.30}$$

Combining (6.27), (6.28), and (6.30), the instantaneous available power capabilities at different cell aging levels can be calculated.

Moreover, physiochemical properties of lithium-ion batteries are temperature dependent and obey the Arrhenius expression [6.42], [6.43]. The standard Arrhenius equation for computing a general physiochemical property value is defined as

$$\eta = \eta_{bas} \exp\left[\frac{E_{act}}{R}\left(\frac{1}{T} - \frac{1}{T_{bas}}\right)\right] \tag{6.31}$$

where η denotes the physiochemical property value at ambient temperature T, η_{bas} the based physiochemical property value at the based temperature T_{bas} (namely 25 °C in the presented study), and E_{act} the activation energy.

As expressed in (6.27) and (6.28), the instantaneous available power capabilities of the battery are mainly governed by the lithium ion diffusion from electrolyte phase to solid phase which is temperature dependent through the Arrhenius law, and consequently, the temperature dependent Power capability can be determined by the Arrhenius expression. Equation (6.31) is a critical application in determining the rate of electrochemical reactions, while the activation energy is theoretically regarded as a constant. However, in most of practical cases, the activation energy changes with variation in temperature [6.44]. With this in consideration, the activation energy of battery power may be temperature dependent, and a modified Arrhenius equation for computing battery instantaneous available power is given by

$$P_{inst} = P_{inst\_bas} \exp\left[\frac{(\omega + \rho T)}{R}\left(\frac{1}{T} - \frac{1}{T_{bas}}\right)\right] \tag{6.32}$$

where P_{inst} denotes the battery instantaneous available power ($P_{chg,inst}$ for charge power and $P_{dis,inst}$ for discharge power); P_{inst_bas} denotes the based instantaneous available power under the temperature of 25 °C; and ω and ρ are two fitting coefficients for the activation energy. It is noted that the based instantaneous charge and discharge power capabilities at the temperature of 25 °C are computed by using (6.27) and (6.28), respectively, and thereby combining with (6.32), the power capabilities at other temperatures can be obtained.

6.3.3 Experimental Verification

Since the battery direct current resistance is typically employed for describing the battery power capability, the battery charge and discharge power capabilities computed by using (6.5) are considered as the “real” values, i.e. the referenced power capabilities of the battery. In particular, the direct current resistance is determined by a current pulse and its

resulting voltage change between 1 s after the start of the current pulse, which is consistent with the instantaneous time horizon for the power prediction. In this work, LiMn2O4 batteries are used for the experiment and verification, and therefore, the maximum and minimum cell terminal voltages are set as 4.2 V and 3.0 V, respectively. The referenced charge and discharge power capabilities at different cell aging levels and ambient temperatures are depicted in Figs. 6.10, 6.12, 6.13, and 6.15 in the following part and are used for parameter fitting.

A. Parameters fitting

Due to its good performance in training model parameters, the Levenberg-Marquardt algorithm is applied to fit the parameters of (6.27), (6.28), (6.30) and (6.32) with the experiment data. The optimal parameters for the positive and negative solid particles are listed in Table 6.5.

Table 6.5 The optimal parameters for the positive and negative solid particles.

Parameter	Positive solid particle coefficient	Negative solid particle coefficient
σ	1.854e-7	1.356e-7
λ	1.075e-16	1.034e-15
ε	2.0e-3	1.631e-3
α	795.814	299.507
β	14965.888	3585.242
ω	54.670	63.184
ρ	-19107.892	-21800.752
R^2	0.995	0.996

Note that the coefficients of determination R^2 are 0.995 and 0.996 for instantaneous discharge and charge power capabilities, respectively. It means that the proposed models can well match the real relationships between the instantaneous available power capabilities and surface lithium concentrations of solid particles. The predictive results of instantaneous available power capabilities are elaborated in the following parts.

B. Instantaneous charge power prediction

To investigate the effectiveness of the proposed approach during the process of battery aging, the battery cell with a rated capacity of 90 Ah degraded from 92 Ah to 69.5 Ah was used for the verification.

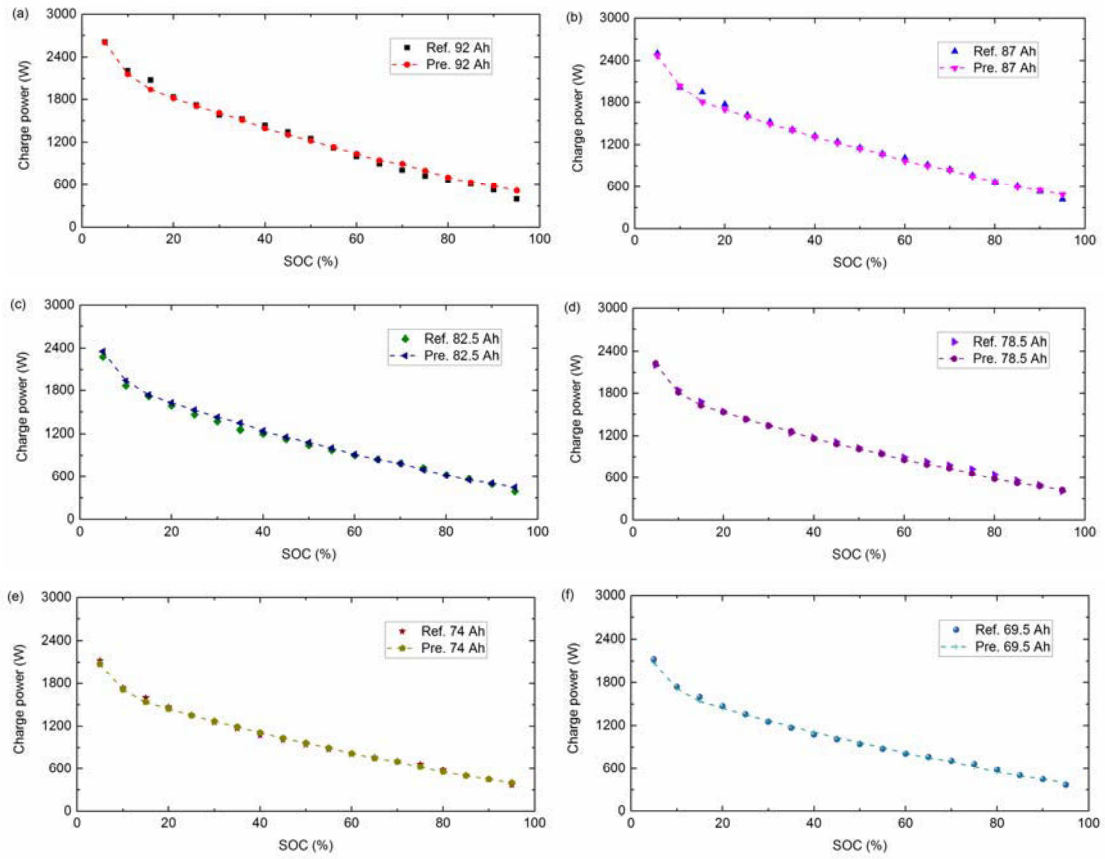

Fig. 6.10 Battery instantaneous charge power prediction results at different aging levels, wherer (a) 92 Ah, (b) 87 Ah, (c) 82.5 Ah, (d) 78.5 Ah, (e) 74 Ah, and (f) 69.5 Ah.

Fig. 6.10 shows the predictive results of battery instantaneous charge power at six various aging levels with the capacities of 92 Ah, 87 Ah, 82.5 Ah, 78.5 Ah, 74 Ah, and 69.5 Ah,

respectively. It can be observed that battery instantaneous available charge power decreases with the rising SOC, and the predictive power capabilities can track well with the referenced values for all the aging levels.

For evaluating the predictive accuracy of the proposed approach at different cell aging levels, one of the most common measures of forecast error, MAPE is employed in the presented study and is governed by (6.8). The MAPEs of battery instantaneous charge power prediction at different aging levels are depicted in Fig. 6.11, where the maximum MAPE is about 5.4% at the capacity of 92 Ah. This relatively large error is attributed to the influence of few outliers in the prediction. However, promising results with the MAPEs of less than 3.5% can be obtained at other aging levels. It indicates that the proposed method can well handle different cell aging levels.

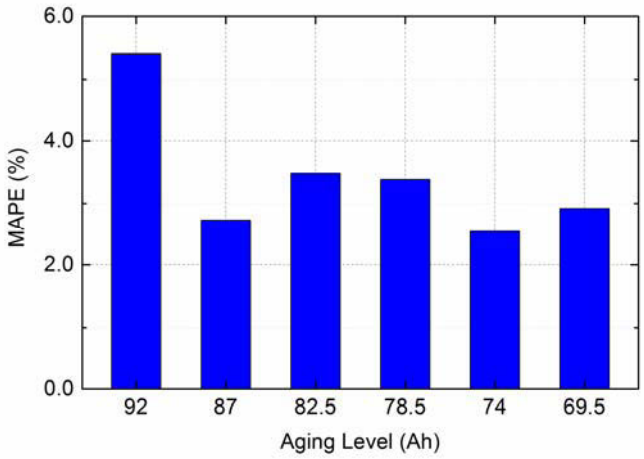

Fig. 6.11 MAPEs of battery instantaneous charge power prediction at different aging levels.

The MAPEs of battery instantaneous charge power prediction at different aging levels are depicted in Fig. 6.11, where the maximum MAPE is about 5.4% at the capacity of 92 Ah. This relatively large error is attributed to the influence of few outliers in the prediction. However, promising results with the MAPEs of less than 3.5% can be obtained at other aging levels. It indicates that the proposed method can well handle different cell aging levels.

To assess the adaptability of the proposed method at various temperatures, the battery was loaded at a commonly used temperature range from 10 °C to 40 °C with the interval of 5 °C for the verification. Fig. 6.12(a) compares battery instantaneous charge power prediction results with referenced data at various SOCs and ambient temperatures, showing that the forecasts are able to follow the tracks of the referenced values. It can also be seen that the ambient temperature has a significant impact on the power capabilities, which decrease with the declining temperature at some battery SOCs. Furthermore, the MAPEs between of the prediction results are presented in Fig. 6.12(b), where all the MAPEs are limited in a small error band of 3.0%, indicating the proposed method can work well and achieve desirable results at various ambient temperatures.

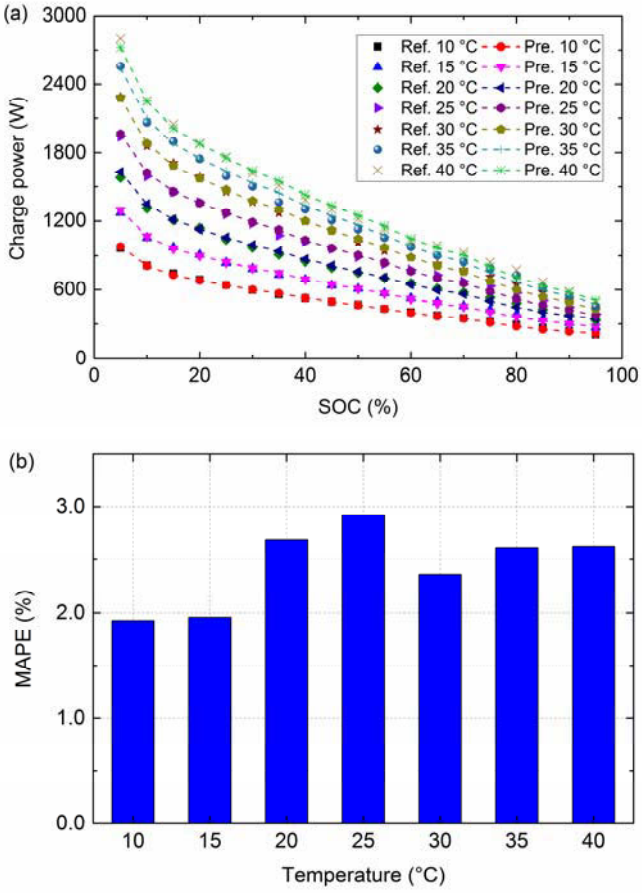

Fig. 6.12 Battery instantaneous charge power prediction results at various temperatures, where (a) referenced and predictive power capabilities, and (b) MAPEs.

C. Instantaneous discharge power prediction

Likewise, the battery operated at six different aging levels are used for evaluating the instantaneous discharge power prediction, and the predictive results are demonstrated in Fig. 6.13. It is clear that the battery instantaneous discharge power increases with the rising SOC which appears an opposite tendency in comparison with the instantaneous charge power, and the predictive power capabilities can effectively follow this trend and approach the referenced values at different aging levels.

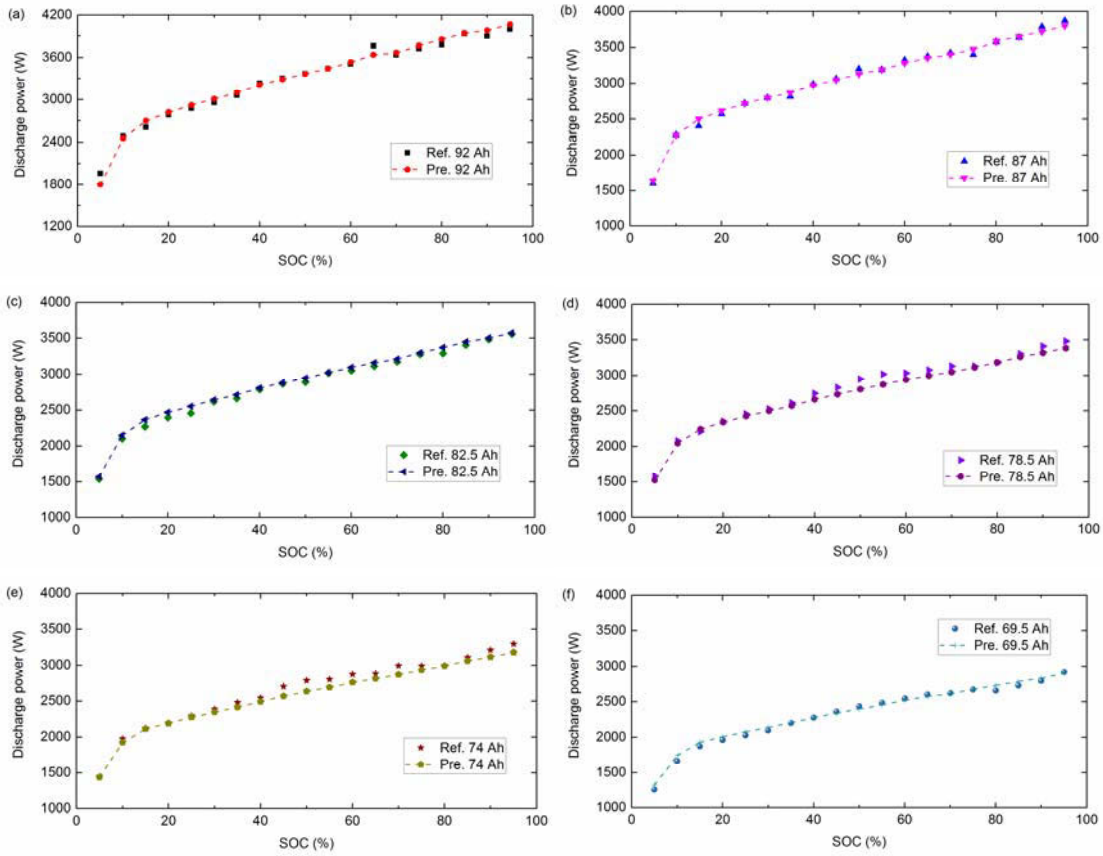

Fig. 6.13 Battery instantaneous discharge power prediction results at different aging levels, where (a) 92 Ah, (b) 87 Ah, (c) 82.5 Ah, (d) 78.5 Ah, (e) 74 Ah, and (f) 69.5 Ah.

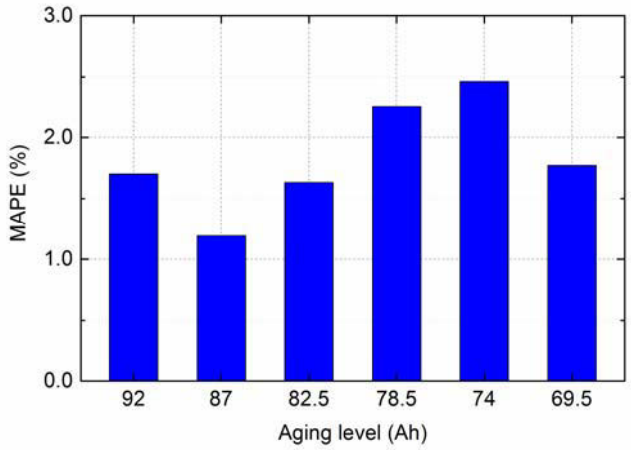

Fig. 6.14 MAPEs of battery instantaneous discharge power prediction at different aging levels.

Fig. 6.14 provides the MAPEs of battery instantaneous discharge power prediction results. It can be observed that at various aging levels, the MAPEs are within 2.50%, which highlights the robustness of the proposed method in forecasting battery instantaneous discharge power against varying battery aging.

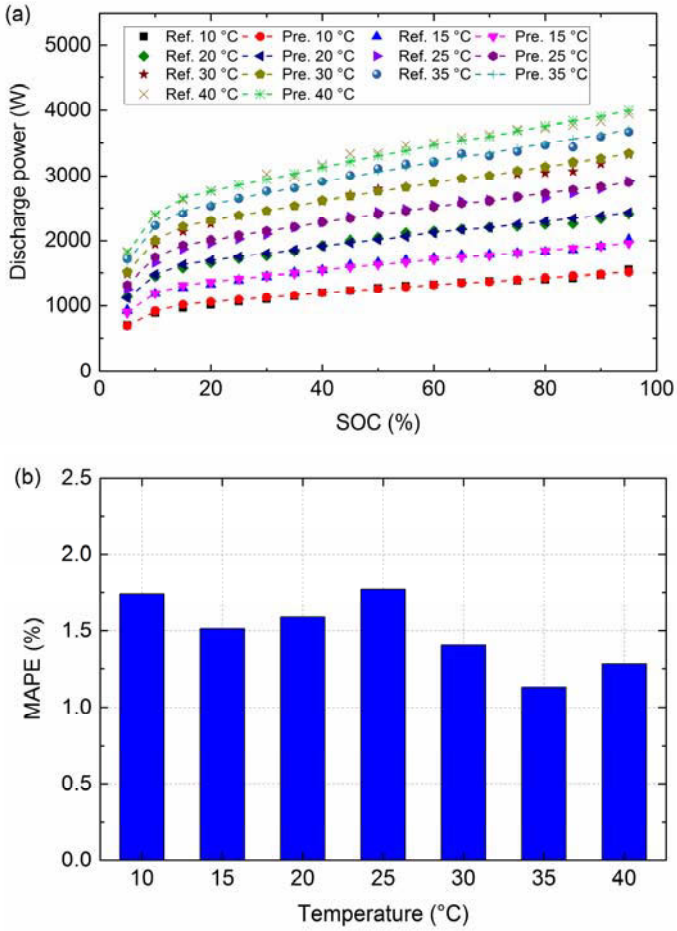

Fig. 6.15 Battery instantaneous discharge power prediction results at various temperatures, where (a) referenced and predictive power capabilities, and (b) MAPEs.

Additionally, the referenced and predictive results of battery instantaneous discharge power at different ambient temperatures are compared in Fig. 6.15(a), and their MAPEs are depicted in Fig. 6.15(b). From Fig. 6.15(a), it can be seen that as the ambient temperature rises, the magnitude of the discharge power capability increases at some battery SOCs. Moreover, the instantaneous discharge power forecasts can still tail after the referenced data. It is noteworthy that the MAPEs showed in Fig. 6.15(b) are successfully confined into a narrow error band of 2.0%, which validates the feasibility of the proposed method for the instantaneous discharge power prediction.

According to the close agreement between the forecasts and experimental data, it can be summarized that the proposed method for both battery instantaneous available charge and

discharge power capabilities prediction can handle various cell aging levels and ambient temperatures quite well.

6.4 Summary

In this chapter, two novel methods based on the battery direct current resistance (DCR) model and electrochemical model, respectively, are proposed for predicting battery power capability. In the first method, a battery DCR model for quantitatively describing its temperature dependence is proposed and then employed for predicting battery power capability. The verification results show that the proposed approaches are capable of accurately forecasting battery DCRs and power capabilities under different temperatures, thus significantly reducing battery test work and the dimensions of the characteristic map as well as the memory-consuming. Different from the conventional methods for battery power capability prediction with macroscopically observed variables such as cell terminal voltage and current as constrained limits, the second method utilizes a physical limit, namely the lithium concentration limit of the solid particle as a constrain, thus providing a direct insight into electrochemical processes inside batteries. Quantitative relationships between battery surface lithium concentration and instantaneous charge and discharge power capabilities are deduced based on the analysis of battery Gibbs power and dissipation power of its internal resistance. The proposed approach is verified with various cell aging levels and ambient temperatures, and the experiments demonstrate the close agreement between the forecasts and experimental data. Most of the mean absolute percentage errors of the forecasts at various battery operation conditions are less than 3.5%, which highlights superior accuracy and robustness of the proposed method.

References

[6.1] J. Cho, S. Jeong and Y. Kim, "Commercial and research battery technologies for electrical energy storage applications," *Progress in Energy and Combustion Science*, vol. 48, pp. 84-101, 2015.

[6.2] M. Cacciato, G. Nobile, G. Scarcella and G. Scelba, "Real-time model-based estimation of SOC and SOH for energy storage systems," *IEEE Transactions on Power Electronics*, vol. 32, no. 1, pp. 794-803, 2017.

[6.3] Z. Wang, J. Ma and L. Zhang, "Finite element thermal model and simulation for a cylindrical li-ion battery," *IEEE Access* 2017.

[6.4] J. Kim, J. Shin, C. Chun and B. Cho, "Stable configuration of a li-ion series battery pack based on a screening process for improved voltage/SOC balancing," *IEEE Transactions on Power Electronics*, vol. 27, no. 1, pp. 411-424, 2012.

[6.5] Z. Zhang, X. Cheng, Z. Lu and D. Gu, "SOC estimation of lithium-ion batteries with AEKF and wavelet transform matrix," *IEEE Transactions on Power Electronics*, vol. 32, no. 10, pp. 7626-7634, 2017.

[6.6] Z. Wei, C. Zou, F. Leng, B.H. Soong and K.J. Tseng, "Online model identification and state of charge estimate for lithium-ion battery with a recursive total least squares-based observer," *IEEE Trans.Ind.Electron.* 2017.

[6.7] L. Zheng, J. Zhu, G. Wang, T. He and Y. Wei, "Novel methods for estimating lithium-ion battery state of energy and maximum available energy," *Appl.Energy*, vol. 178, pp. 1-8, 2016.

[6.8] Z. Zhang, X. Cheng, Z. Lu and D. Gu, "SOC estimation of lithium-ion battery pack considering balancing current," *IEEE Transactions on Power Electronics* 2017.

[6.9] A. Farmann and D.U. Sauer, "A comprehensive review of on-board state-of-available-power prediction techniques for lithium-ion batteries in electric vehicles," *J.Power Sources*, vol. 329, pp. 123-137, 2016.

[6.10] C. Chen, R. Xiong and W. Shen, "A lithium-ion battery-in-the-loop approach to test and validate multi-scale dual H infinity filters for state of charge and capacity estimation," *IEEE Transactions on Power Electronics* 2017.

[6.11] W. Waag, S. Käbitz, and D. U. Sauer, "Experimental investigation of the lithium-ion battery impedance characteristic at various conditions and aging states and its influence on the application," *Appl. Energy*, vol. 102, pp. 885-897, 2013.

[6.12] J. Jiang, S. Liu, Z. Ma, L. Y. Wang, and K. Wu, "Butler-Volmer equation-based model and its implementation on state of power prediction of high-power lithium titanate batteries considering temperature effects," *Energy*, vol. 117, pp. 58-72, 2016.

[6.13] C. Burgos-Mellado, M.E. Orchard, M. Kazerani, R. Cárdenas and D. Sáez, "Particle-filtering-based estimation of maximum available power state in lithium-ion batteries," *Appl.Energy*, vol. 161, pp. 349-363, 2016.

[6.14] F. Zheng, J. Jiang, B. Sun, W. Zhang and M. Pecht, "Temperature dependent power capability estimation of lithium-ion batteries for hybrid electric vehicles," *Energy*, vol. 113, pp. 64-75, 2016.

[6.15] C. Fleischer, W. Waag, Z. Bai and D.U. Sauer, "Adaptive on-line state-of-available-power prediction of lithium-ion batteries," *Journal of Power Electronics*, vol. 13, no. 4, pp. 516-527, 2013.

[6.16] W. Haiying, H. Zhonghua, H. Yu and L. Gechen, "Power state prediction of battery based on BP neural network," in *Strategic Technology (IFOST), 2012 7th International Forum on*, 2012, pp. 1-4.

[6.17] F. Sun, R. Xiong, H. He, W. Li and J.E.E. Aussems, "Model-based dynamic multi-parameter method for peak power estimation of lithium–ion batteries," *Appl.Energy*, vol. 96, pp. 378-386, 2012.

[6.18] W. Zhang, W. Shi and Z. Ma, "Adaptive unscented kalman filter based state of energy and power capability estimation approach for lithium-ion battery," *J.Power Sources*, vol. 289, pp. 50-62, 2015.

[6.19] X. Hu, R. Xiong and B. Egardt, "Model-based dynamic power assessment of lithium-ion batteries considering different operating conditions," *IEEE Transactions on Industrial Informatics*, vol. 10, no. 3, pp. 1948-1959, 2014.

[6.20] Z. Wei, S. Meng, K.J. Tseng, T.M. Lim, B.H. Soong and M. Skyllas-Kazacos, "An adaptive model for vanadium redox flow battery and its application for online peak power estimation," *J.Power Sources*, vol. 344, pp. 195-207, 2017.

[6.21] J. Jiang, S. Liu, Z. Ma, L.Y. Wang and K. Wu, "Butler-volmer equation-based model and its implementation on state of power prediction of high-power lithium titanate batteries considering temperature effects," *Energy*, vol. 117, pp. 58-72, 2016.

[6.22] L. Zheng, L. Zhang, J. Zhu, G. Wang and J. Jiang, "Co-estimation of state-of-charge, capacity and resistance for lithium-ion batteries based on a high-fidelity electrochemical model," *Appl.Energy*, vol. 180, pp. 424-434, 2016.

[6.23] K. Smith and C. Wang, "Pulse discharge power availability of a lithium-ion hybrid vehicle battery pack," *SAE Technical Paper*, 2005-01-3464, 2005.

[6.24] S. Zhang, K. Xu, and T. Jow, "Electrochemical impedance study on the low temperature of Li-ion batteries," *Electrochim. Acta*, vol. 49, no. 7, pp. 1057-1061, 2004.

[6.25] M. Ecker, J. B. Gerschler, J. Vogel, S. Käbitz, F. Hust, P. Dechent, D. U. Sauer, "Development of a lifetime prediction model for lithium-ion batteries based on extended accelerated aging test data," *J. Power Sources*, vol. 215, pp. 248-257, 2012.

[6.26] Y. Iriyama, T. Kako, C. Yada, T. Abe, and Z. Ogumi, "Charge transfer reaction at the lithium phosphorus oxynitride glass electrolyte/lithium cobalt oxide thin film interface," *Solid State Ionics*, vol. 176, no. 31, pp. 2371-2376, 2005.

[6.27] K. Levenberg, "A method for the solution of certain non-linear problems in least squares," *Q. Appl. Math.*, vol. 2, no. 2, pp. 164-168, 1944.

[6.28] D. W. Marquardt, "An algorithm for least-squares estimation of nonlinear parameters," *J. Soc. Ind. Appl. Math.*, vol. 11, no. 2, pp. 431-441, 1963.

[6.29] J. J. Moré, "The levenberg-marquardt algorithm: Implementation and theory," in *Numerical Analysis*, G. A. Watson, Ed. New York: Springer-Verlag, 1978, pp. 105-116.

[6.30] J. R. Belt, "Battery Test Manual for Plug-in Hybrid Electric Vehicles," Idaho National Laboratory, INL/EXT-07-12536, Dec. 2010.

[6.31] C. Zhang, C. Zhang and S. Sharkh, "Estimation of real-time peak power capability of a traction battery pack used in an HEV," in *Power and Energy Engineering Conference (APPEEC), 2010 Asia-Pacific*, 2010, pp. 1-6.

[6.32] G.L. Plett, "High-performance battery-pack power estimation using a dynamic cell model," *IEEE Transactions on Vehicular Technology*, vol. 53, no. 5, pp. 1586-1593, 2004.

[6.33] Y.S. Meng and M.E. Arroyo-de Dompablo, "First principles computational materials design for energy storage materials in lithium ion batteries," *Energy & Environmental Science*, vol. 2, no. 6, pp. 589-609, 2009.

[6.34] N. Chaturvedi, R. Klein, J. Christensen, J. Ahmed and A. Kojic, "Algorithms for advanced battery-management systems," *Control Systems, IEEE*, vol. 30, no. 3, pp. 49-68, 2010.

[6.35] C. Zou, C. Manzie, D. Nešić and A.G. Kallapur, "Multi-time-scale observer design for state-of-charge and state-of-health of a lithium-ion battery," *J.Power Sources*, vol. 335, pp. 121-130, 2016.

[6.36] S.J. Moura, N.A. Chaturvedi and M. Krstic, "PDE estimation techniques for advanced battery management systems—Part I: SOC estimation," in *American Control Conference (ACC), 2012*, pp. 559-565, 2012.

[6.37] X. Han, M. Ouyang, L. Lu and J. Li, "Simplification of physics-based electrochemical model for lithium ion battery on electric vehicle. part I: Diffusion simplification and single particle model," *J.Power Sources*, vol. 278, pp. 802-813, 2015.

[6.38] X. Hu, D. Cao and B. Egardt, "Condition monitoring in advanced battery management systems: Moving horizon estimation using a reduced electrochemical model," *IEEE/ASME Transactions on Mechatronics* 2017.

[6.39] W. Waag, S. Käbitz and D.U. Sauer, "Experimental investigation of the lithium-ion battery impedance characteristic at various conditions and aging states and its influence on the application," *Appl.Energy*, vol. 102, pp. 885-897, 2013.

[6.40] R. Klein, N.A. Chaturvedi, J. Christensen, J. Ahmed, R. Findeisen and A. Kojic, "Electrochemical model based observer design for a lithium-ion battery," *IEEE Trans.Control Syst.Technol.*, vol. 21, no. 2, pp. 289-301, 2013.

[6.41] K. Smith and C. Wang, "Solid-state diffusion limitations on pulse operation of a lithium ion cell for hybrid electric vehicles," *J.Power Sources*, vol. 161, no. 1, pp. 628-639, 2006.

[6.42] K. Smith and C. Wang, "Power and thermal characterization of a lithium-ion battery pack for hybrid-electric vehicles," *J.Power Sources*, vol. 160, no. 1, pp. 662-673, 2006.

[6.43] F. Zheng, J. Jiang, B. Sun, W. Zhang and M. Pecht, "Temperature dependent power capability estimation of lithium-ion batteries for hybrid electric vehicles," *Energy*, vol. 113, pp. 64-75, 2016.

[6.44] M. Ikeda and M. Aniya, "Bond Strength—Coordination number fluctuation model of viscosity: An alternative model for the vogel-fulcher-tammann equation and an application to bulk metallic glass forming liquids," *Materials*, vol. 3, no. 12, pp. 5246-5262, 2010.

[6.45] L. Zheng, J. Zhu, G. Wang, D. D. Lu and T. He, “Lithium-ion battery instantaneous available power prediction using surface lithium concentration of solid particles in a simplified electrochemical model”, DOI 10.1109/TPEL.2018.2791965, *IEEE Transactions on Power Electronics*.

[6.46] L. Zheng, J. Zhu, G. Wang, D. Lu, P. McLean, and T. He, “Experimental analysis and modeling of temperature dependence of lithium-ion battery direct current resistance for power capability prediction”, in proceedings of *20th International Conference on Electrical Machines and Systems (ICEMS)*, 2017.

CHAPTER 7

CONCLUSIONS AND FUTURE WORKS

7.1 Conclusions

Motivated by the requirements of safe, reliable, and efficient utilization of lithium-ion batteries, this thesis developed novel techniques for battery states of interest estimation, which are capable of determining internal battery status accurately. The main work and contributions of this thesis can be summarized as follows:

- A literature survey on the battery management system (BMS) development and estimation techniques of the state of charge (SOC), state of health (SOH), state of energy (SOE), and state of power (SOP) was presented. The focus for each estimation technique was not to detail its solution, but rather the elaboration of its key idea, strengths, and weaknesses as well as its possibilities of improvements. It is worthwhile to systemically summarize the states estimation techniques in the hope of providing some inspiration for BMS practitioners.

- A novel high-fidelity electrochemical model was adopted to capture a battery's dynamics, and was then simplified and discretized to improve its applicability. Based on the model, the co-estimation algorithm using trinal PI observers was proposed to estimate battery SOC, capacity, and resistance simultaneously. Furthermore, the moving-window ampere-hour counting technique and the iteration-approaching method were incorporated for enhancing the estimation precision. Experimental results showed that promising estimates can be achieved with small errors.

- Another SOC and capacity estimation method was proposed using the incremental capacity analysis (ICA) and differential voltage analysis (DVA). The conventional cell terminal voltage based ICA/DVA approaches were transformed

to the SOC based ICA/DVA methods, which is beneficial in the analysis of the relationships between the incremental capacity (IC)/ differential voltage (DV) values and battery intrinsic states. Three feature points extracted from the IC/DV curves were effectively applied for battery SOC and capacity estimation. To improve the adaptability of the ICA/DVA based SOC estimation, extend Kalman filter and particle filter were served as a state observer in the proposed SOC-DV model-based estimation scheme, respectively. The robustness and feasibility of the proposed approaches were validated for different cells.

- By analyzing the temperature, current rate and battery aging level dependencies of battery maximum available energy and SOE, a relationship between the SOE and SOC was quantified and exhibited good robustness against different influential factors. Therefore, with the credible SOC estimates, the SOE can be easily and accurately estimated by using the relationship. A moving-window energy-integral and average method were then incorporated for accurate battery maximum available energy estimation. The simplicity of the proposed SOE estimation method can effectively avoid heavy computation costs required by conventional model-based SOE estimation methods.

- A battery direct current resistance (DCR) model for quantitatively describing its temperature dependence was proposed and implemented on the battery capability prediction. Based on the analysis of battery test data, the logarithmic DCRs could be approximately expressed as a set of quadratic equations for various ambient temperatures. Experimental results indicated that the proposed approaches can achieve high accuracy for both battery DCR and power capability predictions.

- Another approach for battery power capability prediction was derived from the perspective of physical mechanism-based reactions inside the battery using a physical limit, namely lithium concentration limit, which is different from conventional power prediction methods using macroscopically observed variables such as the cell terminal voltage and current as constrained limits. Quantitative

relationships between battery surface lithium concentration and instantaneous charge and discharge power capabilities were proposed based on the analysis of battery Gibbs power and dissipation power of its internal resistance. The experiments demonstrated the close agreement between the forecasts and experimental data at various cell aging levels and ambient temperature.

The proposed modelling and state estimation methods of lithium-ion batteries in this thesis are pretty general, and therefore are promising to provide valuable insight to the investigations of other types of batteries with various chemistries.

7.2 Future Works

Based on the research progress of this thesis, the potential research work that requires further investigations can be described as follows:

- The physics-based electrochemical model has the ability to describe the dynamic behaviors inside the battery. The knowledge of these behaviors can help determine the real status of the battery during battery charging/discharging processes. It has the potential to develop electrochemical model-based fast charging strategies while maintaining a high healthy level of the battery.

- The primary concern comes from the computation burden of the battery electrochemical model-based methods due to the complicated mathematical structure of the model, although some efforts have been made for the model reduction. It seems unlikely to implement the electrochemical model associated with estimation or control algorithms in the on-board BMSs with limited computational capabilities. One promising solution is to employ the cloud-based BMS with sufficient resources for processing the computing task.

- The developed estimation algorithms focus on an individual cell level. However, as one single battery cell has limited capacity and voltage, it normally needs up to hundreds, even thousands of cells connected in series and parallel in a battery pack

for electric vehicles and energy storage systems to provide sufficient power and energy. Thus, the extension of the proposed methods from a cell level to a pack level would be meaningful for applications, especially under the circumstances of lacking efficient balancing techniques.

- Despite the development of battery state estimation techniques, other features of BMSs such as thermal management and balancing are also crucial for improving the performance of battery utilization. Since temperature has a significant impact on battery characteristics, it is of the essence to develop an efficient thermal management system in order to confine batteries to operate within a desirable temperature range. The battery balancing is indispensable to mitigate the inconsistencies among battery cells for improving the capacity of the battery pack and thus prolonging its service life. Some research work on battery balancing has been done during this thesis project, which is presented in Appendixes B and C, and needs further investigations.

APPENDIX A

DV BASED SOC ESTIMATION ALGORITHMS USING EKF AND PF

A.1 SOC Estimation with EKF

The basic steps of the extended Kalman filter (EKF) algorithm include initialization and update of the prediction and measurement. The detailed implementation processes of the differential voltage (DV) based state of charge (SOC) estimation algorithm using EKF are presented as follows.

(1) Initialization: For $k = 0$, set,

a) Initial estimated state: $x^*_{0|0}$.

b) Initial error covariance: $P_{0|0}$.

c) The covariance of the process noise: Q.

d) The covariance of the measurement noise: R.

(2) Prediction update: For $k = 1, 2, \ldots$, compute,

a) Update the prior estimated state:

$$x^*_{k|k-1} = f\left(x^*_{k-1|k-1}, i_k\right) \tag{A.1}$$

where $x^*_{k|k-1}$ and $x^*_{k-1|k-1}$ denote the priori estimated state at the *k-th* time instant and the posterior estimated state at the *(k-1)-th* time instant, respectively.

b) Update the prior error covariance:

$$P_{k|k-1} = F_{k-1} P_{k-1|k-1} F^T_{k-1} + w_k \tag{A.2}$$

where $P_{k|k-1}$ and $P_{k-1|k-1}$ denote the prior error covariance of the state estimation at the *k-th* time instant and the posterior error covariance of the state estimation at the *(k-1)-th* time instant, respectively, and F_{k-1} is defined as the state transition Jacobian matrices governed by

$$F_{k-1} = \left.\frac{\partial f}{\partial x}\right|_{x^*_{k-1|k-1}} \tag{A.3}$$

(3) Measurement update: For k = 1, 2, …, compute,

a) Calculate innovation covariance:

$$S_k = H_k P_{k|k-1} H_k^T + v_k \tag{A.4}$$

where H_k denotes the observation Jacobians matrices given by

$$H_k = \left.\frac{\partial h}{\partial x}\right|_{x^*_{k|k-1}} \tag{A.5}$$

b) Calculate the Kalman gain:

$$K_k = H_k P_{k|k-1} S_k^{-1} \tag{A.6}$$

c) Calculate error innovation:

$$e_k^* = y_k - y_k^* \tag{A.7}$$

d) Update the posterior error covariance:

$$P_{k|k} = \left(1 - K_k H_k\right) P_{k|k-1} \tag{A.8}$$

e) Update the posterior estimated state:

$$x_{k|k}^* = x_{k|k-1}^* + K_k e_k^* \tag{A.9}$$

A.2 SOC Estimation with PF

The primary steps of particle filter (PF) algorithm also include initialization and update of the prediction and measurement, which are based on three fundamental operations involving particle propagation, importance weight computation, and resampling. Detailed implementation processes of the DV based SOC estimation algorithm using PF are presented as follows.

(1) Initialization: For $k = 0$, set,

a) The number of created particles: N_p.

b) The covariance of the process noise: Q.

c) The covariance of the measurement noise: R.

d) Initial values of all particles: $x_{0,j}^{*}$ ($j = 1, 2, \ldots, N_p$).

e) Initial importance weights for all particles:

$$w_{0,j}^{*} = 1 / N_p \tag{A.10}$$

(2) Prediction update: For $k = 1, 2, \ldots$, compute,

Update the values of particles:

$$x_{k,j}^{*} = f\left(x_{k-1,j}^{*}, i_k\right) + w_k \tag{A.11}$$

where $x_{k,j}^{*}$ denotes the value of the j-th particle at the k-*th* time instant.

(3) Measurement update: For $k = 1, 2, \ldots$, compute,

a) Update error innovation:

$$e_{k,j}^{*} = y_k - y_{k,j}^{*} \tag{A.12}$$

where $e^*_{k,j}$ and $y^*_{k,j}$ denote the error innovation and calculation value of the *j*-th particle at the *k-th* time instant, respectively, and y_k is the measurement value at the *k-th* time instant.

b) Calculate the likelihood for each particle

$$L_{k,j} = 1/\sqrt{2\pi R}\exp\left[-\left(e^*_{k,j}\right)^2 \Big/ \left(2R\right)\right] \tag{A.13}$$

where $L_{k,j}$ denotes the likelihood of the *j*-th particle at the *k-th* time instant.

c) Calculate the importance weight for each particle:

$$iw_{k,j} = iw^*_{k-1,j} L_{k,j} \tag{A.14}$$

where $iw_{k,j}$ denotes the importance weight of the *j*-th particle at the *k-th* time instant, and $iw^*_{k-1,j}$ denotes the normalized importance weight of the *j*-th particle at the *(k-1)-th* time instant.

d) Normalize the importance weights:

$$iw^*_{k,j} = iw_{k,j} \Big/ \left(\sum_{j=1}^{N_p} iw_{k,j}\right) \tag{A.15}$$

e) Evaluate the effective number of particles N_{eff} to judge the necessity of the resampling by

$$N_{eff} = \left(\sum_{j=1}^{N_p}\left(iw^*_{k,j}\right)^2\right)^{-1} \tag{A.16}$$

The typical resampling threshold is $0.85N_p$ [A.1]. If $N_{eff} \geqslant 0.85N_p$, it is not necessary to resample the particles. Otherwise, the program executes the following step (f).

f) Resample the particles with a systematic resampling technique.

The core idea of systematic resampling is to generate N_p random numbers, u, with exactly the same interval and use them to select particles. The random numbers are drawn by

$$u(1):\ U\left(0,1/N_p\right] \ \text{ with } \ u(j)=u(1)+(j-1)/N_p \tag{A.17}$$

where $j = 2, 3, \ldots, N_p$.

Compared with other basic resampling techniques such as multinomial resampling, stratified resampling and residual resampling, the systematic resampling method is more favorable in terms of both resampling quality and computational efficiency [A.1], [A.2], and thus employed in the present study. Pseudocodes of the systematic resampling technique are shown in Table A.1, where *sum_iw* represents the cumulative sum of the importance weight of the particles; *x* and *x_new* denote the previous and new particles, respectively. The cumulative sum of the importance weight of the particles is applied to compare with the generated random number to select the top particle [A.2].

g) Compute the estimated state:

$$x_k^* = \sum_{j=1}^{N_p} x_{k,j}^* iw_{k,j}^* \tag{A.18}$$

Table A.1. Pseudocodes of the systematic resampling technique.

Pseudocodes: Systematic resampling
u = linspace(0, 1-1/N_p, N_p) + rand/N_p
for j = 1 : N_p
sum_iw = 0
for i = 1 : N_p
$sum\_iw = sum\_iw + iw(i)$
if $sum\_iw >= u(j)$
$x\_new(j) = x(i)$
break
end
end
end

References

[A.1] J.D. Hol, T.B. Schon and F. Gustafsson, "On resampling algorithms for particle filters," in *Nonlinear Statistical Signal Processing Workshop, 2006 IEEE*, 2006, pp. 79-82.

[A.2] T. Li, T.P. Sattar and D. Tang, "A fast resampling scheme for particle filters," in *Signal Processing (CIWSP 2013), 2013 Constantinides International Workshop on*, 2013, pp. 1-4.

APPENDIX B

A COMPARATIVE STUDY OF BATTERY BALANCING STRATEGIES FOR DIFFERENT BATTERY OPERATION PROCESSES

B.1 Introduction

As one single battery cell has limited capacity and voltage, it normally needs up to hundreds, even thousands of single cells connected in series and parallel for electrified vehicles and energy storage systems to provide sufficient power and energy. In such a battery pack, inevitable cell inconsistencies are concerned due to two categories: the inconsistent manufacturing process such as different internal impedance and self-discharge rate, and the inhomogeneous operating environment such as various ambient temperature [B.1], [B.2]. To improve cell consistencies, increase battery pack capacity and prolong battery pack service life, battery cell balancing techniques are essentially required in battery management systems (BMSs).

Among the literature, most papers focus on battery balancing circuit topologies [B.2]-[B.7] and balancing algorithms [B.1], [B.5]-[B.14]. The battery balancing circuit topologies reported in [B.2]-[B.7] mainly include resistor bleeding (passive balance), cell to cell, cell to pack, pack to cell and cell to pack to cell, and their advantages and disadvantages presented in detail. According to the literature [1, 5-14], the battery balancing algorithms can be mainly divided into two categories: voltage-based balancing algorithms and SOC-based balancing algorithms. The voltage-based balancing algorithm which targets the consistent battery cell terminal voltages is widely used in research and industry [5-10]. The SOC-based balancing algorithm which targets the consistent battery cell SOCs requires accurate cell SOC estimation [B.1], [B.10]-[B.14]. While their pros

A substantial proportion of this appendix has been published as an article [B.16] in the proceedings of 2016 *IEEE Transportation Electrification Conference and Expo* (*ITEC*).

and cons are discussed in the literature, unfortunately, there are few studies that compare these balancing circuits incorporating the balancing algorithms in a comprehensive and systematical manner.

Regardless of balancing circuits and algorithms, when to perform balancing plays a vital role in balancing performance. Performing balancing during different battery operation processes, such as constant current charging processes, dynamic current discharging processes and rest time, may lead to various balancing effects. Therefore, it is essential to carry out a comparative study of battery balancing strategies incorporating balancing circuits and algorithms for different battery operation processes.

B.2 Battery Balancing Strategies

According to the balancing current used for battery cell charging or discharging, we classify battery balancing circuits into four categories: passive discharge balance, active discharge balance, charge balance, and charge-discharge (namely bidirectional) balance. Regardless of balancing circuits, effective balancing algorithms are highly required to maximize balancing effects. It has been reported that the voltage-based balancing algorithm cannot achieve desirable balancing results because a small voltage variation may lead to a large capacity inconsistency, especially for some kinds of batteries with a flat charge/discharge voltage plateau [B.1]. The SOC-based algorithm can really reflect the battery capacity level and therefore it was employed for this study. Combining the classified circuit categories with the SOC-based balancing algorithm, we can obtain four balancing strategies: SOC-based passive discharge balance (PDB), SOC-based active discharge balance (ADB), SOC-based charge balance (CB), and SOC-based charge-discharge balance (CDB).

B.3 Balancing Results and Discussions

In order to investigate the performance of different balancing strategies applied for various battery operation processes, eight lithium-ion cell models connected in series with

different available capacities and SOCs shown in Fig. B.1 were used for balancing experimental simulation. The charge/discharge balance current was set to 4 A while the balance referenced SOC was set to the average SOC with a band of +/-1%. The efficiency of the balancer was set to 85%, which means that 15% of balance energy will be dissipative during balancing.

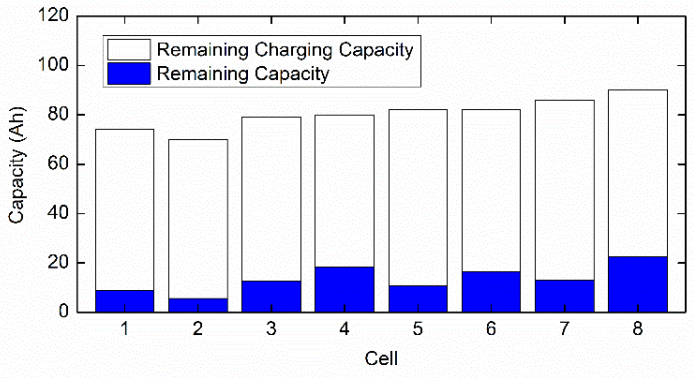

Fig. B.1 Initial cell remaining capacities and remaining charging capacity.

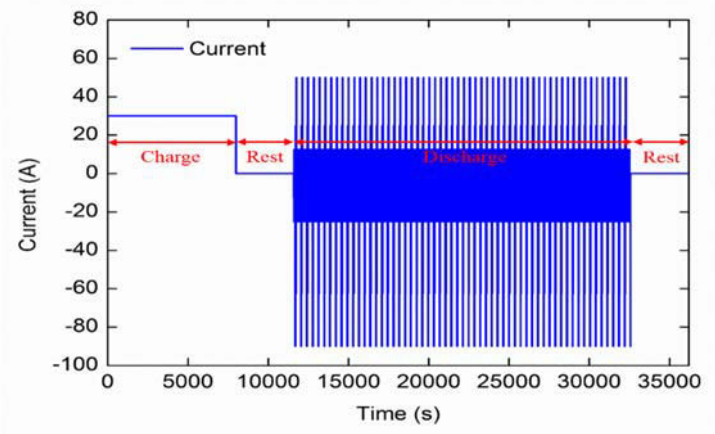

Fig. B.2 Battery operation processes.

The battery operation processes usually include charge process, rest time after charge, discharge process, and rest time after discharge. To simulate the charge and discharge processes of batteries used in electric vehicles, a constant current was used for battery charging and dynamic stress test (DST) [15] profiles were used for battery discharging, as shown in Fig. B.2. Each battery operation cycle began with a constant current at C/3 to charge to the battery pack until one of the battery cells reached the upper limit voltage

of 4.2 V. Then there was a rest for 1 h followed by DST profiles to discharge the battery pack until one of the battery cells reached the lower limit voltage 3 V. Subsequently, it followed a rest for 1 h and then repeated the operation cycle. The battery pack maximum available capacity was calculated by ampere-hour counting during the whole discharge process. Five battery operation cycles were used for evaluating the balancing results including battery pack maximum available capacity, SOC variances at the end of discharge (EOD) and the end of charge (EOC). Without balance, the battery pack maximum available capacity is 65.06 Ah which is less than the minimum cell capacity (cell 2 charged in constant current regime) of 66.63 Ah, while the maximum SOC variance at EOC is 13.05% and the maximum SOC variance at EOD is 18.8%. The mean battery cell capacity (charged in constant current regime) is 77.16 Ah.

When balancing is performed during battery discharge processes, the balancing results are shown in Fig. B.3. In Fig. B.3(a), the ADB, CB and CDB strategies are able to increase the battery pack capacity, and the final battery pack capacities are a little larger than the capacity without balance. However, the balanced pack capacities were still less than the minimum cell capacity. It is noted that the PDB method caused a counterproductive balancing result of the battery pack capacity being less than the value without balance. This is because the PDB method is an energy dissipation method and the dissipative energy could not supply from elsewhere. It can be seen that different balancing strategies were able to make an improvement in decreasing SOC variances at EOD compared with the result without balance as shown in Fig. B.3(b). On the contrary, the SOC variances at EOC were increased, which are larger than the value without balance as shown in Fig. B.3(c).

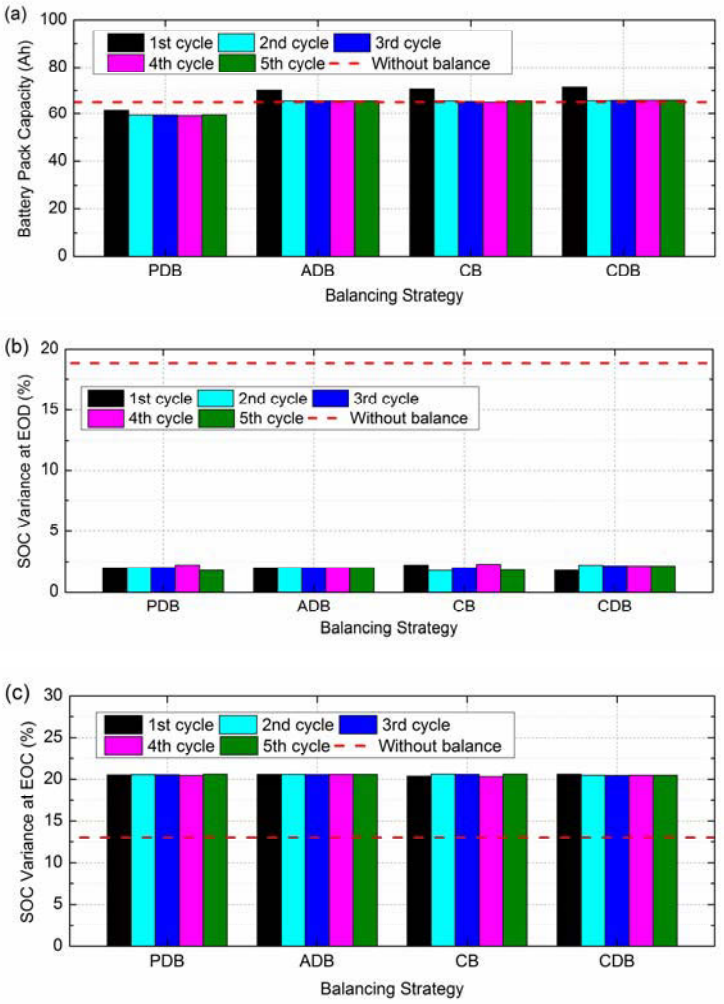

Fig. B.3 Battery balancing results when balancing is performed during battery discharge processes, where (a) battery pack capacity, (b) SOC variance at EOD and (c) SOC variance at EOC.

Fig. B.4 shows the balancing results when balancing is performed during battery charge processes. In Fig. B.4(a), four balancing strategies were able to make an improvement on the battery pack capacities, which are about equal to 67.00 Ah. As shown in Fig. B.4(c), the SOC variances at EOC were shortened to a small level compared with the value without balance. However, SOC variances at EOD presented inconsistent change. For the PDB, ADB and CB strategies, there was a little decrease on the SOC variances at EOD. But for the CDB strategy, the SOC variance at EOD was increased to be larger than the value without balance.

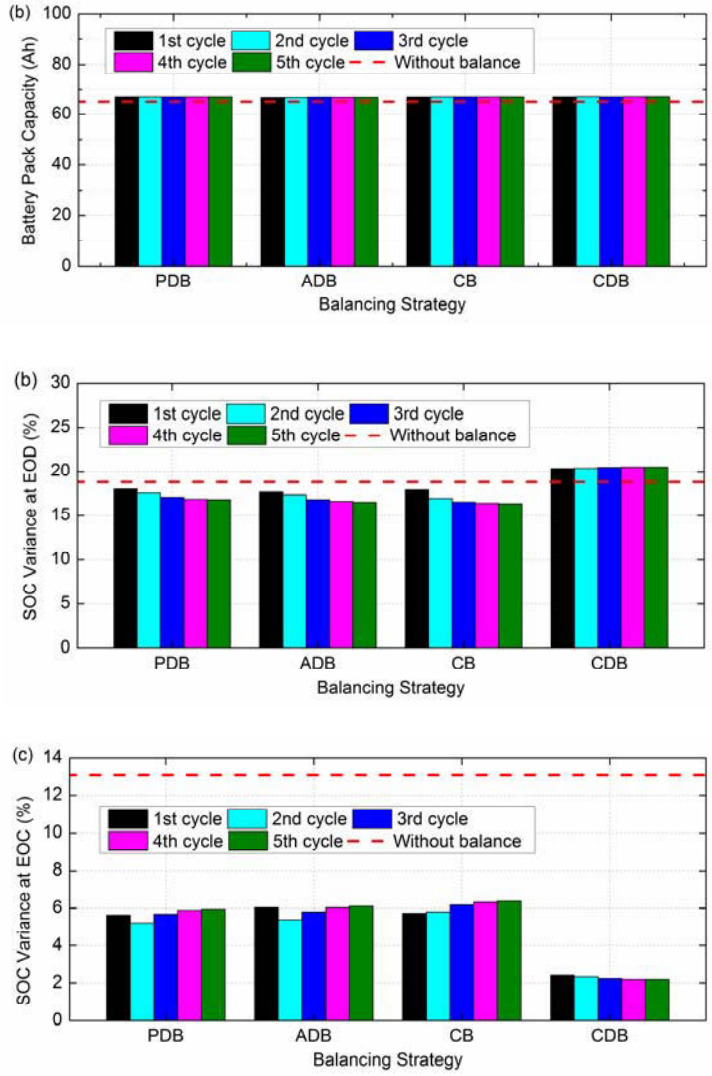

Fig. B.4 Battery balancing results when balancing is performed during battery charge processes, where (a) battery pack capacity, (b) SOC variance at EOD and (c) SOC variance at EOC.

When balancing is performed during battery rest time after discharge, the battery balancing results are shown in Fig. B.5. The battery pack capacities for four different balancing strategies depicted in Fig. B.5(a) showed a shade of increment in comparison with the value without balance. The SOC variances at EOD appeared as a gradual decline trend as shown in Fig. B.5(b) and in the final cycle, the SOC variances can be limited to a small value. However, the SOC variances at EOC shown in Fig. B.5(c) gradually rose with the cycle time and finally achieved a high level. Moreover, the balancing results of

the fifth cycle shown in Fig. B.5 are similar to the results when balancing is performed during battery discharge processes as shown in Fig. B.3. This is because the four above-mentioned balancing strategies are able to limit the SOC variance at EOD in a balance referenced SOC band when balancing is performed during battery discharge process and rest time after discharge. However, it would have a counterproductive effect on the variance at EOC and increase the value of the variance at EOC.

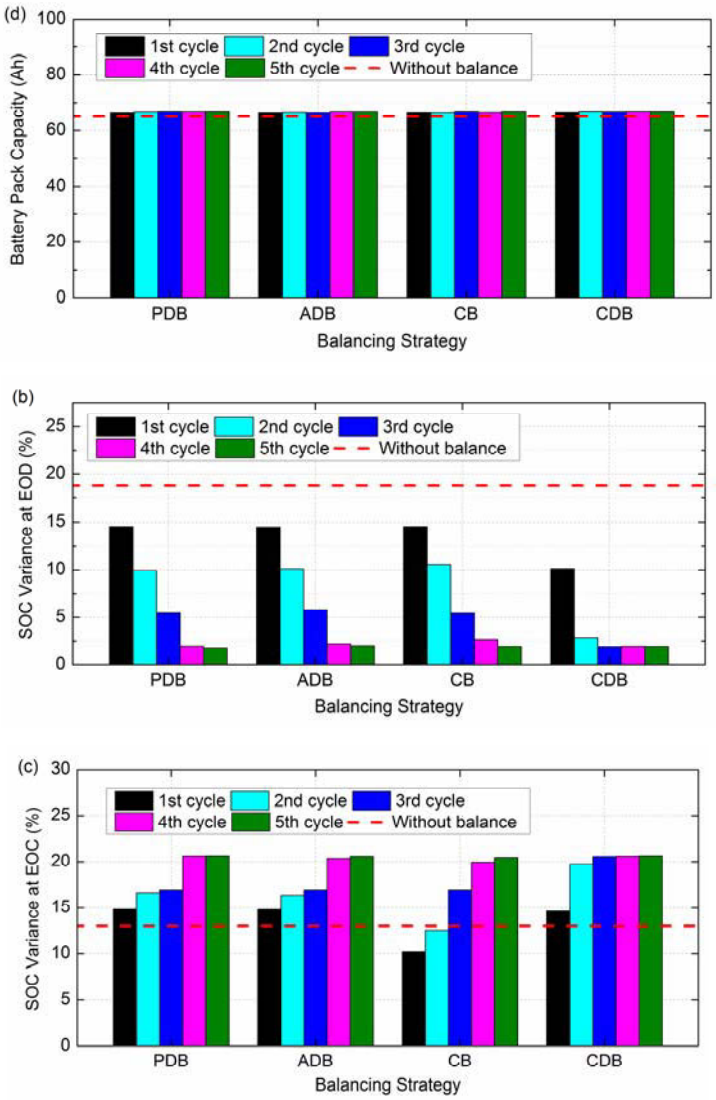

Fig. B.5 Battery balancing results when balancing is performed during battery rest time after discharge, where (a) battery pack capacity, (b) SOC variance at EOD and (c) SOC variance at EOC.

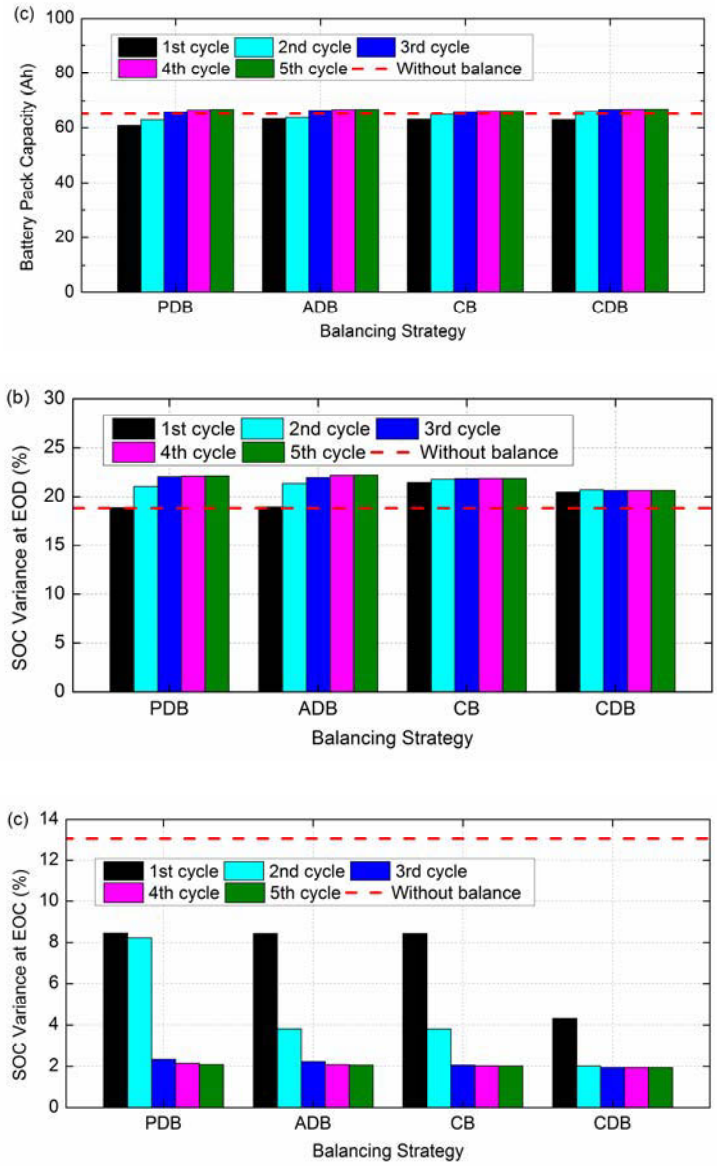

Fig. B.6 Battery balancing results when balancing performed during battery rest time after charge, where (a) battery pack capacity, (b) SOC variance at EOD and (c) SOC variance at EOC.

The balancing results when balancing is performed during battery rest time after charge are drawn in Fig. B.6, where battery pack maximum available capacities of the final cycle can be approximately increased to 66.86 Ah which is a little larger than the battery pack capacity value without balance. SOC variances at EOD and EOC shown in Fig. B.6(b) and B.6(c), respectively, presented exactly opposite results to the balancing results when balancing is performed during battery rest time after charge shown in Fig. B.5(b) and Fig.

B.5(c). It can be seen that in Fig. B.6(b), the SOC variances at EOD dropped gradually and reached a small level. However, the SOC variances at EOD finally increased to become larger than the value without balance.

From the above results, it can be summarized that when balancing performed during one kind of battery charge process, rest time after charge, and rest time after discharge, four above-mentioned balancing strategies are able to increase the battery pack capacity to be approximately equal to the minimum cell capacity. During the discharge processes, the PDB method would make a counterproductive balance result which decreases the battery pack capacity, while other balancing strategies can make an improvement in the battery pack capacity but cannot reach the minimum cell capacity.

In addition to comparing how much battery pack capacity can be increased, other important factors are SOC variances at EOC and EOD. It would decrease the SOC variance at EOD when balancing is performed during battery discharge processes and rest time after discharge, and therefore the battery pack is able to discharge more capacity. On the contrary, the SOC variance at EOC would decrease to a small value when balancing is performed during battery charge processes and rest time after charge, and therefore the battery pack can be charged to a greater capacity. The above balanced battery pack capacity can be maximally increased to close to the minimum cell capacity, but it is still much less than the mean battery cell capacity. To maximally utilize the battery pack capacity, namely the mean battery cell capacity, it should fully charge and discharge each cell of the battery pack. In other words, the SOC variances at both EOC and EOD should be maximally decreased to a small level, and therefore it would maximally increase the battery pack maximum available capacity. Thus, the battery balancing should be performed during both battery charge and discharge processes.

Fig. B.7 shows the battery balancing results when balancing is performed during both battery charge and discharge processes. In Fig. B.7(a), the ADB, CB and CDB strategies are able to increase the battery pack capacity to a high value which is more than the minimum cell capacity. Especially in regards to the CDB strategy, the battery pack

capacity can be increased to 75.30 Ah, which improves 15.74% compared with the capacity without balance (65.05 Ah) and is very close to the mean battery cell capacity.

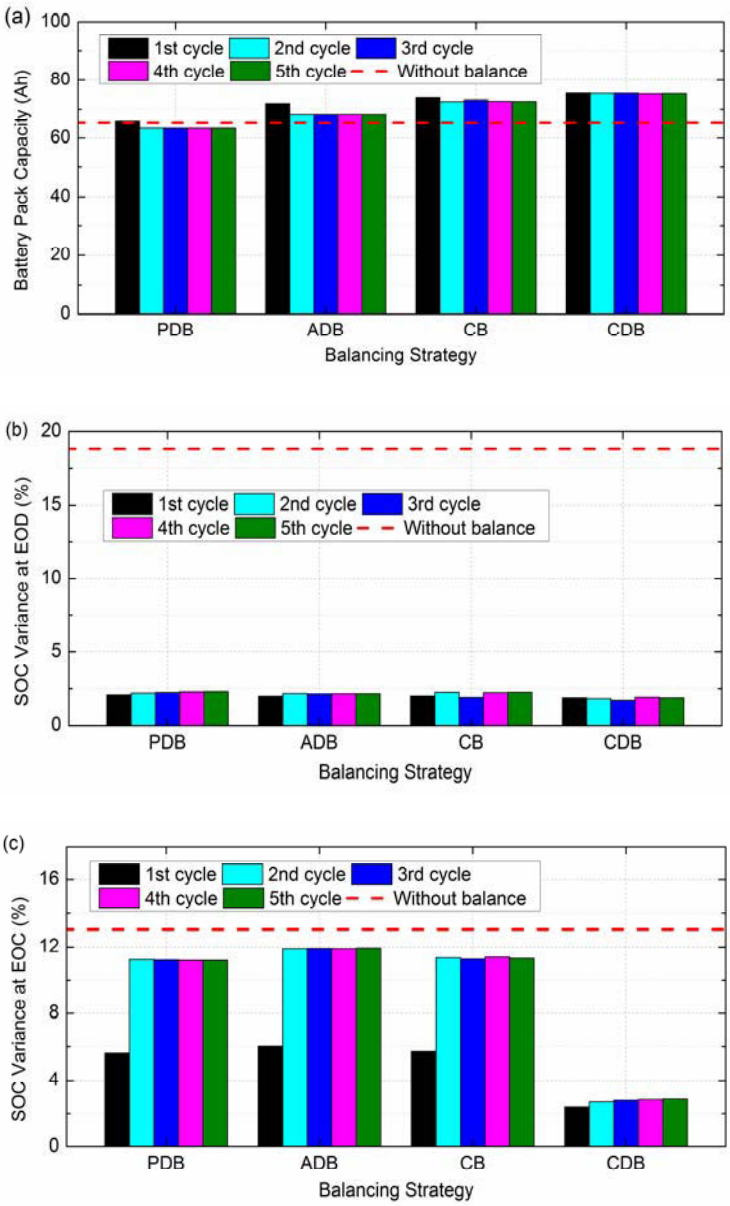

Fig. B.7 Battery balancing results when balancing performed during both battery charge and discharge processes, where (a) battery pack capacity, (b) SOC variance at EOD and (c) SOC variance at EOC.

It is noted that for the CDB strategy, SOC variances at EOC and EOD were able to be significantly dropped to a small level, and therefore the battery capacity of the CDB strategy is larger than other strategies. As for the PDB strategy, although SOC variances

at both EOD and EOC can be declined, there was a large amount of energy consumption due to resistor bleeding during the battery discharge processes, which caused the battery pack capacity decrement.

Summary

Battery balancing techniques are essentially required in BMSs for increasing battery pack capacity and prolonging its service life. Regardless of balancing circuits and algorithms, when to perform balancing plays a vital role in balancing performance. Performing balancing during different battery operation processes would lead to various balancing effects. In this work, four battery balancing strategies including PDB, ADB, CB and CDB were developed from the state-of-the-art balancing circuits and balancing algorithms for simulation experiments. During one single kind of battery charge processes, rest time after charge and rest time after discharge, the four above-mentioned balancing strategies can increase the battery pack capacity to be close to the minimum cell capacity. During the battery discharge processes, the PDB strategy would make a counterproductive balance result which decreases the battery pack capacity, while other balancing strategies can make an improvement in the battery pack capacity but cannot reach the minimum cell capacity. To maximally utilize the battery pack capacity, the SOC variances at both EOC and EOD should be maximally decreased to a small value, and therefore it would maximally increase the battery pack capacity. Performing balancing during both battery charge and discharge processes with the ADB, CB and CDB strategies can effectively increase the battery pack capacity to a higher level, which can be approximately close to the mean cell capacity. Actual battery balancing experiments and energy consumption analysis during battery balancing will be investigated in future work.

References

[B.1] Y. Zheng, M. Ouyang, L. Lu, J. Li, X. Han and L. Xu, "On-line equalization for lithium-ion battery packs based on charging cell voltages: Part 1. Equalization based on remaining charging capacity estimation," *J. Power Sources*, vol. 247, pp. 676-686, 2014.

[B.2] J. Gallardo-Lozano, E. Romero-Cadaval, M. I. Milanes-Montero and M. A. Guerrero-Martinez, "Battery equalization active methods," *J. Power Sources*, vol. 246, pp. 934-949, 2014.

[B.3] F. Baronti, R. Roncella and R. Saletti, "Performance comparison of active balancing techniques for lithium-ion batteries," *J. Power Sources*, vol. 267, pp. 603-609, 2014.

[B.4] M. Caspar, T. Eiler and S. Hohmann, "Comparison of active battery balancing systems," in *Vehicle Power and Propulsion Conference (VPPC), 2014 IEEE*, 2014, pp. 1-8.

[B.5] S. Li; C. C. Mi and M. Zhang, "A high-efficiency active battery-balancing circuit using multiwinding transformer," *IEEE Transactions on Industry Applications*, vol. 49 pp. 198-207, 2013.

[B.6] M. Daowd, N. Omar, P. Van Den Bossche and J. Van Mierlo, "Passive and active battery balancing comparison based on MATLAB simulation." in *Vehicle Power and Propulsion Conference (VPPC), 2011 IEEE*, 2011, pp. 1-7.

[B.7] F. Mestrallet, L. Kerachev, J. Crebier and A. Collet, "Multiphase interleaved converter for lithium battery active balancing," *IEEE Transactions On Power Electronics*, vol. 29, pp. 2874-2881, 2014.

[B.8] C. H. Kim, M. Y. Kim; H. S. Park and G. W. Moon, "A modularized two-stage charge equalizer with cell selection switches for series-connected lithium-ion battery string in an HEV," *IEEE Transactions On Power Electronics*, vol. 27, pp. 3764-3774, 2012.

[B.9] Y. S. Lee and M. W. Cheng, "Intelligent control battery equalization for series connected lithium-ion battery strings," *IEEE Transactions on Industrial Electronics*, vol. 52, pp. 1297-1307, 2005.

[B.10] M. Daowd, N. Omar, P. Van Den Bossche and J. Van Mierlo, "A review of passive and active battery balancing based on MATLAB/Simulink," *J. Int. Rev. Electr. Eng*, vol. 6, pp. 2974-2989, 2011.

[B.11] W. Huang and J. A. Abu Qahouq. "Energy sharing control scheme for state-of-charge balancing of distributed battery energy storage system," *IEEE Transactions on Industrial Electronics*, vol. 62, pp. 2764-2776, 2015.

[B.12] R. Ugle, Y. Li and A. Dhingra, "Equalization integrated online monitoring of health map and worthiness of replacement for battery pack of electric vehicles." *J. Power Sources*, vol. 223, pp. 293-305, 2013.

[B.13] J. Gallardo-Lozano, E. Romero-Cadaval, M. I. Milanes-Montero and M. A. Guerrero-Martinez, "A novel active battery equalization control with on-line unhealthy cell detection and cell change decision," *J. Power Sources*, vol. 299, pp. 356-370, 2015.

[B.14] Y. Wang, C. Zhang, Z. Chen, J. Xie and X. Zhang, "A novel active equalization method for lithium-ion batteries in electric vehicles," *Appl. Energy*, vol. 145, pp. 36-42, 2015.

[B.15] United States Advanced Battery Consortium, "Electric vehicle battery test procedures manual." USABC, Jan 1996.

[B.16] L. Zheng, J. Zhu, and G. Wang, "A Comparative Study of Battery Balancing Strategies for Different Battery Operation Processes", 2016 *IEEE Transportation Electrification Conference and Expo* (*ITEC*), pp. 1-5, 27-29 June 2016, Dearborn, MI, USA.

APPENDIX C

MODEL PREDICTIVE CONTROL BASED BALANCING STRATEGY FOR SERIES-CONNECTED BATTERY PACKS

C.1 Introduction

Due to the non-uniform manufacturing processes and inhomogeneous operating environment, inconsistent battery cell internal conditions are inevitable in a series-connected lithium-ion battery pack, which lead to the insufficient use of the battery pack and even cause safety issues [C.1], [C.2]. Therefore, renewable energy storage systems and electric vehicles with lithium-ion batteries significantly require balancing techniques for making the full use of battery packs and improving the safety of battery operations.

Most of the reported balancing techniques focus on the research of balancing circuits, and remarkable results have been achieved on improving the performance of balancing circuits [C.3]-[C.10]. Except for balancing circuits, the balancing strategy is also essential in determining the balancing performance. However, compared with balancing circuits, there are fewer studies reporting the research on the balancing strategy. It is well recognized that the voltage based balancing strategies are not applicable for some kinds of batteries with flat voltage plateau [C.1], [C.10]. Alternatively, the state of charge (SOC) based balancing strategies targeted at converging each cell's SOC to a band of their average value, which can achieve desirable balancing results in [C.2], [C.9]-[C.11], especially for fresh battery packs with relatively uniform cell capacities.

However, the balancing strategy for aged battery packs is more challenging than that for new battery packs. It is because that aged battery packs usually suffer from not only non-

A substantial proportion of this appendix has been published as an article [C.13] in the proceedings of 2017 19*th European Conference on Power Electronics and Applications, EPE'*17 *ECCE Europe*.

uniform cell SOCs and voltages but also non-uniform cell capacities. This results in over-equalization which means that a cell that was supposed to be charged (discharged) balancing was in fact discharged (charged) for a while by its equalizer [C.1] during the battery balancing processes, thus increasing balancing energy consumption. Accordingly, it is indispensable to develop balancing strategies for aged battery packs.

In this work, a novel balancing strategy based on the model predictive control (MPC) is proposed for series-connected battery packs, especially for aged battery packs. Aiming at eliminating over-equalization and fully charging a battery pack, the required average balancing current and the predicted balancing current for each cell can be computed in advance. A cost function related to these two currents is employed to select the optimal operation mode for each equalizer. The simulation results of an aged battery pack with eight cells validate the effectiveness of the proposed method.

C.2 Battery Balancing System

Bidirectional equalizers can concurrently charge and discharge individual cells and have been proved to be more efficient in improving battery pack capacity than other types of equalizers in [C.10]. Therefore, bidirectional equalizers are deployed to each cell, and the balancing system is shown in Fig. C.1.

In the balancing system, each cell equalizer can be operated in three modes including cell charging balancing mode, cell discharging balancing mode, and idle mode by controlling the driving signals of the primary and secondary switches. The cell charging balancing mode happens when the equalizer transfers the pack energy to the cell, while the cell discharging balancing mode operates when the equalizer transfers the cell energy to the pack. The idle mode means that the equalizer is currently not in operation. The switch signals are generated by balancing strategies, which are elaborated in the following sections.

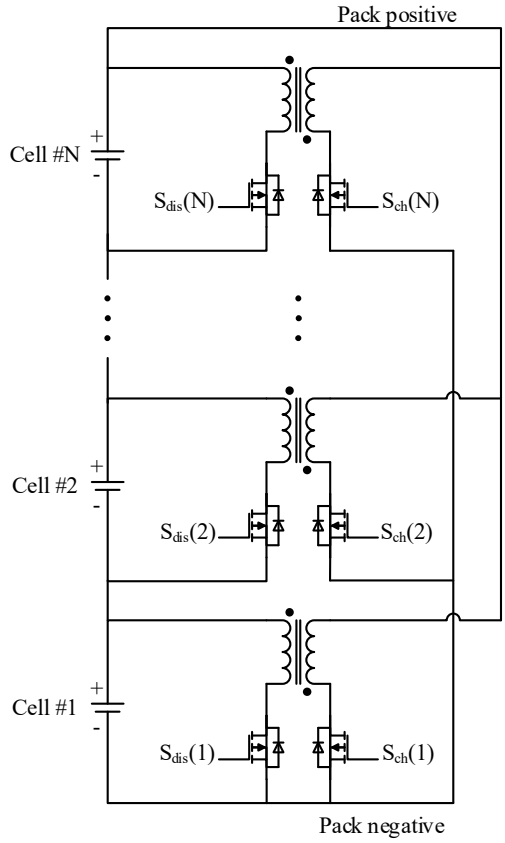

Fig. C.1 Schematic of battery balancing system.

C.3 Battery Balancing Strategies

C.3.1 Conventional average SOC strategy

The working principle of the conventional average SOC balancing strategy is to compare the SOC of each cell with the average SOC of the battery pack. A positive balancing threshold and a negative value are usually applied to the average SOC to compose a balancing band. If a cell's SOC is higher than the balancing band, the cell needs to be discharged until the SOC falls within the balancing band. On the contrary, if a cell's SOC is lower than the balancing band, the cell needs charging balancing until the SOC increases to the balancing band.

Since cell capacities are usually non-uniform in aged battery packs, a cell with a low capacity tends to have a higher SOC when the battery pack is near fully charged state, but

it has a lower SOC when the pack is near fully discharged state. With the average SOC strategy, over-equalization may occur during battery balancing processes due to the non-uniform cell capacities, thus increasing balancing energy consumption.

C.3.2 Proposed MPC based strategy

To eliminate over-equalization during battery balancing process, an MPC based balancing strategy is proposed in this study. The remaining charging capacity of each cell is determined by

$$Q_{Cell\_remch}(i) = \left(1 - SOC(i)\right) Q_{Cell}(i) \tag{C.1}$$

where $Q_{Cell\_remch}(i)$ denotes the remaining charging capacity of the ith cell, $SOC(i)$ the SOC value of the ith cell, and $Q_{Cell}(i)$ the actual capacity of the ith cell when it is fully charged.

The average remaining charging capacity of the battery string is governed by

$$Q_{Ave\_remch} = \left(\sum_{i=1}^{N} Q_{Cell\_remch}(i) \right) \Big/ N \tag{C.2}$$

where Q_{Ave_remch} denotes the average remaining charging capacity of the battery pack, and N represents the number of the series-connected cells.

It is worth mentioning that the balancing system could not offer energy to alleviate the average remaining charging capacity during balancing processes. The average remaining charging capacity is gradually reduced by external charging current before one of the cells reaches to its upper limited voltage. But during the battery charging process, the balancing system should have the ability to redistribute the imbalance energy for achieving the objective of fully charging the battery pack.

Thus, for fully charging the battery pack, the charging time can be approximately computed by

$$t = Q_{Ave\_remch} / I_{ch} \tag{C.3}$$

where t denotes the battery charging time, and I_{ch} denotes the charging current of the battery pack.

During the battery charging process, the average balancing current (positive for charging and negative for discharging) for each cell is expected as

$$I_{bc\_ref}(i) = \left(Q_{Cell\_remch}(i) - Q_{Ave\_remch}\right) / t \tag{C.4}$$

where $I_{bc\_ref}(i)$ denotes the average balancing current of the ith cell during the battery charging process, which is considered as the referenced balancing current in the proposed MPC based strategy.

Three operation modes of cell equalizers including cell charging balancing mode, cell discharging balancing mode, and idle mode can be expressed as (C.5) to (C.7), respectively.

$$\left[S_{ch}(i) \quad S_{dis}(i)\right] = \left[1 \quad 0\right] \tag{C.5}$$

$$\left[S_{ch}(i) \quad S_{dis}(i)\right] = \left[0 \quad 1\right] \tag{C.6}$$

$$\left[S_{ch}(i) \quad S_{dis}(i)\right] = \left[0 \quad 0\right] \tag{C.7}$$

where $S_{ch}(i)$ and $S_{dis}(i)$ denote the states of the charging and discharging modes of the ith cell equalizer, respectively. It is noted that $S_{ch}(i)$ and $S_{dis}(i)$ cannot be equal to 1 simultaneously due to the fact that each cell equalizer cannot be concurrently operated in both the charging and discharging modes.

In this work, the operation efficiency of each equalizer is assumed to be of the same value. If one cell equalizer is in the charging balancing mode, the absorbed or drawn balancing current of each cell can be described as

$$\mathbf{I_{bc\_ch}} = I_{e\_ch}\begin{bmatrix} 1-\dfrac{U_{Cell}(1)}{U_{Pack}\eta_{ch}} & -\dfrac{U_{Cell}(2)}{U_{Pack}\eta_{ch}} & \text{L} & -\dfrac{U_{Cell}(N)}{U_{Pack}\eta_{ch}} \\ -\dfrac{U_{Cell}(1)}{U_{Pack}\eta_{ch}} & 1-\dfrac{U_{Cell}(2)}{U_{Pack}\eta_{ch}} & \text{L} & -\dfrac{U_{Cell}(N)}{U_{Pack}\eta_{ch}} \\ \text{M} & \text{M} & \text{O} & \text{M} \\ -\dfrac{U_{Cell}(1)}{U_{Pack}\eta_{ch}} & -\dfrac{U_{Cell}(2)}{U_{Pack}\eta_{ch}} & \text{L} & 1-\dfrac{U_{Cell}(N)}{U_{Pack}\eta_{ch}} \end{bmatrix} \tag{C.8}$$

where $U_{Cell}(i)$ (i = 1, 2, …, N) denotes the terminal voltage of the ith cell, U_{Pack} the total voltage of the series-connected cells, η_{ch} the charging balancing efficiency, and I_{e_ch} the cell charging balancing current of each equalizer.

Likewise, if one cell equalizer is in the discharging balancing mode, the absorbed or drawn balancing current of each cell is determined by

$$\mathbf{I_{bc\_dis}} = I_{e\_dis}\begin{bmatrix} \dfrac{\eta_{dis}U_{Cell}(1)}{U_{Pack}}-1 & \dfrac{\eta_{dis}U_{Cell}(2)}{U_{Pack}} & \text{L} & \dfrac{\eta_{dis}U_{Cell}(N)}{U_{Pack}} \\ \dfrac{\eta_{dis}U_{Cell}(1)}{U_{Pack}} & \dfrac{\eta_{dis}U_{Cell}(2)}{U_{Pack}}-1 & \text{L} & \dfrac{\eta_{dis}U_{Cell}(N)}{U_{Pack}} \\ \text{M} & \text{M} & \text{O} & \text{M} \\ \dfrac{\eta_{dis}U_{Cell}(1)}{U_{Pack}} & \dfrac{\eta_{dis}U_{Cell}(2)}{U_{Pack}} & \text{L} & \dfrac{\eta_{dis}U_{Cell}(N)}{U_{Pack}}-1 \end{bmatrix} \tag{C.9}$$

where η_{dis} denotes the discharging balancing efficiency and I_{e_dis} represents the cell discharging balancing current of each equalizer.

The states of the charging and discharging modes of each cell equalizer can be written as

$$\mathbf{S_{dis}} = \begin{bmatrix} S_{dis}(1) & S_{dis}(2) & \text{L} & S_{dis}(N) \end{bmatrix}^{\text{T}} \tag{C.10}$$

$$\mathbf{S_{ch}} = \begin{bmatrix} S_{ch}(1) & S_{ch}(2) & \text{L} & S_{ch}(N) \end{bmatrix}^{\text{T}} \tag{C.11}$$

where $\mathbf{S_{dis}}$ and $\mathbf{S_{ch}}$ denote the states matrices of charging and discharging modes of the equalizers, respectively.

Then, the predictive balancing current for each cell is the sum value of charging balancing currents and discharging balancing currents, which can be governed by

$$\mathbf{I_{bc\_pre}} = \left[I_{bc\_pre}(1) \quad I_{bc\_pre}(2) \quad \mathrm{L} \quad I_{bc\_pre}(N) \right]^{\mathrm{T}} = \mathbf{I_{bc\_ch}}\mathbf{S_{ch}} + \mathbf{I_{bc\_dis}}\mathbf{S_{dis}} \tag{C.12}$$

where $I_{bc\_pre}(i)$ denotes the predictive balancing current of the ith cell.

To control the cell balancing current, the cost function J is defined as

$$J = \sum_{i=1}^{N} \left(I_{bc\_pre}(i) - I_{bc\_ref}(i) \right)^2 \tag{C.13}$$

Since the state combinations in the matrices $\mathbf{S_{dis}}$ and $\mathbf{S_{ch}}$ can be varied, there are different predictive balancing currents can be obtained according to (C.12), thus leading to different cost function values in (C.13). Among the cost function values, the minimum value means that its predictive balancing currents are overall the closest ones to the referenced balancing currents, and therefore its state matrices $\mathbf{S_{dis}}$ and $\mathbf{S_{ch}}$ are employed for controlling the operation modes of cell equalizers.

C.4 Verifications and Discussions

Since the techniques of SOC estimation and battery modeling are not the emphases of this paper, the presented work excludes discussions of these techniques and employs the effective approaches reported in our previous work [C.12]. To investigate the effectiveness of the proposed MPC based balancing strategy, eight simulated cells were randomly set with non-uniform initial SOCs and capacities as shown in Fig. C.2.

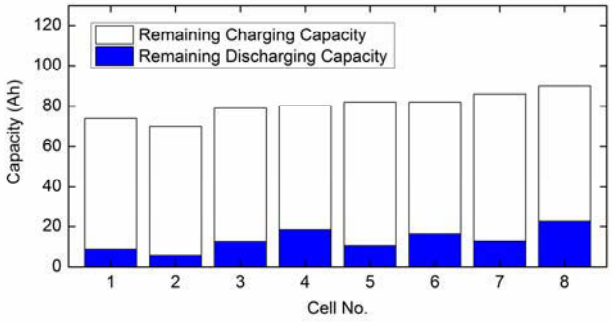

Fig. C.2 Eight simulated cells with non-uniform initial SOCs and capacities.

Since the presented balancing strategies aim at fully charging the battery pack, the balancing strategies are validated during battery charging processes. Figs. C.3(a) and C.3(b) demonstrate balancing results with the average SOC and MPC based strategies, respectively. As can be observed, both the average SOC and MPC based balancing strategies can finally eliminate the SOC imbalance, and each cell can be charged to a high SOC level. The SOC values of the cells with the average SOC strategy shown in Fig. C.3(a) converge to its balancing band in about 3800 s, which is much faster than that with the MPC based strategy. In Fig. C.3(b), the MPC based balancing strategy can converge the cell SOCs to relatively uniform values at the end of charging (EOC).

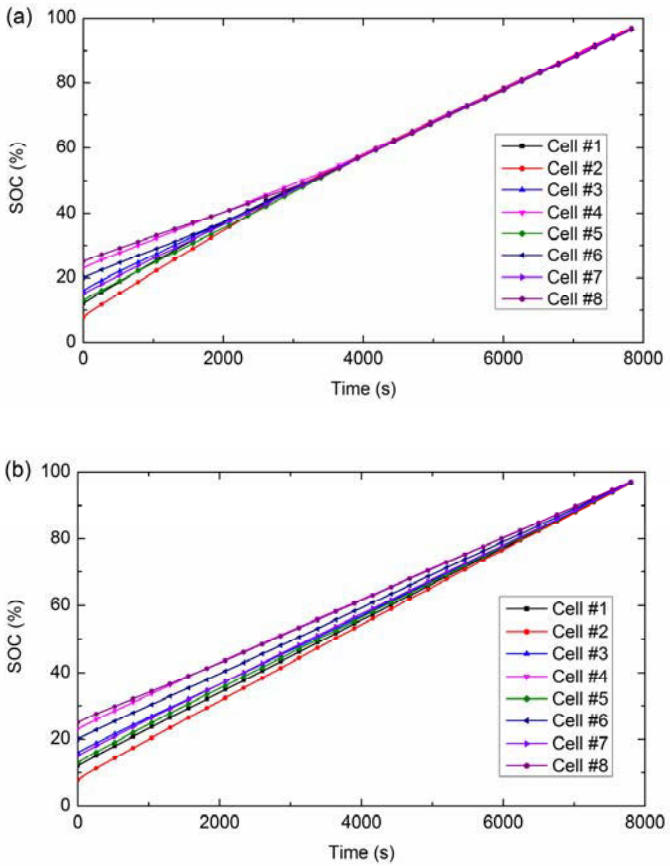

Fig. C.3 Balancing results with (a) the average SOC strategy and (b) the MPC based strategy.

During battery charging and balancing processes, voltage curves of the eight cells are shown in Fig. C.4. At the beginning of battery charging process, the maximum voltage

variance among the eight cells is 130.7 mV. However, the voltage imbalance can be alleviated with these two balancing strategies. As can be seen in Fig. C.4(a), the average SOC balancing strategy can rapidly converge the cell voltages, and the maximum voltage variance can be reduced to 19.1 mV at the EOC. By observing Fig. C.4(b), although the cell voltage convergence rate with the MPC based balancing strategy is slower than that with the average SOC strategy, the maximum voltage variance can also finally reduce to a small value, namely12.2 mV.

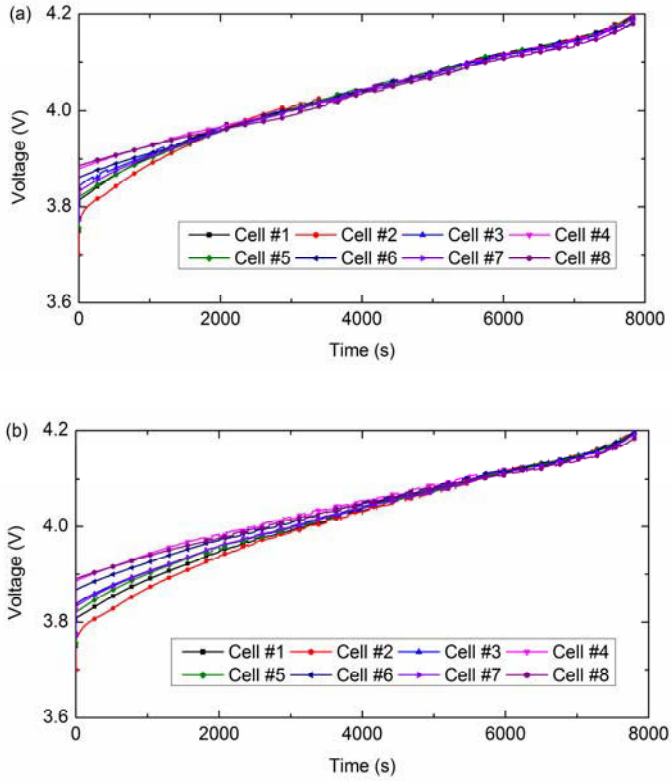

Fig. C.4 Voltage curves of the eight cells during charging and balancing processes with (a) the average SOC strategy and (b) the MPC based strategy.

To demonstrate the operation modes of cell equalizers during battery balancing processes, the cell charging balancing mode is represented by 1; the cell discharging balancing mode is represented by -1; and the idle mode is represented by 0. Figs. C.5 and C.6 demonstrate the operation modes of Cell #2 and Cell #8 equalizers with the average SOC and MPC based balancing strategies, respectively.

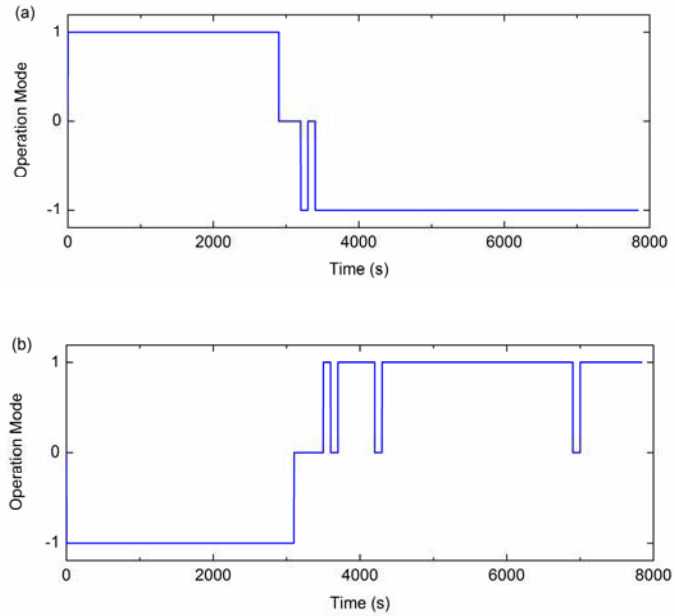

Fig. C.5 The operation modes of cell equalizers with the average SOC strategy, where (a) Cell #2 and (b) Cell #8.

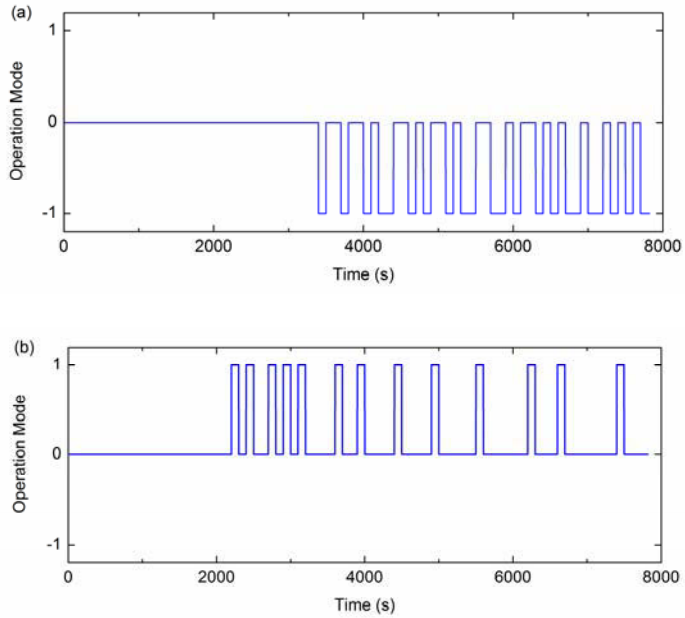

Fig. C.6 The operation modes of cell equalizers with the MPC based strategy, where (a) Cell #2 and (b) Cell #8.

Over-equalization can be observed in both Figs. C.5(a) and C.5(b). In Fig. C.5(a), Cell #2 is charged by its equalizer from the beginning of charging to about 2900 s. After a short

idle rest, the equalizer mainly discharges the cell until the EOC. In contrast to Cell #2, Cell #8 is discharged by its equalizer at the first 3100 s, followed by mostly charging balancing shown in Fig. C.5(b). As can be seen from Fig. C.6(a), with the MPC based strategy, Cell #2 equalizer operates in idle and discharging balancing operation modes, which means that there is no over-equalization occurs during the whole balancing processes. Likewise, there are only idle and charging balancing operation modes in Cell #8 equalizer as depicted in Fig. C.6(b), and no over-equalization can be observed.

The balancing energy consumption can be computed during balancing processes, and with the average SOC and MPC based strategies, they are 1.001×10^5 J and 5.275×10^4 J, respectively. In comparison with the conventional average SOC strategy, the proposed MPC based strategy can effectively avoid over-equalization during balancing process, thus achieving less balancing energy consumption.

Summary

Compared with new battery packs, aged battery packs usually suffer from not only non-uniform cell SOCs and voltages but also non-uniform cell capacities, thus leading to more challenging in balancing strategies. A novel balancing strategy based on the MPC was proposed in this paper for series-connected lithium-ion battery packs, especially for aged battery packs. In the presented work, the balancing system aims at fully charging a battery pack during battery charging process. Therefore, the imbalance cell capacities need to be redistributed, and the required average balancing currents for each cell can be determined by their SOC and capacity values. Bidirectional cell equalizers were employed in the balancing system, and their operation modes can be predicted in advance as well as the balancing currents for each cell. The minimum cost function value between the required average balancing currents and the predicted balancing currents was applied for controlling operation modes of cell equalizers. In comparison with the balancing results of conventional average SOC strategy, the proposed MPC based strategy can converge SOCs of the cells and their voltage values to high and relatively uniform levels at the EOC while reducing balancing energy consumption. The results also demonstrate that the

MPC based strategy can effectively avoid over-equalization. However, the algorithm of the MPC based balancing strategy is more complicated than that of the average SOC strategy, which means more computational efforts are required in the MPC based strategy. The main tasks for reducing the computational cost of the MPC based strategy and implementing it in embedded battery management systems constitute our future work.

References

[C.1] Y. Zheng, M. Ouyang, L. Lu, J. Li, X. Han and L. Xu, "On-line equalization for lithium-ion battery packs based on charging cell voltages: Part 1. Equalization based on remaining charging capacity estimation," *J. Power Sources*, vol. 247, pp. 676-686, 2014.

[C.2] L. McCurlie, M. Preindl and A. Emadi, "Fast Model Predictive Control for Redistributive Lithium-Ion Battery Balancing," *IEEE Trans. Ind. Electron.*, vol. 64, pp. 1350-1357, 2017.

[C.3] J. Gallardo-Lozano *et al*, "Battery equalization active methods," *J. Power Sources*, vol. 246, pp. 934-949, 2014.

[C.4] F. Baronti, R. Roncella and R. Saletti, "Performance comparison of active balancing techniques for lithium-ion batteries," *J. Power Sources*, vol. 267, pp. 603-609, 2014.

[C.5] M. Uno and A. Kukita, "Bidirectional PWM converter integrating cell voltage equalizer using series-resonant voltage multiplier for series-connected energy storage cells," *IEEE Trans. on Power Electron.*, vol. 30, pp. 3077-3090, 2015.

[C.6] C. Lim *et al*, "A modularized equalization method based on magnetizing energy for a series-connected lithium-ion battery string," *IEEE Trans. on Power Electron.*, vol. 29, pp. 1791-1799, 2014.

[C.7] H. Xiong, Y. Fu and K. Dong, "A Novel Point-to-Point Energy Transmission Voltage Equalizer for Series-Connected Supercapacitors," *IEEE Trans. on Veh. Technol.*, vol. 65, pp. 4669-4675, 2016.

[C.8] F. Mestrallet et al, "Multiphase interleaved converter for lithium battery active balancing," *IEEE Trans. on Power Electron.*, vol. 29, pp. 2874-2881, 2014.

[C.9] W. Huang and J. A. A. Qahouq, "Energy sharing control scheme for state-of-charge balancing of distributed battery energy storage system," *IEEE Trans. Ind. Electron.*, vol. 62, pp. 2764-2776, 2015.

[C.10] L. Zheng, J. Zhu and G. Wang, "A comparative study of battery balancing strategies for different battery operation processes," in *Transportation Electrification Conference and Expo (ITEC), 2016 IEEE*, 2016, pp. 1-5.

[C.11] Y. Wang et al, "A novel active equalization method for lithium-ion batteries in electric vehicles," *Appl. Energy*, vol. 145, pp. 36-42, 2015.

[C.12] L. Zheng, L. Zhang, J. Zhu, G. Wang and J. Jiang, "Co-estimation of state-of-charge, capacity and resistance for lithium-ion batteries based on a high-fidelity electrochemical model," *Appl.Energy*, vol. 180, pp. 424-434 2016.

[C.13] L. Zheng, J. Zhu, G. Wang, D. D. Lu, P. McLean, and T. He, "Model predictive control based balancing strategy for series-connected lithium-ion battery packs", 2017 19*th European Conference on Power Electronics and Applications, EPE'*17 *ECCE Europe*, pp. 1-8, 11-14 September 2017, Warsaw, Poland.

APPENDIX D

LIST OF PUBLICATIONS DURING THE THESIS PROJECT

D.1 Publications based on the Thesis Work

- L. Zheng, J. Zhu, G. Wang, T. He, and Y. Wei, "Novel methods for estimating lithium-ion battery state of energy and maximum available energy", *Applied Energy*, vol. 178, pp. 1-8, 2016.

- L. Zheng, L. Zhang, J. Zhu, G. Wang, and J. Jiang, "Co-estimation of state-of-charge, capacity and resistance for lithium-ion batteries based on a high-fidelity electrochemical model", *Applied Energy*, vol. 180, pp. 424-434, 2016.

- L. Zheng, J. Zhu, G. Wang, D. D. Lu, and T. He, "Instantaneous available power prediction of lithium-ion batteries based on the lithium concentration at the surface of solid particles of battery electrodes", DOI 10.1109/TPEL.2018.2791965, *IEEE Transactions on Power Electronics*.

- L. Zheng, J. Zhu, G. Wang, D. D. Lu, and T. He, "Incremental capacity analysis and differential voltage analysis based state of charge and capacity estimation for lithium-ion batteries", *Energy*, vol. 150, pp. 759-769, 2018.

- L. Zheng, J. Zhu, G. Wang, D. D. Lu, and T. He, "Differential voltage analysis based state of charge estimation methods for lithium-ion batteries using extended Kalman filter and particle filter", *Energy*, vo. 158, pp. 1028-1037, 2018.

- L. Zheng, J. Zhu, and G. Wang, "A Comparative Study of Battery Balancing Strategies for Different Battery Operation Processes", 2016 *IEEE Transportation Electrification Conference and Expo* (*ITEC*), pp. 1-5, 27-29 June 2016, Dearborn, MI, USA.

- L. Zheng, J. Zhu, G. Wang, D. D. Lu, P. McLean, and T. He, "Experimental analysis and modeling of temperature dependence of lithium-ion battery direct current resistance for power capability prediction", 2017 20*th International Conference on Electrical Machines and Systems* (*ICEMS*), pp. 1-4, 11-14 August 2017, Sydney, NSW, Australia.

- L. Zheng, J. Zhu, G. Wang, D. D. Lu, P. McLean, and T. He, "Model predictive control based balancing strategy for series-connected lithium-ion battery packs", 2017 19*th European Conference on Power Electronics and Applications, EPE'*17 *ECCE Europe*, pp. 1-8, 11-14 September 2017, Warsaw, Poland.

D.2 Planned Publications

- "Estimation techniques of key lithium-ion battery states in energy storage sector: A review of the state-of-the-art" (in preparing)